Driving force computation for fatigue crack growth based on the integration of fracture mechanics with artificial neural networks

S. Navid S. Mortazavi

A Thesis
In the Department of
Mechanical, Industrial, and Aerospace Engineering

Presented in Partial Fulfillment of the Requirements for the Degree of
Doctor of Philosophy (Mechanical Engineering) at
Concordia University
Montreal, Quebec, Canada

September 2023

CONCORDIA UNIVERSITY

School of Graduate Studies

This is to certify that the thesis prepared

By: Seyed Navid Seyed Mortazavi

Entitled: **Driving force computation for fatigue crack growth based on the integration of fracture mechanics with artificial neural networks**

And submitted in partial fulfilment of the requirements for the degree of

Doctor of Philosophy (Mechanical Engineering)

Complies with the regulations of the University and meets the accepted standards with respect to originality and quality.

Signed by the final examining committee:

Dr. Pantcho Stoyanov	Chair
Dr. Azzeddine Soulaïmani	External examiner
Dr. Biao Li	External to program
Dr. Ion Stiharu	Examiner
Dr. Behrooz Yousefzadeh	Examiner
Dr. Ayhan Ince	Thesis supervisor

Approved by

Date of Defense: 20, September 2023

Abstract:

Driving force computation for fatigue crack growth based on the integration of fracture mechanics with artificial neural networks

S. Navid S. Mortazavi, PhD.

Concordia University, 2023

Fracture mechanics principles play a crucial role in characterizing fatigue crack growth (FCG) rates based on the concept of driving force. Two well-known and promising driving forces in fracture mechanics are the stress intensity factor range (ΔK) and cyclic J-integral (ΔJ). While ΔK is a linear elastic fracture mechanics (LEFM) parameter, ΔJ is an elasto-plastic fracture mechanics (EPFM) parameter. However, both driving forces have limitations when it comes to FCG characterization. ΔK fails to account for relatively large-scale plasticity, rendering it inadequate for describing the short crack (SC) regime. On the other hand, ΔJ inherently has the potential to consider large-scale plasticity, but its application on real engineering problems is challenging. The difficulty arises from the need to perform complex and time-consuming elasto-plastic analyses to compute the actual elasto-plastic stress, strain, and displacement fields near the crack tip for the calculation of ΔJ. This study explores the integration of artificial neural networks (ANNs) with fracture mechanics principles to overcome these challenges. The research is carried out in three phases:

Phase 1 focuses on integrating ANN with ΔK as a LEFM parameter. Unlike ΔK-based models that solely formulate FCG rate based on the maximum stress intensity factor (K_{max}) and ΔK, this approach incorporates other controlling parameters. FCG rate is considered as a function of ΔK and stress ratio (R) in the long crack (LC) regime, and as a function of stress level (σ) in addition to ΔK and R in the SC regime. ANNs are developed to reveal these non-linear and complex functions in both regimes, using experimental FCG data sets from Ti-6Al-4V titanium alloy, 2024-T3, and 7075-T6 aluminum alloys for training and verification. Although this phase shows potential, the reliance on limited FCG data sets due to costly procedures remains a challenge. Moreover, ΔK as a LEFM parameter inherently cannot handle large-scale plasticity in the SC regime.

To address these issues, a novel approach is suggested and investigated in Phases 2 and 3. Phases 2 and 3 propose replacing ΔK with ΔJ as a promising EPFM driving force and combining finite element (FE) analyses with ANN algorithms. Firstly, the implementation of FE models provides ample datasets for training the ANNs. Secondly, this integration allows for the determination of ΔJ through a linear elastic solution rather than complex elasto-plastic analyses.

Phase 2 involves FE analyses to determine stress, strain, and displacement fields under elastic and elasto-plastic states near a crack tip for a notched specimen made of stainless steel (SS304) under monotonic loading. Hypothetical elastic stress, strain, and displacement fields around the crack tip are used as input data for the developed ANNs. The corresponding actual elasto-plastic stress, strain, and displacement fields are the output of the ANNs. Well-trained ANNs successfully establish relationships between the elastic and elasto-plastic fields, enabling predictions of elasto-plastic stress, strain, and displacement based on hypothetical elastic data. An in-house model based on the equivalent domain integral (EDI) method is developed to determine J-integral as a function

of stress, strain, and displacement fields around the crack tip. This model can be served as a post-processing step after elasto-plastic FE analyses. In addition, it can be employed to determine J-integral based on ANN predictions. The accuracy of the in-house model is verified by the J-integral data in the literature. ANN predicted elasto-plastic stress, strain, and displacement fields are compared and verified with those obtained from elasto-plastic FE analyses. The proposed method demonstrates significant accuracy in determining J-integral values.

Phase 3 extends the approach to cyclic loading conditions. The developed ANNs are trained on cyclic stress, strain, and displacement fields. The in-house model is upgraded to determine ΔJ under cyclic loading. The accuracy of cyclic ANN-predicted elasto-plastic stress, strain, and displacement fields is compared with those obtained from elasto-plastic FE models, resulting in significant agreement. The in-house model is verified by the ΔJ data in the literature. Moreover, ΔJ values predicted by the proposed model are comparable to those directly determined by elasto-plastic FE analyses.

The integration of artificial neural networks with fracture mechanics principles provides valuable insights into overcoming traditional driving force limitations in FCG characterization. This research offers a promising avenue for future research and practical applications in the field of fatigue crack growth analysis.

Dedications

To my beloved supportive parents, Sima and Masoud

Acknowledgments

I would like to express my heartfelt gratitude to my esteemed supervisor, Prof. Ayhan Ince, for his unwavering guidance, support, and encouragement throughout this research journey. His profound knowledge, valuable insights, and constructive feedback have been instrumental in shaping the direction of this thesis. I am deeply grateful for his patience, dedication, and mentorship, which have significantly enriched my academic and personal growth.

I would like to extend my sincere appreciation to Concordia University and Prof. Ayhan Ince for providing me with the opportunity to pursue this research and for granting me the resources necessary to carry out my study.

Lastly, I would like to extend my heartfelt appreciation to my parents for their unconditional love, constant encouragement, and unending support. Their belief in my abilities and their sacrifices have been the cornerstone of my achievements. I am eternally grateful for their presence in my life, serving as a constant source of strength and motivation.

Co-Authorship

To adhere to the requirements of a manuscript-based format, this thesis has been developed in accordance with these regulations. Coauthored works are therefore included in chapters 3, 4, and 5. Following is a description of the contribution of each coauthor other than the author of this thesis:

Chapter 3 Article 1 "An Artificial Neural Network Modeling Approach for Short and Long Fatigue Crack Propagation", Reprinted from the published article with the DOI of https://doi.org/10.1016/j.commatsci.2020.109962. Contribution of the Authors:

S. Navid S. Mortazavi: Conceptualization, All the coding & modelling, Analysis of the results, validation, writing the manuscript.

Ayhan Ince: Conceptualization, Review & editing the manuscript, Supervision, and Funding acquisition.

Chapter 4 Article 2 "Artificial Neural Networks-Based J-integral Prediction for Cracked Bodies Under Elasto-Plastic Deformation State- Monotonic Loading", Reprinted from the published article with the DOI of https://doi.org/10.1016/j.ijfatigue.2022.107311. Contribution of the Authors:

S. Navid S. Mortazavi: Conceptualization, All the coding & modelling, Analysis of the results, validation, writing the manuscript.

Ayhan Ince: Conceptualization, Review & editing the manuscript, Supervision, and Funding acquisition.

Chapter 5 Article 3 "Artificial Neural Networks-Based Modeling Approach for Elasto-Plastic Cyclic J-integral Prediction for Cracked Bodies", Ready for submission:

S. Navid S. Mortazavi: Conceptualization, All the coding & modelling, Analysis of the results, validation, writing the manuscript.

Ayhan Ince: Conceptualization, Review & editing the manuscript, Supervision, and Funding acquisition.

Table of Contents

List of Figures

List of Tables

Abbreviations

AI	Artificial Intelligence
ANN	Artificial Neural Network
CLD	Constant Life Diagram
CNN	Convolution Neural Network
a	crack length
CTOD	Crack Tip Opening Displacement
DT	Decision Tree
DMD	Direct Metal Deposition
EPFM	Elasto-Plastic Fracture Mechanics
EDI	Equivalent Domain Integral
ESED	Equivalent Strain Energy Density
ELM	Extreme Learning Machine
FCG	Fatigue Crack Growth
FE	Finite Element
FEM	Finite Element Model
HCF	High Cycle Fatigue
HCF	High Cycle Fatigue
LEFM	Linear Elastic Fracture Mechanics
ε_{ij}^{a}	local actual strain tensor
σ_{ij}^{e}	local actual stress tensor
ε_{ij}^{e}	local elastic strain tensor
σ_{ij}^{e}	local elastic stress tensor

LC	Long Crack
LCF	Low Cycle Fatigue
ML	Machine Learning
MLA	Machine Learning Algorithm
MAE	Mean Absolute Error
MRE	Mean Relative Error
MSE	Mean Square Error
σ_m	mean stress
MSC	Microstructurally Short Crack
NN	Neural Network
S	nominal stress
N_i	number of cycles for crack initiation
N_p	number of cycles for crack propagation
ODB	Output Database
POE	Percentage of Error
PSC	Physically Short Crack
PDZ	Plastic Deformation Zone
r_y	plasticity size radius
RBFNN	Radial Basis Function Neural Network
ReLU	Rectified Linear Unit
RNN	Recurrent Neural Network
RMSE	Root Mean Square Error

SC	Short Crack
SRBF	Spread of Radial Basis Function
W	strain energy density
G	strain energy release rate
σ_a	stress amplitude
K	stress intensity factor
SIF	Stress Intensity Factor
ΔK	stress intensity factor range
$\Delta\sigma$	stress range
R	stress ratio
SVM	Support Vector Machine
N_t	total number of cycles
VCE	Virtual Crack Extension

Chapter 1:

Introduction and Literature review

In this chapter, fatigue crack growth (FCG), its definition and significance in the industry are briefly provided. Additionally, different fatigue crack regimes during the progress of crack propagation before the final fracture are discussed. Subsequently, the primary conventional approaches to determine the total life of a component subjected to fatigue are categorized. The significant studies in the literature for each category are reviewed to specify the limitations of current models in accurately and efficiently determining the fatigue life of engineering components. Furthermore, neural network algorithms as machine learning methods are introduced. Finally, the application of neural networks in the fields of fatigue crack growth and elasto-plastic mechanics is discussed.

1.1. Fatigue crack growth and different crack regimes

The fatigue damage process comprises multiple damage phases, including crack nucleation, crack growth, including early propagation of short cracks and long crack propagation, and the final fracture [1]. It is broadly accepted that fatigue failure is the most common failure mode in numerous industries [2]. Since the fatigue damage process occurs under cyclic loading, the primary purpose of almost all investigations on fatigue failure mode is to determine the fatigue life or the total number of loading cycles (N_t) a component withstands before the final fracture. It is widely accepted that the total fatigue life includes the number of loading cycles that cause the initiation of incipient crack (N_i), and subsequently, the number of loading cycles within crack propagation from its initial to its final length just before the final fracture, as shown in Eq. (1.1)

$$N_t = N_i + N_p \tag{1.1}$$

The crack initiation is defined based on its detectability. A crack is considered to be initiated when it is '0.01 inch-long', as a criterion firstly suggested by the US Navy. Consequently, crack initiation is defined as "*the inception and growth of a short crack to the experimentally detectable limit*" [1].

Fatigue crack propagation consists of different crack regimes based on the crack size and the controlling parameters that govern the FCG behavior. FCG involves the propagation of short cracks (SCs) and long cracks (LCs). SCs are classified as those cracks shorter than 0.5 to 1 mm. The microstructure significantly affects the FCG behavior in the SC regime. SCs are divided into microstructurally short cracks (MSCs) and physically short cracks (PSCs). The length of an MSC is comparable with the microstructural characteristics of the material, i.e., the grain size. As a result, the material cannot be considered a continuum at that length scale. However, the size of a PSC is adequately long to assume the material behavior as a continuum. The size of LCs is longer than 0.5 to 1 mm. It is widely acknowledged that microstructural characteristics have no influence on the LC regime [1]. The different crack regimes based on the crack size are schematically shown in Figure 1.1.

There are mainly two distinguished approaches to determine the fatigue life of components: 1) the "crack initiation" approach and 2) the "fracture mechanics" approach discussed as follows:

1.2. Crack initiation

The crack nucleation-based models consider the number of loading cycles for crack initiation (N_i) as the total life. In other words, such models assume that components initially have no cracks and the components should be replaced or repaired after the crack nucleation. The crack initiation methods are categorized based on stress-life (S-N approach) and strain-life (ε-N approach)

prediction methods. S-N approaches quantify fatigue damage and, subsequently, fatigue life based on the nominal stress. On the other hand, the ε-N approach employs the local notch tip strains and stresses to determine the fatigue damage. Since crack initiation methods are noticeably applicable in many industries, the S-N approach [3-5] and ε-N approach [6-12] have received great interest among the researchers. One of the most critical shortcomings of the crack initiations approach is the principal assumption that components have no pre-existing cracks. According to most of the fabrication processes, such an assumption contradicts reality.

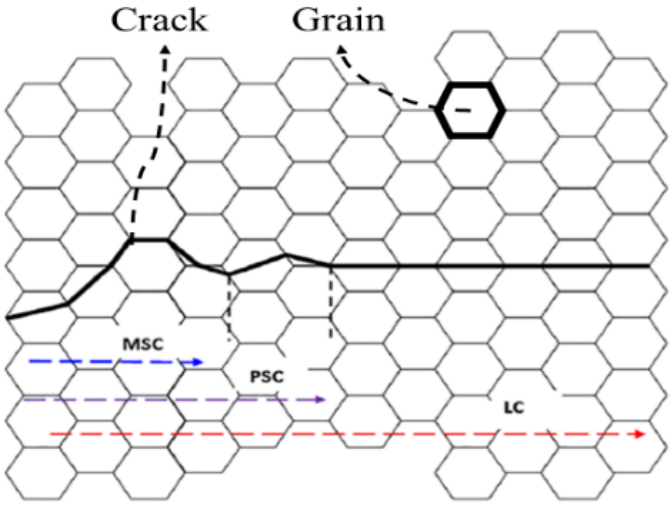

Figure 1.1 Schematic of different crack regimes [13]

1.3. Fracture Mechanics

To the contrary of the crack initiation approach, the fracture mechanics approach assumes that the cracks are pre-existing in structures. Such principal assumption is in more accordance in comparison with the one in crack initiation approach. The main aim of fracture mechanics is to determine the FCG rate based on a proper driving force, as shown in Eq. (1.2):

$$\frac{da}{dN} = f(driving\ force) \tag{1.2}$$

N and a are the number of cycles and crack size, respectively. There is significant number of controlling parameters affecting the FCG rate, e.g. the geometry of structures, the loading type, alternative stress, mean stress, etc. The suggested driving force in Eq. (1.2) is required to be comprehensive to account for as many controlling parameters affecting the FCG rate in order to accurately calculate the fatigue life of structures. Almost all of the fracture mechanics-based models can be classified into the two main groups based on the elected driving force. The first group is linear elastic fracture mechanics (LEFM), and the second one is elasto-plastic fracture mechanics (EPFM) discussed in detail as follows:

1.3.1. Linear elastic fracture mechanics

On of the most prominent parameters in fracture mechanics is the stress intensity factor (K). The stress intensity factor (SIF) is defined as "*the magnitude of the stress singularity at the tip of a*

mathematically sharp crack in a linear elastic material" [14] or a "*direct measure of the elastic strain energy in a stressed material that contains a crack*" [15]. The SIF is mainly used to specify the stress state around the crack tip of an elastic material in fracture mechanics. The SIF is quantified by Eq. (1.3):

$$K = YS\sqrt{\pi a} \tag{1.3}$$

where Y represents the geometry factor, S stands for the nominal stress, and a denotes the crack length. Two well-known SIF-based models used to characterize the stress/strain field around the tip of cracks and deep notches are the Westergaard method [16] and the Creager-Paris solution [17]. The closed form Creager-Paris solution under mode I type of loading, which determines the stress distribution in the vicinity of a blunt crack tip, is shown in Eq. (1.4):

$$\begin{aligned}
\sigma_x &= \frac{K}{\sqrt{2\pi r}} cos\left(\frac{\theta}{2}\right)\left[1 - sin\left(\frac{\theta}{2}\right) sin\left(\frac{3\theta}{2}\right)\right] - \frac{K}{\sqrt{2\pi r}}\frac{\rho}{2r} cos\left(\frac{3\theta}{2}\right) \\
\sigma_y &= \frac{K}{\sqrt{2\pi r}} cos\left(\frac{\theta}{2}\right)\left[1 + sin\left(\frac{\theta}{2}\right) sin\left(\frac{3\theta}{2}\right)\right] + \frac{K}{\sqrt{2\pi r}}\frac{\rho}{2r} cos\left(\frac{3\theta}{2}\right) \\
\tau_{xy} &= \frac{K}{\sqrt{2\pi r}} sin\left(\frac{\theta}{2}\right) cos\left(\frac{\theta}{2}\right) cos\left(\frac{3\theta}{2}\right) - \frac{K}{\sqrt{2\pi r}}\frac{\rho}{2r} sin\left(\frac{3\theta}{2}\right)
\end{aligned} \tag{1.4}$$

where ρ is the radius of the crack tip, K stands for the SIF, r is the radial distance between an arbitrary point and the origin of coordinate system, and θ is the angle between the r and the horizontal coordinate axis. The origin of the coordinate system is located behind the crack tip at a distance of $\left|\frac{\rho}{2}\right|$ as schematically shown in Figure 1.2.

It has been widely acknowledged that stress and strain fields around the crack tip govern the behavior of FCG. As a result, Paris and Erdogan [18] suggested the SIF range ($\Delta K = K_{max} - K_{min}$) as the driving force in Eq. (1.2). K_{max} and K_{min}, correspond to the maximum and minimum stress levels under cyclic loading, as schematically shown in Figure 1.3 for constant amplitude loading. As depicted in Figure 1.3, the stress amplitude (σ_a), mean stress (σ_m), and stress range ($\Delta\sigma$) are determined by Eq. (1.5)-(1.7).

$$\sigma_a = \frac{\sigma_{max} - \sigma_{min}}{2} \tag{1.5}$$

$$\sigma_m = \frac{\sigma_{max} + \sigma_{min}}{2} \tag{1.6}$$

$$\Delta\sigma = \sigma_{max} - \sigma_{min} \tag{1.7}$$

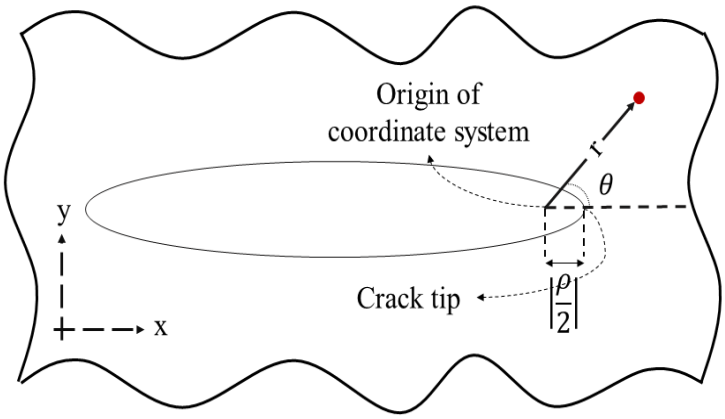

Figure 1.2 Schematic of coordinate system in Creager-Paris solution.

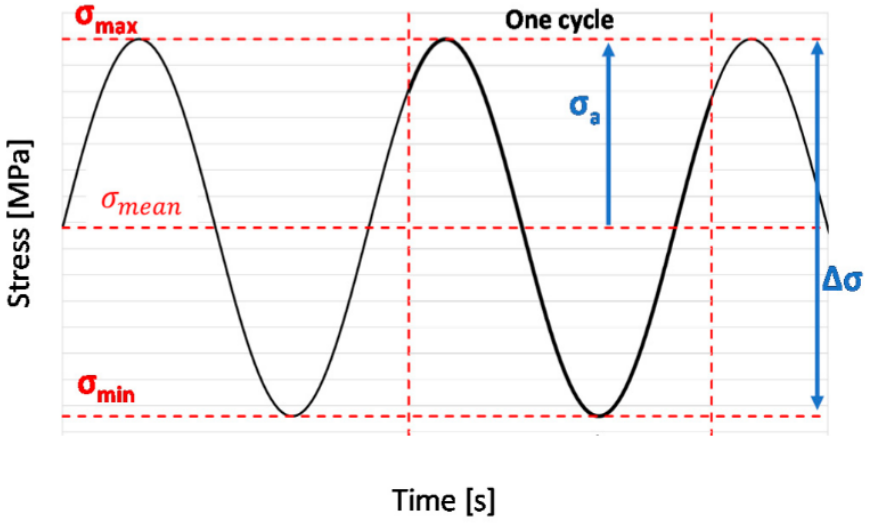

Figure 1.3 Main characteristics of a constant amplitude loading [19].

The model suggested by Paris and Erdogan is one of the most well-known fracture mechanics models used to characterize FCG rate. This model is known as Paris' law as expressed in Eq. (1.8):

$$\frac{da}{dN} = C\Delta K^m \tag{1.8}$$

where a and N represent crack size and the number of loading cycles, respectively, while C and m are the material constants. The Paris model is schematically shown in Figure 1.4. As depicted in Figure 1.4, Paris' law depicts the second phase, which is between the ΔK_{th} and ΔK_c. The SIF range threshold (ΔK_{th}) specifies the minimum driving force required to cause the fatigue crack propagation in the LC regime and the critical SIF range (ΔK_c) is corresponded to the final crack size and the instantaneous fracture. Although Paris' law is considered as one of the principals of LEFM, it has noticeable shortcomings. One of the most crucial deficiencies of the Paris model is its incapability to account for the mean stress or R-ratio. R-ratio, as an influential parameter in FCG behavior, is defined as Eq. (1.9).

$$R = \frac{\sigma_{min}}{\sigma_{max}} \tag{1.9}$$

As schematically shown in Figure 1.5, the Paris model exhibits different curves under various R-ratios in the LC regime for a particular material. Consequently, the FCG rate can be quantified by means of Eq. (1.10) as a function of ΔK and R.

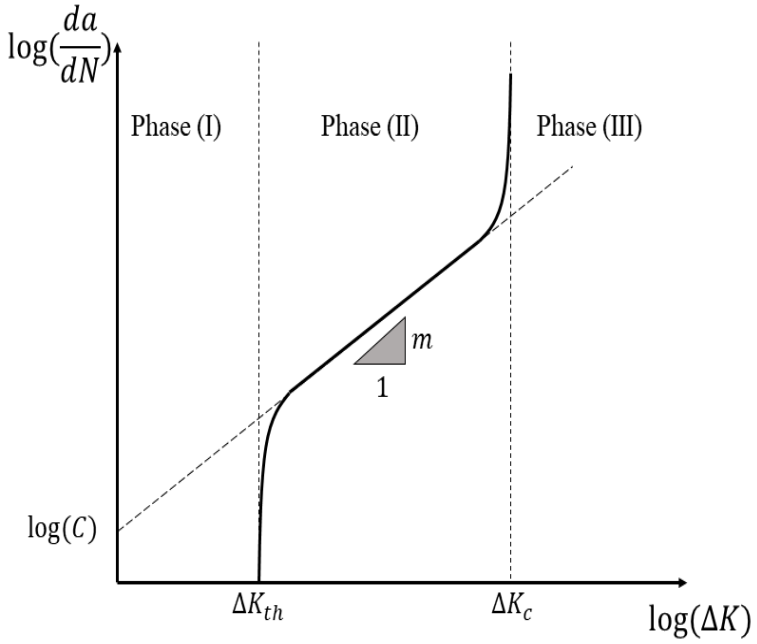

Figure 1.4 Schematic of Paris' law.

$$\left.\frac{da}{dN}\right|_{LC} = f(\Delta K, R) \tag{1.10}$$

However, it has been demonstrated that such characterization, as illustrated in Eq. (1.10) is only feasible in the LC regime [1]. The inherent disparities between the LC and SC regimes, known as "similitude breakdown" are as follows [1]:

i) FCG rates in the SC regime are higher than those in the LC regime $\left(\frac{da}{dN_{SC}} > \frac{da}{dN_{LC}}\right)$.

ii) The threshold in the SC regime is lower than that in the LC regime $\left(\Delta K_{th,SC} < \Delta K_{th,LC}\right)$.

iii) The threshold in the SC regime varies with crack length, in contrast to the LC regime, where the threshold remains constant.

Experimental FCG data demonstrate that the FCG rate in the SC regime can be quantified based on stress level (σ) in addition to the ΔK and R as shown in Eq. (1.11)

$$\left.\frac{da}{dN}\right|_{SC} = f(\Delta K, R, \sigma) \tag{1.11}$$

The FCG rate and the mentioned similitude breakdown schematically shown in Figure 1.6.

The limitations of Paris' law have prompted many researchers to advocate for various ΔK-based models that account for the R-ratio effect.

Elber [20] and Newman [21] were among the first to propose the concept of crack closure as a crucial parameter that significantly influences the FCG behavior. It was claimed that comprehending the concept of plasticity-induced crack closure is pivotal in quantifying the effect of R-ratio on the FCG rate. According to the concept of plasticity-induced crack closure, plastic deformation zone (PDZ) forms ahead of a relatively short crack, as depicted schematically in Figure 1.7 (a). As the crack propagates, it penetrates through this PDZ. As a result, the crack-wake plasticity is formed. Consequently, the surfaces of a relatively larger crack size become involved with the crack-wake plasticity and its closure effect. The influence of the crack-wake plasticity increases and finally stabilizes once the crack enters the LC regime. It has been widely acknowledged by many researchers that the change in slope observed in the load-displacement curve during fatigue crack propagation results from the plasticity-induced crack closure concept [22]. To determine the SIF at the point of crack closure corresponding to the change in slope in the load-displacement curve, it was suggested that both the opening SIF (K_{op} during loading) and closing SIF (K_{cl} during unloading) must be specified [23]. Consequently, the effective SIF range (see Eq. (1.12)) was proposed as the driving force to calculate the FCG rate.

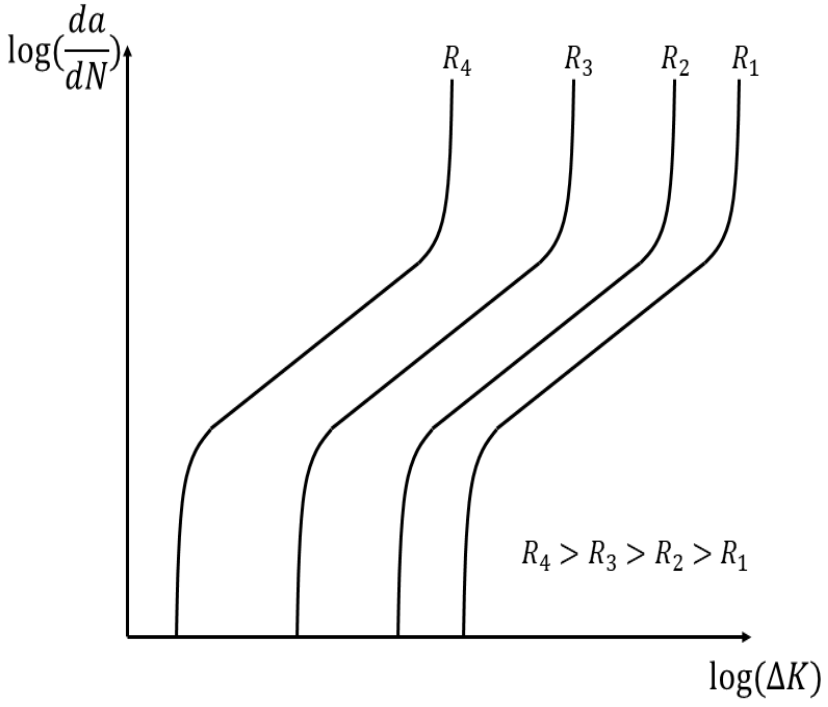

Figure 1.5 The effect of R-ratio on FCG.

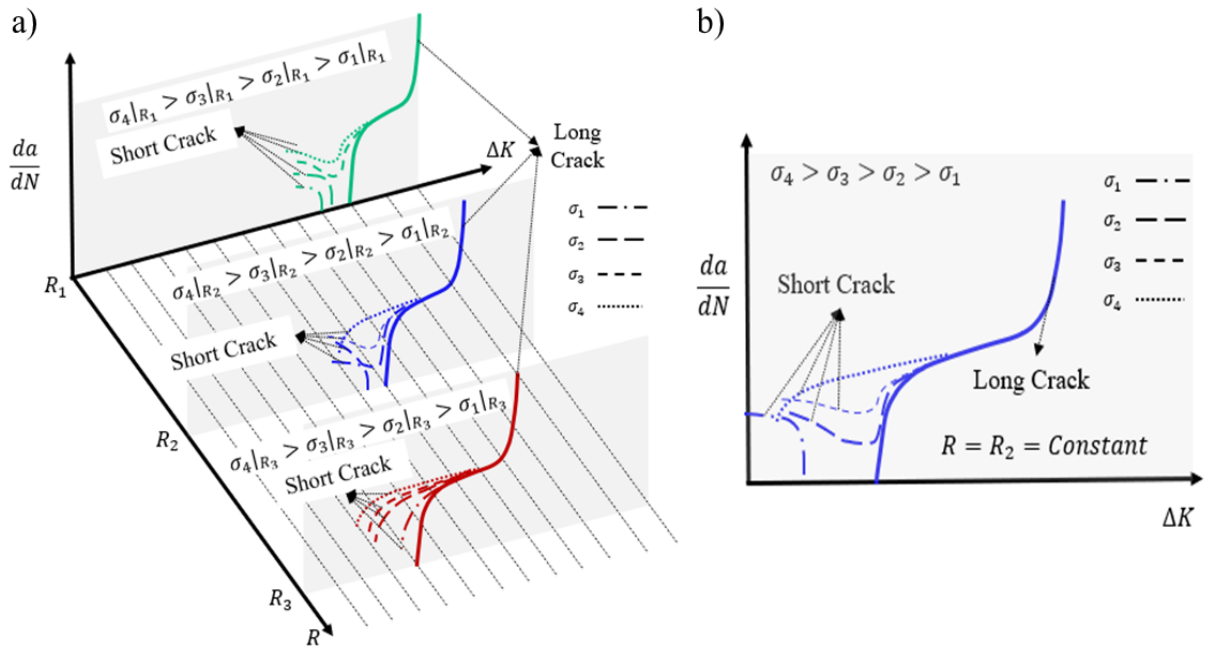

Figure 1.6 FCG rate in the SC and LC regime: a) 3D view for different R-ratios, b) 2D view for a constant R-ratio.

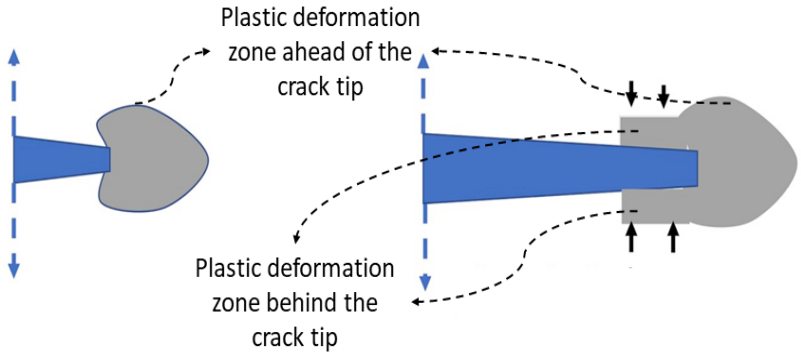

Figure 1.7 Description of plasticity induced crack closure [1].

$$\Delta K_{eff} = K_{max} - K_{op}(or\ K_{cl}) \tag{1.12}$$

The literature comprises numerous studies, ΔK-based models, and finite element (FE) analyses that focus on crack closure [24-36]. Among these models, the NASGRO model, known as the Forman/Mettu equation [37], shown in Eq. (1.13), stands out as one of the most renowned crack closure-based models.

$$\frac{da}{dN} = C\left(\frac{1-f}{1-R}\Delta K\right)^n \frac{\left(1-\frac{\Delta K_{th}}{\Delta K}\right)^p}{\left(1-\frac{K_{max}}{K_{crit}}\right)^q} \tag{1.13}$$

where R is the stress ratio, ΔK_{th} is the SIF threshold, K_{crit} is the critical value of SIF, C, n, p, and q are calibration coefficients, and f is the Newman's function describing the crack closure. The mentioned parameters are discussed in detail in the literature [38].

Crack closure-based models have significantly advanced the characterization of FCG rates in terms of applicability. Therefore, these models have found practical applications even in the aerospace industry. Nevertheless, uncertainties and questions have emerged regarding whether crack closure truly serves as the primary lost-controlling parameter in ΔK-based models. Diverse perspectives have been proposed to reinforce these uncertainties [1]. One of the most critical points among these perspectives is the revelation that the change in slope observed in load-displacement curves may also be attributed to the presence of a PDZ ahead of the crack tip during the development of a monotonic plastic zone [39, 40]. Additionally, numerous constants need to be calibrated in the majority of crack closure-based models, which presents a considerable challenge in many cases. These uncertainties and the need for extensive calibrations have hindered the widespread success of crack closure-based models, especially in the SC regime.

Besides the crack-closure concept, the "Unified approach" has garnered significant interest among researchers as a means to modify the ΔK-based models in order to address the effect of R-ratio, which is not considered in Paris' law. The Unified approach proposes the inclusion of K_{max} in addition to ΔK as part of the driving force in Eq. (1.2). One of the initial models based on the two parameter driving force was proposed by Walker [41] as shown in Eq. (1.14).

$$\frac{da}{dN} = C[(1-R)^p K_{max}]^\gamma = C\left[\Delta K^{(1-p)} K_{max}^P\right]^\gamma \tag{1.14}$$

where p and γ are constants that need to be determined based on the procedure discussed in the literature [41]. The walker model was later modified by Donald and Paris [42]. While both models demonstrate significant agreement with FCG rate data in cases of relatively higher R-ratios, this agreement diminishes notably in situations with lower R-ratios. To enhance the accuracy of the two-parameter driving force-based model, Kujawski [43] proposed replacing ΔK with the tensile part of the stress intensity factor range (ΔK^+), as shown in Eq. (1.15).

$$\frac{da}{dN} = C\left[(\Delta K^+)^{(1-p)} K_{max}^p\right]^\gamma \tag{1.15}$$

Kujawski's model indicates noteworthy correlation with experimental FCG data. However, the correlation for positive R-ratios is significantly higher than that within the range of negative R-ratios. The two-parameter driving force-based model was also proposed by Sadananda and Vasudevan [44, 45]. Sadananda and Vasudevan [44] claimed that two distinct thresholds should be taken in to account in addition to the two-parameter driving force. It was suggested that both K_{max} and ΔK must exceed their threshold values, denoted as $K_{max,th}$ and ΔK_{th}, respectively, in order to cause fatigue crack propagation. Noroozi et al. [46, 47] proposed employing the residual SIF (K_r) in addition to the two-parameter driving force and two thresholds. That model is known as the UniGrow model shown in Eq. (1.16):

$$\frac{da}{dN} = C\left[\left(K_{max,tot}\right)^p (\Delta K_{tot})^{1-p}\right]^\gamma \tag{1.16}$$

where p and γ are the constants that need to be determine based on the procedure discussed in the literature [46] and $K_{max,tot}$ and ΔK_{tot} are defined as Eq. (1.17)-(1.18).

$$K_{max,tot} = K_{max} + K_r \tag{1.17}$$

$$\Delta K_{tot} = \Delta K + K_r \tag{1.18}$$

where residual SIF (K_r) is defined as:

$$K_r = \int_0^a \sigma_r(x) m(x,a) dx \tag{1.19}$$

where a is the crack length, $m(x,a)$ is the weight function determined by the procedure discussed in the literature [48], and σ_r is the residual stress ahead of the crack tip, and x is the coordinate axis along the crack axis. It should be noted that the crack is considered a micro notch in the UniGrow model.

UniGrow model is considered one of the most recent and significant improvement in LEFM. This model indicates that a proper driving force can account for different controlling parameters affecting FCG rate. The UniGrow model demonstrates that by employing a promising two-parameter driving force to characterize FCG rate, different curves based on various R-ratios collapse into a single FCG curve predicted by the model for each material, as schematically shown in Figure 1.8. This highlights the importance of using a comprehensive and appropriate driving force in fracture mechanics. The UniGrow model has received significant attention in many studies [49-54]. Unfortunately, application of UniGrow model or unified approaches, in general, has not been reported successful so far in the case of the SC regime [55, 56]. It should be emphasized that the success of the UniGrow model in the LC regime is attributed to the employment of residual SIF (K_r) accounting for the effects of residual stress field ahead of the crack tip in addition to using a two-parameter driving force.

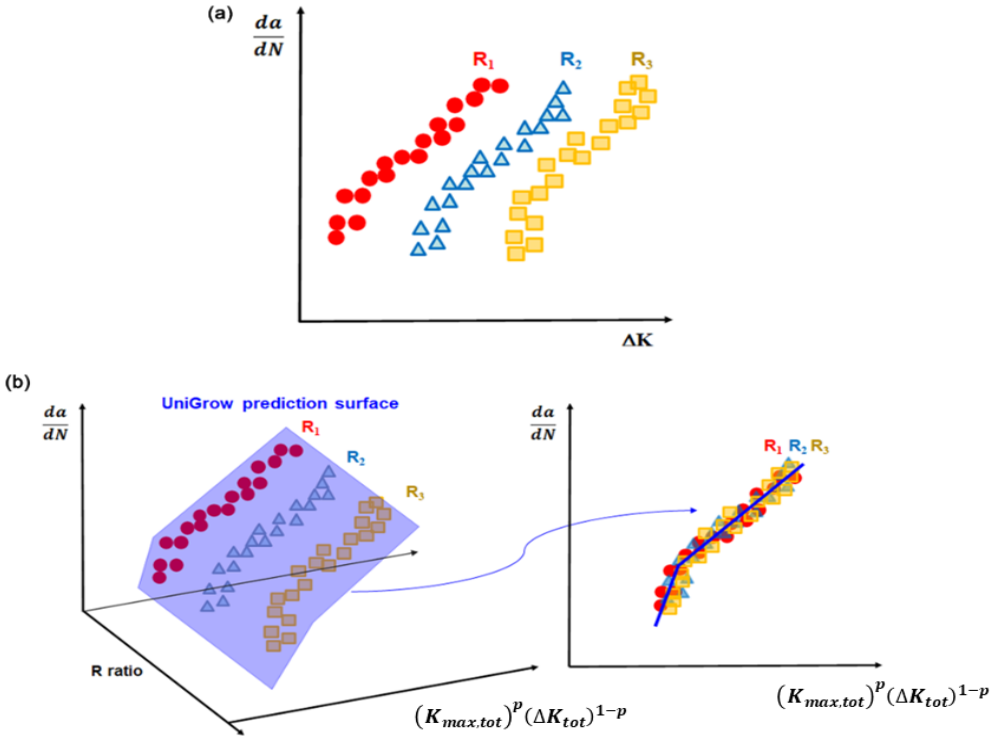

Figure 1.8 a) Representative of FCG data under different R-ratios; b) UniGrow FCG prediction and its correlation with experimental data [57].

One may realize that the actual elasto-plastic stress around the crack tip is required to determine the residual stress σ_r and subsequently the residual SIF (K_r). However, SIF, as a LEFM parameter, is only capable of converting nominal stress to the elastic stress field and does not account for the actual elasto-plastic stress field around the crack tip. As a result, the UniGrow model integrates the Creager-Paris solution introduced in Eq. (1.4) with Neuber rule to determine the actual elasto-plastic stress/strain fields ahead of the crack tip.

Neuber [58] developed one of the most famous notch correction methods known as Neuber's rule. Neuber's rule states that "*the total strain energy density at the notch root equals to the pseudo strain energy density and complementary energy density as if a body was to hypothetically remain elastic*" [59] as shown graphically in Figure 1.9 (a).The superscripts "e" in ($\sigma_{22}^{e}, \varepsilon_{22}^{e}$) and "a" in ($\sigma_{22}^{a}, \varepsilon_{22}^{a}$) stand for elastic and actual stress/strain fields, respectively. Neuber's rule can be derived for uniaxial loading type as:

$$\sigma^{e}\varepsilon^{e} = \sigma^{a}\varepsilon^{a} \tag{1.20}$$

Topper et al. [60] extended the Neuber's rule to account for a wide range of geometries under uniaxial cyclic loadings. Molski et al. [61] proposed the equivalent strain energy density (ESED) stating that "*the actual elasto-plastic strain energy density at the notch root equals to the pseudo strain energy density as if a body hypothetically behaved elastic*" [59] as shown in Figure 1.9 (b). Hoffman and Seeger [62] extended Neuber's rule to an equivalent form as:

$$\sigma_{eq}^{a}\varepsilon_{eq}^{a} = \sigma_{eq}^{e}\varepsilon_{eq}^{e} \tag{1.21}$$

where σ_{eq}^{e} and ε_{eq}^{e} are the equivalent elastic stress and strain, respectively, if the material remained elastic, and σ_{eq}^{a} and ε_{eq}^{a} are the actual elasto-plastic equivalent stress and strain at the notch root, respectively. Neuber's rule has received a grate interest among researchers, and it has been further extended under proportional and nonproportional loading, as well as for micro notches [59, 63-68]. Unfortunately, Neuber's rule is limited to the notches and micro notches and has not been extended to the cracks so far.

As discussed in this section, ΔK-based models have been significantly improved to address all controlling parameters in the LC regime, enabling them to characterize FCG rates in this regime. However, ΔK-based models show significant limitations in the case of the SC regime so far. That is attributed to the fact that ΔK is inherently a LEFM parameter. Although it is possible to employ ΔK to characterize FCG rates in the presence of relatively small and ignorable PDZs around the crack tip, ΔK is not able to account for the relatively large scale of plasticity around the crack tip. Large-scale plasticity occurs either under high stress levels, or in the case of the SC regime where the size of the crack is comparable with the PDZ size. Therefore, it is not possible to ignore the plastic deformation around the crack tip in the latter case.

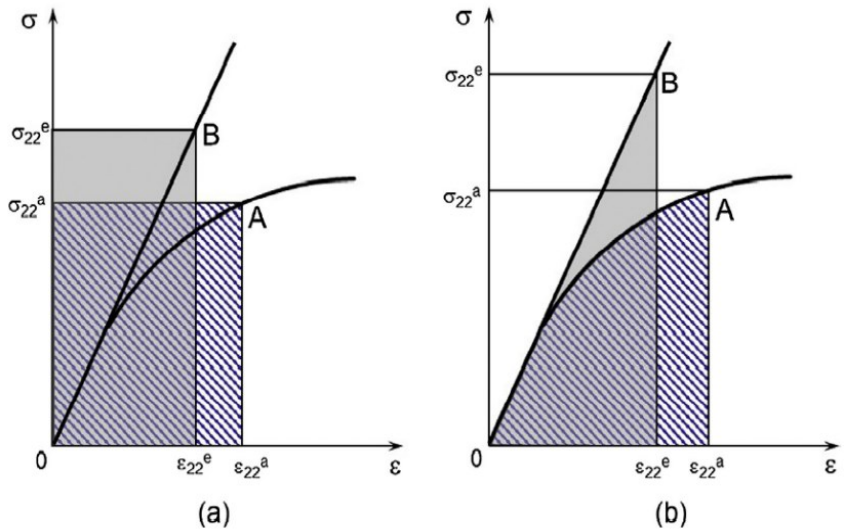

Figure 1.9 Graphical interpretation of Neuber's rule [59].

1.3.2. Elasto-plastic fracture mechanics

Elasto-plastic fracture mechanics (EPFM) employs a driving force (see Eq. (1.2)) that is potentially able to account for relatively large-scale plasticity in the vicinity of the crack tip in order to accurately determine the FCG rate. According to the literature, such driving forces mainly include crack tip opening displacement (CTOD) and ΔJ-integral.

CTOD (δ_t) can be defined as the distance between the opposite faces of a crack tip at the positions where the intercept of lines between these positions and the crack tip establishes the angle of 90 degrees, as shown in Figure 1.10. CTOD-based models have garnered great interest among researchers [69-73]. One of the most notable models based on CTOD to characterize FCG rate in both the SC and LC regimes is the one proposed by Shyam et al. [74-76]. This model suggests considering two stages. The first stage involves the accumulation of irreversible damage as a result of plastic response of material in the vicinity of the crack tip. The second stage involves localized fracture ahead of the crack tip due to the accumulated plastic damages exceeding their critical value. The latter stage causes the crack to extend. Shyam et al. adopted CTOD to address the accumulation of damage from plasticity or the plastic strain around the crack tip. That model is given as Eq. (1.22):

$$\frac{da}{dN} = k\varphi_m\varphi_c \tag{1.22}$$

where k is a constant that required to be calibrated based on the material, temperature, and loading frequency. φ_m and φ_c are the monotonic and cyclic CTOD, respectively. According to that model, crack extension occurs if and only if φ_m exceeds its critical value (φ_{cr}), which can be defined based on the procedure explained in the literature [74-76]. Although this model was further improved [77, 78], it is not successful in the full range of the SC regime.

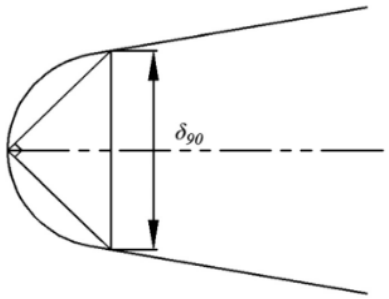

Figure 1.10 Definition of CTOD based on the 90° intercept procedure [73].

J-integral is a line integral in a two-dimensional state. Rice [79] introduced J-integral to characterize stress and strain fields around the notch tip for the first time. Rice suggested that the integral path must start from one surface on the notch, continue through the notched body, embrace the notch tip, and reach the other surface of the notch. The schematic of an arbitrary path (Γ) to define the J-integral is depicted in Figure 1.11. The J-integral is quantified by the means of Eq. (1.23):

$$J = \int_{\Gamma} \left(W dy - T_i . \frac{\partial u_i}{\partial x} ds \right) \tag{1.23}$$

where W is the strain energy density, x and y are the coordinate axes ($x = x_1$ & $y = x_2$), T is the traction vector defined with respect to the normal vector (n) along the path integral (Γ), u is the displacement vector, and s is the infinitesimal element of the integral path (Γ). W and T can be defined as shown in Eq. (1.24) and (1.25), respectively.

$$W = W(x, y) = W(\varepsilon) = \int_0^{\varepsilon} \sigma_{ij} d\varepsilon_{ij} \tag{1.24}$$

$$T_i = \sigma_{ij} n_j \tag{1.25}$$

where σ_{ij} and ε_{ij} are the stress and strain tensor, respectively. According to Green's theorem, Eq. (1.23) as a line integral can be rewritten as a surface integral in a 2D analysis as follows:

$$J = \int \left(\frac{\partial W}{\partial x} - \frac{\partial}{\partial x_j} \left(\sigma_{ij} \frac{\partial u_i}{\partial x} \right) \right) dA \tag{1.26}$$

where dA is an infinitesimal area element (dA=dx.dy) surrounded by Γ in Figure 1.11.

The J-integral can be defined as the potential energy density release rate with respect to the notch length extension, as shown in Eq. (1.27) and depicted schematically in Figure 1.12.

$$J = -\frac{dP}{dl} \tag{1.27}$$

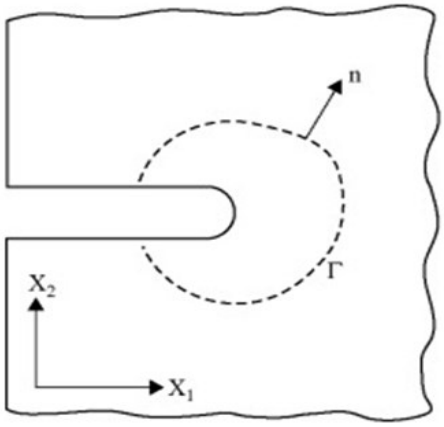

Figure 1.11 Schematic of a path-integral to calculate J-integral in a 2D state.

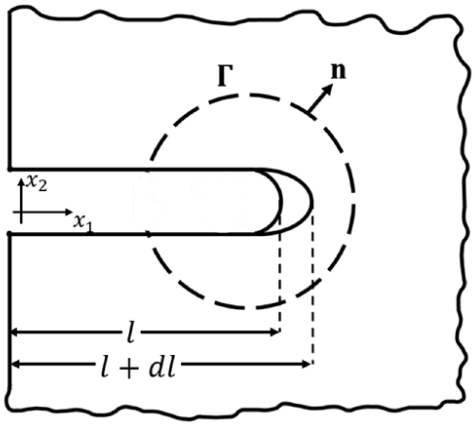

Figure 1.12 Schematic of potential energy release rate with respect to the notch length extension.

where P is defined as the potential energy per unit thickness in the $(z = x_3)$ direction (See Figure 1.12). The J-integral should be regarded in two different states to be physically interpreted [79].

In the elastic state, the potential energy density only consists of elastic strain energy density. As a result, the J-integral equals the strain energy release rate with respect to the notch length in the absence of any external traction force on the notch ($J = G$). In this case, two distinguished energy types can be considered during the notch extension. The first one is the surface energy density related to the new surfaces created as the result of the notch extension. That energy increases the potential energy density. The second energy type is the elastic strain energy density decreasing the potential energy density with the notch extension [80]. The conflict between the density of surface energy and the elastic strain energy is schematically depicted in Figure 1.13. As shown in Figure 1.13, the extension of the notch beyond a critical value (l^*) results in the decreasing of potential energy density. As a result, l^* is the minimum notch length required to have notch extension in the elastic state.

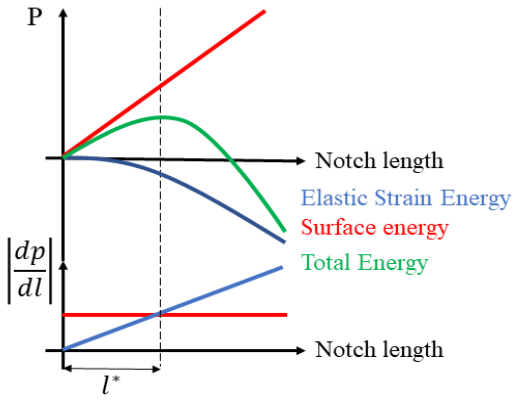

Figure 1.13 Schematic of the different energy types with respect to the notch length.

Since the J-integral equals G, the strain energy release rate in the elastic state, the J-integral has a closed-form relationship with the SIF in the case of elasticity, as shown in Eq. (1.28) and (1.29) under plane stress and plane strain condition, respectively [79]:

$$K = \sqrt{EJ} \tag{1.28}$$

$$K = \sqrt{\frac{EJ}{1-\upsilon^2}} \tag{1.29}$$

where E and υ are the elastic modulus and Poisson's ratio, respectively. One of the most important advantages of J-integral in the elastic state is its path-independency. It has been proved that the value of the J-integral is the same for any arbitrary path, such as the one schematically shown in Figure 1.11 if and only if [79, 81]:

i) material response to the load is linear elastic, non-linear elastic, or deformation-type elasto-plastic. In other words, the stress is one-to-one function of strain (Mashing behavior).

ii) there is an absence of any force or stress on the notch faces and tip.

On the other hand, the J-integral loses its physical interpretation as the strain energy density release rate in the elasto-plastic state. The reason is attributed to the fact that there is the plastic strain energy type in addition to the elastic strain energy and surface energy shown in Figure 1.13. That being said, a portion of energy is lost and cannot be quantified directly as the result of plastic deformation around the notch tip.

It has been shown that the concept of J-integral can be extended to cracks and three-dimensional cracked/notched bodies [79]. The J-integral has been defined based on deformation theory of plasticity and not incremental theory of plasticity. In other words, unloading is forbidden when the J-integral is employed. With this in mind, the critical question that arose is: is it is possible to adopt the J-integral to characterize FCG rate? Dowling and Begeley [82] and Lamba [83] suggested that cyclic J-integral (ΔJ) required to be defined only based on the loading half cycles to characterize fatigue cracks' behavior. In that case, ΔJ can be defined as shown in Eq. (1.30):

$$\Delta J = \int_{\Gamma} \left(\Delta W dy - \Delta T_i . \frac{\partial \Delta u_i}{\partial x} ds \right) \tag{1.30}$$

Dowling and Begeley [84] employed both ΔJ and ΔK as the driving forces to characterize FCG rates in both the LC and SC regimes. It was experimentally shown that the agreement between suggested ΔJ-based model (as EPFM model) and experimental FCG data is significantly better than the agreement between Paris' law (as LEFM model) and experimental FCG data in the SC regime or large-scale plasticity. However, the accuracy of both models was reported to be the same in the case of LC regime or small-scale plasticity. El Hedad et al. [85] further investigated the application of the ΔJ-based model in the SC regime for different materials and geometries, and a noticeable agreement between the ΔJ-based model and experimental FCG rates was observed. As a result, ΔJ-based models have received great interest in determining FCG rate in the case of large-scale plasticity [86-88]. One of the most crucial studies on ΔJ was provided by Tanaka [80], in which the physical interpretation of ΔJ under elasto-plastic state is suggested. Tanaka [80] defined ΔJ as a measure of energy dissipation spent on movement of dislocations in the PDZ around the crack tip during one cycle.

Although ΔJ has been suggested as a promising driving force in order to calculate FCG rates in the presence of large-scale plasticity, its application has been reported significantly difficult, either by the means of experimental procedures or numerical methods. Ngoula et al. [89] developed an in-house model to numerically determine ΔJ to characterize FCG rates for the cracks initiated in various butt and welded joints. Unfortunately, calculation of stress and strain tensors during the crack deflection was reported dramatically difficult and time consuming. Metzger et al. [90] suggested to employ virtual crack extension (VCE) method as a built-in functionality of commercial FE package ABAQUS to determine ΔJ. However, since the built-in functionality of ABAQUS is not able to calculate cyclic J integral, Metzger et al. developed a restart analysis via post-processing and a user-material subroutine. Such an approach was reported to be significantly complicated. Therefore, this method is strictly limited to the lab specimens. There are different approaches to determine ΔJ, e.g. employing handbook solutions, analytical approximation equations, experimental procedures based on load deflection curves, and FE analyses [91-95]. Unfortunately almost all of the mentioned approach are either very time consuming or limited to particular geometry or loading conditions [81].

One of the most appealing method to calculate J and ΔJ is equivalent domain integral (EDI) method, first introduced by Miyakazi et al. [96] and further developed by Nikishkov et al. [97, 98]. The EDI method suggests calculating J and ΔJ in an equivalent domain surrounded by an inner boundary (Γ_1) and an outer boundary (Γ_0), as schismatically shown in Figure 1.14. A proper q-function (known as s-function as well) as schematically shown in Figure 1.14 is required to be adopted in order to achieve the same value of J or ΔJ based on conventional and EDI methods. Such q-function was first introduced by Lorenzi [99] to define the virtual crack extension in a 3D cracked body. The procedure to choose the appropriate q-function is discussed in the literature [100]. According to the EDI method, Eq. (1.26) can be rewritten as Eq. (1.31) using the weight function (q).

$$J = \int_A \left(\sigma_{ij} \frac{\partial u_j}{\partial x} - W \delta_{1i} \right) \frac{\partial q}{\partial x_i} dA \tag{1.31}$$

where δ_{1i} is Kronecker delta and q is a wight function of $x_1(x)$ and $x_2(y)$ as the coordinate axes. The q-function has its maximum value on Γ_1, and it decreases linearly to zero on Γ_0. The maximum value of q in a 2D problem is one.

General formulation of the EDI method under mode I and II loading in cracked bodies has been discussed in the Appendix A.

The EDI method has a significant advantage over the conventional method in calculating J and ΔJ values. That advantage lies in the fact that it is possible to exclude the crack tip and its vicinity in the EDI method calculation. One of the most crucial difficulties in analysing a cracked body problem is dealing with the singularity problem around the crack tip. There are different approaches to overcome this problem. One such approaches is considering the crack as a micro notch as a simplifier assumption. As a result, the radios of the crack tip would be a finite non-zero value. Another approach is employing Barsoum elements in FE analyses. These elements, first introduced by Barsoum [101], are high order elements that account for the singularity problem. The required characteristics of such high order elements are described in detail in literature [101]. However, almost all of the approaches to overcome the singularity problem are either not coincident with reality or difficult to employ. The other crucial difficulty of FE analyses in the presence of cracks is the necessity of using very fine mesh around the crack tip, which increases the computational time especially in the real-life problems. As a result, the EDI method, which avoids dealing with singularity problem and the vicinity of the crack tip, has a compelling advantage over conventional method in the J-integral calculation. Additionally, it has been proved that the EDI method is a mesh-independent approach [102], substantially easing the FE analyses to determine J-integral. Consequently, EDI method has received great interest among researchers.

Raju and Shivakumar [103] compared the EDI method and conventional method to calculate J-integral values under different modes of loading in a FE analysis. The accuracy of the EDI method was confirmed under various types of loading in that study. Shivikumar and Raju [100] employed the EDI method in a FE analysis for three-dimensional mixed-mode fracture problems, and the determined J-integral values were reported to be in good agreement with the ones in the literature. Okada and Ohata [104] used the EDI method in a FE analysis for cracks with different curvatures and kinks in a 3D space. A noticeable accuracy was observed in that study for cracks with kinks and various curvatures.

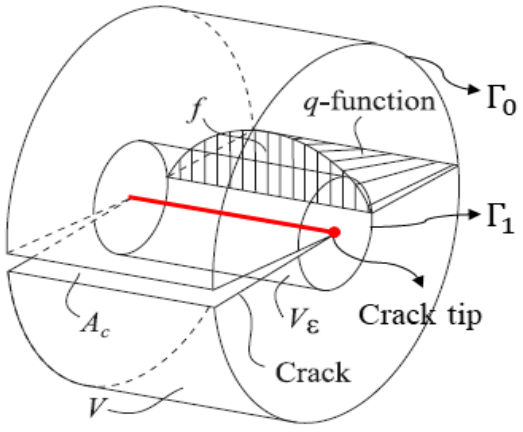

Figure 1.14 Schematic of EDI method and q-function.

Wang et al. [81] developed a FE model to characterize FCG rate for 304 stainless steel by using EDI method. The results confirmed the accuracy of predicted FCG rates based on EDI method.

Although the EDI method significantly simplifies the J and ΔJ calculations in comparison with the conventional method, a complicated non-linear elasto-plastic analysis is required to characterise FCG rate using ΔJ-based models. Unfortunately, such analyses are not time-efficient to be applied in many industries. That reason has led many researchers to apply higher level of analyses, such as machine learning algorithms, to estimate the lifetime of engineering specimens.

1.4. Machine learning

Artificial intelligence (AI) has received great interest in almost all engineering and scientific areas. AI is simply defined as the simulation of the whole processes and procedures of human intelligence by means of machines, specifically computer systems. AI embraces various techniques and approaches. However, the most developed and numerously applied branch of AI is machine learning as shown in Figure 1.15. Machine learning (ML) includes any developed algorithm that is able to extract specific pattern(s) from a given dataset and establish logical relationship(s) between its input(s) and output(s). ML was initially developed to be applied in limited areas such as image and voice recognition, traffic controls, marketing, and weather forecasting. However, its application has spread through almost any field. The first and the most crucial step of ML application is to provide a dataset. The term "dataset" in the application of ML refers to the sequence of inputs and their corresponding outputs. ML methods are mainly categorized into four different classes based on the learning program, as shown in Figure 1.16: Supervised learning, unsupervised learning, semi-supervised learning, and reinforcement learning. Supervised learning is a type of ML technique that establishes a logical relationship between labeled datasets. In other words, the inputs and their corresponding output(s) are determined in advanced and then fed to the training process. Training process is referred to the process in which the machine learns from the datasets.

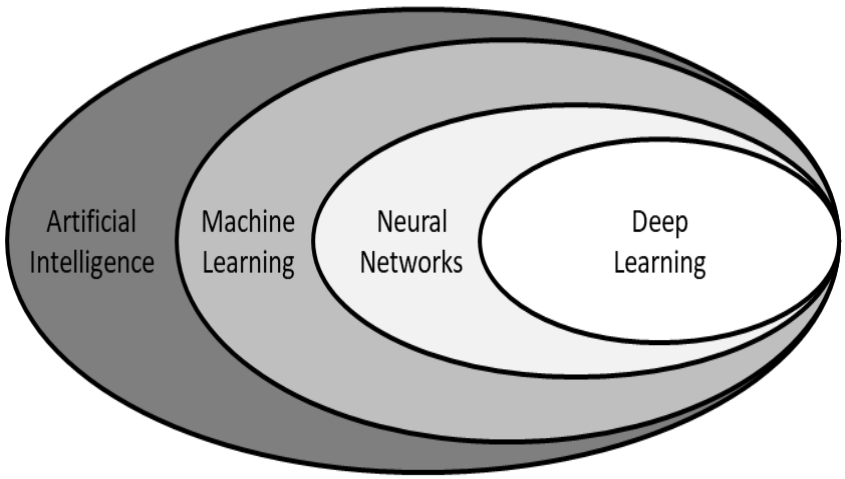

Figure 1.15 AI as a broad term.

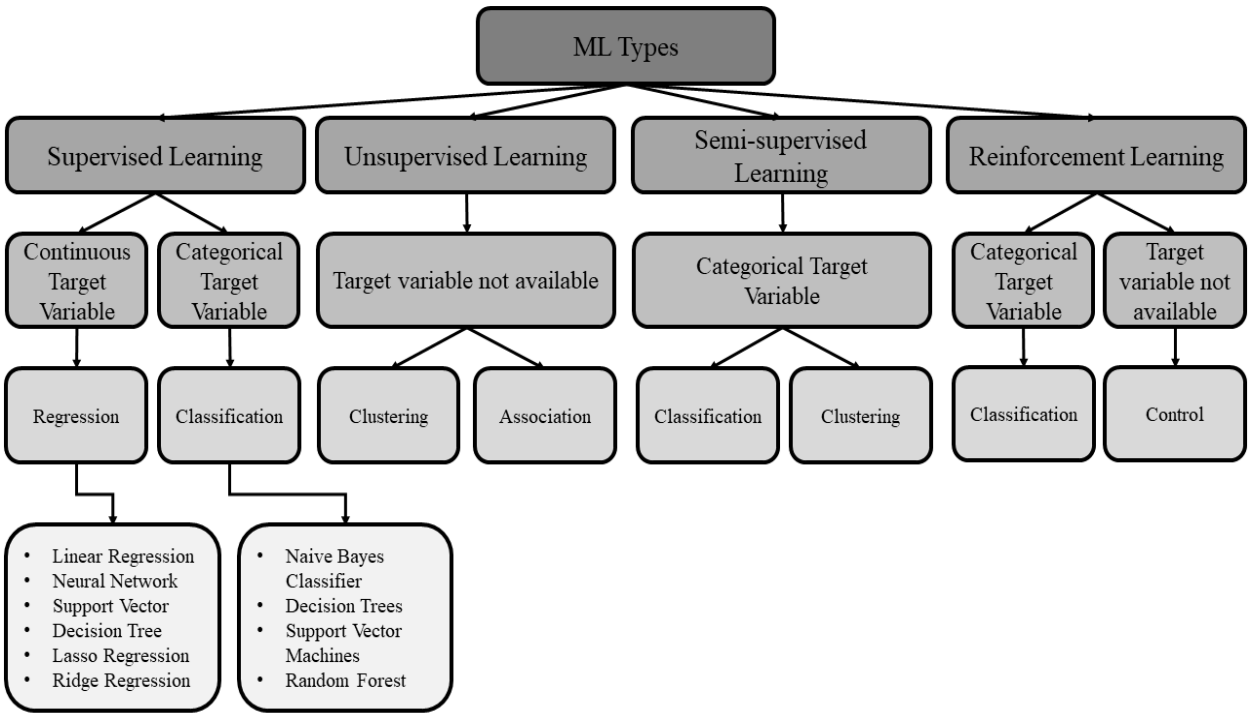

Figure 1.16 Different Types of ML

Such types of ML are mainly applied for regression (e.g., distortion assessment of DMD parts) and classification (e.g., failure detection in none-destructive evaluation methods) types of problems. The most important algorithms implemented in regression type of problems are linear regression, neural network, support vector, decision trees, lasso regression, ridge regression, etc. The most well-known techniques in the case of classification type of problems are Naive Bayes classifier, decision trees, support vector machines, and random forest as shown in Figure 1.16. On the other hand, the algorithms implemented in unsupervised learning methods are trained based on unlabeled data. In such cases, the target variable is not available, or particular outputs cannot be assigned to the corresponding inputs. In these algorithms, the machine tries to determine the similarities and differences between the data. As a result, such methods are well-suited for clustering types of problems. The reinforcement learning algorithms, known as decision making algorithms, try to determine the best decision for so-called intelligent agents in a particular environment in order to maximize the cumulative reward.

Many of mentioned algorithms have been received noticeable interest from researchers in solid mechanics, such as artificial neural networks (ANNs), decision trees (DTs), support vector machines (SVMs), etc. However, unlike the numerous and well-organized datasets that are available in many fields such as image recognition, the reliable datasets that are appropriate to be fed to the ML algorithms are limited in solid mechanics. The reason is attributed to the fact that such datasets in solid mechanics are provided by expensive experimental tests, which make them exclusive to the companies that performed the tests. Therefore, the application of ML algorithms is in its early stages in solid mechanics compared to other research domains.

1.4.1. Neural Networks

As shown in Figure 1.15, neural networks (NNs) are one of the strongest and most appealing approaches among researchers as a ML method that is able to extract complex relationship(s) between the inputs and output(s) through a well-organized dataset. NNs are mainly developed into three groups based on the application, as shown in Figure 1.17.

- Artificial neural networks (ANNs): ANNs are the most well-known and extensively utilized type of NNs that can be implemented in both regression and classification problems (see Figure 1.16). ANNs have shown a noticeable potential to extract any pattern or relationships, including complicated and non-linear relationships, between the inputs and output(s) of a properly-organized and adequate dataset through its layer-based structures schematically shown in Figure 1.17. There are different types of hyperparameters, in addition to the number of layers, such as the number of neurons, weights, and biases that are employed to extract the relationships.

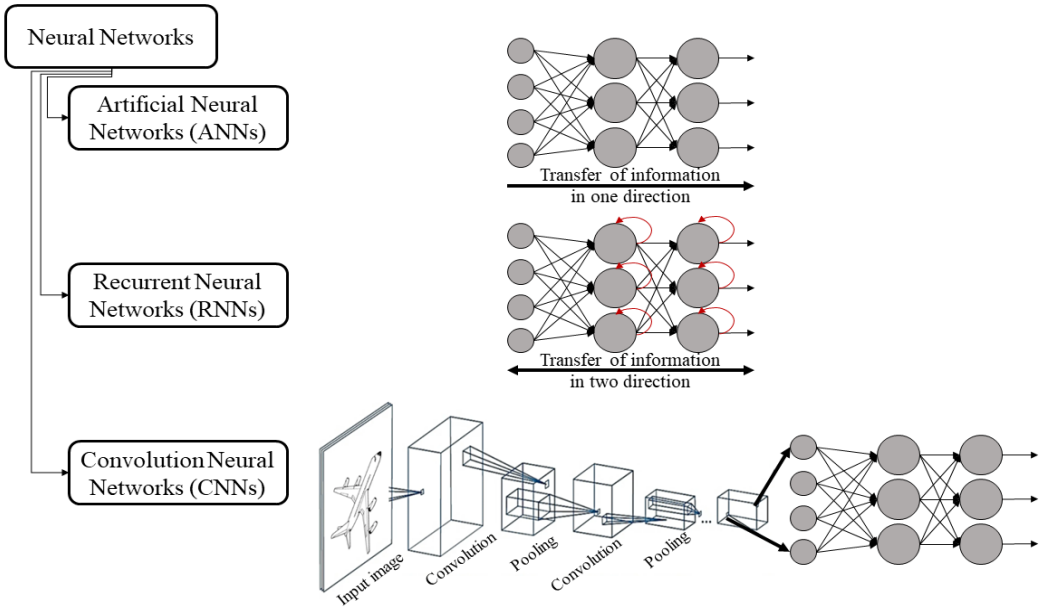

Figure 1.17 Different types of neural networks.

The mentioned hyperparameters will be discussed in detail in the following. ANNs estimate the output as a function of inputs and all initially determined hyperparameters through a forward propagation. Then a backward propagation is operated to evaluate the error and subsequently minimize that error by adjusting the weights and biases. Such a process is known as the network training, and the combination of one forward and backward propagations is known as an epoch. Training of an ANN may take hundreds of epochs. As shown in Figure 1.17, information is transferred only in one direction in the training process of an ANN. The structure of an ANN and its hyperparameters will be discussed in detail in the following.

- Recurrent neural networks (RNN): RNN is higher level of NN algorithm compared to the ANN approach. RNNs are developed to overcome particular limitations of ANNs. RNNs can handle a given dataset that includes different types of data sizes and/or formats, which cannot be

analyzed through an ANN. RNNs are mostly employed in the case of sequential data series (e.g., text/audio data) where the sequence and occurrence of the data are prominent factors. One of the most important difference between RNNs and ANNs is how information is transferred through the network. In an ANN structure, information is passed in a forward direction. However, in RNNs, the information of a particular neuron in a hidden layer may be transferred back to the previous neuron, as shown in Figure 1.17.

- Convolution neural networks (CNNs): CNNs consist of various layers, including convolutional layers, filter or kernel layers, and pooling layers, in addition to the fully connected NNs similar to ANNs, as shown in Figure 1.17. Convolutional layers are the filters that can detect and extract features from a given image and convert them into numerical values. Pooling layers are used for size reduction, and the main NN is implemented and trained similar to the one in the case of ANN. CNNs are mostly implemented in the area of image recognition. CNN is the most similar NN to the human brain, as it can distinguish different parts of an image and consider them separately while retaining the arrangement of the original image.

Base on the differences between all types of NNs, it is concluded that ANNs are well-suited for many regression-types of problems in solid mechanics. Although ANNs are capable of extracting any type of relationships between inputs and outputs of the system, there are major limitations and shortcomings in their applications. One of the most crucial limitations is the requirement for a large-size and well-organized dataset. In other words, the dataset needs to be adequately comprehensive to thoroughly reveal all aspects of the problems. Unfortunately, providing such dataset(s) is often very challenging in many problems in solid mechanics due to the restrictive regulations and standards required to be followed during experimental tests. The construction of ANNs itself and the determination of numerous hyperparameters need optimization processes involving lots of trial and error to achieve a well-trained ANN. It should be noted that the hyperparameters cannot be determined based on a straightforward or theoretical method [105, 106]. The ANNs cannot be implemented for the extrapolation in the case of regression type of problems [107-110].

As discussed in detail by Rosenblatt [111], a multi-layer artificial neuron consists of two crucial mathematical operators known as activation function (φ) and the net input of the neuron (z). The net input of the neuron is defined as:

$$z = \vec{w}^T \vec{x} + b \tag{1.32}$$

where w is the weight, x is the input, and b is the bias, as shown in Figure 1.18. The ANN model consists of one input layer, one output layer, and one or more hidden layers. The number of neurons in the input layer equals the number of inputs, and the number of neurons in each hidden layer varies as a hyperparameter that needs to be tuned. The schematic of an ANN with one hidden layer is described in Figure 1.19. Each neuron in an ANN may be remain silent or become active based on the activation criterion. The weights are the values between zero to one, and the higher the weight, the higher influence of the neuron on output. Initially, preliminary values are considered for weights and biases. Feeding the inputs vector to the preliminary ANN results in the outputs. A proper error function can be established to measure the deviation of results from actual output values.

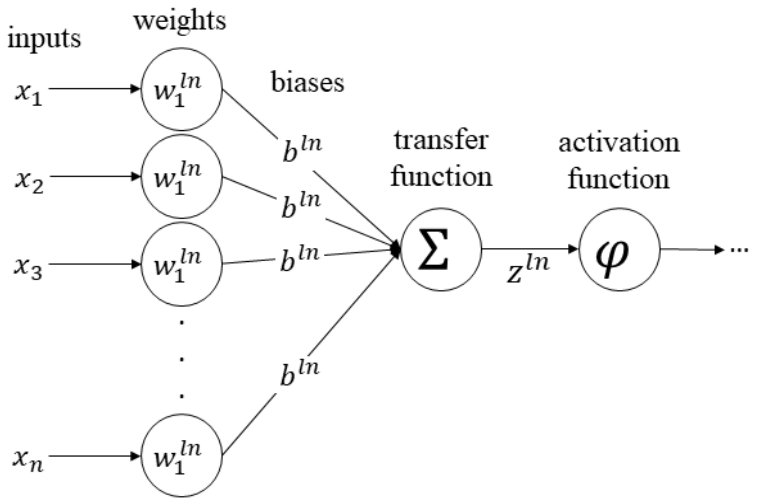

Figure 1.18 Schematic of a multilayer neuron in artificial neural networks.

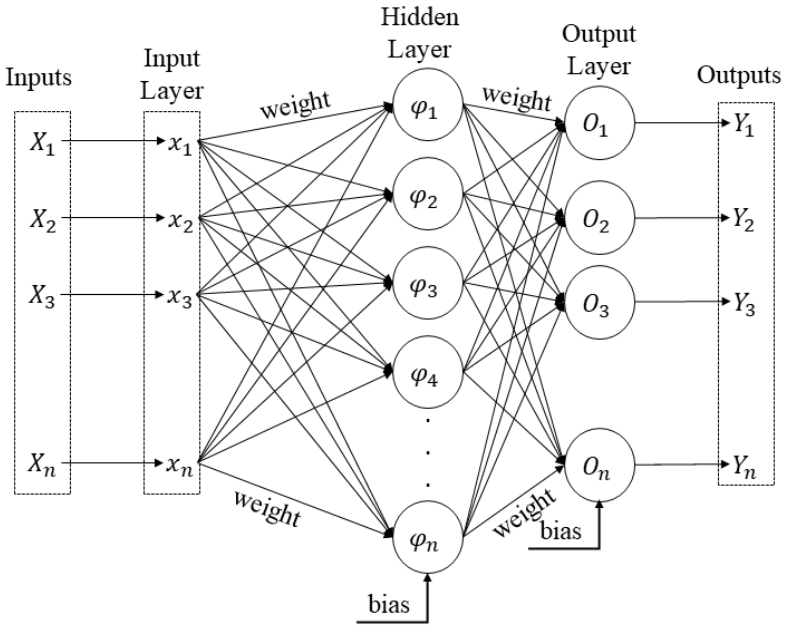

Figure 1.19 Configuration of a three layers artificial neural network.

Thus, adjusting and tuning the weights and biases in order to minimize the error function is performed. Such minimization known as training algorithms. One of the most efficient training algorithms is the "gradient descent approach with backpropagation" [112], which minimizes the error by determining of the local optima of the loss function. The basics of gradient descent approach can be interpreted by Taylor expansion [112] as follows:

$$f(\vec{x}+h\vec{s}) = f(\vec{x}) + (\nabla f)^T \vec{s} h + O(h^2)$$
$$df = f(\vec{x}+h\vec{s}) - f(\vec{x}) \approx (\nabla f)^T \vec{s} \tag{1.33}$$

where f represents the loss function, h is a step size known as the learning rate, and s is a vector of the derivatives of the loss function with respect to the inputs in the network. As a result, each component of s can be expressed as [112]:

$$\delta^{n,l} = \frac{\partial f}{\partial z^{n,l}} \tag{1.34}$$

After the determination of optimal step direction ($\vec{s}$), the weights and biases can be adjusted to minimize the loss function based on the reverse computation, which is known as the backward propagation method. The gradient descent algorithm with backpropagation in the ANN is applied thoroughly on the network, and the predicted outputs of each epoch are stored to update the weights and biases for the next epoch. Once the loss function is minimized, the training is completed. A well-trained model can be employed for prediction purposes. Some of the most important parameters, as well as the characteristics related to the ANN configuration, are listed as follows:

- The number of hidden layers and the number of neurons in each layer. The number of hidden layers and the number of neurons depend on the size of the inputs and the nonlinearity and complexity of the relationship between inputs and output(s). On one hand, the number of hidden layers and neurons should be large enough to comprehensively acknowledge the effect of each input parameter and detect any interrelationships between them. On the other hand, an excessive number of hidden layers can result in overlooking the effect of inputs in the ANN model.
- Activation function. It is highly recommended to employ a non-linear activation function to establish the non-linear and complex relationship(s) in a dataset. Activation functions specify whether a neuron is active or inactive. The most well-known non-linear activation functions with continuous and non-zero derivatives are the sigmoid, hyperbolic tangent, and rectified linear unit (ReLU) functions.
- Loss function. A proper loss function is required to determine the deviation of predicted results by the ANN from the real outputs to complete the training process discussed earlier, using the gradient descent approach with backpropagation. Mean squared error (MSE) and cross-entropy are the most popular loss functions for regression and classification types of problems, respectively.
- Learning rate. Learning rate is one of the most important hyperparameters that need to be properly tuned by the user of ANN algorithms. That hyperparameter is expressed as h in Eq. (1.33). The learning rate determines the step size at each iteration in order to move towards the minimum value for the chosen loss function. Consequently, the loss function specifies the speed of the training process. The effect of learning rate on loss function during the epochs/training is demonstrated in Figure 1.20. A very high learning rate is not capable of decreasing the loss values due to the unbalanced condition that occurs when updating all of the weights and biases. Similarly, a high learning rate is not capable of reaching the minimum loss value because the step size is too high, causing it to miss the appropriate ranges for biases and weights through the iterations. On the other hand, a low learning rate substantially increases the training time and may not allow the loss function to reach its potential minimum value.

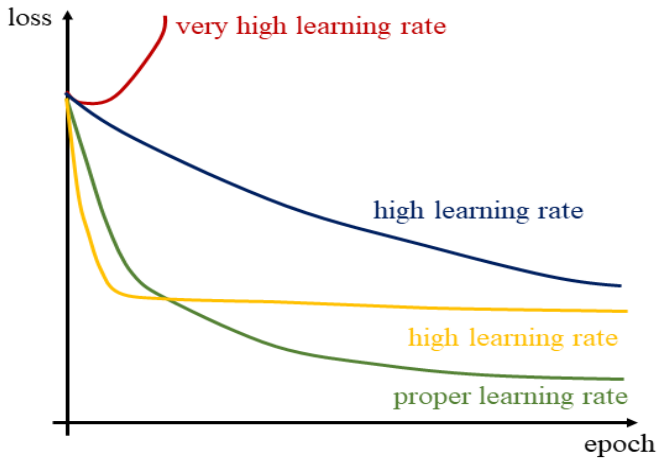

Figure 1.20 Effect of the learning rate in the ANN training

- Number of epochs. The number of epochs should be determined based on the complexity and level of non-linearity of the problem. Additionally, the number of epochs should be consistent with the learning rate to avoid overfitting and underfitting problems, which are among the most common obstacles during ANNs training.
- Overfitting and underfitting. One of the most common problems that cause inaccurate predictions in the implementation of ANNs is related to underfitting or overfitting (see Figure 1.21). Underfitting occurs when the ANN has not established the relationships within the dataset. One of the reasons for this problem may be the small number of epochs. That being said, the algorithm needs more time and/or more iterations to discover the relationships between inputs and output(s). Another reason may be related to the dataset. The dataset is required to be well-organized, large in size, and accurate enough to result in a well-trained ANN. Overfitting refers to the state where the trained ANN shows high accuracy with the training data but a high error with the test data. In other words, the trained ANN predicts the output(s) of the datasets that have been seen during the training process, but it cannot predict the output(s) based on new inputs.

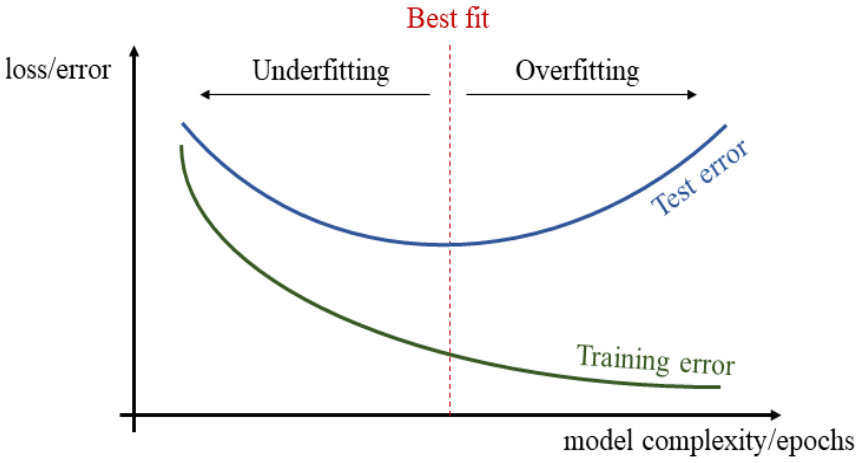

Figure 1.21 Description of underfitting and overfitting problems during the ANN training

1.4.1.1. Neural network Application in Fatigue

It has been widely acknowledged that NNs are powerful tools for finding and establishing relationships between inputs and outputs in a given dataset. They are capable of learning complex patterns and structures from data and can uncover relationships that are not easily discernible by human observers. ANNs consist of interconnected nodes that process information in a hierarchical manner, with each layer building upon the features learned by the previous layer. This allows NNs to identify and extract relevant features from the input data, and then use these features to make predictions about the output. Additionally, NNs can also reveal the interrelationships between inputs, which can provide valuable insights into the underlying mechanisms that drive the system being modeled. As a result of these capabilities, ANNs have become an increasingly popular tool even in fatigue-related engineering fields. The reason is that fatigue-related engineering problems are usually very complex due to the large number of controlling parameters, such as crack length, mechanical properties, microstructural properties of the material, mean stress, amplitude stress, geometric characteristics, etc. These controlling parameters not only affect the fatigue life and/or fatigue cracks behavior but also may have interinfluence on each other. With this in mind, NNs have received noticeable interest among researchers to investigate this area. Figure 1.22 shows the number of publications that investigate the application of NNs in fatigue-related problems in the past three decades.

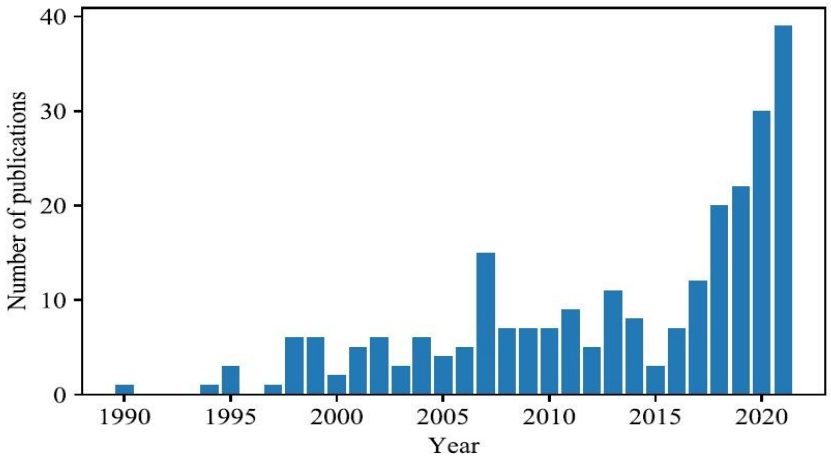

Figure 1.22 Number of researches in application of NNs in fatigue-related problems in the last three decades [113].

NN applications in Fatigue can be categorized into five main groups: a) fatigue life prediction, b) fatigue crack, c) fatigue diagnosis and prognosis, d) fatigue strength, and e) fatigue load, as shown in Figure 1.23. Some of most important researches in each group are reviewed as follows:

Fatigue life prediction has been the most extensively researched topic among all NN applications for fatigue. Typically, the input variables comprise material and experimental variables, while the output is the fatigue life [114]. A standard approach involves employing an ANN with one or multiple hidden layers, an input layer, and an output layer. The fatigue life may be predicted indirectly, or it can be utilized as an output variable.

Maleki et al. [115] studied the effect of shot peening on the fatigue life of steels by employing a feedforward ANN. The inputs were chosen as shot peening variables, fatigue loadings, and the

type of steel, while the fatigue life was assigned to the output. The experimental data size of 94 was used. Different loss functions, coefficient of correlation (R^2), root mean square error (RMSE), mean relative error (MRE), and mean absolute error (MAE), were employed to assess the application of developed ANN. The error of all mentioned criteria was reported to be less than 1% for testing data. Vassilopoulos et al. [116] employed ANN to establish the constant life diagram for two different composite materials. The prediction of the ANN model was reported to be successful in generating an almost identical constant life diagram to the one based on conventional methods. Yan et al. [117] developed a fatigue life prediction model utilizing an ANN algorithm.

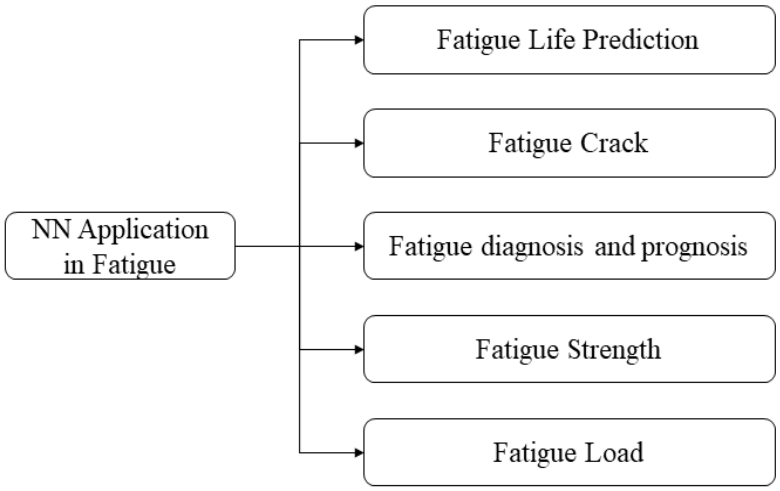

Figure 1.23 Classification of NN application in fatigue.

The suggested ANN model was developed based on a single hidden layer and constructed within the MATLAB environment. The inputs were chosen to be asphalt content, air void, and strain level. Training data for the ANN model was obtained by conducting four-point bending fatigue tests under various conditions. The results revealed that the ANN predictions were superior to the empirical fatigue life prediction model in the particular cases that were investigated in that study. Dresia et al. [118] developed an ANN to predict the fatigue life of liquid rocket engine combustion chambers. The finite element method was used to generate the training data. The inputs of the model were the dimensions of the chambers, pressure, and temperature, while the output of the model was the fatigue life. The results showed that the developed ANN model can predict the fatigue life of unseen data (test data) 10^7 times faster than the finite element method, with a mean absolute error of around 7%. All of the developed ANN models reviewed in the literature [115-118] directly predict the fatigue life. That being said, the output of the model is fatigue life in the mentioned studies, while the inputs differ with respect to the problems and their controlling parameters. The same approach has been used in many studies to directly predict the fatigue life of components made in metals [119-148] and composite materials [116, 117, 149-160].

In some research, fatigue life has been used as an input. Junior et al. [161, 162] developed ANNs to build constant life diagrams of composite materials. The mean stress (S_m) and fatigue life (N) were considered as inputs, and the amplitude stress (S_a) was assigned as the output. The experimental data were collected under different R-ratios to be fed to the network. Various network structures in terms of the number of neurons, data, and R-ratios were used to develop a well-trained model. The results showed that with a proper structure, the suggested model can build constant

life diagrams with significant accuracy. Similar studies have been conducted to build constant life diagrams of composite materials under different temperatures [163-166]. The results demonstrated good agreement with those obtained by conventional methods.

The other approach is calculating fatigue life indirectly. That being said, ANNs are employed to calculate other valuable parameters as the outputs. Subsequently, the fatigue life is determined based on those outputs by using other/conventional models. The reason lies the fact that conventional models are not easy to use or they are significantly time consuming. Genel [167] developed four different ANNs to predict the fatigue ductility coefficient (ε_f'), fatigue strength coefficient (σ_f'), fatigue strength exponent (b), and fatigue ductility exponent (c), which are used in the Manson-Coffin relationship. The Manson-Coffin relationship is a well-known approach categorized under the strain-life method discussed earlier. Manson-Coffin relationship estimates the fatigue life (N) as follows:

$$\frac{\Delta\varepsilon}{2} = \frac{\sigma_f'}{E}(2N)^b + \varepsilon_f'(2N)^c \tag{1.35}$$

The outputs of each the four models were assigned to represent one of the mentioned Manson-Coffin coefficients/exponents, while the material properties served as the inputs for the ANNs. Subsequently, the Manson-Coffin relationship was utilized to determine the fatigue-life. The suggested method demonstrated superior performance compared to conventional approach. Cai et al. [168] developed an ANN model to determine the ultimate failure strain and, consequently, the fatigue life of epoxy molding compound. The same approach has also been adopted in various other studies, which can be found in literature [169-171].

In addition to ANN, other types of NNs have been utilized for fatigue life prediction. Li et al. [172] developed an RNN to estimate the influence of load-keeping time on the fatigue life in the case of creep-fatigue life of steels. The load-keeping time and the fatigue life were assigned as the input and output of the RNN, respectively. The results were then compared with those obtained by conventional methods, and the suggested model demonstrated significantly accurate outcomes. Several studies have explored the application of different types of NNs (beyond ANN) for "fatigue life prediction," which can be found in the literature [173-185]. However, the number of such studies is significantly less than those focusing on ANN applications. Nevertheless, there are studies that compare the application of different types of NNs in the context of "fatigue life prediction," as presented in [150, 178, 186-196]. Such studies revealed that it is not possible to designate a single type of NNs as superior for “fatigue life prediction”. However, it appears that ANN can be considered a better choice due to its more straightforward implementation. Moreover, ANN achieves almost the same accuracy as higher-level NNs without the need to deal with their complexity.

All of the studies discussed in "fatigue life prediction" involve the technical coupling of NN algorithms with conventional theories known as the "crack initiation" method, as discussed earlier, to achieve safe-life design. On the other hand, "fatigue crack" entails the application of NNs in "fracture mechanics" to investigate fatigue crack and damage tolerance design. Typically, the SIF range is used as the input (or one of the inputs), and the FCG rate is considered as the output in this context. Similar to the previous section, ANN is the most frequently used type of NN for this approach. Mohanty et al. [197] developed an ANN model to investigate the effect of stress ratio on the FCG rate for different aluminium alloys. The SIF range, SIF maximum, and the R-ratio

were used as inputs, while the FCG rate was assigned as the output in their study. The predicted results were then compared with the experimental results, with the reported error of predicted fatigue life being less than 5%. The noticeable potential of ANNs in predicting the nonlinearity of FCG rate based on the SIF range and their ability to establish relationships between the FCG rate and a chosen fatigue crack propagation driving force (see Equation (1.2)) has attracted the interest of many researchers. Similar approaches have been employed in other studies, such as [198-211] in the LC regime. One limitation of this method lies in its poor prediction in the threshold and final fracture phase (phase (I) and phase (III) in Figure 1.4). That being said, those phases are challenging for the developed ANNs to learn from the dataset. Iacoviello et al. [212] developed an ANN model with the FCG rate as input and the SIF range as output to address that limitation. Additionally, different types of NNs, such as the extreme learning machine (ELM) and radial basis function neural networks (RBFNNs), have been used to characterize the FCG rate based on a proper driving force, as seen in [213-218]. All of the mentioned studies reported accurate predictions. Moreover, it has been concluded that there is no a superior type of NN in the case "fatigue crack" so far.

For fatigue diagnosis, fatigue damage mainly represents the state of health of the material (e.g., reduction of static strength [219]). Durodola et al. [220] developed an ANN model to predict fatigue damage under Gaussian stationary loadings. The input and output of the ANN model were chosen to be material properties and fatigue damage fraction, respectively. The results of the developed ANN model were compared with one of the most well-know conventional methods known as rain flow counting-Miner's rule framework. The comparison demonstrated good performance for the suggested ANN model. Ramachandra et al. [221] further investigated the approach proposed in [220] and compared the ANN predictions with experimental results. A good agreement was observed between the ANN predictions and the experimental results. This model was subsequently extended to account for mean stress effects [222] and non- Gaussian loading [223], and the prediction results showed a high potential for ANN models in the suggested approach.

Other types of NN algorithms, such as RNN, have been developed using the same approach for fatigue diagnosis. These studies can be found in [224-228]. However, no specific advantage(s) over ANNs were identified.

Numerous studies have been conducted to implement NN algorithms for estimating the remaining fatigue life of materials and structures, categorized as fatigue prognosis. For instance, Feng et al. [229] employed ANN to create a predictive model for real-time fatigue life. They generated 700 data points from FE analyses utilizing stochastic parameters within specific ranges. The resulting structural responses were then assigned as input variables for the ANN model. The predictions of the suggested ANN model were reported to be in good agreement with the results of conventional models. Gabraeel et al. [230] developed ANN models to predict bearing failures. An experimental setup was established to perform accelerated bearing tests and generate vibration information. Subsequently, this information was fed to the ANNs as input, with the remaining fatigue life chosen as the output. It was observed that 90% of the suggested model's predictions had an error of less than 20%. Amiri et al. [231] employed ANNs to establish relationships between ultrasonic testing (UT) results and fatigue life of resistance spot weld specimens made of different types of low carbon steels. The suggested ANN models demonstrated that fatigue life can be predicted based on UT results with acceptable accuracy. Chatterjee et al. [232] developed an ANN model to predict the remaining fatigue life of a topside piping. In this study, the stress level, crack size, and

mechanical properties of the material were assigned as inputs to the model, with the remaining fatigue life chosen as the output. The predictions of the suggested model showed an accuracy of 96%. Similar studies applying ANN models for fatigue prognosis can be found in the literature [233-236].

In addition to ANNs, RNN [237-240] and CNN [241] have been employed for fatigue prognosis using similar approaches. Comparisons between different types of NNs indicate that there is no superior type of NN in all of the approaches [113].

Fatigue strength refers to the stress level that a material can endure for a given life period, and this approach is commonly utilized in safe-life design across various fields. The input variables typically include microstructure, chemical composition, processing parameters, and work conditions, such as temperature and fatigue loadings, while the output is the fatigue strength. Lotfi and Beiss [242] suggested an ANN model to predict the fatigue strength of porous steels. The inputs were the iron morphology, an important microstructural characteristic, the fabrication process (as sintered, machined), and loading mode (axial, plane bending, rotary bending). The predictions showed that the suggested model has an accuracy of more than 96%. Zhao et al. [243] used ANN models to predict the high-cycle fatigue strength of Ti-6Al-4V based on microstructure properties and loading types as the inputs. The maximum error of the suggested model was reported to be less than 20%. Similar studies in which the fatigue strength is assigned as the output can be found in the literature [244-250].

NNs algorithm have also been employed to predict fatigue load spectrums. Cabell et al. [251] developed a ANN model to predict the spectrum of loading for critical parts of a helicopter, such as pitch links. The training data were obtained experimentally from 13 flights. The correlation coefficient of the predicted results was reported to be between 0.6 and 0.9. Vera-Tudela and Kuhn [252] employed ANN algorithms to determine the bending moment for wind farm flow. The correlation coefficient of predictions ranged from 0.817 to 0.899. Similar studies with the aim of fatigue load estimation employing ANNs can be found in [253-257].

1.4.1.2. Neural network application in elasto-plastic mechanics

Neural network algorithms have recently received noticeable attention in elasto-plastic mechanics. Hajializadeh and Ince [258, 259] proposed a novel approach to determine residual stress in components made by direct metal deposition (DMD) as an additive manufacturing (AM) process. It was suggested that integrating FE-based models with ANN algorithms is able to significantly reduce the computation time of residual stresses. The residual stresses predicted by the developed ANN models were compared with those determined by conventional FE analyses, and a noticeable agreement was observed. In their study, Burghardt et al. [260] created an ANN model to determine the correlation between elastic and elasto-plastic stress and strain in notch roots, considering both uniaxial and multiaxial proportional loading conditions. The outcomes demonstrated significant promise for the proposed approach. Kazeruni and Ince [261] presented a similar strategy, employing an ANN algorithm to forecast the elasto-plastic stress-strain behavior of diverse materials, utilizing their elastic response as a basis. The proposed method demonstrated a notable ability to predict local elasto-plastic stress and strain at various positions within notch roots. Zhang and Mohr [262] recommended employing ANNs to establish the relationship between stress and strain, as an alternative to using constitutive equations. The study compared the results obtained from ANNs with those derived from the Von-Mises equation, revealing a promising level of

agreement. Masi et al. [263, 264] suggested using ANN to predict a constitutive model based on a novel data-driven approach. It was suggested that the physics law, specifically derivatives of the free-energy, should be embedded in the training algorithms of ANN models.

Additionally, apart from ANNs, RNNs and CNNs have been utilized in the realm of elasto-plastic mechanics. Addressing a comparative perspective, Mozaffar et al. [265] compared the application of ANNs and RNNs to establish the path-dependent stress-strain relationship. The results indicated RNNs' superiority over ANNs in this particular case. However, it was observed that the number of data required to train an RNN is significantly larger than that for ANN training. Furthermore, in related research, Tancogne-Dejean et al. [266] and Wu et al. [267] developed RNNs to model path-dependent plasticity in the context of heterogeneous materials.

Chapter 2:

Motivations and novelty of the present research

The various approaches investigating fatigue crack behavior have been discussed in detail in Chapter 1. Figure 2.1 provides a concise summary of most of these approaches. As depicted in Figure 2.1, the conventional methods for addressing fatigue crack behavior can be categorized as "crack initiation methods" and "fracture mechanics" approaches. The crack initiation methods consider components without cracks and propose that the fatigue life of components equals the number of cycles required for crack initiation. As a result, crack initiation methods do not align with reality. Fracture mechanics approaches can be further classified into linear elastic fracture mechanics (LEFM) and elasto-plastic fracture mechanics (EPFM). LEFM methods, primarily based on ΔK models, inherently cannot account for relatively large-scale plasticity. A common scenario involving the presence of large-scale plasticity is a fatigue crack in the short crack regime. EPFM models possess the capability to address large-scale plasticity, with one of the most promising parameters being the J-integral. Unfortunately, the application of J-integral-based models is straightforward and time-efficient only for specific geometries. However, significantly complex and time-consuming elasto-plastic finite element (FE) analyses are required to calculate the J-integral for engineering problems. Consequently, researchers have been attempting to modify LEFM methods, which solely require linear elastic solutions, to incorporate large-scale plasticity. Regrettably, these modifications have not yet yielded successful results. In addition to the classical approaches, there has been considerable attention given to the application of neural network models as machine learning algorithms to address fatigue crack behavior. Among these models, artificial neural networks (ANN) have been extensively utilized in this field. Although ANNs have demonstrated significant potential in characterizing fatigue crack behavior, they heavily rely on a substantial amount of data. The present dissertation integrates robust ANN models with fracture mechanics approaches to overcome the aforementioned limitations.

- In Chapter 3, ANN models are developed to characterize fatigue crack growth (FCG) rate based on ΔK as a parameter in LEFM. The proposed approach has been applied to both the long and short crack regimes. The ANN predictions have compared with the experimental FCG data to assess the ANN models. The investigation conducted in this chapter demonstrates the high potential of ANNs in capturing the nonlinear relationship between FCG and its controlling parameters. However, the realization of this promising potential heavily relies on the availability of a sufficient amount of data required to train the ANN models. Unfortunately, obtaining experimental data for characterizing FCG involves expensive and time-consuming procedures, particularly in the case of the short crack regime. The majority of such data have been provided by NASA. As a result, the integration of ANN algorithms with LEFM-based models is limited to conditions where an adequate amount of experimental data is available. The novelty of Chapter 3 is applying ANN algorithms in the case of short crack regime for the first time.
- In Chapter 4, the study focuses on integrating ANN models with FE analyses to address the issue raised in Chapter 3. FE analyses are suggested to provide extensive and well-structured data required for training ANN models. Hence, FE analyses are conducted on a standard notched specimen with varying crack sizes, considering both elastic and elasto-plastic conditions. The outcomes of the analyses in the elastic state are collected to serve as input data for the ANN models. Correspondingly, the results obtained under the elasto-plastic state are designated as the output data for the ANN models. It has been proposed that developing well-trained ANN(s) enables the identification of relationships between hypothetical elastic stress, strain, and displacement fields and the actual elasto-plastic fields around the crack tip. Consequently, the J-integral, as a function of actual elasto-

plastic stress, strain, and displacement fields around the crack tip, can be determined using a linear elastic solution instead of a complex and nonlinear elasto-plastic solution. In this stage, an in-house model based on equivalent domain integral (EDI) method is developed to determine the J-integral based on the results of FE analyses and ANN predictions under different conditions. The EDI method offers significant advantages over conventional techniques, which will be thoroughly discussed in Chapter 4. The suggested approach has been evaluated under monotonic loading conditions in Chapter 4. The in-house model based on EDI method is verified by the built-in functionality of ABAQUS and the result in the literature. The ANN predicted elasto-plastic stress, strain, and displacement fields are compared with the ones determined by the elasto-plastic FE analyses. The results demonstrate a noticeable accuracy in predicting the elasto-plastic stress, strain, and displacement fields around the crack tip, as well as the J-integral for various crack sizes.

- In Chapter 5, the application of the aforementioned method under cyclic loading conditions is discussed. The in-house model was upgraded to determine ΔJ under cyclic loading. The developed ANN models establish the relationship between cyclic elastic stress, strain, and displacement fields and the corresponding cyclic elasto-plastic fields. Based on the predictions of the ANN models, ΔJ values for different crack sizes are estimated. The developed in-house model has been verified by the results in the literature and the ANN predicted stress, strain, and displacement fields are compared with the results of elasto-plastic FE analyses. The results demonstrate the promising nature of the proposed method under cyclic loading.

The novelty of chapter 4 and 5 is addressing two of most important challenges of using fracture mechanics and ANN models. Integration of FE analyses with ANN models can provide adequate data to train the ANN models. Such integration also enables effective handling of the inherent limitations of ANN models in extrapolation tasks. On the other hand, the proposed approach can determine J-integral as an EPFM parameter through a linear elastic solution under the both monotonic and cyclic loading. Such ability is significantly appealing in the FCG characterization problems.

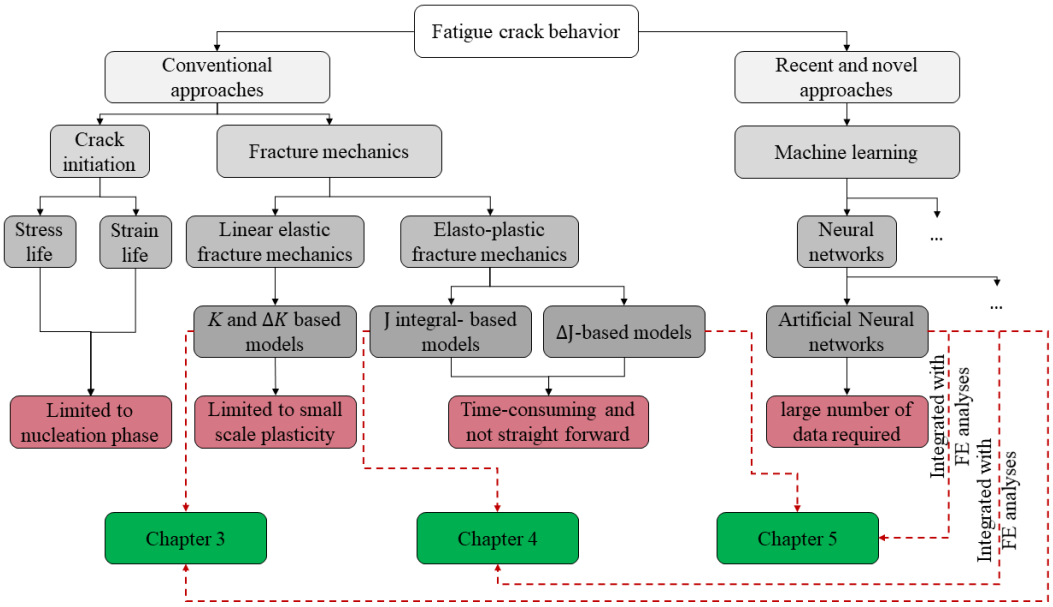

Figure 2.1 Different approaches for FCG characterization and the suggested ones in the different chapters.

Chapter 3

An Artificial Neural Network Modeling Approach for Short and Long Fatigue Crack Propagation

3.1. Abstract

Fatigue crack growth-based damage modeling approaches have received great interest due to its critical importance in the industry. However, a substantial deficiency of an explicit fatigue damage model to quantify the accurate fatigue crack growth behavior remains due to the complex fatigue crack growth behavior in different length scales. This complexity arises from the fact that fatigue crack growth (FCG) in different length scales depends on many damage controlling parameters. Machine learning-based fatigue damage modeling approaches have received noticeable attention for fatigue crack growth analysis due to their abilities to account for numerous damage parameters simultaneously. In the presented paper, a radial basis function artificial neural network (RBF-ANN) model has been developed to predict the FCG behavior, including the short and long crack regimes. The presented RBF-ANN model has been trained and verified by experimental data sets of Ti-6Al-4V titanium alloy, 2024-T3 and 7075-T6 aluminum alloys. The predictions showed that the RBF-ANN model has a good interpolation capability to predict the nonlinearity of both short and long crack growth behavior. However, the model shows poor extrapolation capability for accurate short crack growth predictions for cases that there are limited data sets in hand. The model effectiveness greatly depends on sufficient available input data.

3.2. Introduction

Fatigue failure is encountered as the most common failure mode in many industries. It is widely accepted that the fatigue damage process inherently has multiscale damage characteristics. Fatigue process is comprised of multiple damage phases including initiation of an incipient crack known as crack nucleation, early propagation of the short crack, and finally long crack propagation leading to the final fracture. All the traditional "crack initiation" methods, which consider the crack initiation phase of total fatigue life, are based on stress-life [3-5, 268] and strain-life prediction methods [6-12] On the other hand, linear elastic fracture mechanics (LEFM) method was developed to predict fatigue crack propagation mainly in the long crack regime. However, it is well-known that the short crack (SC) propagation dominates total fatigue life at lower stress levels corresponded to high cycle fatigue [1]. One of the earliest and most popular LEFM methods to quantify the fatigue crack growth (FCG) rate was proposed by Paris and Erdogan [18] in Eq. (3.1):

$$\frac{da}{dN} = C(\Delta K)^m \tag{3.1}$$

Where $\frac{da}{dN}$ is the crack growth rate, ΔK is the stress intensity factor range, and C and m are materials constants. As broadly recognized, the FCG rate in terms of stress intensity factor (SIF) range shows three different regions, which are namely, the threshold region, Paris-region/linear region and fracture region. Shortcomings in Paris' law lead many researchers to propose modifications for Paris' law to address additional controlling parameters affecting the FCG rate. Elber [20] and Newman [21] suggested the crack closure concept to quantify the stress ratio effects on the crack growth behavior. Although the crack closure concept is widely utilized in the aircraft industry, there is a noticeable ambiguity that if crack closure really happens in the short crack regime and/or if this is an influential parameter controlling the fatigue crack growth [1]. In addition, crack closure based models require a number of fitting parameters derived from extensive experimental data [47]. Noroozi et al. [47] recently introduced UniGrow model based on the two-parameter driving force concept to predict the FCG behavior in the long crack regime. The authors suggested that the residual stress at the crack tip induces the residual stress intensity factor (K_r). The residual stress intensity factor (K_r) subsequently affects both the stress intensity factor range (ΔK) and

maximum stress intensity factor (K_{max}) in order to account for the R-ratio effects. Vasudevan et al. [44] introduced the "Unified Approach" employing two controlling parameters as a FCG driving force. The first one is the maximum stress intensity factor (K_{max}) corresponded to the monotonic plastic deformation zone, and the second one is the (ΔK) corresponded to the cyclic plastic deformation zone. Many different crack growth models have been proposed to consider only long crack behaviors by considering the ΔK, R-ratio, and K_{max}. However, multi-length scales characteristics of the fatigue damage mechanism needs to be studied to account for the SC and LC growth behaviors. Fatigue cracks in different length scales are generally defined as the short crack including microstructurally short cracks (MSCs) and physically short cracks (PSCs) up to the long crack (LC) regimes, as graphically depicted in Kitagawa- Takahashi type diagram in Figure 3.1. Bang and Ince [55, 56] recently modified UniGrow model taking into account the rates of crack propagation in both short crack and long crack regimes. The authors presented that the modified UniGrow model provides good correlations with long crack growth data, but the it shows poor correlations with the short crack data [56]. It is widely agreed that total life in high cycle fatigue (HCF) regime is mostly driven by the SC growth and the LC propagation is considered as of less importance [56]. In addition, the SCs may grow faster than the LCs at the same stress intensity range and they may even grow at a ΔK below the threshold traditionally defined for LCs [1]. Considering these essential points, it is crucially prominent to develop an accurate FCG model in a multiscale framework to account for the complete crack length shown in Figure 3.1. To quantify the FCG rate in the SC regime, two main approaches are suggested so far. First one, formulation of ΔK as the crack growth driving force. Second one, replacement of ΔK mostly by crack-tip plasticity, cyclic J-integral (ΔJ), and strain energy factor range [13].

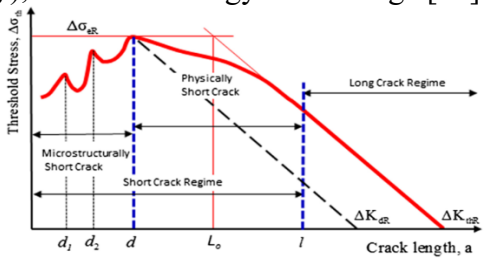

Figure 3.1 Kitagawa-Takahashi type diagram [56].

For instance, Xiulin and Hirt [269] proposed a model based on the idea of replacing $\Delta K = K_{max} - K_{min}$ by the effective SIF range, $\Delta K_{eff} = K_{max} - K_{th}$ due to the fact that FCG occurs if the SIF meet K_{th}. This method received more improvements by further studies [270-272] and finally was proposed in Eq. (3.2) as follows:

$$\frac{da}{dN} = C(\Delta K - \Delta K_{th})^m \tag{3.2}$$

A noticeable work was suggested by Chapetti [270] in which the SIF range threshold is formulated with respect to some microstructural and mechanical properties, which can be obtained by simple experimental tests. He assumed that ΔK_{th} should be regarded as a variable varying according to the crack length. This concept first introduced by Tanaka and Akiniwa [273] and known as the R-curve behavior. In this model, two important concepts have been cleverly incorporated as the microstructural properties and the crack closure concept that increases slowly with respect to the crack length until steady-state conditions are reached [1]. However, the Chapetti model is just suitable for PSCs but it is not capable of explaining the behavior of MSCs [13]. All of the mentioned models characterize the FCG rate in terms of ΔK. The critical factor, ΔK is a quantity

defined in LEFM and it is not capable of accounting for the plastic deformation zone (PDZ) at the crack tip. Although utilizing LEFM in the presence of the relatively small yielded zone size responses proper enough, it collapses when the PDZ size is comparable with the crack size. In other words, the limitation of LEFM is the relatively large PDZ size at the crack tip. The question that arises here is: Under which circumstances, the PDZ size is comparable with crack length? One can easily predict that either the stress level is significantly high or the crack size is small. As a result, LEFM is not applicable to explain FCG rate behavior in the case of short cracks. Many modifications have been suggested to approximately address the PDZ at the crack tip. However, replacing ΔK with a criterion related to energy seems to be a logical solution [13]. Shyam et al. [74-76] suggested a crack growth model based on the dislocation theory by replacing the SIF with monotonic and cyclic crack tip opening displacement (CTOD) parameters. In this model, if CTOD meets a critical value, crack propagation occurs. This model was improved by Deng et al. [77], but the results showed that the crack tip opening displacement is not suitable to account for MSCs. Another replacement of ΔK is based on the cyclic J-integral concept, firstly introduced by Dowling and Begley [82]. Many researchers tried to use this parameter defined in elasto-plastic fracture mechanics to characterize the fatigue cracks behavior [274-276]. However, describing the fatigue damage mechanism of short cracks remains a challenge. Almost all research efforts to predict the FCG behavior lead us to realize that the final aim is to quantify the FCG rate ($\frac{da}{dN}$) by an explicit mathematical model. Such FCG model should be capable of predicting complex nonlinear behavior of crack propagation characteristics in such a way that crack growth rates can be formulated based on a so-called crack growth driving force depending on a number of controlling variables. To achieve this goal, researchers have been trying to account for critical damage controlling variables to come up with a suitable mathematical formula. Experimental fatigue can be very useful to map out key damage controlling variables on FCG rates. Those parameters subsequently can be employed in the mathematical formation of an FCG model. The most noticeable of such parameters are R-ratio, ΔK, ΔK_{th} and K_c, which are traditionally introduced to describe crack propagation behavior for long cracks as depicted in Figure 3.2a). Short crack growth behavior shows complex propagation characteristics such a way that crack growth rates depend on additional controlling parameters e.g. the stress levels and the crack length-dependent short crack threshold as shown in Figure 3.2b). With all these in mind, machine learning is considered as a promising modeling method due to its strong nonlinear prediction and multi-variables capability to account for not only many variables, but also the interplay relationship among those variables. Therefore, several research studies have been recently undertaken to adopt the machine learning approach to shed light on the characterization of FCG behavior. Machine learning algorithm (MLA)s are classified into a large number of groups. Two main groups of MLAs are regarded as supervised learning and unsupervised learning methods. Almost all of the (MLA)s methods which are applicable to function approximation are classified in the supervised learning group. Most of methods in this group are regression-based techniques such as linear regression, support vector regression (SVR), ensemble methods, decision trees, etc. Among them, the artificial neural network (ANN) has been received substantial attention since its capability to fit the relationship among nonlinear multivariable. Subsequently, ANN has been adapted in different areas such as material science [214, 277-279] and fracture mechanics problems including fatigue failure, creep, and even corrosion fatigue [142, 143, 216]. Artymiak et al. [121] estimated the application of artificial neural networks to predict S-N curves and fatigue limit by means of a comprehensive database from different materials. The prediction results showed accurate agreement with experimental data sets

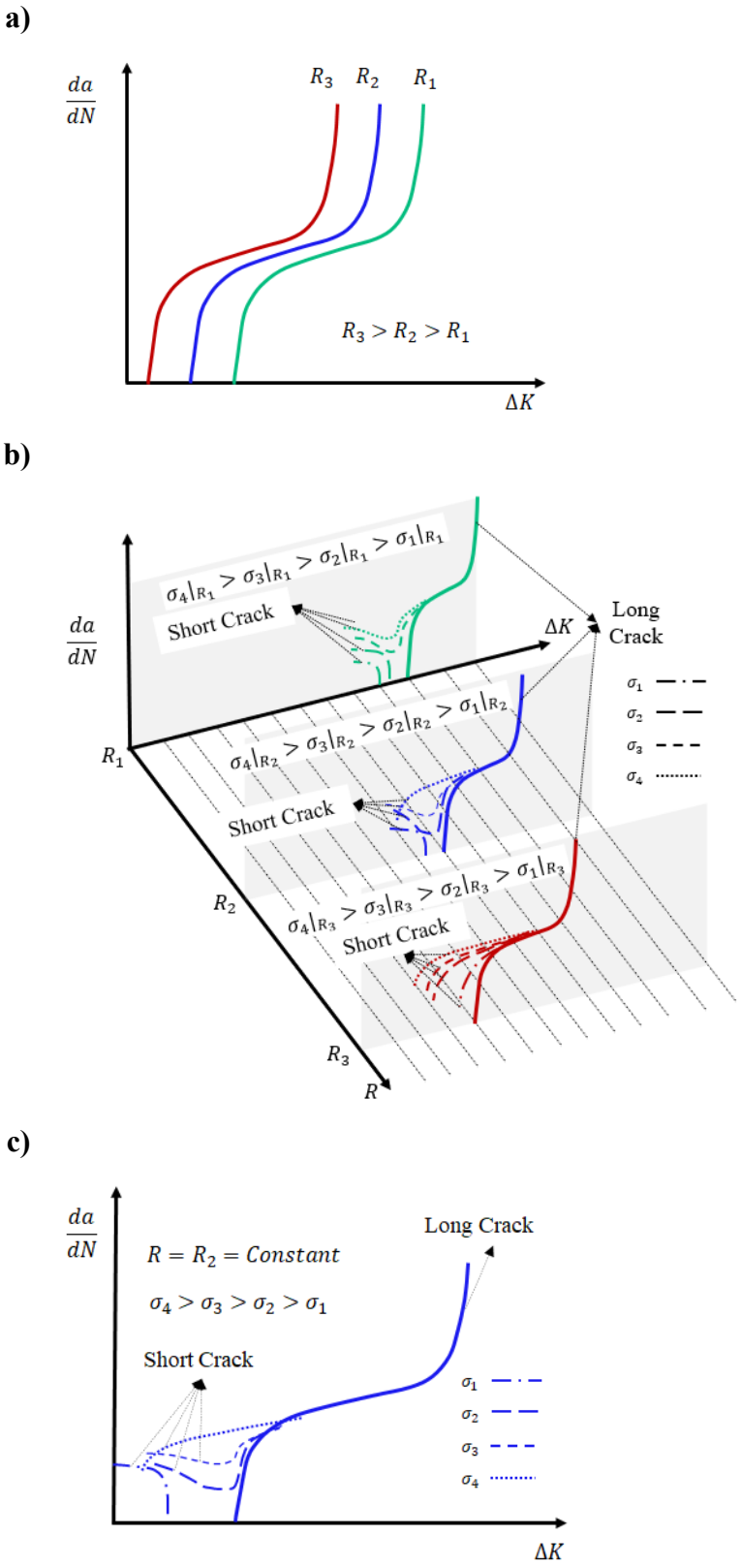

Figure 3.2 FCG rate depends on a) SIF and R-ratio in the LC regime, b) SIF, R-ratio, and stress level in the SC regime, and c) SIF and stress level in the SC regime under a constant R-ratio.

Wang et al. [199] developed different types of ANN, including radial basis function artificial neural network (RBF-ANN), extreme learning machine (ELM), and genetic algorithms optimized backpropagation network (GABP) to predict FCG rates in the LC regime. Wang et al. compared the results obtained from different ANN models mentioned above to determine the advantages and disadvantages of each model. It should be pointed out that all of the methods showed significant potential to predict FCG rates in the LC regime. Zhang et al. [214] developed an RBF-ANN model to predict the FCG rates in terms of the ΔK in the LC regime under different R-ratios. The authors compared the predicted results with experimental data for several materials. The excellent agreement revealed the high potential of ANN algorithms to describe the nonlinearity of FCG rate behavior in terms of ΔK under different R-ratios in the LC regime. Barbosa et al. [280] developed a new constant life diagram (CLD) for P355NL1 steel based on an artificial neural network algorithm. The experimental data of S-N curves, which are basically used in LC regime, under different R-ratio were employed to train the network. The proposed model is able to estimate the safety region as a function of the mean stress and stress amplitude. Martinez et al. [166] proposed an approach to predict the fatigue life of steel S420MC based on an artificial neural network algorithm. The suggested model can account for load sequences and temperature effects. As a result, ANN-based algorithms are suggested as promising approaches to stablish the relationship between sequence effects and the fatigue life. As mentioned earlier, FCG rate depends on many damage controlling parameters. Therefore, machine learning algorithms have recently received much attention in order to study fatigue failure. It is worth mentioning that in addition to the machine learning algorithms, Muc [281] suggested a fuzzy approach as another robust method to describe the uncertainty and randomness of parameters controlling fatigue strength of composite materials. In spite of all those research works, no successful FCG model has been developed yet to address complete damage mechanisms on all crack length scales.

According to the literature review provided in this section, it is crucially important to come up with a model to account for both the SC and LC regimes in Figure 3.1. However, due to the limitation of the stress intensity factor as a LEFM parameter to deal with relatively large-scale plasticity at a given short crack tip, traditional models failed to address the short FCG rate. Besides, employing other fracture mechanics parameters such as CTOD and J-integral has not been successful so far. The reason is the complexity of using such parameters and quantifying them under various conditions of geometries and loading types. Fortunately, using artificial neural networks showed a high potential to address the fatigue cracks' behavior in the LC regime. However, there is not any report to reveal the capability of such algorithms in the SC regime. The significant potential of machine learning-based models shed light into the characterization of the FCG rate even in the SC regime, which remained a challenging problem. It is in this spirit that an RBF-ANN algorithm is proposed to provide an integrated modeling framework to predict both the short and long crack propagation by considering multivariable crack growth controlling parameters in the present study.

3.3. Modeling Methodology

3.3.1. Radial Basis Function Artificial Neural Network

It has been for decades that researchers utilize biological neural network-based methods to approach practical problems. Among all neural network-based algorithms, the radial basis function neural network has received significant attention as a robust method when it comes to function

approximation, system control, etc. [214]. As for the ANN applied to an approximation problem, the key idea is that every point in a particular data set influences the value of the hypothesis at an arbitrary point. The question that emerges here is how this influence should be defined? In the RBF-ANN, as the word "Radial" suggests, the hypothesis affected through the distance. It means closer a data point to the hypothesis, more influence on the hypothesis. Assuming h as a function standing for the hypothesis mentioned above, D as a particular 2-dimensional domain including the data set, and X as coordinates of data in a 2D domain (X=(x,y)), Eq. (3.3) can be written as follows:

$$\forall\ (x_n, y_n) \in D\ \ influences\ \ h(X)\ \ based\ on\ \ ||X - X_n|| \tag{3.3}$$

To quantify such a purpose, different types of functions can be employed e.g. Gaussian functions, multi-quadric functions, linear functions, etc. The most operational function, which is engaged in the present paper as well, is the Gaussian function shown graphically in Figure 3.3. As a result, the hypothesis function can be defined as follows:

$$h(x) = \sum_{k=1}^{K} w_k exp(-\gamma \|X - \mu_k\|^2) + b_k\ \ and\ K \leq N \tag{3.4}$$

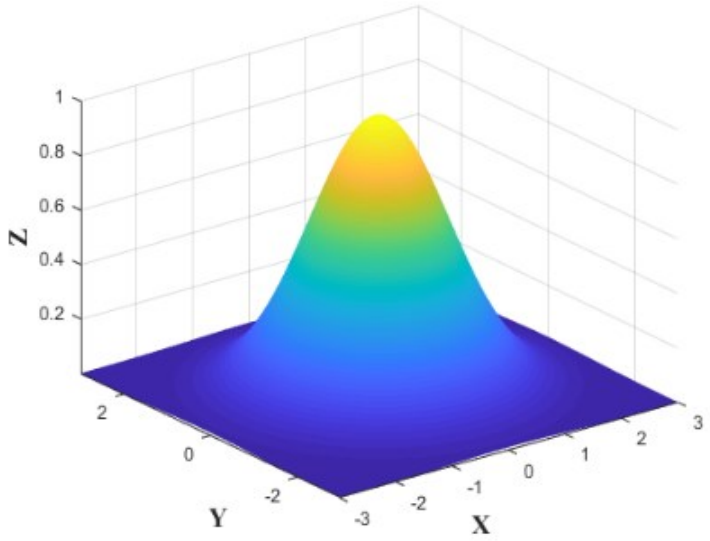

Figure 3.3 A schematic of Gaussian functions.

In the equation above, N is the number of data, K is the number of radial basis functions, or in this case gaussian functions, b is a parameter named bias, μ_i are the center of each activation function, W_i are called weights, and γ is a positive constant parameter. It is noticeable that the maximum number of activation functions is N. In this case, Eq. (3.4) can be replaced as follows:

$$h(x) = \sum_{n=1}^{N} w_n exp(-\gamma \|X - X_n\|^2) + b_n \tag{3.5}$$

As shown in Figure 3.3, $\mu_k(X_n)$ as the centers of the bumps are the most influential coordinates, and the influence gradually decreases and finally dies symmetrically as the distance increases. With this in mind, RBF-ANN is suitable at local approximation. Figure 3.4 illustrates the schematic structure of an RBF-ANN used in the present study. As presented in Figure 3.4, the RBF-ANN is a network consisting of 3 main layers. The first layer consists of all input data shown by $\{X_1, X_2, X_3, \dots, X_N\}$. The model clusters K subdomains and assigns a center, μ_i, to each of them. Thereafter, the distance from all data to their corresponded centers, $\|X_i - \mu_i\|$, is calculated and delivered to the only hidden layer employing Gaussian functions,φ_i. Afterward, a set of N equations and K unknowns ($K \leq N$) is solved simultaneously to calculate w_i and b_i, as shown in Eq. (3.6).

$$\begin{bmatrix} exp(-\gamma\|X_1-\mu_1\|^2) & \dots & exp(-\gamma\|X_1-\mu_K\|^2) \\ exp(-\gamma\|X_2-\mu_1\|^2) & \dots & exp(-\gamma\|X_2-\mu_K\|^2) \\ \vdots & \vdots & \vdots \\ exp(-\gamma\|X_N-\mu_1\|^2) & \dots & exp(-\gamma\|X_N-\mu_K\|^2) \end{bmatrix} \begin{bmatrix} w_1 \\ w_2 \\ \vdots \\ w_K \end{bmatrix} + \begin{bmatrix} b_1 \\ b_2 \\ \vdots \\ b_K \end{bmatrix} \approx \begin{bmatrix} y_1 \\ y_2 \\ \vdots \\ y_N \end{bmatrix} \tag{3.6}$$

Finally, the mathematical formula to calculate the FCG rate is proposed as the output in the third layer. It is noticeable that RBF-ANN is a feedforward static neural network.

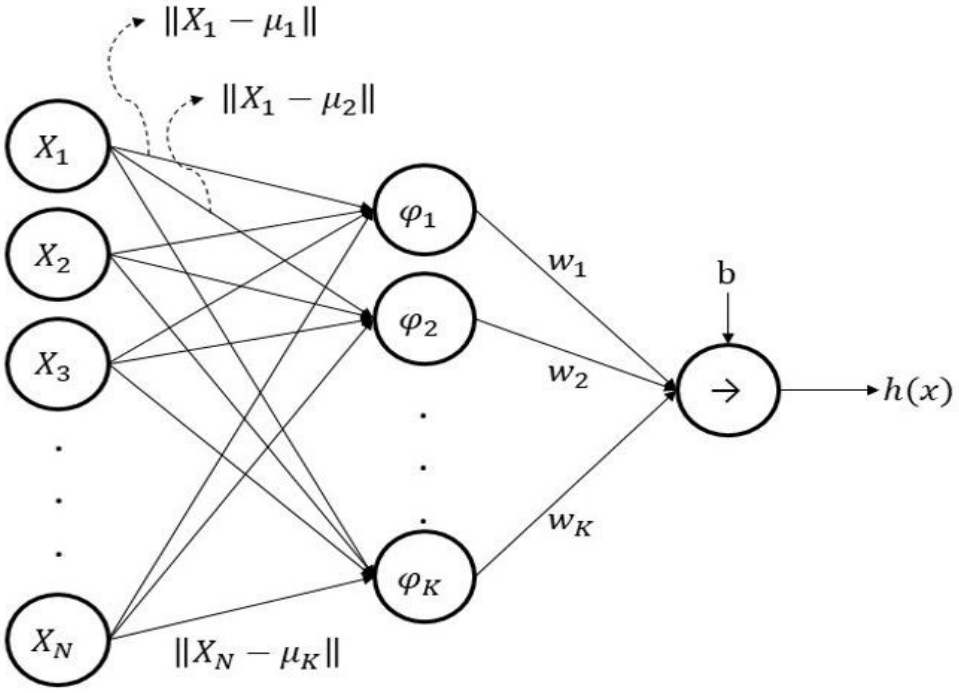

Figure 3.4 The structure of RBF-ANN.

It means that the transformation of information is done in just one direction (see Figure 3.4) in contrast to backpropagation models. There have been efforts to show that feedforward neural network-based models have significant advantages over backpropagation ones in the matter of nonlinear problems [175, 282].

3.3.2. The Establishment and Training of the Artificial Neural Network (ANN)

One of the most important advantages of characterizing the FCG rate in terms of ΔK in LC regime is that propagation rates are independent of specimen geometry, crack length, stress level, etc. In contrast, in SC regime:

I) FCG rates depend on crack length,

II) FCG rates are higher than those of LCs,

III) SIF range threshold varies with crack length, and

IV) SIF range threshold is below the SIF range threshold of LCs.

These differences have been known as "break down of similitude" for short cracks [1]. The break down of similitude is shown in Figure 3.2b) schematically. As discussed earlier, Figure 3.2a) shows FCG rate in LC regime depends on R-ratio and ΔK. With this in mind, the FCG rate can be written as a function of ΔK and R for the long crack regime in Eq. (3.7).

$$\frac{da}{dN} = f(\Delta K, R) \tag{3.7}$$

Equation (3.7) emphasizes that two controlling parameters are needed as R-ratio and ΔK to calculate the FCG rate in the LC regime. On the other hand, the stress level (σ) is a controlling damage parameter in addition to the ΔK and R-ratio in the SC regime as schematically shown in Figure 3.2 b). As a result, the short crack regime the FCG rate can be expressed as a function of ΔK, R and σ in Eq. (3.8).

$$\frac{da}{dN} = g(\Delta K, R, \sigma) \tag{3.8}$$

It should be pointed out that the break down of similitude for short cracks may be the result of characterizing fatigue cracks behavior in terms of the SIF. Recently, Sadananda et al. [1] stated that there would not be any break down of similitude if an appropriate two-parameter driving force in terms of K_{max} and ΔK is chosen. However, such characterization needs to quantify internal stresses imposed by microstructural properties of materials, which is not practically possible, at least currently.

With all these in mind, in the present paper, two separate RBF-ANN models are developed in order to account for the FCG rate in both the SC and LC regimes. First model deals with the LC regime and the second one predicts SCs propagation behavior. As shown in Figure 3.5, in the first model a two-input single-output RBF-ANN is proposed.

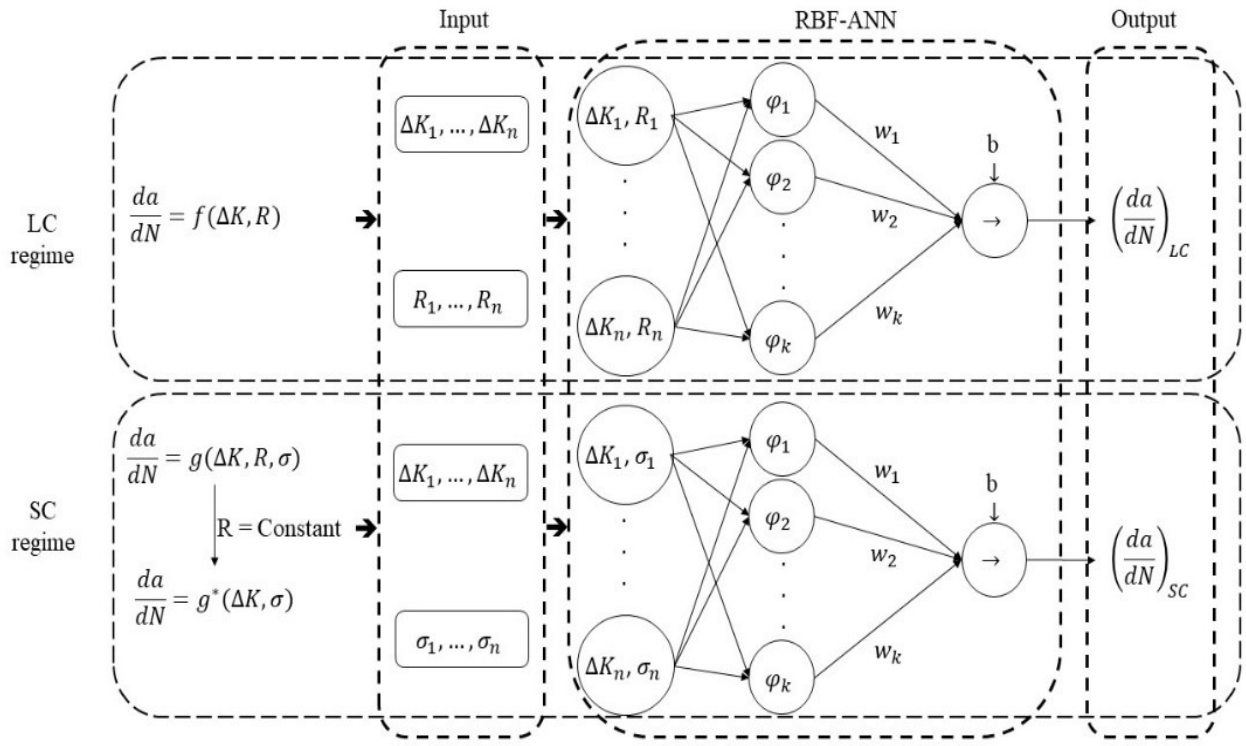

Figure 3.5 Input and output data in RBF-ANN models in SC and LC regimes.

The inputs are ΔK and R-ratio and the output is fatigue crack growth rate ($^{da}/_{dN}$). Based on the inputs and output quantities for the LC regimes, it is intended to formulate the function "f" in Eq. (3.7) to model the crack growth behavior. As for the SC regime, the function "g" is considered on the basis of three input parameters in Eq. (3.8). However, considering the fact that the FCG data in the literature is limited, short fatigue crack growth behavior is characterised for a constant R-ratio. Let's consider the schematic of Figure 3.2b) as a behavior of FCG rate for a given material. This figure shows that for different R-ratios (R_1, R_2, R_3), stress levels ($\sigma_1, \sigma_2, \sigma_3, \sigma_4$) and ΔK, there would be a corresponded $\frac{da}{dN}$ as FCG rate. However, in the case of limited data at R_1 and R_3, it is possible to consider only a particular R-ratio e.g. R_2. As a result, the behavior of FCG rate can be depicted by Figure 3.2c) in SC regime. It should be pointed out that Figure 3.2c) shows a 2D view of a 3D FCG space of Figure 3.2b). The normal vector of this surface is axis R in Figure 3.2b). In other words, instead of obtaining the function "g" in Eq. (3.8), it is possible to come up with the function g^* defined as follow:

$$\frac{da}{dN} = g(\Delta K, R, \sigma) \xrightarrow{if: R=constant} \frac{da}{dN} = g^*(\Delta K, \sigma) \tag{3.9}$$

In this way, the potential of RBF-ANN can be evaluated in the SC regime. Based on this assumption, a two-input single-out put RBF-ANN has been developed to account for the SC regime as depicted in Figure 3.5. In this model ΔK and stress level are inputs and $^{da}/_{dN}$ is the output. In addition, the important assumption is that the stress ratio is constant in the short crack regime. Both the SC and LC regime should be considered simultaneously and two separate RBF-

ANN should be integrated in a same modeling framework in order to calculate total propagation fatigue life. The schematic flowchart is developed to establish such a procedure shown in Figure 3.6. As shown in Figure 3.6, the first step is data preprocessing, including two parts, 1) taking the logarithm of ΔK in order to decrease the scatter influence imposed by order of the magnitude, 2) normalizing the data from the first part. The second and most essential step is the development and training the neural network model. Therefore, Neural Network toolbox of MATLAB R2018b software is employed to developed ANN model(s) on the basis of the method explained in section 3.2.1. The neural network toolbox provides a function called "newrb" modeling a radial basis network. This function is adapted in the presented study and its formulation can be expressed as the command shown in Eq. (3.10).

$$\text{Net} = \text{newrb (P, T, goal, spread)} \tag{3.10}$$

Where P and T are the input and output data (described in Figure 3.5), respectively, "goal" presents mean square error, and "spread" shows the spread of radial basis function. These parameters are further discussed in next parts. The modeling steps taken by the "newrb" are indicated as green boxes in flowchart of Figure 3.6. The third step is comparing the model results with the experimental data. In order to do that, experimental data sets of 2024-T3, 7075-T6 aluminum alloys, and Ti-6Al-4V titanium alloy are used to verify if all the unknown factors in Eq. (3.6) are obtained properly. The last step is adjusting the parameters calculated in the previous step and optimizing the RBF-ANN. These parameters are the number of the neurons, value of bias, weights, etc. discussed earlier. The optimized values of almost all of these parameters are obtained by the ANN model via an iteration method (see Figure 3.6). This optimization is operated by the ANN model and mentioned parameters are updated automatically.

However, the model is developed in such a way that a user is able to adjust a few parameters, e.g., the maximum number of neurons and the mean square error (MSE) goal, as a criterion should be satisfied before the end of the procedure main loop. In addition, the user can determine the portion of the data used for verification. The data are chosen randomly by the model. In the presented study, 30% of the data have been used to verify the model. It means the model continues the loop shown in Figure 3.6 until the MSE calculated by 30% of data decreases to the criterion determined by the user. The other prominent parameter is the spread of radial basis function (SRBF) which is introduced as γ in Eq. (3.5). As discussed earlier, the activation function in RBF-ANN is a Gaussian function. The spread of radial basis function determines how sharp or smooth this function varies with respect to the distance. This dependency is shown in Figure 3.7. It is evident that in Figure 3.7a) the hypothesis may be under the influence of data located in the large distance. On the other hand, in Figure 3.7 the impact decreases sharply. It means only extremely close data can affect the hypothesis. By considering this fact, tuning the spread of radial basis function is significantly crucial due to the estimation of the two different capabilities of RBF-ANN. First one is the capability of producing a nonlinear function to fit scatter fatigue crack growth data. In order to do that a sharp activation function like Figure 3.7c) is a better choice since the interpolation would be more accurate. Subsequently, presenting a nonlinear function to fit scattered data, would be more likely to achieve. Second one is how powerful RBF-ANN is when it comes to extrapolation. In other words, the capability of crack behavior prediction in situations in which there is no data in hand.

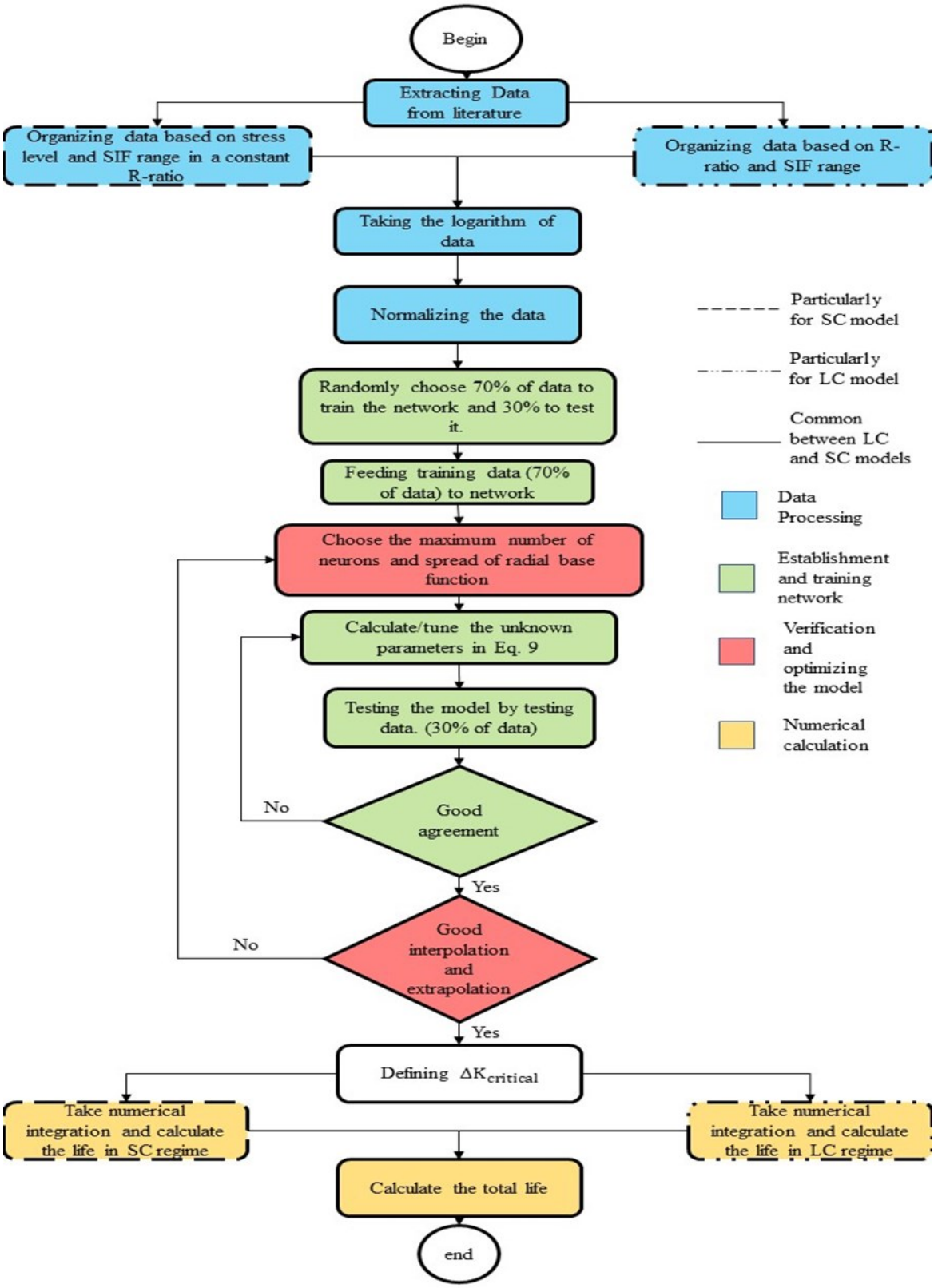

Figure 3.6 Schematic flowchart of the ANN model.

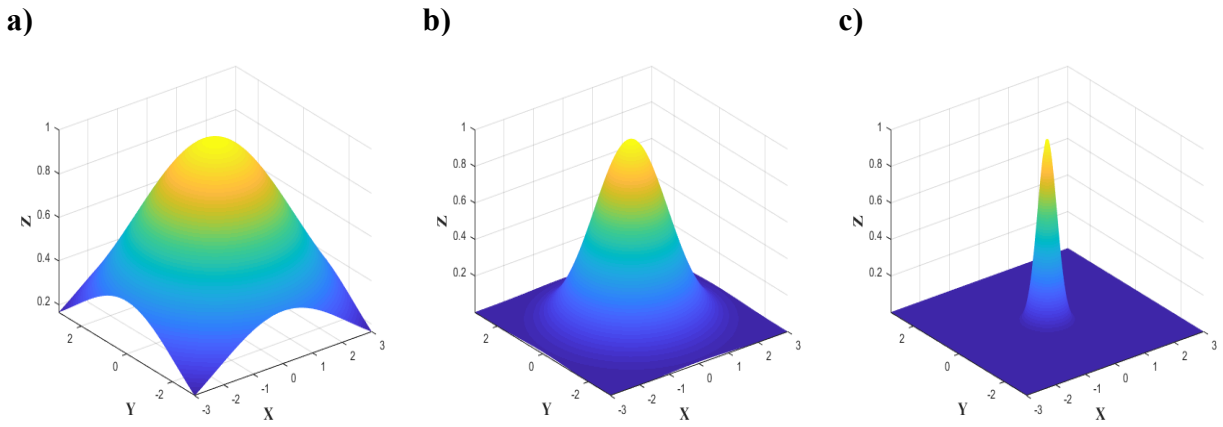

Figure 3.7 The influence of the spread of the radial basis function on the Gaussian function. a) high SRBF, b) average SRBF, and c) low SRBF.

Under such circumstances, choosing an activation function like Figure 3.7a) would be the solution. It is evident that if there is no data located at a small distance to the hypothesis, the only way is to predict based on data located in the larger distance. As a result, the determination of a proper value as the spread of radial basis function is challenging to balance both sides. This challenge would be more crucial when the input data are not chosen appropriately, or when there are not appropriate input data in hand. Basically, such a challenge occurs under three conditions: 1) the number of data (it is better to say the density of data) is not large enough 2) the data are not sufficiently accurate 3) the data is not properly distributed.

3.4. Results and discussion

3.4.1. Experimental details

In the presented study, experimental FCG data sets of 2024-T3 and 7075-T6 aluminum and Ti-6Al-4V titanium alloys have been utilized to train and verify the presented ANN models. Original FCG data sets of those materials can be found in literature [46, 47, 56, 214, 283] for the LC regime and [56, 284-288] for the SC regime, respectively. In the case of LC data for Al7075-T6, FCG data were obtained by center-cracked tension (CCT) specimens. These specimens were milled to the dimensions of 75 mm wide by 300 mm long by 2.3 mm thick. The crack starter notch was considered as a slot with the dimensions of 5 mm long and 0.5 mm high. Applied loading conditions were consistent with the ASTM Standard Test for measurement of FCG rates (E- 647) [289]. FCG data of Al7075-T6 in the SC regime, were obtained by single-edge-notch tension (SENT) specimens. The SENT specimens' dimensions were 50 mm wide by 300 mm long by 2.3 mm thick. The radius of semicircular notch as the starter notch was 3.2 mm. The loading conditions were the same as ones for LC regime [289]. The LC experimental data of Al2024-T3 were obtained by round side-grooved specimens with chevron notches. The tests were operated by using an in-plane bending fatigue testing machine. The length and thickness of the specimens were 75 mm and 4 mm respectively. The width of the specimens was 14 mm and 5 mm in the grip side and force side respectively. The detailed dimensions of specimens and the testing machine can be found in the literature [290]. The loading conditions were based on the ASTM standard of (E-647). In the case of Al2024-T3 and Ti6Al4V in the SC regime, SENT specimens were tested to obtain

the FCG data. The SENT specimens' dimensions were 50 mm wide by 305 mm long by 2.3 mm thick. The radius of semicircular notch in these specimens was 3.18 mm [285]. The loading conditions were based on the guidelines of AGARD Cooperative Test Programme [291]. As for Ti6Al4V in the LC regime, compact-tension (CT) specimens were used o obtain FCG data for this alloy. The dimensions of these specimens were 400× 25 × 8 mm. The loading conditions were in accordance with the ASTM standard of (E-647) [292].

3.4.2. Long Cracks

To train RBF-ANN discussed in section 3.2.2, FCG data in terms of ΔK under different R-ratios is required. The experimental data sets of 2024-T3 and 7075-T6 aluminum and Ti-6Al-4V titanium alloys have been utilized. Figure 3.8 presents the long fatigue crack growth data of those alloys extracted from literature [46, 47, 56, 214, 283] under different R-ratios. It should be noted that 30% of the data are randomly chosen to verify the model predictions by means of the RBF-ANN. In other words, only 70% of the data are utilized in order to train the network. Figure 3.9 presents the results of interpolation and extrapolation of the model for the Al7075-T6 by using input data shown in Figure 3.8a). Figure 3.9a) indicates that the RBF-ANN model can predict the crack growth behavior of the LCs as a 3D prediction surface at different R-ratios. In this case, the model is somehow capable of showing acceptable extrapolation in the regions determined by the red dashed closed curves as shown in Figure 3.9a). Furthermore, the model shows good prediction in the threshold and high ΔK regions. Figure 3.9b) presents the crack growth curves as a function of ΔK under various R-ratios to show the potential capability of RBF-ANN to predict the nonlinearity of the FCG rate in terms of ΔK, even in the Paris-region the Al7075-T6. Figure 3.10 presents the model predictions in the LC regime for the Al2024-T3 indicated in Figure 3.8b). To deeply assess the capability of RBF-ANN, two separate models have been developed in the case of the Al2024-T3 in the LC regime. The only difference between these two models is the value of SRBF. As a result, it is possible to present the importance of this spread parameter and its effects on the prediction of RBF-ANN. SRBF is defined as γ in Eq. (3.5) and a more detailed discussion can be found in section 3.2.2 (see Figure 3.7). Figure 3.10a) and b), show accurate interpolation to predict the nonlinearity of FCG rate in terms of stress intensity factor range based on a low spread of radial basis function ($\gamma = 5$) for the Al 2024 such as the one schematically shown in Figure 3.7c). On the other hand, Figure 3.10c) and d) indicated extrapolation capability of the high spread of radial basis function ($\gamma = 11$) such as the one schematically shown in Figure 3.7a) to predict the behavior of long cracks in areas shown by red dashed closed curves which are beyond the input data.

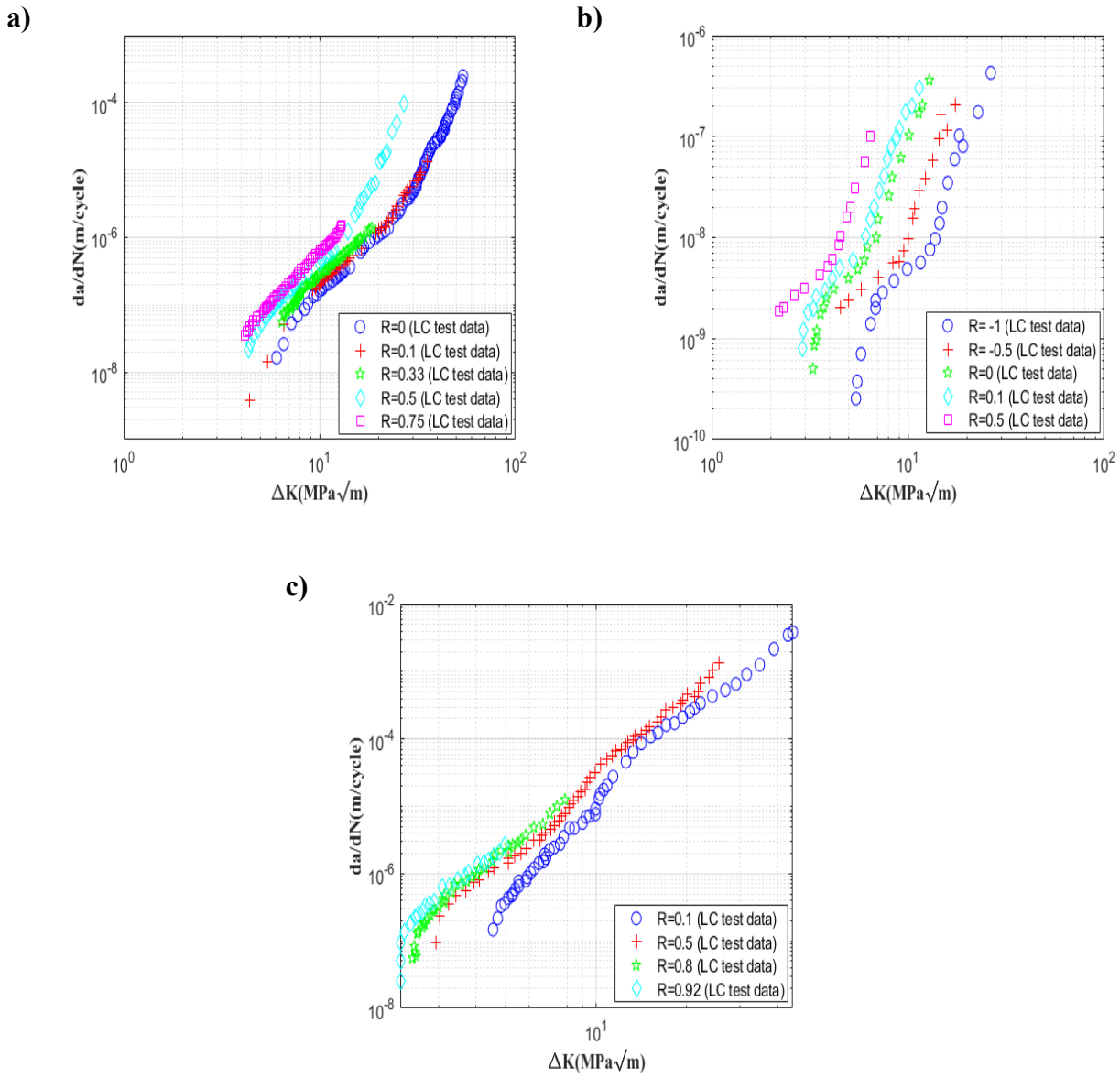

Figure 3.8 FCG data in LC regime of a) Al7075-T6, b) Al2024-T3 and c) Ti-6Al-4V.

Based on the effects of the spread of radial basis function in Figure 3.10, it is evident that the spread parameter in Figure 3.10a) and b) is smaller than the one used to obtain the results in Figure 3.10c) and d). As depicted in Figure 3.10a) and c), it can be stated that by increasing the spread of radial basis function (from $\gamma = 5$ to $\gamma = 11$), it is possible to predict the behavior of the FCG rate even in the areas in which there is limited crack growth data in hand. From this point of view, the higher SRBF corresponded to Figure 3.10c) has the advantage of extrapolation over the lower SRBF in Figure 3.10a).

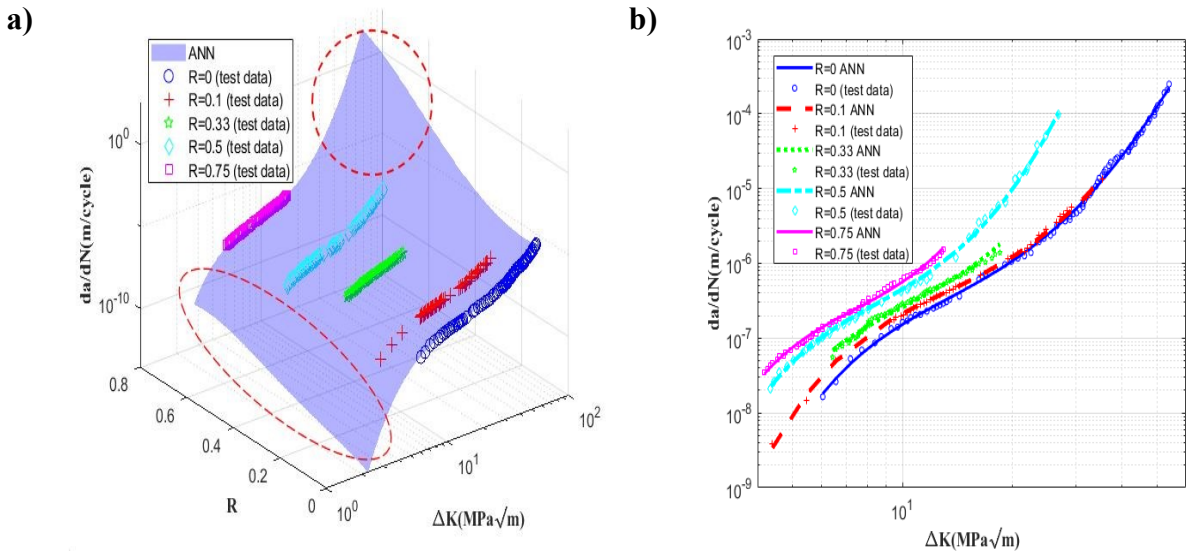

Figure 3.9 LCs experimental and corresponded ANN results of Al7075-T6 in a) 3D vies and b) 2D view.

However, Figure 3.10b) and d) indicate that the cost of extrapolation reduces the accuracy of results and capability of predicting the nonlinear behavior in the Paris-region. The question that arises here is that why it is essential to employ two different models with two diverse spread values of radial basis function in the case of the Al2024-T3 demonstrated in Figure 3.10. On the other hand, the results show that both the extrapolation and high accuracy in predicting nonlinear behavior are possible simultaneously in the case of the Al7075-T6 shown in Figure 3.9. The key to answering this question is a number or density of input data points. In the case of the Al7075-T6 (see Figure 3.9), the number of input data is 365, but in the case of the Al2024-T3 (see Figure 3.10), the size of the input data decreases to 93. In addition, in the case of the Al7075-T6, the domain of prediction is between the R-ratio of 0 to 0.75. However, this domain is between R-ratio of -1 to 0.5 in the case of the Al2024-T3. It means the higher density of input data increases the possibility of achieving accurate interpolation and extrapolation simultaneously. For instance, predicting the FCG behavior of the Al7075-T6 at R-ratio of -1 or -0.5 dramatically decreases prediction accuracy at the R-ratio of 0 to 0.75 and thus degrading the capability of the model to predict nonlinear behavior. It should be noticed that most of the neural network-based methods, especially RBF-ANN, are not developed for extrapolation. As a result, extrapolation is limited to regions shown by the red dashed closed curves in Figure 3.9a) and Figure 3.10c). The other important point about extrapolation is the behavior of FCG rate data in terms of SIF range at different R-ratios in the LC regime and at different stress levels in the SC regime.

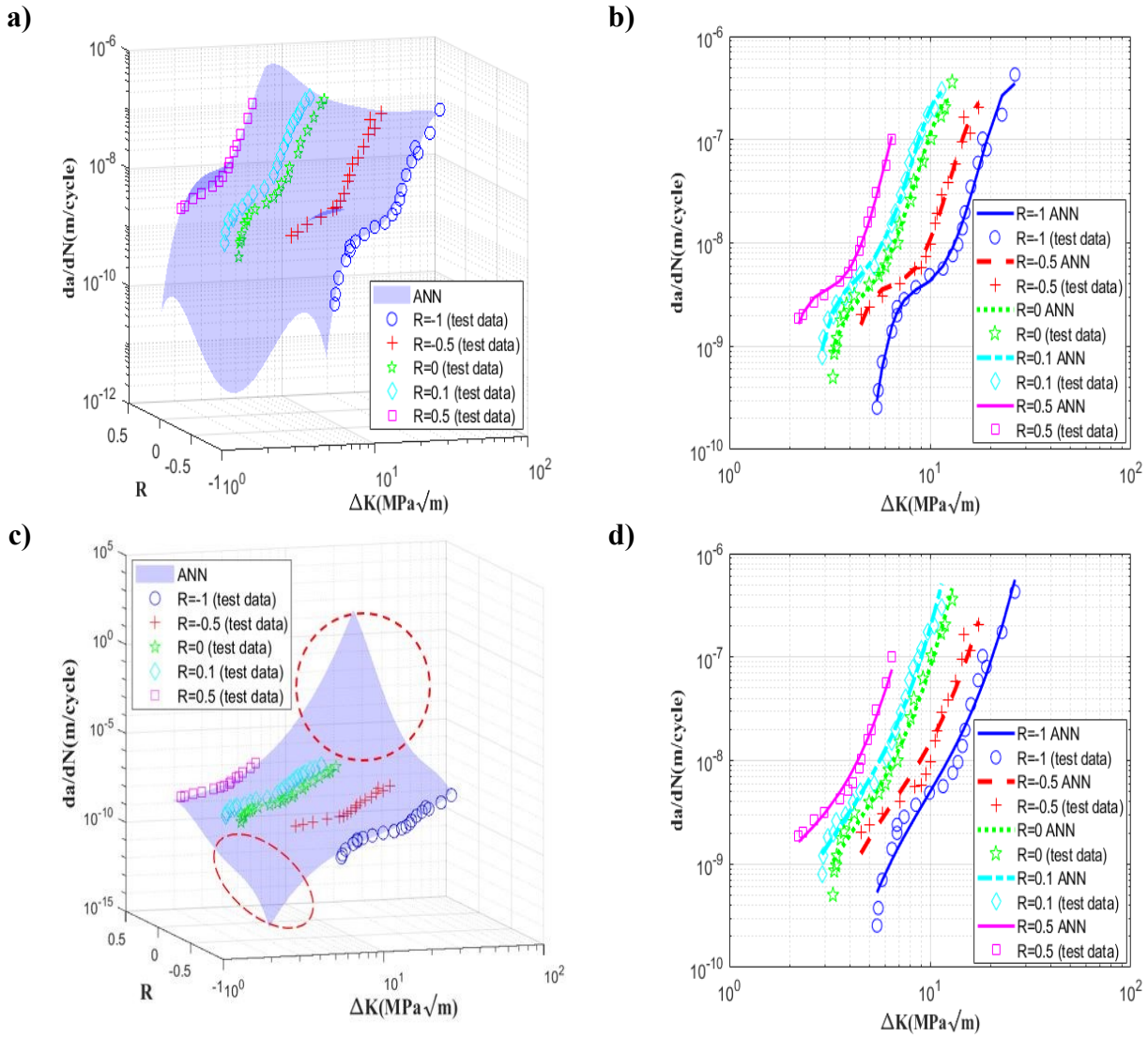

Figure 3.10 LCs experimental and corresponded ANN results of Al2024-T3 a) 3D view and low SRBF, b) 2D view and low SRBF, c) 3D view and high SRBF, and d) 2D view and high SRBF.

As mentioned earlier, in the case of LCs shown schematically in Figure 3.2a), the response of the FCG rate at different R-ratios is somehow the same. It means all of the curves corresponded to different R-ratios show that the FCG rate increases by increasing the SIF range. On the other hand, in the case of SCs shown schematically in Figure 3.2b), the response of the FCG rate at different stress levels is very complicated. In other words, different curves corresponded to different stress levels are not necessarily monotonic with respect to the SIF range. As a result, extrapolation would be more achievable in the case of the LC regime rather than the SC regime. Figure 3.11 shows the results of ANN for the Ti-6Al-4V. Good agreement has been obtained between the ANN results and the experimental data, as shown in Figure 3.11.

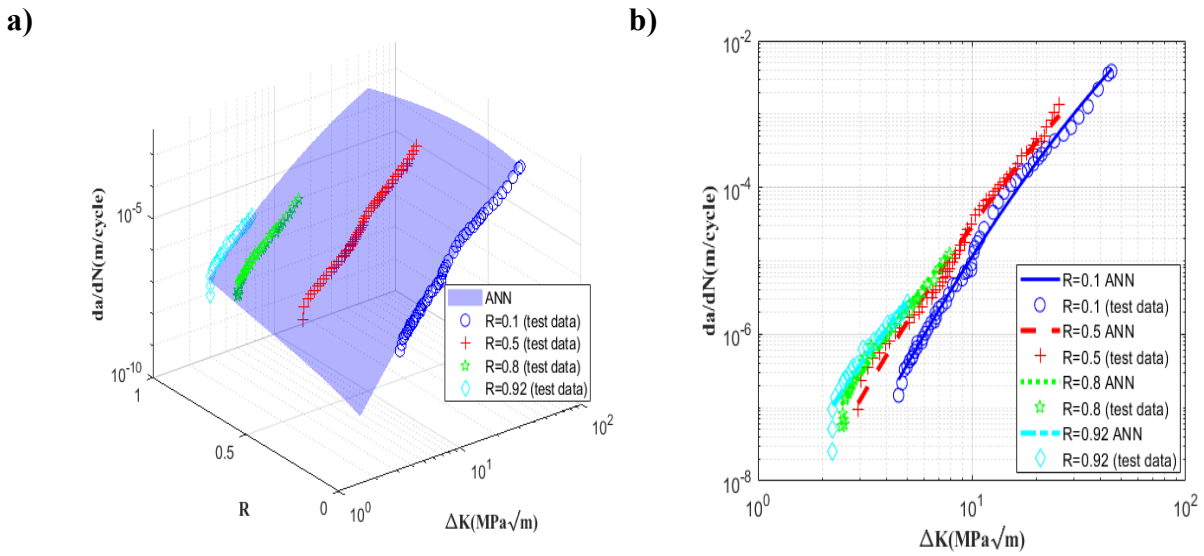

Figure 3.11 LCs experimental data and corresponded ANN results of Ti6Al4V in a) 3D view and b) 2D view.

$$error = (da/dN)_p - (da/dN)_e \tag{3.11}$$

Probability density function (PDF) is used to evaluate the prediction accuracy of the RBF-ANN model for each analyzed material at different R-ratios in the LC regime. The PDF measures the prediction error values between the predicted FCG rates $(da/dN)_p$ and the experimental FCG rates $(da/dN)_e$ for a given material as expressed in Eq. (3.11). The model prediction is regarded conservative for positive error values and non-conservative for negative error values. Error distributions have been considered as normal probability distribution to fit PDFs. Figure 3.12 (a)-(d) show error PDFs for Al7075-T6, Al2024-T3 for low SRBF, Al2024-T3 for high SRBF and Ti6Al4V, respectively. The scatter of the error distribution of PDFs show that the developed RBF-ANN is capable for accurate predictions of FCG behavior of all three analyzed at various R-ratios in LC regime.

3.4.3. Short Cracks

In this section, the FCG behavior of the SC regime is investigated by the RBF-ANN method. It should be emphasized that the propagation behavior of SCs is significantly more complicated than that of the LCs. It is due to the fact that the number of damage controlling parameters affecting the FCG rate in the SC regime is noticeably larger than the one in the LC regime. As shown in Eq. (3.9), the explicit mathematical model to predict short FCG rates should be based on a function of both the ΔK and stress level under a constant R-ratio.

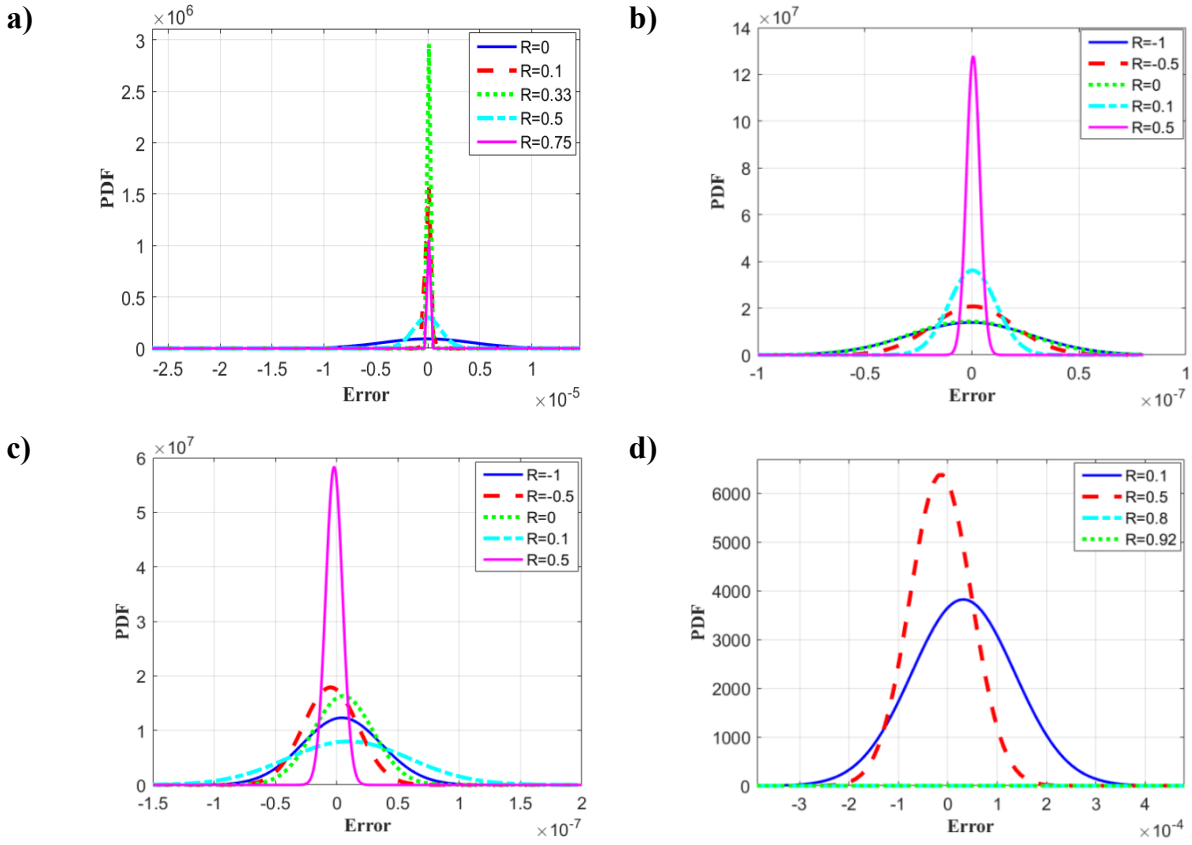

Figure 3.12 Probability Density Function (PDF) of prediction error in LC regime for a) Al7075-T6, b) Al2024-T3 and low SRBF, c) Al2024-T3 and high SRBF and d) Ti6Al4V.

The experimental data sets of 2024-T3 and 7075-T6 aluminum and Ti-6Al-4V titanium alloys have been utilized in the present section in order to train the RBF-ANN. These materials are the same ones employed in the case of LCs in section 3.3.1. The R- ratio for each material during investigation in the SC regime is a constant and is equal to 0.0, 0.5, and 0.1 for the Al7075-T6, Al2024-T3, and Ti-6Al-4V, respectively. Figure 3.13 presents the experimental data sets of each material. These data sets classified by maximum stress levels can be found in the literature [56, 285-289]. An RBF-ANN model as discussed in section 3.2.2 was developed to characterize the FCG rate in terms of SIF range and stress level while R-ratio is kept constant (see Figure 3.5). Figure 3.14 shows the experimental data and ANN results for the Al7075-T6 in both 2D and 3D views. As shown in Figure 3.14, the RBF-ANN is not capable of predicting nonlinearities in the case of the Al7075-T6 in the SC regime due to the lack of data. It should be pointed out that one can decrease the domain of prediction and choose the spread of radial basis function in such a way to obtain a more accurate prediction for each stress level (at $\sigma_{max} = 120\ and\ \sigma_{max} = 140\ MPa$).

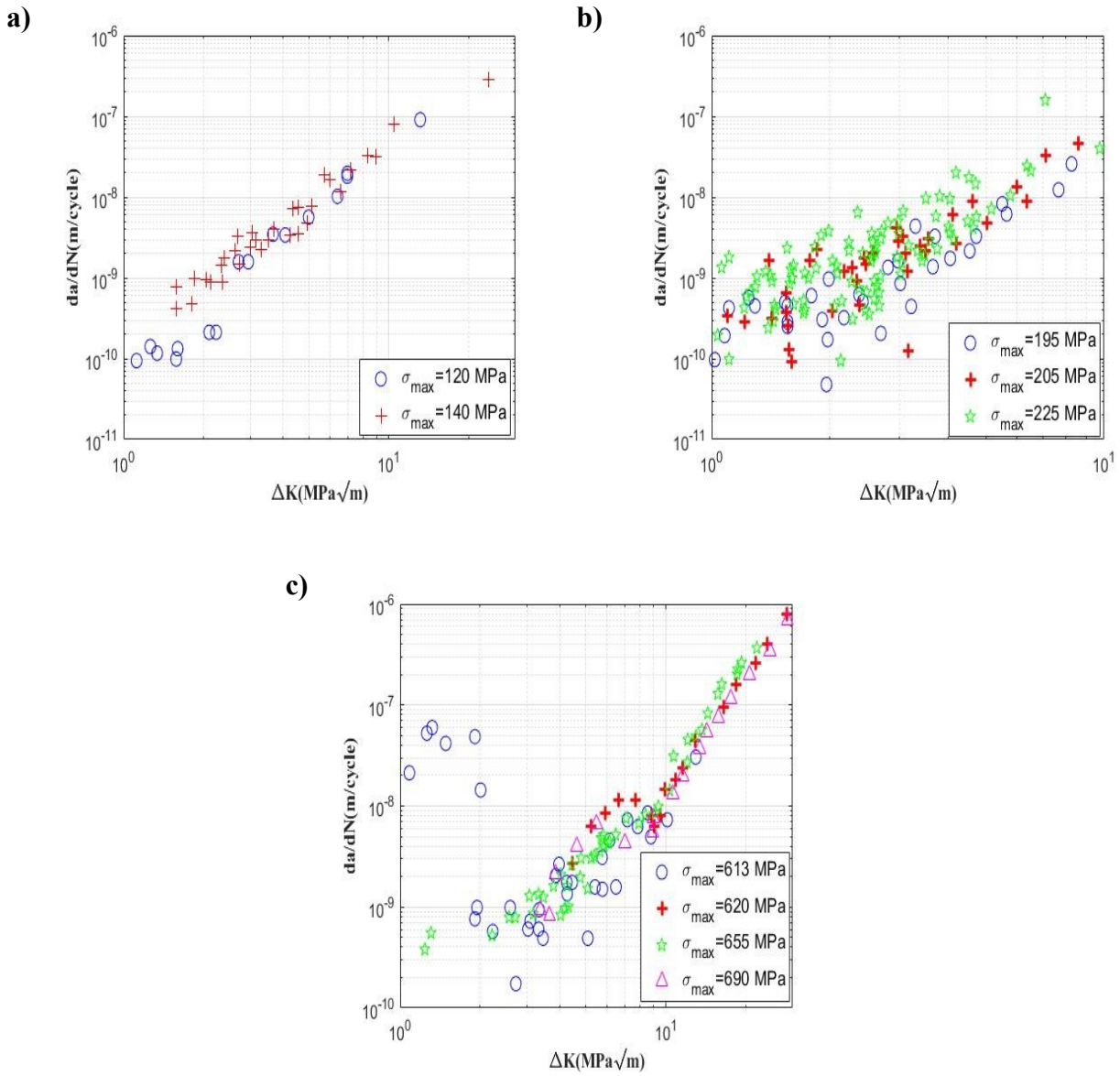

Figure 3.13 FCG data in SC regime of a) Al 7075-T6, b) Al 2024-T3, and c) Ti-6Al-4V.

However, this approach induces the lack of accuracy in predicting the FCG rate for stress levels in which there is no data in hand (at $120\ MPa < \sigma_{max} < 140\ MPa$). This is precisely similar to the argument discussed in the case of Al2024-T3 in the LC regime (See Figure 3.10). Figure 3.15 presents a comparison of the predicted results and the short crack growth data of the Al2024-T3. As shown in Figure 3.15, the RBF-ANN model is able to predict nonlinear behaviors at a constant stress level and to predict the FCG rate at different stress levels simultaneously. Comparing the results of the Al7075-T6 and Al2024-T3 in Figure 3.14 and Figure 3.15 shows how prominent the input data distribution could be in an RBF-ANN method.

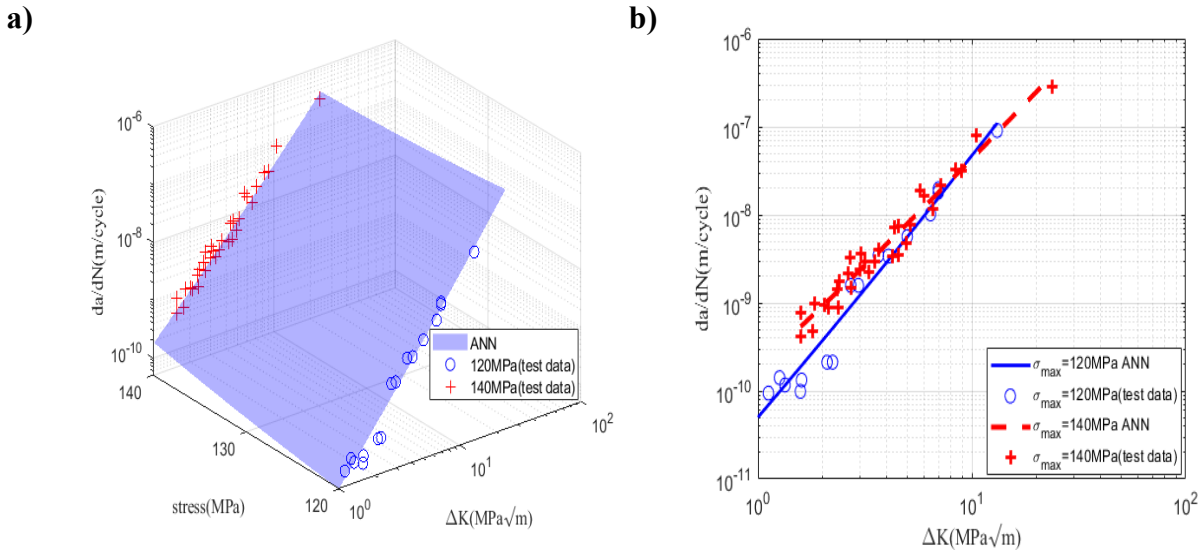

Figure 3.14 SCs experimental data and corresponded ANN results of Al 7075-T6 in a) 3D view and b) 2D view.

Since the presented model is multi-input single-output, an appropriate prediction is achievable if the number of data is sufficient with respect to both the stress level and ΔK. In other words, the number of data in both dimensions (stress intensity factor range and stress level) in Figure 3.14a) and Figure 3.15a) is important to achieve accurate predictions of the FCG rate. In the case of the Al7075-T6 as shown in Figure 3.13a) the FCG data are provided at only two different stress levels (120 and 140 MPa). On the other hand, in the case of the Al2024-T3 as shown in Figure 3.13b), the data are provided at three different stress levels (195, 205, and 225 MPa).

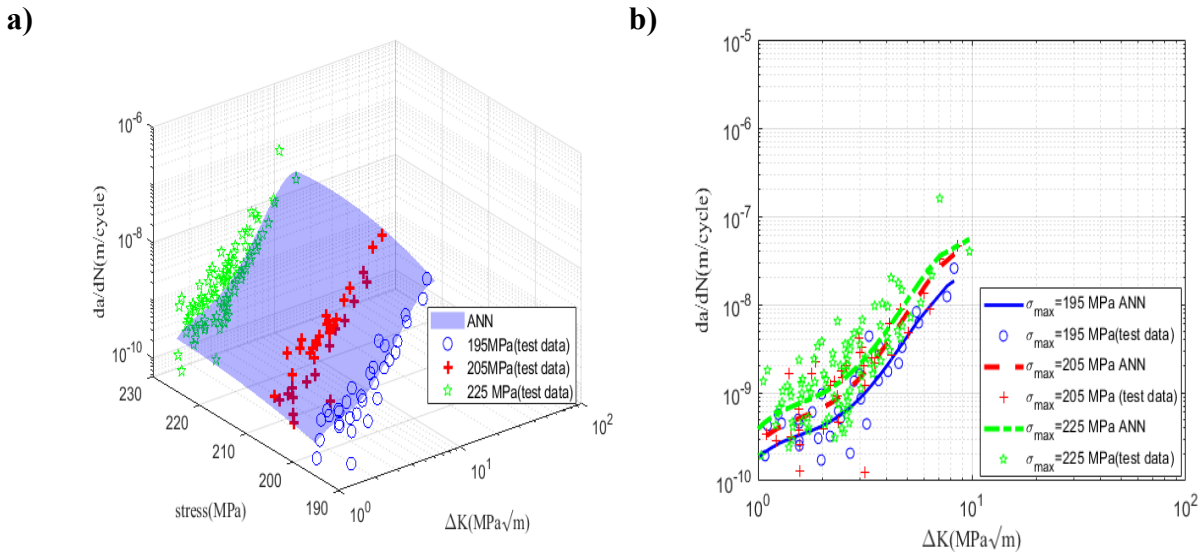

Figure 3.15 SCs experimental data and corresponded ANN results of Al 2024-T3 in a) 3D view and b) 2D view.

Therefore, that is the reason why RBF-ANN can predict the nonlinearity well enough in the case of the Al2024-T3 in Figure 3.15, but it is not satisfactorily accurate in the matter of the Al7075-T6 due to the lack of the FCG data as indicated in Figure 3.14. It is obvious that only a line can be fitted between two points. To fit the data by a curve at least three points are required. Although the model is unable to predict the nonlinearity in Figure 3.14, it is still acceptable when it comes to

FCG rate estimation approximately in the range of 120 to 140 MPa. Figure 3.16 compares experimental data and ANN results in the case of Ti-6Al-4V. The input data are distributed at four stress levels (613, 620, 655, and 690 MPa). As a result, it is possible to observe the complexity of short cracks response with respect to stress levels. It is important to declare that the final desire of estimating the FCG rate is obtaining the fatigue life under a wide range of the applied load. However, as shown in Figure 3.14 and Figure 3.15, in the case of Al7075-T6 and Al2024-T3, the prediction of the model is limited to a narrow range of various stress levels. That is because of the limited input data and deficiency of the extrapolating ability of most of the neural network methods. With this in mind, in the case of Ti-6Al-4V, a set of artificial data called boundary condition at $\sigma_{max} = 500$ and $\sigma_{max} = 800\ MPa$, is employed to increase the range of prediction. Those two values are chosen based on the full range of experimental fatigue lives data that can be found in the literature [56]. The artificial data is obtained by an iteration method. In each stress level ($\sigma_{max} = 500$ and $\sigma_{max} = 800\ MPa$), a polynomial function from the order of two was considered.

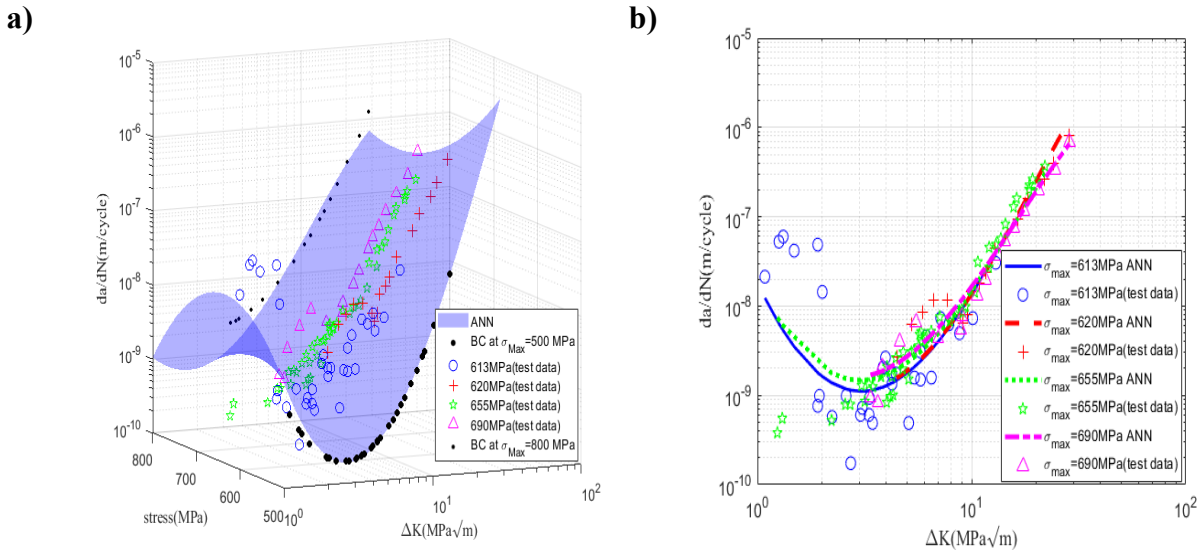

Figure 3.16 SCs experimental data and corresponded ANN results of Ti-6Al-4V in a) 3D view and b) 2D view.

The iteration procedure calculates the coefficients one by one, by assuming the others as constants. The iteration method is subjected to three constraints. First, the fatigue crack growth rate should be higher than $10^{-10}\ {}^{m}/_{cycle}$, since it is not possible to consider the crack propagation length less than the distance between atoms in each cycle. Second, as the stress level increases, the FCG rate rises as well. It means the boundary condition has to be located under all ANN results in Figure 3.16b) for $\sigma_{max} = 500\ MPa$ and be above of them for $\sigma_{max} = 800\ MPa$. Third, the FCG rate of the SC regime has to be collapsed on the LC curve at $\Delta K_{critical}$, in which the SCs are transitioned into the LCs. $\Delta K_{critical}$ is discussed in detail in the next section. The iteration method stops if all three constraints mentioned above are satisfied. Figure 3.16 presents a good agreement between ANN results and the experimental data. By considering Figure 3.14-Figure 3.16, it can be realized that the ANN model(s) can predict even complicated behavior of the SCs with acceptable accuracy. The only shortcoming of this approach is that the predicted region is limited to a narrow range of applied stress levels. This problem can be overcome by providing more experimental data to produce an appropriate distribution of input data. Unlike FCG behaviors in LC regime, applied

stress levels are considered as a controlling variable on FCG behaviors in SC regime. Therefore, predictions errors of PDF are provided for Al7075-T6, Al2024-T3, and Ti6Al4V under different stress levels in SC regime in Figure 3.17a) - Figure 3.17c), respectively. Different PDF curves shows the prediction error values between the predicted FCG rates $(da/dN)_p$ and the experimental FCG rates $(da/dN)_e$ for each stress level. As seen from these figures that less scatter error distributions can be observed for lower stress values. Nonetheless, the distribution of the PDFs and the range of errors in Figure 3.17a)- Figure 3.17c) indicate the acceptable prediction accuracy of the ANN model for all different stress levels in SC regime.

3.4.4. Predicted short and long crack growth behavior

Figure 3.18a)-c) show predicted FCG curves for the Al7075-T6, Al2024-T3, and Ti-6Al-4V alloys, respectively at a constant R-ratio. As shown in Figure 3.18, the FCG rate in terms of ΔK is described by different curves in the SC regime. This is due to the fact that the stress level is a controlling parameter in addition to the ΔK in the SC regime. However, the FCG rate is described by a single curve since the influence of the stress level is not considered as a controlling parameter in the LC regime.

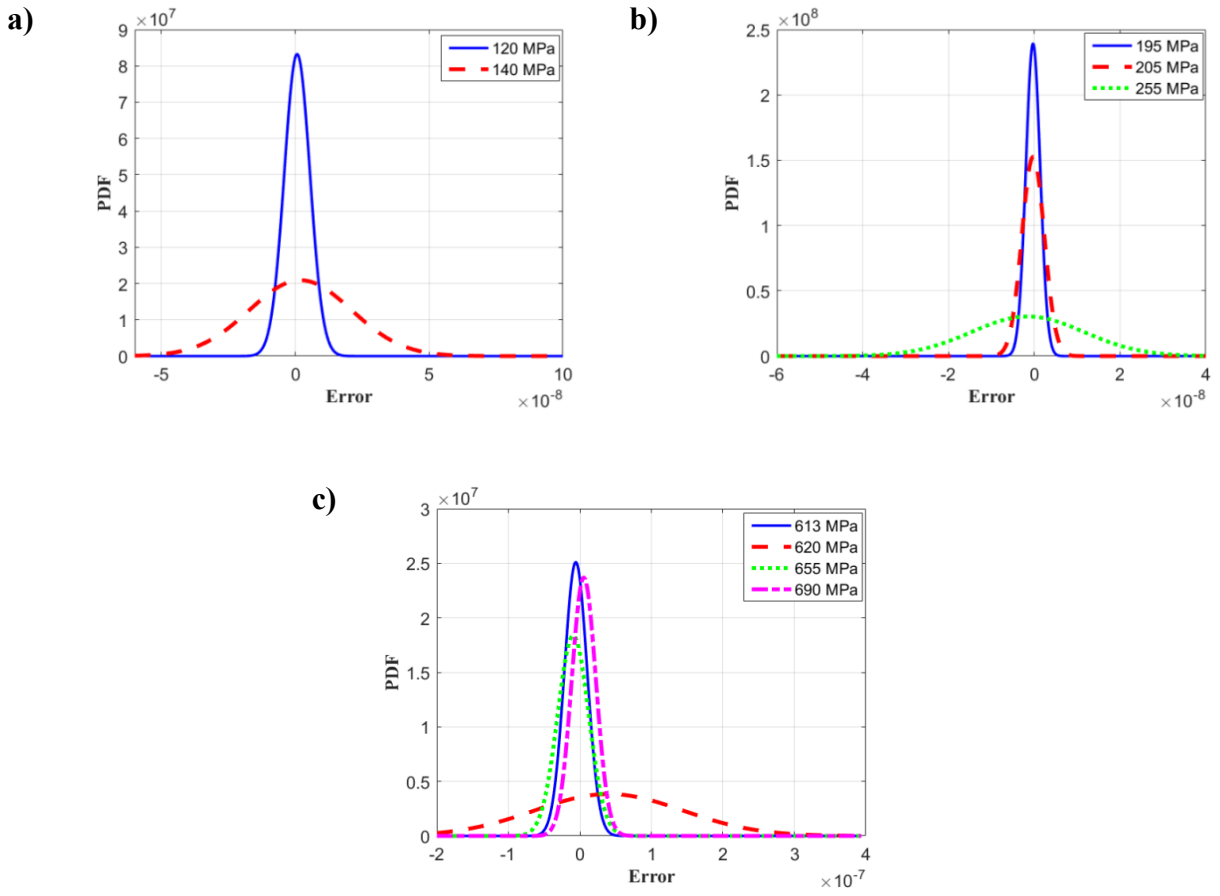

Figure 3.17 Probability Density Function (PDF) of prediction error in SC regime for a) Al7075-T6, b) Al2024-T3, and c) Ti6Al4V.

A pivotal point to calculate fatigue life is to determine the transition point in which a short crack changes to a long crack. In the presented model, a critical stress intensity factor range is defined to distinguish the short and long crack regimes. The critical stress intensity factor range should be defined for each material under a constant R-ratio. That is to say, the critical stress intensity factor range is a function of the material and the R-ratio. By taking this assumption into consideration, the behavior of cracks can be presented by Figure 3.19 for each of these materials. This figure shows that under a constant R-ratio, the FCG rate depends on the stress level and it is described by different curves up to the SC and LC transition point in which the stress intensity factor range reaches $\Delta K_{critical}$. However, under SIF ranges higher than $\Delta K_{critical}$ the FCG rate is characterized by a single curve in the LC regime. $\Delta K_{critical}$ is determined to be to 4 $MPa\sqrt{m}$ for the Al7075-T6 and Al2024-T3 and 11 $MPa\sqrt{m}$ for the Ti-6Al-4V.

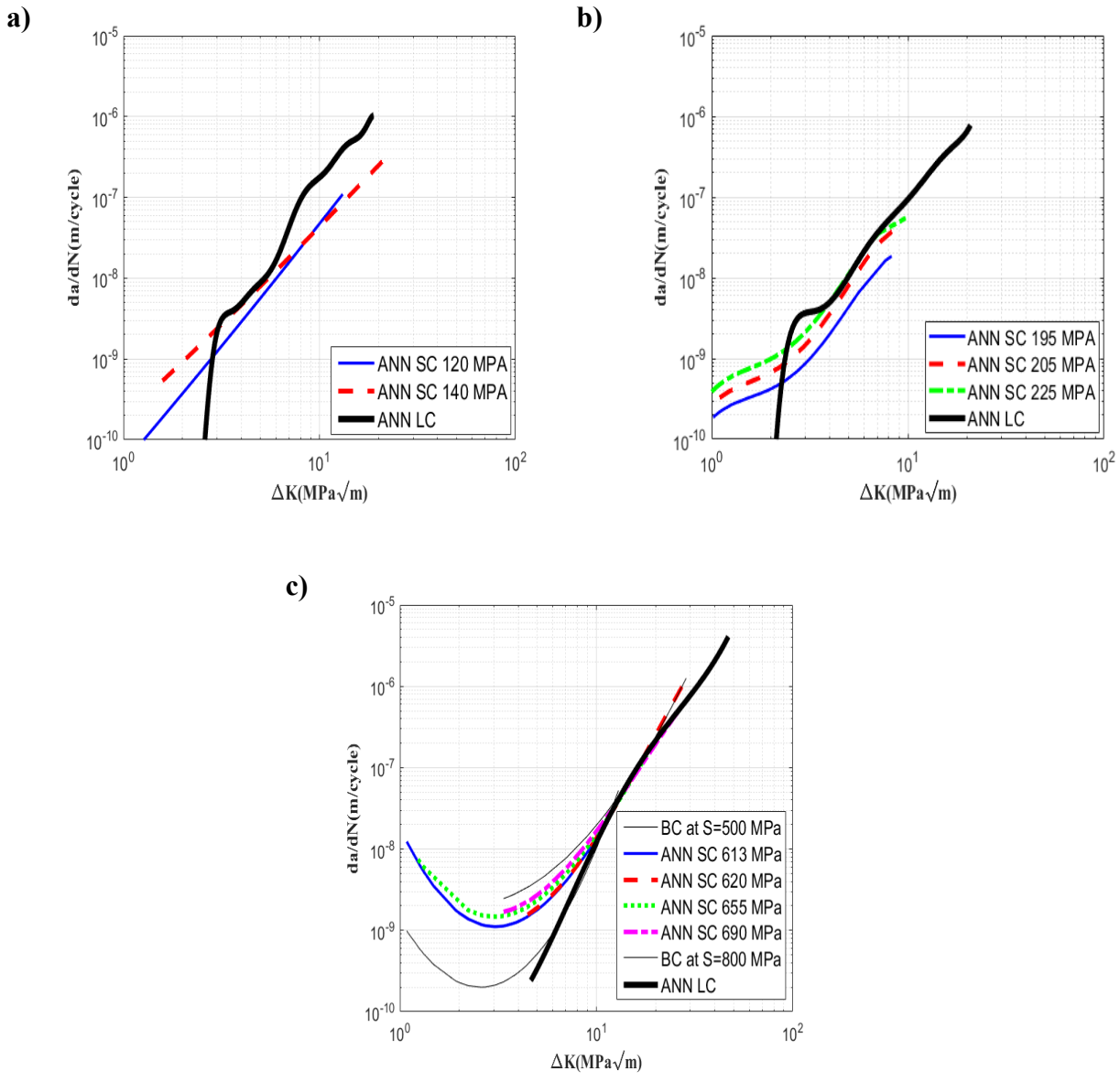

Figure 3.18 ANN results of SCs and LCs in the same framework under constant R-ratio of a) Al 7075-T6, b) Al 2024-T3, and d) Ti-6Al-4V.

To obtain those values, experimental data and ANN results have been explored and the transition point where the SC data collapse on the LC data is chosen as $\Delta K_{critical}$. That is to say, $\Delta K_{critical}$ distinguishes the SC ($\Delta K < \Delta K_{th}$) and LC ($\Delta K \geq \Delta K_{th}$) regimes under a constant R-ratio as depicted in Figure 3.19. As a result, it is possible to take the numerical integration from FCG rates in both regimes to obtain the crack propagation life and stress-life curves. As mentioned earlier, the FCG prediction is limited to a narrow range of applied stress levels for the Al7075-T6 and Al2024-T3 in Figure 3.19a) and Figure 3.19b), respectively.

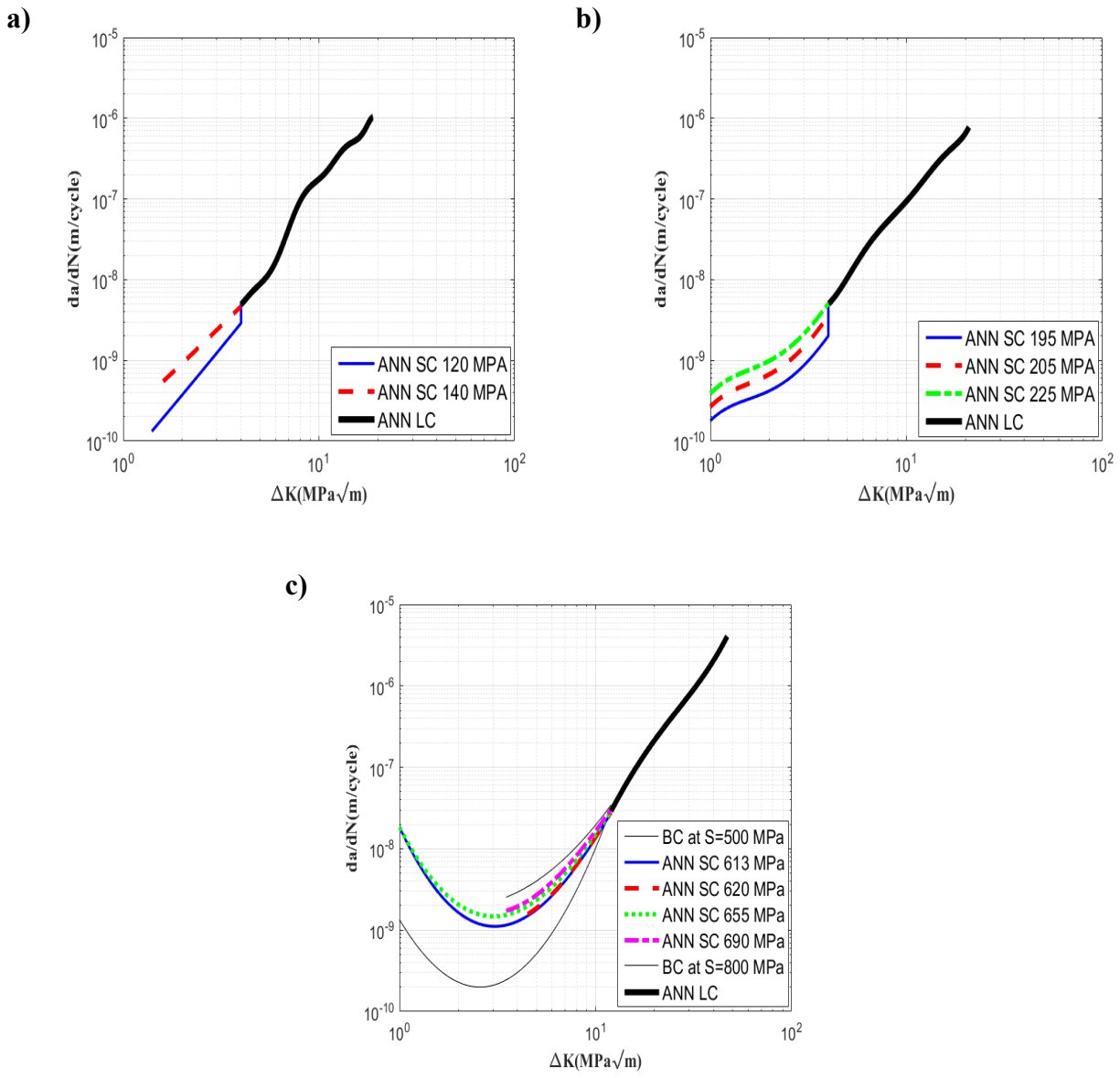

Figure 3.19 The transition of cracks between SC and LC regime. a) Al 7075-T6, b) Al 2024-T3, and c) Ti-6AL-4V.

However, by introducing boundary conditions for the Ti-6Al-4V discussed in section 3.3.2, it is possible to expand this prediction range. It should be pointed out that boundary conditions or artificial data are employed only in the case of Ti-6Al-4V. The reason is that the number of data points for this material is sufficiently large in the SC regime unlike Al7075-T6 and Al2024-T3

alloys. As a result, the Ti-6Al-4V is used to assess the application of artificial data to expand the range of prediction. As discussed before, the higher number and less scattered FCG data would yield improved prediction of the ANN model(s) by increasing the model extrapolation and nonlinear capabilities. The numerical integrations of predicted FCG by RBF-ANN in both the SC and LC regime can then be used to calculate fatigue lives as depicted in the flowchart shown in Figure 3.6.

3.5. Conclusion

In this chapter, a machine learning-based method is developed to predict the FCG rate in both the short and long crack regimes. The model is based on the radial basis function artificial neural network. To validate the model, the results of the presented model are compared with experimental FCG data sets of 2024-T3 and 7075-T6 aluminum alloys, and Ti-6Al-4V titanium alloy. The results show that RBF-ANN based on a neural network algorithm has a potent capability of predicting nonlinearity of crack growth behavior in both of the SC and LC regimes. In addition, RBF-ANN can predict fatigue crack behavior under conditions in which there are limited data in hand. However, the efficiency of the RBF-ANN method significantly depends on the number of input data point and range. To establish a proper set of FCG data, three data characteristics should be considered; 1) density of the input data (number of data in the predicted region), 2) distribution of data, 3) accuracy of data.

3.6. CRediT authorship contribution statement

S.N.S. Mortazavi: Methodology, Software, Writing – original draft, Software, Validation. A. Ince: Conceptualization, Supervision, Writing – review & editing.

3.7. Declaration of Competing Interest

The authors declare that they have no known competing financial interests or personal relationships that could have appeared to influence the work reported in this paper.

3.8. Acknowledgments

The authors would like to acknowledge the financial support of Natural Science and Engineering Research Council of Canada (NSERC) (DGECR-2018-00232).

3.9. Data availability

The raw/processed data required to reproduce these findings cannot be shared at this time due to technical or time limitations, but it will be provided upon request.

Chapter 4

Artificial neural networks-based *J*-integral prediction for cracked bodies under elasto-plastic deformation state –monotonic loading

4.1. Abstract

Artificial neural networks (ANNs) integrated with a finite element (FE)-based equivalent domain integral method are developed to compute J-integral at the vicinity of crack tips through a time-efficient approach. Robust ANN models are trained to establish nonlinear relationships between FE predicted elastic and elasto-plastic stress, strain, and displacement fields of stainless steel (SS304). Subsequently, elastic-plastic J-integral can be determined by using only elastic FE analysis solution rather than computationally expensive elasto-plastic FE analysis solution. The results show that well-trained ANN models can efficiently and accurately determine J-integral around the crack tips on the basis of numerical elastic FE analysis solution.

4.2. Introduction

Fatigue failure has been reported as the most common failure in the industry [2]. Consequently, accurate fatigue life assessment methods of components have been considered as attractive topic(s) among researchers for decades. Damage tolerance design philosophy has been developed to assess the remaining useful life of structural components containing initial cracks induced by manufacturing and environmental factors. Damage tolerance methods use fracture mechanics principles to assess effects of initial defects/cracks on the remaining fatigue life of structural components in service conditions [1]. Fracture mechanics approach assumes that the initial crack(s) are always present in the components. It has been widely accepted that such assumption is compatible with real life engineering applications. This is attributed to the fact that emergence of microscopic defects and cracks during fabrication processes and in-service conditions is almost inevitable in most of the engineering applications. Linear elastic fracture mechanics (LEFM) methods have been developed for carrying out fatigue crack growth (FCG) analysis to predict the remaining residual life of the structures containing initial cracks. As for LEFM-based FCG analysis methods, stress intensity factor (SIF), is deemed as a controlling crack growth driving force parameter to determine the crack growth and characterize stress, strains and displacement fields in the crack tip region [16, 17]. Paris and Erdogan [18] suggested that the SIF range can be used to determine the FCG rate known as the Paris equation in Eq. (4.1).

$$\frac{da}{dN} = C(\Delta K)^m \tag{4.1}$$

where a is the crack length, N is the number of cycles, ΔK is the SIF range, and C and m are experimentally determined material constants.

One of the crucial limitations of the Paris equation is that the mean stress effect or R-ratio is not accounted for. Therefore, the Paris equation has received many modifications to account for R-ratio on crack growth behavior. Some of such modifications have been developed based on the "crack closure" concept [284, 293] introduced by Elber [20] and further improved by Newman [21]. One of the most well-known crack closure-based models is the NASGRO model known as Forman/Mettu equation [37] in Eq. (4.2) where R is the stress ratio, ΔK_{th} is the SIF threshold, K_{crit} is the critical value of SIF, C, n, p, and q are calibration coefficients, and f is the Newman's function describing the crack closure.

$$\frac{da}{dN} = C\left(\frac{1-f}{1-R}\Delta K\right)^{n} \frac{\left(1-\frac{\Delta K_{th}}{\Delta K}\right)^{p}}{\left(1-\frac{K_{max}}{K_{crit}}\right)^{q}} \tag{4.2}$$

The detail description of these parameters can be found the literature [38]. The crack closure-based models considered ΔK_{eff} as the driving force parameter effected by crack-wake plasticity behind the crack tip to characterize FCG rate. The other group of modifications are based on "unified approach" employing two crack driving forces parameters, K_{max} and ΔK [45, 294, 295]. One of the most important and successful models on the basis of two-parameter driving force models is UniGrow model [46, 47]. Although the UniGrow model is significantly successful in long crack (LC) regime, it has shortcomings in short crack (SC) regime [55-57]. Bang and Ince [55-57] modified the UniGrow model in the application of the SC regime. In spite of successful developments of all LEFM-based FCG models. The ΔK-based models are still considered to have certain limitations to completely account for crack growth behavior in the SC regime. Such limitation can be attributed to the fact that SIF is a linear elastic fracture mechanics (LEFM) parameter, and it inherently cannot account for the plastic deformation zone (PDZ) near the crack tip. Even though the application of SIF-based model is significantly time efficient, such models can be only employed in the presence of small-scale plasticity (see Figure 4.1a)). However, application of LEFM cannot be extended in the presence of large-scale plasticity. In other words, PDZ at the crack tip cannot be neglected when the plasticity size radius (r_y) is comparable with other significant dimensions e.g. notch root radius (ρ) and crack length (a) (see Figure 4.1b)) [82]. One may realize that large-scale plasticity ahead of the crack tip emerges either under relatively high load levels, e.g. low cycle fatigue (LCF), or crack tip plasticity in the SC regime. Under such conditions, mainly two different approaches have been suggested so far.

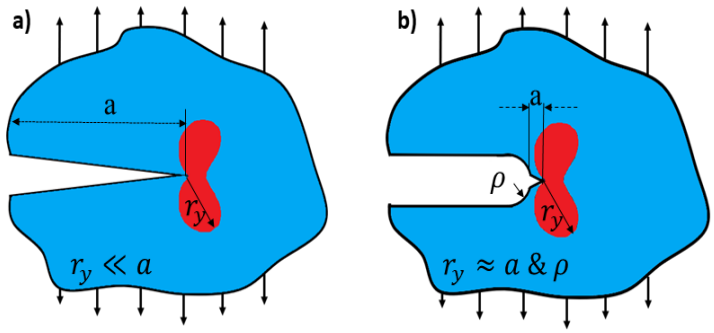

Figure 4.1 Plastic deformation zone around the crack tip. a) small-scale plasticity, and b) large-scale plasticity

The first one is based on the integration of the multiaxial Neuber rule and material constitutive model very recently proposed by Ince and Glinka [68] to transform hypothetical elastic stress/strain fields to the actual elasto-plastic fields in the vicinity of crack tips. The application of the multiaxial Neuber rule has been reported successful for notches under the multiaxial cyclic loading [59, 66], however it has not been proven for its distinct success for cracked bodies made of different metallic alloys yet. Furthermore, the multiaxial Neuber rule has not been able to account for sharp cracks, unless crack tips are assumed to have a small finite radius [68]. The second approach is replacing the SIF range as an LEFM parameter with an elasto-plastic fracture mechanics (EPFM) parameter. One of the promising EPFM parameters is J-integral introduced by

Rice [79]. It was shown that J-integral as a line integral has the same value for all paths imbedding the notch tip in a 2D strain field of elastic and elasto-plastic deformation states of materials [79]. Such definition has been extended in the presence of cracks as well. Subsequently, J-integral has been known as a parameter to characterize the elasto-plastic stress/strain fields at the notch and crack tips. With this in mind, the application of J-integral is mostly limited to the condition as follows: a) the deformation theory of plasticity (and not the incremental theory of plasticity) is employed to determine the elasto-plastic behavior of materials, b) there is no force or stress at the notch faces or crack flanks, c) material represents Mashing behavior [79, 81]. The later condition points out that strain should be a unique and one-to-one function of stress. As a result, the unloading is forbidden in order to have path-independency of J-integral [82]. The question comes to mind is that "is it possible to extend the application of J-integral under cyclic loading?". Dowling and Begley [82] answered this question for the first time and proposed cyclic J-integral (ΔJ). It was suggested that only loading half-cycles should be considered to determine ΔJ to characterize the FCG rate. In addition, Wuthrich [91] showed that ΔJ is also path-independent under the mentioned a-c conditions. J and ΔJ can be interpreted as the energy release rate with respect to the variation of crack length for elastic materials. Such interpretation is lost in the case of elasto-plastic material. Subsequently, Tanaka [80] interpreted path-independent ΔJ as a measure of energy lost or dissipated to heat due to dislocations movement in the PDZ during one cycle. It should be pointed out that J-integral (J) and cyclic J-integral (ΔJ) are advantageous to characterize FCG rate even under the condition in which path-independency is lost. However, in such case the application of J and ΔJ cannot be considered as computational and time efficient. This can be attributed to the fact that a complex elasto-plastic analysis is required to determine stress, strain, and displacement field and subsequently J and ΔJ around the crack tip. Consequently, the most crucial challenge is efficient and accurate determination of ΔJ. Ngoula et al. [89] developed an in-house numerical code to determine ΔJ for various welded joints. It was reported that a strict numerical modeling process is required to specify a path for accurate calculation of ΔJ. In addition, Ngoula et al. reported that the calculation of stress and strain components were crucially difficult through the in-house code during crack deflection. Metzger et al. [90] suggested using built-in functionality of Abaqus to calculate ΔJ. Since built-in functionality of Abaqus is only able to determine J-integral based on virtual crack extension (VCE) under monotonic loading, it was suggested to replace the parameters (i.e. σ, ε, and u) with their counterparts (i.e. $\Delta\sigma$, $\Delta\varepsilon$, and Δu) in order to determine ΔJ. However, such approach requires a relatively complicated post-processing technique to carry out a restart finite element (FE) analysis to shift the stress/strain coordinate system with respect to the crack tip and a user-material subroutine needs to be developed. Hence, a significant complicated procedure is required to carry out the later approach. Chen [296] proposed a linear matching method (LMM) to determine the ΔJ. The proposed method utilizes some geometric coefficient limiting the application of LMM significantly. Wang et al. [81] developed an equivalent domain integral (EDI) method to compute J and ΔJ. The proposed method was verified under monotonic loading by comparing the J-integral values computed by the EDI method with ones determined by means of the built-in functionality of Abaqus based on the VCE method. The verified method was also successfully applied to the cyclic loading. There are several other approaches in the literature [91-93] to calculate J and ΔJ based on using analytical solutions, and experimental procedures using load-deflection data. However, those approaches are significantly limited to specific geometries. According to early works in the literature, finite element methods (FEMs) are considered to provide the best generality and expandability in comparison to other suggested methods so far [81].

Artificial neural networks, (ANN)s as machine learning algorithms has been developed to establish any relationships among nonlinear multivariable. Subsequently, ANNs have received noticeable attention in various areas such as material science [214, 277-279] and fracture mechanics problems e.g. creep and fatigue failure [142, 143, 216]. Hajializadeh and Ince [259] employed an ANN model to predict the residual stress field for additively manufactured components during the fabrication process. Zhan and Li [148] used the integration of continuum damage mechanics theory with two different machine learning algorithms, ANN and random forest, in order to investigate the fatigue damage behavior of additively manufactured aerospace alloys. Artymiak et al. [121] successfully trained an ANN by comprehensive datasets of a wide range of materials to predict the S-N curve and, subsequently, the fatigue limit of materials. Gan et al. [297] investigated the application of the random forest and the kernel extreme learning machine as two well-known machine learning algorithms to estimate the fatigue life of different metallic alloys in the presence of mean stress. Wang et al. [199] developed radial basis function artificial neural network (RBF-ANN), extreme learning machine (ELM), and genetic algorithms optimized backpropagation network (GABP) as different types of ANNs to predict the FCG rate of metallic materials in the LC regime. Zhang et al. [214] trained an RBF-ANN model to predict FCG rate in the LC regime in terms of stress ratio and SIF range. Mortazavi and Ince [298, 299] developed two separate ANNs using SIF range and stress ratio as input variables in the LC regime and using SIF range, stress ratio, and stress level as input variables in the SC regime. Himmiche et al. [300] compared the potential of RBF-ANN and ELM to predict the FCG rate of different lightweight alloys in the SC regime. Wang et al. [301] developed a procedure to predict FCG failure in the presence of curved crack under variable amplitude loading based on ANN and FCG path/life predictions models. The noticeable potential of different types of ANN algorithms for prediction of the fatigue failure attract significant attention in recent years [113]. Burghardt et al. [260] developed ANN model to predict the actual elasto-plastic local equivalent stress based on the hypothetical elastic local equivalent stress in the vicinity of notch tip for different geometries and materials. It should be noted that sufficiently large and well-structured datasets have been deemed to be necessary in almost all of the ANN-based modeling approaches. Therefore, the application of ANN models is limited to the circumstances in which there are enough datasets in hand [298].

In addition to the ANN, convolutional neural network (CNN) algorithms have been recognized as noticeably powerful machine learning algorithms. CNN algorithms are used in the case of image recognition and analyses [302, 303]. It means the input or output, or both are fed to networks in the form of image dataset. The robust CNN algorithms are capable to analyze the images and convert them to numerical dataset(s). Such algorithms have received great interest in the solid mechanics field such as fatigue, creep, and prediction of stress/strain fields. Zhang et al. [119] employed CNN algorithms to present a method to predict the life of components under creep, fatigue, and the creep-fatigue conditions. Kamiyama et al. [304] used deep CNN to predict the microscopic image of fatigue cracks after being under low-cycle fatigue for a sputtered Cu thin film. Nie et al. [305] developed a CNN model to predict the von Mises stress filed of cantilevered structures under static load(s) in elastic state. The inputs of that model are the structure geometry, the applied loads, displacement boundary conditions. Since the present study is based on the numerical input and output datasets and ANN algorithms have shown a noticeable potential in the case of similar regression-type of problems [259, 260], ANN algorithms are chosen over CNN ones in the present study. Employing CNN and using the image of the cracked-specimen to predict the elasto-plastic stress/strain fields can be considered for the future studies.

The present chapter aims to propose an innovative modeling method to determine J-integral by integrating numerical FE methods and artificial neural network (ANN) algorithms. Robust ANN models are developed to establish the interconnection between elastic and elasto-plastic behavior of grade 304 (SS304) stainless steel around the crack tip in a plate body. As a result, a linear elastic FE analysis would be enough to predict the elasto-plastic response of the material in the presence of the crack. In order to do so, two discrete FE models are developed under elastic and elasto-plastic states. The obtained stress, strain, and displacement components around the crack tip under elastic and elasto-plastic states are fed to the ANN models as input and output data, respectively. An in-house EDI-based model is developed to calculate J-integral based on the predicted results of developed ANNs and those results obtained from the elasto-plastic FEM. The results show that the ANN model accurately predicts elasto-plastic stress, strain, and displacement fields around the crack tip through the proposed method under monotonic loading. Subsequently, the determined J-integral values based on predicted results of ANNs show a good agreement with the ones obtained by a complicated elasto-plastic FEM.

4.3. Modeling approach

In the present chapter, ANN models are developed to predict elasto-plastic stress, strain, and displacement fields around the crack tip based on elastic FE analysis results. Consequently, J-integral as an EPFM parameter can be determined from ANN predicted elasto-plastic stress, strain and displacement results on the basis of a linear and time-efficient FE analysis. The proposed modeling framework is schematically illustrated in Figure 4.2. In the first step, two independent finite element models have been developed to determine local stress, strain, and displacement fields around the crack tip in a 2D cracked plate under both elastic and elasto-plastic states to obtain numerical input and output data for ANN models.

FE datasets for various crack lengths have been obtained to generate datasets for various crack sizes. Subsequently, all components of stress, strain, and displacement fields were extracted and divided into three groups of training, verification, and test data under each state. In the next step, three different ANN models were developed in order to establish the relationships between elastic and elasto-plastic stress (σ_{ij}^{el} and σ_{ij}^{el-pl}), strain (ε_{ij}^{el} and ε_{ij}^{el-pl}), and displacement (u_i^{el} and u_i^{el-pl}) fields. The extracted field datasets under the elastic state were fed to the ANN models as input data. The corresponding datasets obtained under the elasto-plastic state were considered as output data for the ANN models as schematically illustrated in Figure 4.2. Then, the trained ANN models were verified and tested by using different verification and test datasets. The elastic components of the stress, strain and displacement fields were fed to the trained models to predict elasto-plastic fields. The predicted ANN results were compared against elasto-plastic FE analysis data. Subsequently, an in-house model based on the EDI method was developed to calculate J-integral by using the stress, strain, and displacement results predicted by ANN models and elasto-plastic FEMs. Finally, the J-integral results determined by ANN models were compared with those calculated by elasto-plastic FE models. The developed FE models, EDI method, and ANN models are discussed in detail in the following sections.

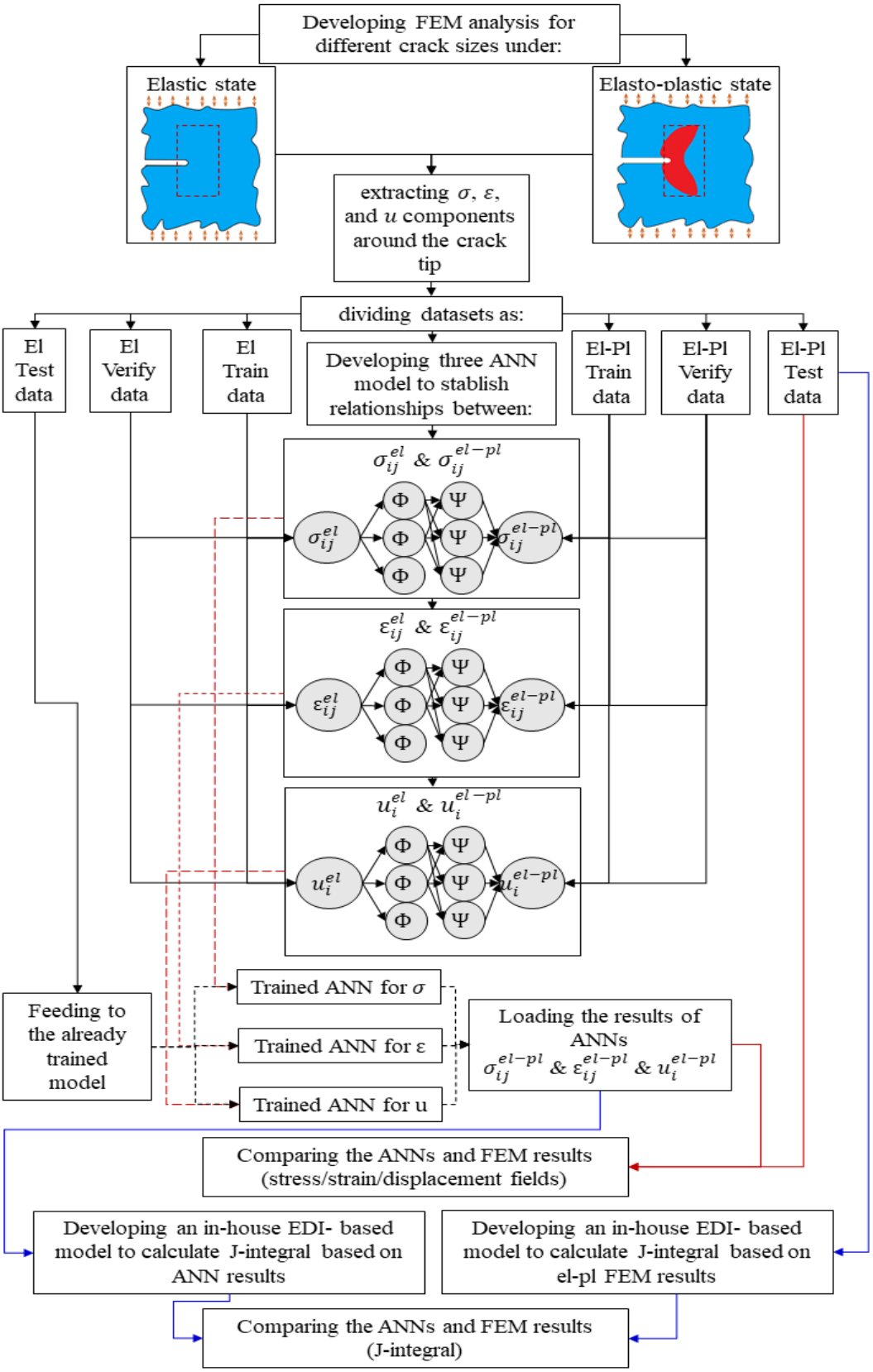

Figure 4.2 The flowchart of modeling framework

4.3.1. Finite element modeling

Abaqus commercial FE software package was employed to perform elastic and elasto-plastic FE analyses to determine stress, strain, and displacement fields around the crack tip. FE models were developed as a parameterized model through the Abaqus script file in Python to carry out efficient post-processing of numerical data extraction. The script file includes designing compact tension (CT) notched specimens, defining material properties, specification of load and boundary conditions, and mesh generation. The analysis results of FE model(s) in terms of stress, strain, and displacement data are accessible via the output databases (ODB) file generated by Abaqus. As a result, the script file also includes post-processing coding to extract stress, strain, and displacement components of particular elements and nodes around the crack tip in a desired configuration which can be fed to the ANN models afterward. Data extraction configuration is discussed in section 4.2.3. Geometrical dimensional parameters of the CT specimen used in the present study are shown in Figure 4.3. The material was chosen as the 304 stainless steel (304SS) for FE models and material properties of 304SS are given in Table 4.1 [81].

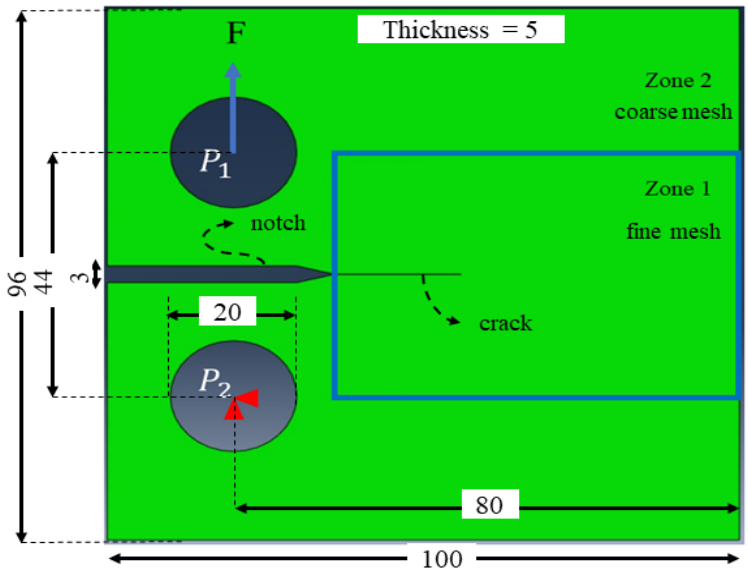

Figure 4.3 The CT specimen for FE models.

Table 4.1 Material properties of 304SS

Modulus of elasticity	Poisson's ratio	Yield stress	Hardening modulus	Elastic-plastic model
195100 MPa	0.267	206 MPa	570 MPa	Bilinear isotropic hardening

As shown in Figure 4.3, two reference points (P_1 and P_2) were set up in the center of each pin hole. The kinematic type coupling constraint of full degree freedom was assigned between the reference point and the inner wall of each pin hole. A vertical (mode I) point force (F) was applied to the upper reference point (P_1) and the fixed displacement constraints were applied to the lower reference point (P_2) as shown in Figure 4.3. Two partitions, zone 1 and zone 2, were used to generate two different mesh sizes to allow finer mesh in the close vicinity of the crack tip to obtain

accurate stress, strain and displacement results. The element type was fully integrated linear plane strain element (CPE4) for both zones. Structured mesh with the size of 0.1 mm and 2.0 mm was used in zone 1 and zone 2, illustrated in Figure 4.3, respectively. As shown in Figure 4.4, an area consisting of 480 (40×12) elements (blue elements) in the vicinity of the crack tip is chosen to extract the dataset. The mesh size in zone 1 and the number of elements in the particular area shown in Figure 4.4 were selected so that the chosen area can embrace the PDZ around the crack tip and a portion of the elastic area around the PDZ.

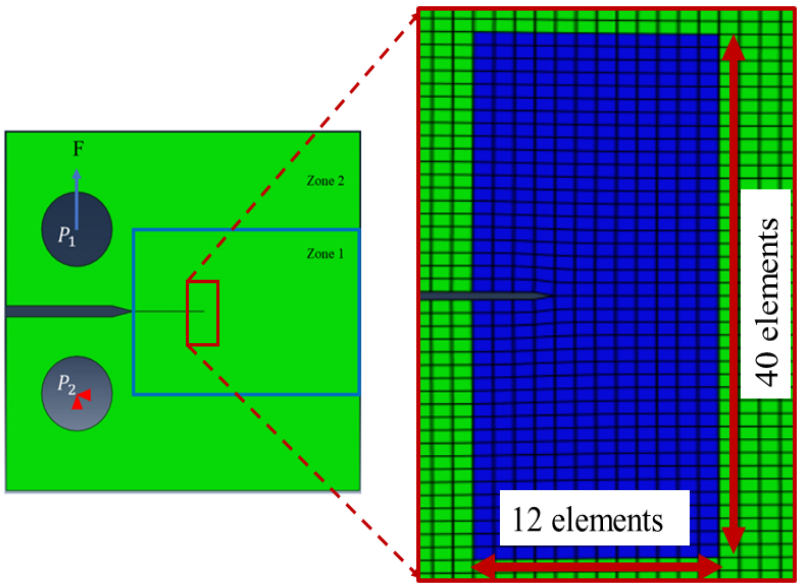

Figure 4.4 The chosen area around the crack tip to extract datasets.

In other words, the chosen area is larger than the PDZ size generated under the maximum applied load (20 KN) and maximum crack length (10 mm) used in the present study. The results of J-integral values calculated by the present elasto-plastic FE analysis have been compared with those results reported by Wang et al. [81]. As shown in the result and discussion section, the element size of 0.1 mm is fine enough to provide accurate FE results. The selected element size of 0.1 mm is relatively larger than those element sizes, which are commonly used around the crack tip in the literature, to reduce the run time of the post-processing model to extract data. It has been accepted that the J-integral calculated based on EDI method is not sensitive to the mesh size in the vicinity of the crack tip [101]. It should be reminded here that one of the most important objectives of this study is to propose a time-efficient modeling method to calculate J-integral under the elasto-plastic deformation state. The determined J-integral by the means of 0.1 mm element size is compared with the ones calculated with finer mesh such as 0.004 mm as discussed in section 4.3.1.

4.3.2. J-integral calculation based on equivalent domain integral method

J-integral is a surface integral or a line integral in a 3D or 2D state, respectively. According to the Green's theorem, a line integral can be rewritten as a surface integral in a 2D state in Eq. (4.3).

$$J = \int \left(\frac{\partial W}{\partial x} - \frac{\partial}{\partial x_j} \left(\sigma_{ij} \frac{\partial u_i}{\partial x} \right) \right) dA \tag{4.3}$$

where dA is an infinitesimal area element ($dA=dx.dy=dx_1.dx_2$), u is the displacement vector, W is strain-energy density, and x (x_1) and y (x_2) are cartesian axes. x is parallel to the crack, and y is perpendicular to the crack face.

The value of J-integral corresponds to the hatch area surrounded by Γ as shown in Figure 4.5a). That approach is known as the conventional method. On the other hand, the J-integral value corresponds to the hatched area surrounded by the inner boundary (Γ_1) and outer boundary (Γ_0) as shown in Figure 4.5b) is based on the EDI method introduced by several researchers [100-102]. The J-integral expression in Eq. (4.3) can be rewritten on the basis of the EDI method in Eq. (4.4) [100]:

$$J = \int_A \left(\sigma_{ij} \frac{\partial u_j}{\partial x} - W \delta_{1i} \right) \frac{\partial q}{\partial x_i} dA \tag{4.4}$$

where δ_{1i} is Kronecker delta and q is a weight function of $x_1(x)$ and $x_2(y)$ as the coordinate axes. The integral region shown in Figure 4.5b) can be replaced by a finite number of elements as shown in Figure 4.5c) in a FE-based model. One of the most prominent advantages of the EDI method over the conventional method is that the area or the elements adjacent to the crack tip can be excluded in the calculation of J-integral. As for dealing with singularity problem, extremely fine mesh around the crack tip, and employing the extended finite element method (XFEM) or Barsoum elements [101] at the crack tip are not necessary. Another important feature of the EDI method is that it was showed as a mesh size-independent approach which facile its application in FE methods [101]. The value of q is 1 for the inner boundary, and it decreases linearly to its minimum value (0) on the outer boundary for a two-dimensional problem [81, 100]. The expansion of Eq. (4.4) in a 2D cartesian system is derived as follows:

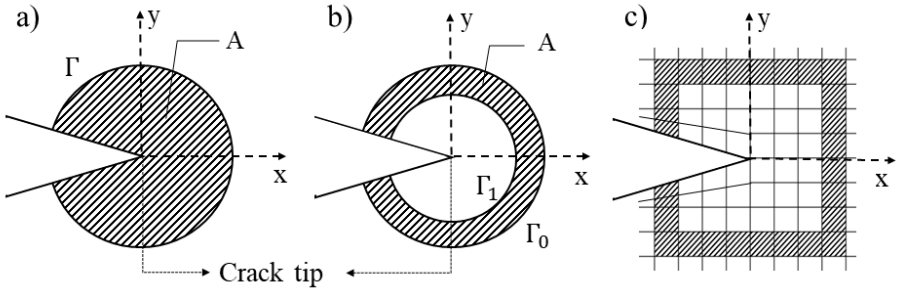

Figure 4.5 Different methods of J-integral calculation. a) Conventional method; b) EDI method; c) EDI method in a FEM-based model

$$J = \int_A \left[\left(\sigma_{11} \frac{\partial u_1}{\partial x} + \sigma_{12} \frac{\partial u_2}{\partial x} - W \right) \frac{\partial q}{\partial x} + \left(\sigma_{12} \frac{\partial u_1}{\partial x} + \sigma_{22} \frac{\partial u_2}{\partial x} \right) \frac{\partial q}{\partial y} \right] dA \tag{4.5}$$

The Abaqus FE package is employed to analyze the cracked problem in both elastic and elasto-plastic states. Therefore, stress, strain, and displacement fields around the crack tip can be obtained from the ODB file provided by Abaqus. However, the in-house model should calculate other parameters, such as $\frac{\partial u_2}{\partial x_1}$ introduced in Eq. (4.5) as a part of the post-processing file mentioned

before. In order to carry out numerical calculations, the in-house model has been developed as an object-oriented programming method in Python. As a result, it can be compiled by Abaqus and calculate J-integral based on stress, strain, and displacement fields around the crack tip obtained by elasto-plastic FE analysis. In addition, the same model can be used in the script, including the ANNs training, compiled by Python integrated development and learning environment (IDLE) to calculate J-integral based on ANNs predictions. It should be emphasized that stress and strain components are obtained on Gaussian points. However, displacement components are received on the nodes of elements.

4.3.3. Artificial Neural Network models

ANN algorithms have been developed to investigate probable patterns from a given dataset and determine the relationship between input and output dataset. In this dissertation, the term "dataset" is defined as a sequence of numerical input(s) and their corresponded output(s). As a result, ANN algorithms are theoretically able to establish any complex nonlinear relationships among input and output variables. It is significantly prominent to provide well-structured datasets in the application of ANN algorithms. Such datasets are able to represent all aspects and characteristics of a given problem. In other words, well-structured datasets represent complete controlling parameters of a problem in order to fully establish any relationship among nonlinear multivariable. The structure of a hypothetical ANN, including one input layer, two hidden layers, and one output layer, is schematically shown in Figure 4.6. Let's assume the input data of a particular dataset is given as $(X_1, X_2, \dots, X_n)$. The first step in training of an ANN model is to prepare raw input data into a proper data structure to feed to the network. Data preparation may be different for different types of problems. Data normalization is a common process for a vast majority of problems to achieve proper training if dataset with an order of the magnitude in the case of multivariable problems. In the present study, data normalization is carried out by using Eq. (4.6).

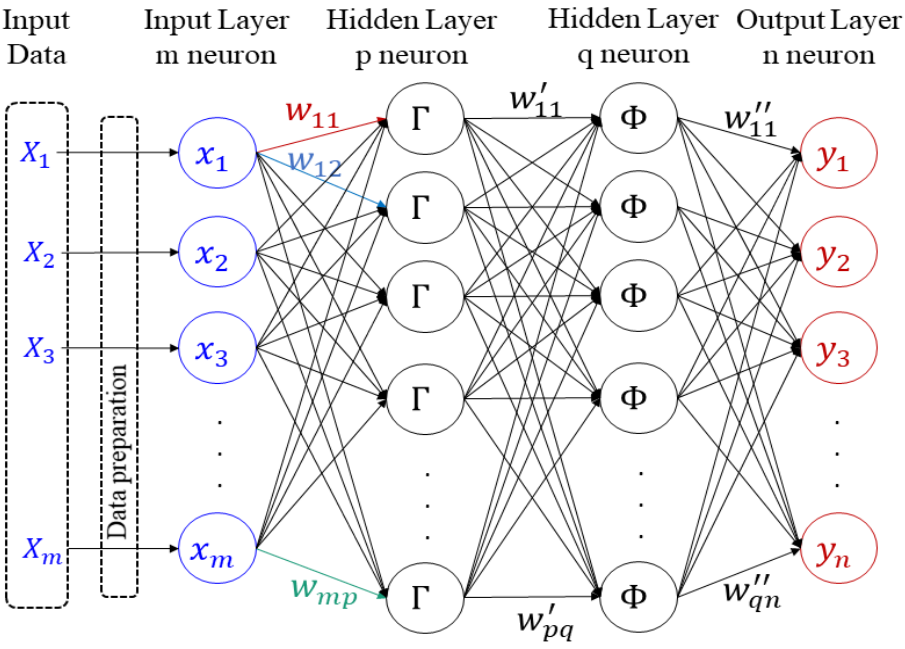

Figure 4.6 Structure of an ANN.

$$x_i = \frac{X_i - X_{min}}{X_{max} - X_{min}} \tag{4.6}$$

where X_{min} and X_{max} are the minimum and maximum values among the input data, respectively. The prepared data in the input layer is fed to the network. The input layer shown in Figure 4.6 includes *m* nodes or neurons. In the next step, each neuron is multiplied by a positive value called weight (w_{ij}) and results in the activated neuron ($x_i w_{ij}$). Weights are positive values between 0 to 1. The higher value of weight means that a particular neuron is highly activated and has more impact on the output. The sum of all activated neurons is added to a positive value called bias (b) and delivered to the first hidden layer. For an example, the value received by the first neuron in the first hidden layer is $(x_1 w_{11} + x_2 w_{21} + \cdots + x_n w_{n1} + b)$. First and second hidden layers have activation functions, Γ and Φ, respectively which can be differently chosen for each hidden layer based on the type of problem. In the next step the output of each neuron in the first hidden layer is activated by weights (w'_{ij}). The same process is carried out to transfer the calculated values to the second hidden layer and output layer. It should be pointed out that each input and output have one single value named x_i and y_i, respectively, in Figure 4.6. However, each neuron in input and output layers may consist of different values such as $x_i = [x'_{i1}, x'_{i2}, \dots, x'_{ij}]$. In the latter example the i^{th} neuron has j distinct values or j features. In the present study, each neuron in the input and output layer has four features in the case of stress, three features in the case of strain, and two features in the case of displacement predictions, as shown in Figure 4.7-Figure 4.9. All the hyperparameters, including weights, biases, the number of hidden layers, the number of neurons in each layer, and activation functions, must be appropriately determined to develop a well-trained network. There are different functions that can be employed as activation functions such as tanh or sigmoid functions. Rectified linear activation unit (ReLU) is known as one of the best choices when it comes to nonlinear problems, and it is used in the present study. The non-complicated formulation of ReLU provides less intense computation and makes it an efficient activation function. Given datasets used in ANN are commonly categorized into three different groups of training data, verification data, and testing data in the application of ANNs. The ANN algorithms use training datasets in the structure of ANN illustrated in Figure 4.6 to perform a combination of hyperparameters to achieve desired accuracy in the training process. In the present study, mean square error (MSE) has been used as the measure of accuracy. Afterward, a particular combination of hyperparameters is evaluated in the case of verification data. The combination should be updated if the desired MSE or accuracy is achieved only for training data and not for verification data. This procedure is repeated until a particular combination of hyperparameters provides desirable accuracy in terms of MSE for both the training data and verification data. In the end, the selected ANN structure should be tested for a new dataset (i.e. testing data) that has not been introduced during the network training and verification stages. Many different algorithms have been suggested to properly determine hyperparameters of ANNs. ANN developed by Keras with TensorFlow that has a high-level neural networks application programming interface (API), written in Python is adopted in this study. Implementing Keras API facilitates the construction and modification of the ANN and guarantees high-performance computations using parallel computation. In the application of Keras, number of hidden layers, number of neurons in each layer, and type of activation functions are chosen by a user, and values for weights and biases are determined automatically through the Keras algorithms.

In the present study, the hypothetical elastic stress, strain, and displacement fields around the crack tip of a cracked body under the elastic deformation state obtained from the linear elastic FE

analysis are fed to the network as the input data. Subsequently, the elasto-plastic stress, strain, and displacement fields around the crack tip of the same cracked body under the elastic-plastic deformation state obtained from an elasto-plastic FE analysis are used as the network's output data so that ANN model(s) can determine any nonlinear relationship between the elastic and elasto-plastic responses of the material in the presence of cracks. Three different ANNs are trained to predict the elasto-plastic stress, strain, and displacement distribution around the crack tip. It should be noted that it is possible to develop a single network structure that can receive elastic stress, strain, and displacement fields as the input and deliver the elasto-plastic stress, strain, and displacement fields as the output. In the latter case, trained ANN algorithms are able to detect and take advantage of the particular relationships between stress and strain fields (expressed by constitutive models) and between strain and displacement fields (known as the Kinematic rule). In this study, three different networks are separately trained by using stress, strain, and displacement datasets as separate data for each network in order not to take advantage of interplay relationships among these quantities. As expressed in Eq. (4.5), stress, strain, and displacement components are required to calculate J-integral. However, there are many engineering applications in which only elasto-plastic stress or strain fields are desirable. With this in mind, separate networks have a wider range of engineering applications. As shown in Figure 4.4, 2D FE models are developed under plane strain condition. The stress tensor on each GP has four independent stress components. That being said, the ANN model for the stress prediction is trained based on the datasets with four features. Input variables in this case is:

$$X_1 = (\sigma_{11}, \sigma_{22}, \sigma_{33}, \sigma_{12}) \tag{4.7}$$

where σ_{ij} are the stress components of the first GP in the first element in Figure 4.4.

The FE models are developed for various crack sizes between 1 to 10 mm. Table 4.2 presents different crack sizes used to provide training, verification, and test data. According to Table 4.2, all stress, strain, and displacement results from elastic and elasto-plastic FE models in the presence of ten, six, and three different crack sizes are used as the training, verification, and testing datasets, respectively. The structure of input and output stress data used as training data in order to train the ANN model to predict elasto-plastic stress fields are shown in Figure 4.7. $\sigma_{ij}^{n,s}$ is used as the notation to show input and output data matrices in Figure 4.7. The subscript i and j refers to the location of stress component in the stress tensor. The first superscript “n” refers to the number or order of the dataset in the input and output matrices. Finally, the second superscript “s” refers to the state of the material as elastic or elasto-plastic in the FE analyses. The letter “e” and “a” are employed to refer to the elastic, and elasto-plastic states, respectively. The same notation and the same superscripts are used in the case of strain and displacement, respectively, in Figure 4.8-Figure 4.10.

FE analyses for 25 load increments, and 10 different crack sizes have been performed to provide training datasets. It means training input and output matrices have 480000 ($4 \times 480 \times 25 \times 10$) numerical data points considering that each element has 4 GPs, the chosen area (see Figure 4.11) has 480 elements.

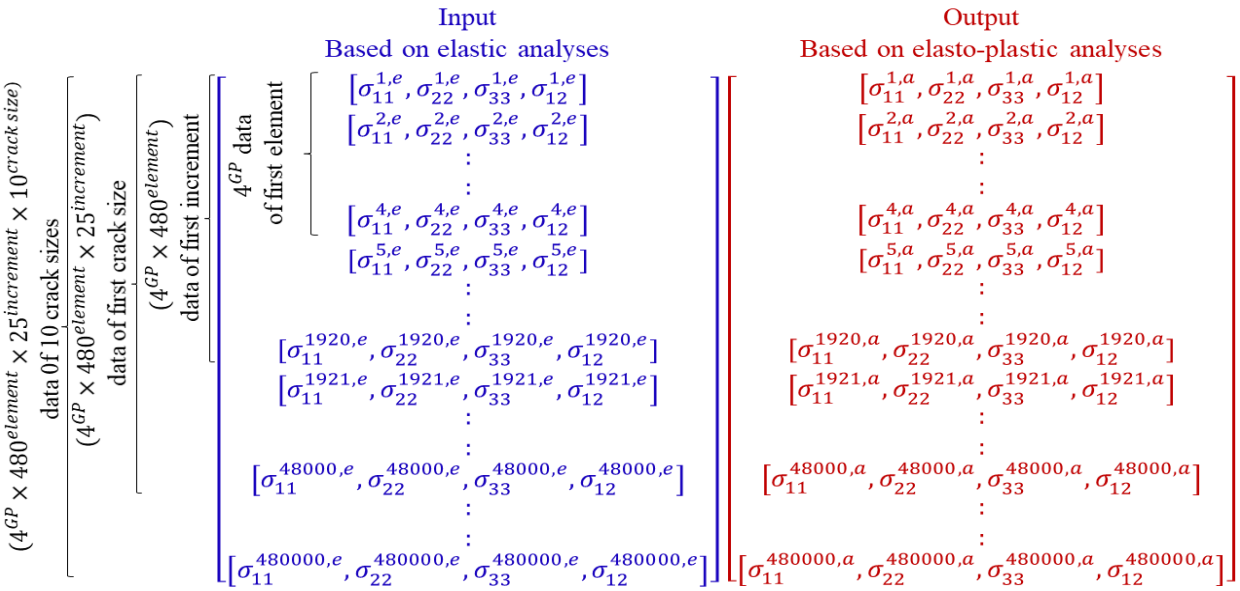

Figure 4.7 Structure of input and output data array for elasto-plastic stress prediction.

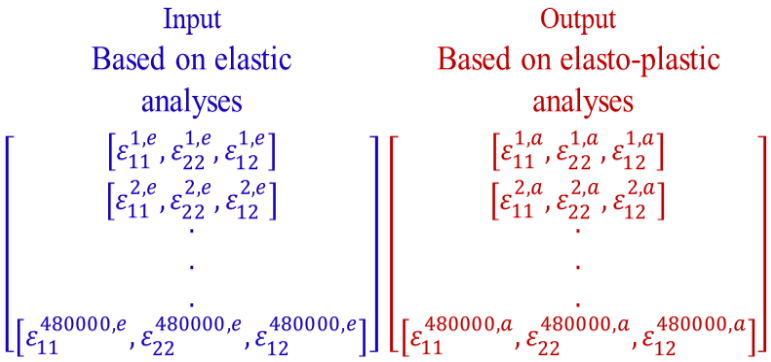

Figure 4.8 Structure of input and output data array for elasto-plastic strain prediction.

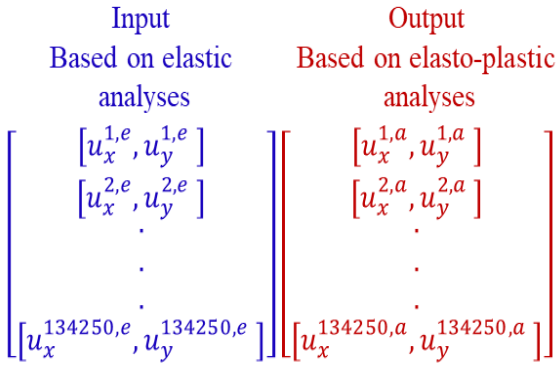

Figure 4.9 Structure of input and output data array for elasto-plastic displacement prediction.

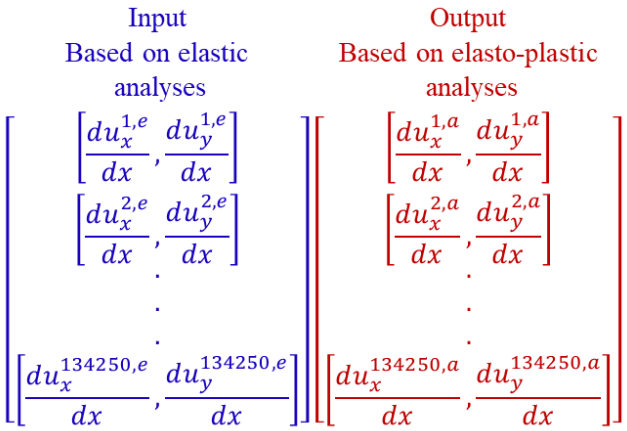

Figure 4.10 Structure input and output data array for elasto-plastic displacement derivative prediction.

Table 4.2 ANN datasets for a range of different crack sizes.

Type of data	Crack size (mm)
training data	1.0, 2.0, 3.0, 4.0, 5.0, 6.0, 7.0, 8.0, 9.0, 10.0
verification data	1.5, 3.5, 4.5, 6.5, 7.5, 9.5
testing data	2.5, 5.5, 8.5 (used in section 4.3.2) 1.2, 2.2, 3.2, 4.2, 5.2, 6.2, 7.2, 8.2, 9.2 (used in section 4.3.3)

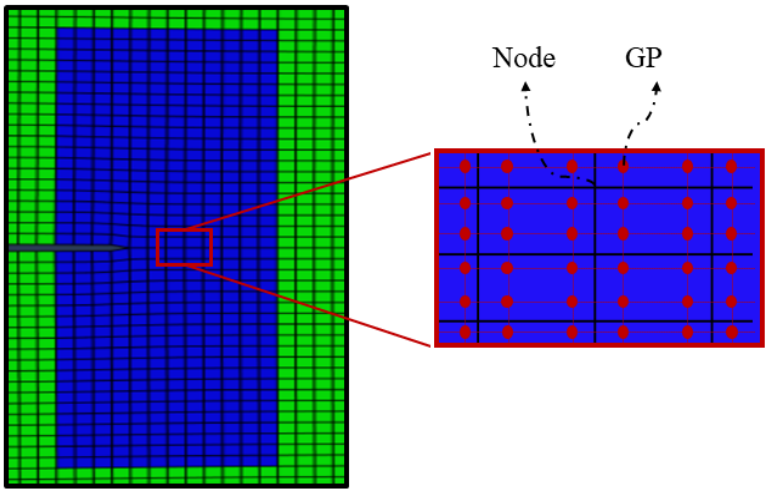

Figure 4.11 Gridding used in the contours based on GPs.

The input and output data structure for verification datasets have been generated in a similar manner and fed to the ANN algorithms. Verification stress data has a size of 288000 ($4 \times 480 \times 25 \times 6$) numerical data points. The training datasets to train the ANN in order to predict elasto-plastic strain and displacement fields around the crack tip can be organized by using the same approach as shown in Figure 4.8- Figure 4.9. Since the FE models are developed based on plane strain condition. Therefore, strain data has three (corresponded to the three non-zero independent strain components) and displacement data has two displacement quantities

considering two degrees of freedom for each nodal displacement. The displacement components are extracted from the nodes of elements and the stress and strain components are extracted from the GPs. It means the size of strain training datasets has also 4880000 data points similar to stress data (See Figure 4.8). However, the size of displacement training data has 134250 $(537 \times 25 \times 10)$ data points in which the value of 537 corresponds to the number of nodes in the selected data area shown in Figure 4.11.

The J-integral value is a function of stress, strain and displacement components as expressed in Eq. (4.5). However, displacement components are not directly employed in Eq. (4.5), contrary to the stress and strain components. The derivative of displacement components with respect to the (x) as a coordinate axis is required to determine the J-integral value. With this in mind, two different approaches are taken to calculate the derivative of displacements. First one is based on elastic and elasto-plastic displacement fields around the crack tip. It means an ANN is trained based on the values of displacement components, as shown in Figure 4.9. One may realize that if this approach is employed to determine J-integral based on ANN predictions, the accuracy of calculated J-integral may be comprimised. The reason is attributed to the fact that the error of the predicted displacement field by the ANN model is magnified by the numerical error for calculation of the displacement derivative. To overcome that problem, another approach can be adopted. As for the second an ANN model can be trained by using the derivative of displacement data rather than the displacement data. It means that the derivative of displacement in elastic and elasto-plastic states can be used as the input and output of the network, respectively, as shown in Figure 4.10.

The number of hidden layers, number of neurons, learning rates, and other essential hyperparameters to train all three ANNs are given in Table 4.3. The initial number of neurons in each hidden layer was chosen as 256. Then that number was increased to 512 and 1024 and so on until the acceptable accuracy was achieved. Learning rate is considered as a tuning hyperparameter during the optimization algorithm that specify the step size at each iteration or epoch while approaching a minimum of loss function. That being said, a relatively larger learning rate decreases the training time significantly. However, the optimum values of weights and biases may not be determined if the learning rate is too high.

Table 4.3 Description of different hyperparameters to train the ANNs.

ANN model		Num. of input variable	Num. of hidden layers	Num. of neurons in 1st hidden layer	Number of neurons in 2nd hidden layer	Activation function in 1st hidden layer	Activation function in 2nd hidden layer	Learning rate
Stress		4	2	1024	512	relu	relu	1e-4
Strain		3	2	1024	512	relu	relu	1e-5
Displacement	1st approach	2	2	1024	512	relu	relu	1e-8
	2nd approach	2	2	1024	512	relu	relu	1e-4

In the present study, all of the ANN models were initially trained by using learning rate values of 1e-1, 1e-2, 1e-3, and so on until a good acceptable accuracy was achieved. In other words, the learning rate(s) are chosen in such a way that the reducing of MSE and/or increasing of accuracy are acceptable in terms of prediction accuracy and computation time. The present ANN-based modeling approach can establish the relationships between the hypothetical elastic stress, strain, and displacement fields of the cracked body in elastic state with actual elasto-plastic corresponding components. With having such ANNs in hand, only a linear and relatively simple FE analysis rather than a complex and computationally expensive non-linear FE analysis is required to determine elasto-plastic stress, strain, and displacement fields around the crack tip. Such ANNs can be employed in various applications such as J-integral calculation, as in the present study. In addition to crack geometries, the present approach can be also applied to notches, micro notches and crack propagation modeling for different engineering applications. The present study also aims to shed light on calculating cyclic J-integral under cyclic loading using the same approach for a future study. The present approach can be extended to modeling fatigue crack growth on the basis of the cyclic J-integral.

4.4. Results and discussion

The J-integral results predicted by the developed in-house model based on the EDI method, are compared against results obtained from the model developed by Wang et al. [81] and results of built-in functionality of ABAQUS to verify the accuracy of the in-house model in section 4.3.1 for calculating the J-integral. Elasto-plastic stress, strain, displacement, and derivative of displacements fields in the vicinity of the crack tip predicted by the developed ANN models are compared with corresponding results obtained from the elasto-plastic FE analysis in section 4.3.2 to verify the prediction accuracy of ANN models to determine stress, strain, displacement, and derivative of displacements fields. Finally, J-integral values calculated based on the ANN predicted stress, strain and displacement results are compared against J-integral results obtained from elasto-plastic FE analysis to verify the proposed modeling approach to compute the J-integral as an EPFM parameter in section 4.3.3.

4.4.1. J-integral based on Finite Element Analysis and the in-house Equivalent Domain Integral model

J-integral results predicted by the EDI-based in-house model are compared to the conventional method (i.e. Abaqus built-in functionality) and the original EDI method developed by Wang et al. [81] for 10 different load levels in the range of 1 to 10 KN as shown in Figure 4.12. The dashed blue, dotted green and solid black lines represent the J-integral results obtained from the EDI-based in-house model, the conventional method and the original EDI method respectively. All of the FE parameters used in the original EDI method [81] are the same as the ones employed in the present study except for the mesh size and pattern. However, the EDI method is considered as a mesh-independent method [102]. Therefore, different mesh size and pattern are not deemed to have significant effects on the calculated J-integral results.

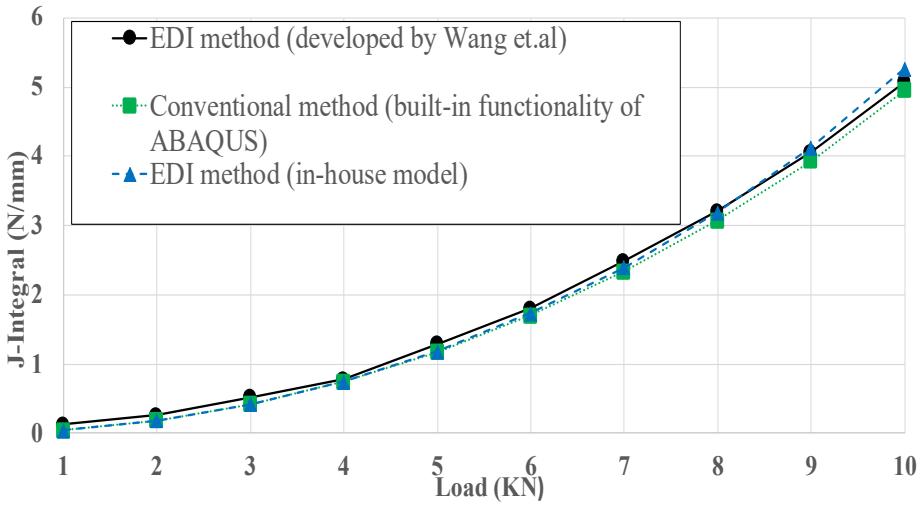

Figure 4.12 Comparison of J integral results under monotonic load.

Figure 4.12 shows that all three J-integral calculation methods are in a good agreeement since all three J-integral curves almost collapse onto each other. Figure 4.13 presents an investigation on the effect of mesh size on calculated J-integral. The solid black line shows the results of Wang et al. model with the mesh size of 0.004 mm around the crack tip. Purple and blue dash dotted lines present the results of in-house model with the element size of 0.05 and 0.1 mm, respectively. The calculated J-integral curves in Figure 4.13 confirm that different mesh sizes do not have any considerable effects on the results.

The present approach does not rely on the built-in functionality of ABAQUS. Because the developed in-house model can be employed in the ABAQUS FE package as the post-processing model in addition to the Python IDLE in order to calculate J-integral on the basis of ANN stress, strain and displacement predictions. Applying the built-in functionality of ABAQUS to determine J-integral based on ANN models is not time-efficient. Furthermore, the built-in functionality of ABAQUS is not applicable to determine cyclic J-integral under cyclic loading. Although in the current study, the cyclic J-integral is not considered, the present authors plan to extend the current modeling approach to predict the cyclic J-integral for various cracked bodies under cyclic loading conditions.

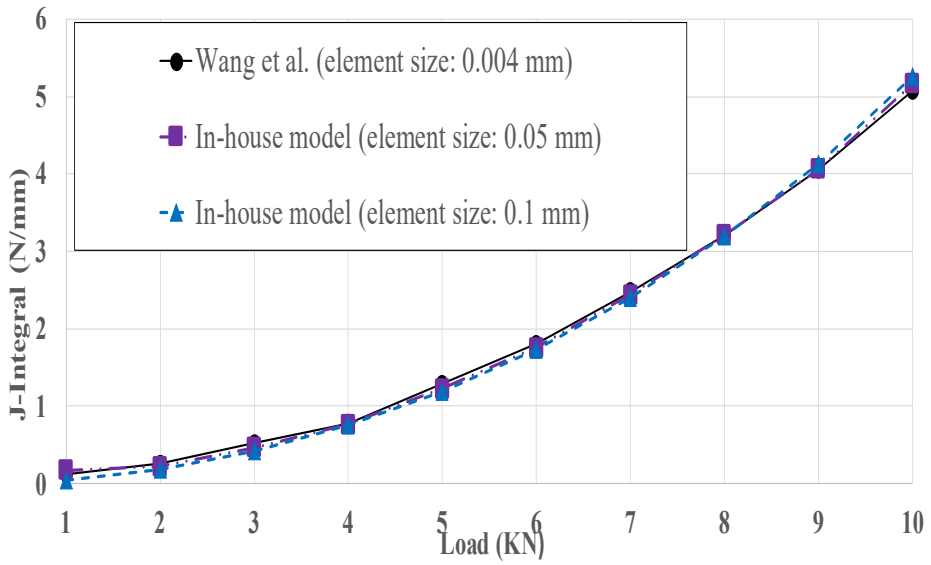

Figure 4.13 The effect of mesh size on the J-integral calculation.

4.4.2. ANN predicted stress, strain, and displacement fields

In this section, ANN predicted stress, strain and displacement fields of the test data in Table 4.2 are presented. One of the most common problem of training ANN models is the occurrence of overfitting. There is a significant number of hyperparameters in the ANN structures (see Figure 4.6), which can be fitted and tuned in such a way underlying patterns between input(s) and output(s) can be learned. Overfitting problem is described as once the hyperparameters are chosen in such a way that the ANN only produce good results for training dataset, however it shows a relatively high error when it comes to other dataset such as validation/verification and testing datasets. The accuracy and the MSE values for training and validation datasets for stress and strain ANNs are presented in Figure 4.14a) and Figure 4.14b), respectively, to investigate the absence of such problem in the present study. ANN models encounter overfitting when the accuracy or the MSE values of training and validation dataset start to diverge after a number of epochs during the training process. However, high accuracy of ANN predictions (approximately 98%) for training and validation data in these figures shows that ANNs for stress and strain generalize well from the training dataset to the validation dataset. The same behaviour has been observed in the case of displacement and derivative of displacement data. Furthermore, the developed ANN models are also tested by testing/unseen data (see Table 4.2), which have not been used during the training process to ensure the absence of overfitting in the present study. One of the differences between Figure 4.14a) and Figure 4.14b) is the number of epochs required to achieve the minimum MSE or loss function.

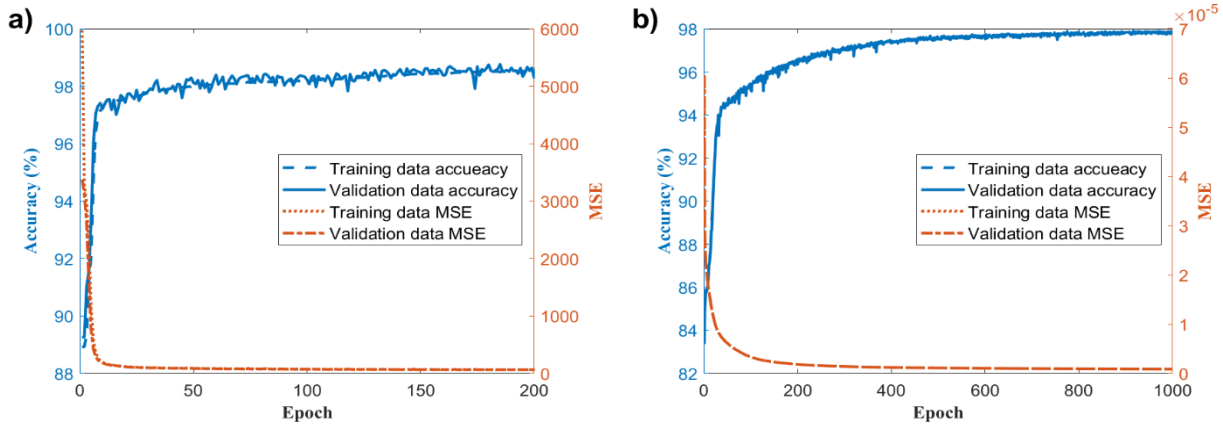

Figure 4.14 Accuracy and MSE trends for training and validation datasets during training the ANN model to predict: a) stress distribution, b) strain distribution.

Since the learning rate for strain distribution is significantly smaller than that for stress distribution, the number of epochs for strain distribution is approximately five times more than that in the case of stress distribution. A well-trained ANN model is capable of predicting the stress, strain, and displacement fields with good accuracy for any crack sizes that have not been used during the training and verification stages of ANN model(s). Therefore, the ANN predicted results only for testing data are discussed in this section. The crack tip is located at the origin of the coordinate system (x=y=0) for all result contours presented in this chapter. As previously discussed, the number of datasets in the case of stress and strain fields in Figure 4.11 corresponds to the number of GPs but not the number of nodes. The comparison of ANN predicted elasto-plastic σ_{11} stress distributions around of the crack tip with those results obtained from the elasto-plastic FE analysis is shown for the crack size of 8.5 mm under the force of 20 KN in Figure 4.15. 25 load increments have been used to reach the peak loading point of 20 KN. The stress and strain components in all incremental points of the load are required to determine strain energy in Eq. (4.5). However, due to the amount of the large datasets for all 25 load increments, only the results of the last load increment (25 out of 25) is presented in Figure 4.15. The prediction error of stress components between ANN model and elasto-plastic FE analysis is defined as the percentage of error (POE) to quantify prediction errors as expressed in Eq. (4.8).

$$POE(\%) = \frac{\sigma_{ij}^{ANN} - \sigma_{ij}^{el-pl\ FEM}}{\sigma_{ij}^{el-pl\ FEM}} \times 100 \tag{4.8}$$

Figure 4.15a) and Figure 4.15b) show that the ANN model can accurately predict the first component of stress tensor σ_{11} field. In addition, Figure 4.15c) shows that prediction error values are approximately $\pm 10\%$ range which is deemed to be acceptable. As shown in Figure 4.15c), only a small number of GP points, behind the crack tip have error values greater $\pm 10\%$. However, the POE is less than $\pm 5\%$ in most elements around the crack tip. Figure 4.16- Figure 4.17 present the second and third components of stress tensor (σ_{22}, σ_{33}) around the crack tip. The POE for the ANN predictions is approximately between -12 to 8% and -8 to 6% for σ_{22} and σ_{33} stress components, respectively. Only an ignorable number of locations (GPs) show POE values higher than -12% or 8%. Figure 4.15- Figure 4.17 show that the stress distributions of normal stress components predicted by the ANN are in a good agreement with elasto-plastic FE analysis results. Figure 4.18 shows results of shear stress (σ_{12}) for ANN and elasto-plastic FE models.

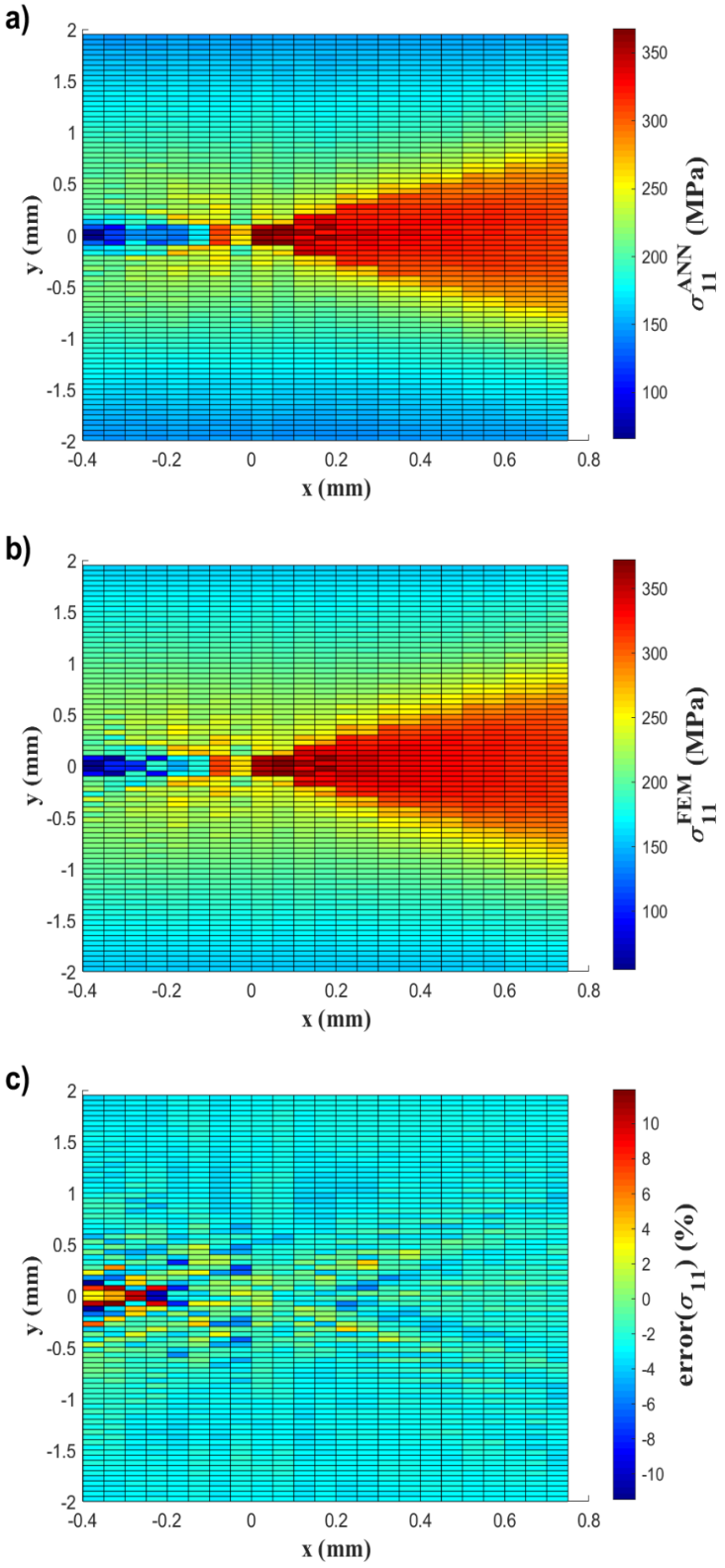

Figure 4.15 σ_{11} stress field for a=8.5 mm, F=20 KN a) ANN prediction, b) FE results, c) prediction error

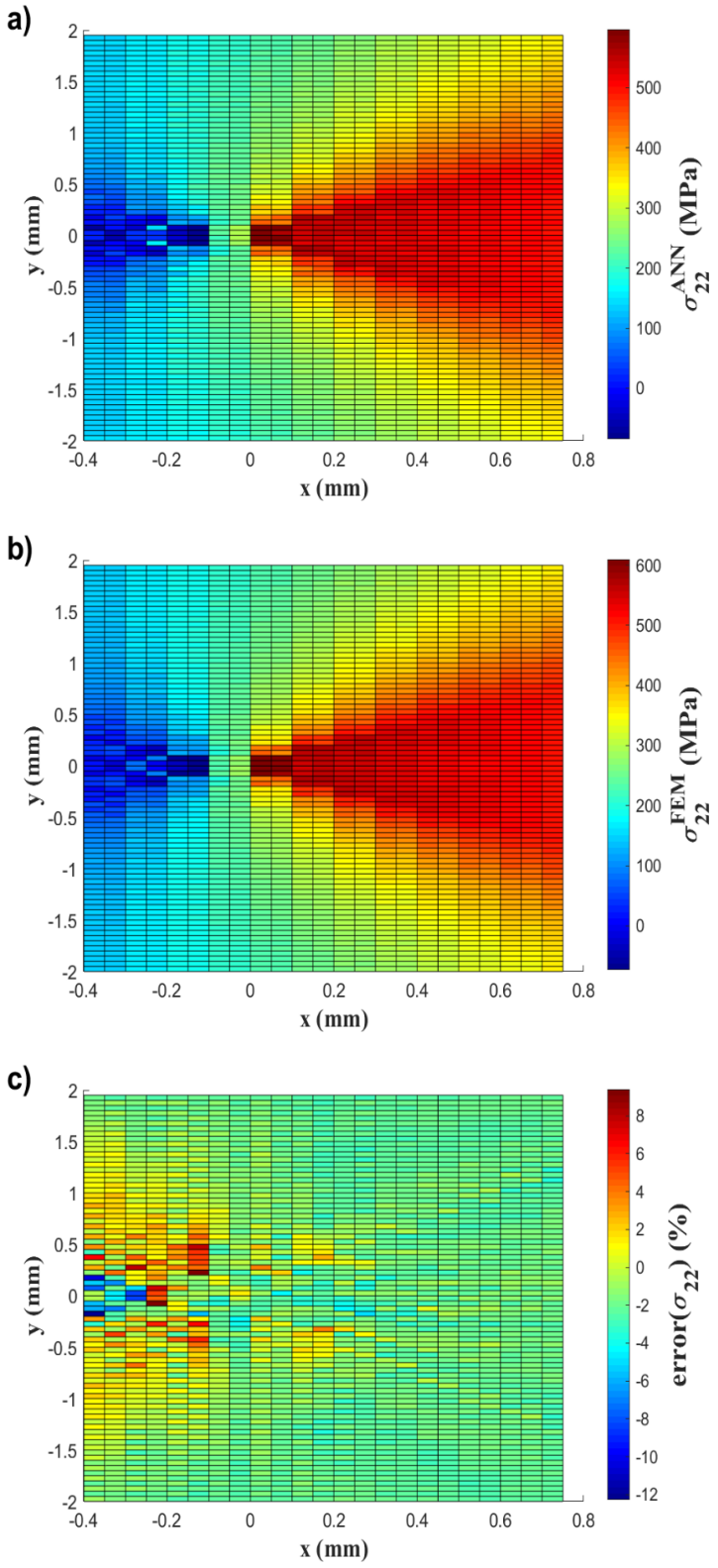

Figure 4.16 σ_{22} field for a=8.5 mm, F=20 KN, and increment 25. a) ANN prediction, b) FE results, c) prediction error.

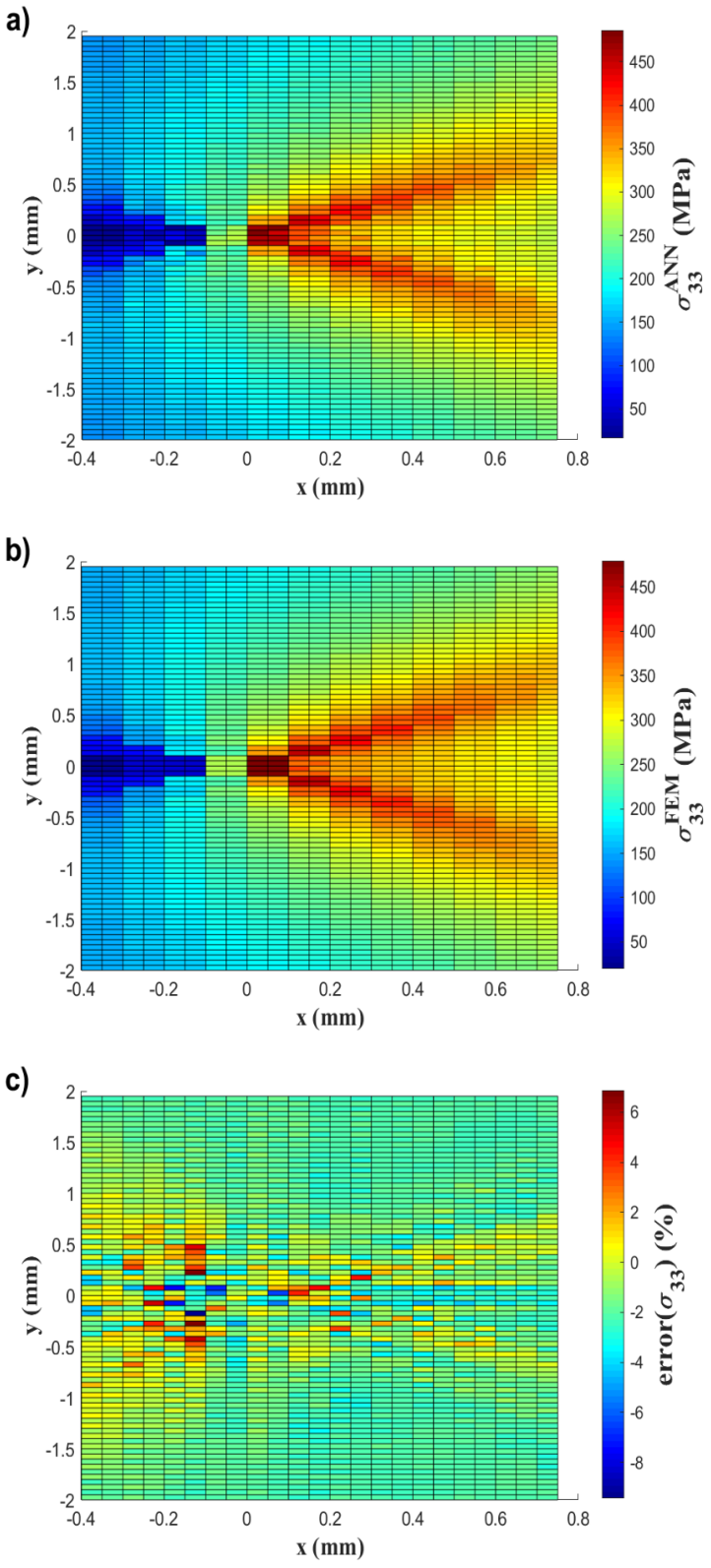

Figure 4.17 σ_{33} field for a=8.5 mm, F=20 KN, and increment 25. a) ANN prediction, b) FE results, c) prediction error.

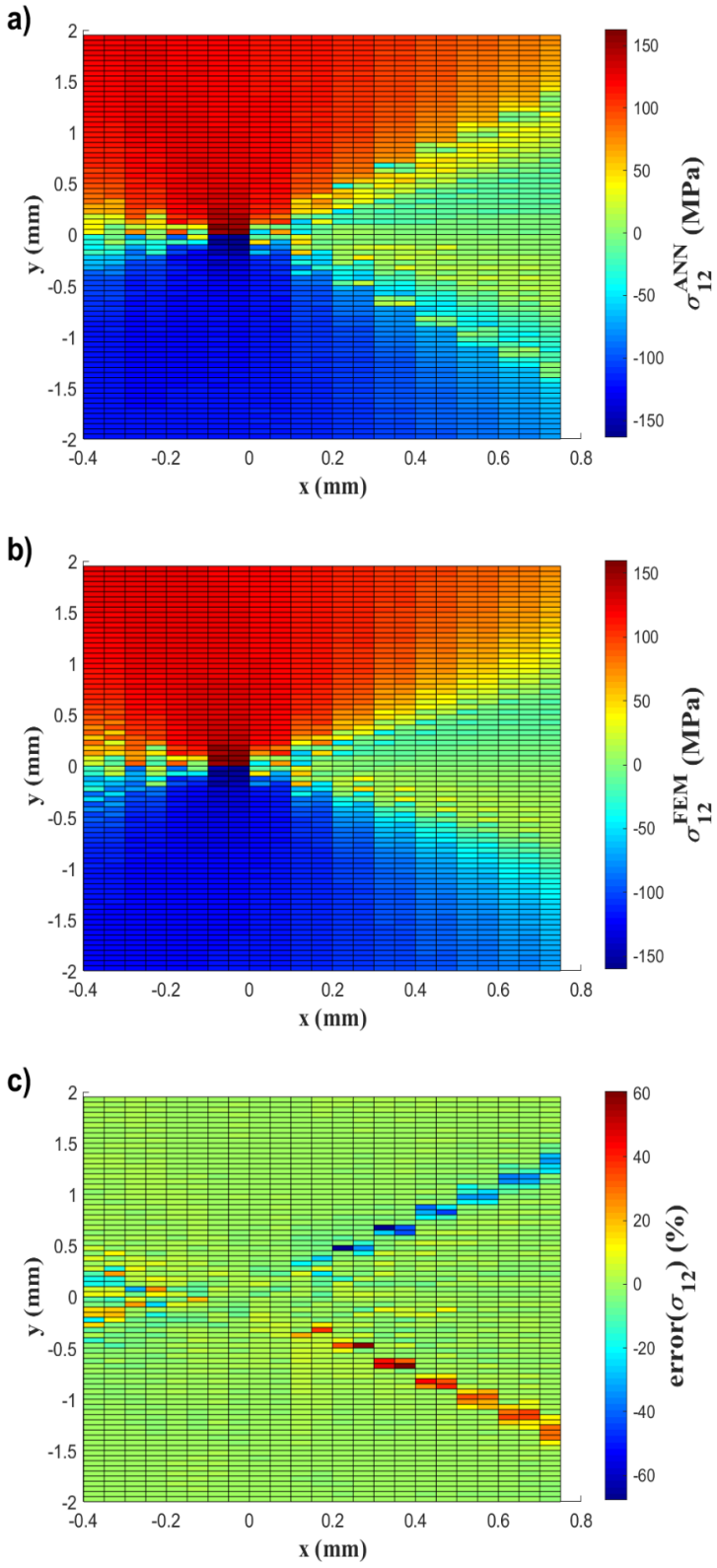

Figure 4.18 σ_{12} field for a=8.5 mm, F=20 KN, and increment 25. a) ANN prediction, b) FE results, c) prediction error.

The POE values for shear stress (σ_{12}) in Figure 4.18c) are in the range of $\pm$60%, which is significantly higher than the ones in the case of normal stress components (Figure 4.15- Figure 4.17). However, those relatively high POE values belong to narrowly localized points along approximately $\pm$ 45 degrees of the crack axis (see Figure 4.18c)). According to the shear stress distribution in Figure 4.18a) and Figure 4.18b), those high stress locations correspond to relatively high stress gradient locations. In addition, the area above the crack axis is under the positive shear stress and the area below that is under the negative shear stress. However, the contours are symmetric in the case of all three normal stresses. With all these in mind, the number of training data in the case of shear stress component is almost half of the data in the case of normal stresses because of symmetry conditions. The accuracy of ANN models in the case of shear stress can be increased by introducing more crack sizes as the training data or increasing the number of increments in applications where higher accuracy is required. Figure 4.18c) shows that the POE values in the vicinity of the crack tip where J-integral should be determined is approximately in the range of $\pm$15, which is acceptable for the purpose of this study. Figure 4.19 shows the second stress component σ_{22} for the load increment 15 out of 25. The accuracy of the ANN model for the increment of 15 is almost the same as the last increment of 25 previously discussed. Almost the similar accuracy for all increments has been observed in all prediction quantities including stress, strain, displacement, and derivative of displacement fields. Therefore, only the last increment results of strain, displacement, and derivative of displacement are discussed in the following parts even although the ANN models can predict stress, strain, and displacement fields for all load increments between 0 to 20 KN. It should be pointed out that the learning rate in the case of stress predictions has been chosen as 1e-4 as shown in Table 4.2. According to the high accuracy of ANN models shown in Figure 4.14 for training and validation data and prediction results for testing data in Figure 4.15 to Figure 4.18, the chosen learning rate is considered to be small enough. Figure 4.20 shows the first strain component, ε_{11} field around the crack tip for the crack size of 5.5 mm (testing data). The accuracy of the ANN model is in the range of-15 to +10% except for two GPs shown with the dark blue color with a POE value of approximately -30% behind the crack tip in Figure 4.20c). Figure 4.21 presents the values of the second component of the strain tensor (ε_{22}). The POE values are between -5 to 15% except for only two GPs with 20% of POE shown with dark red in the error contour of Figure 4.21c).

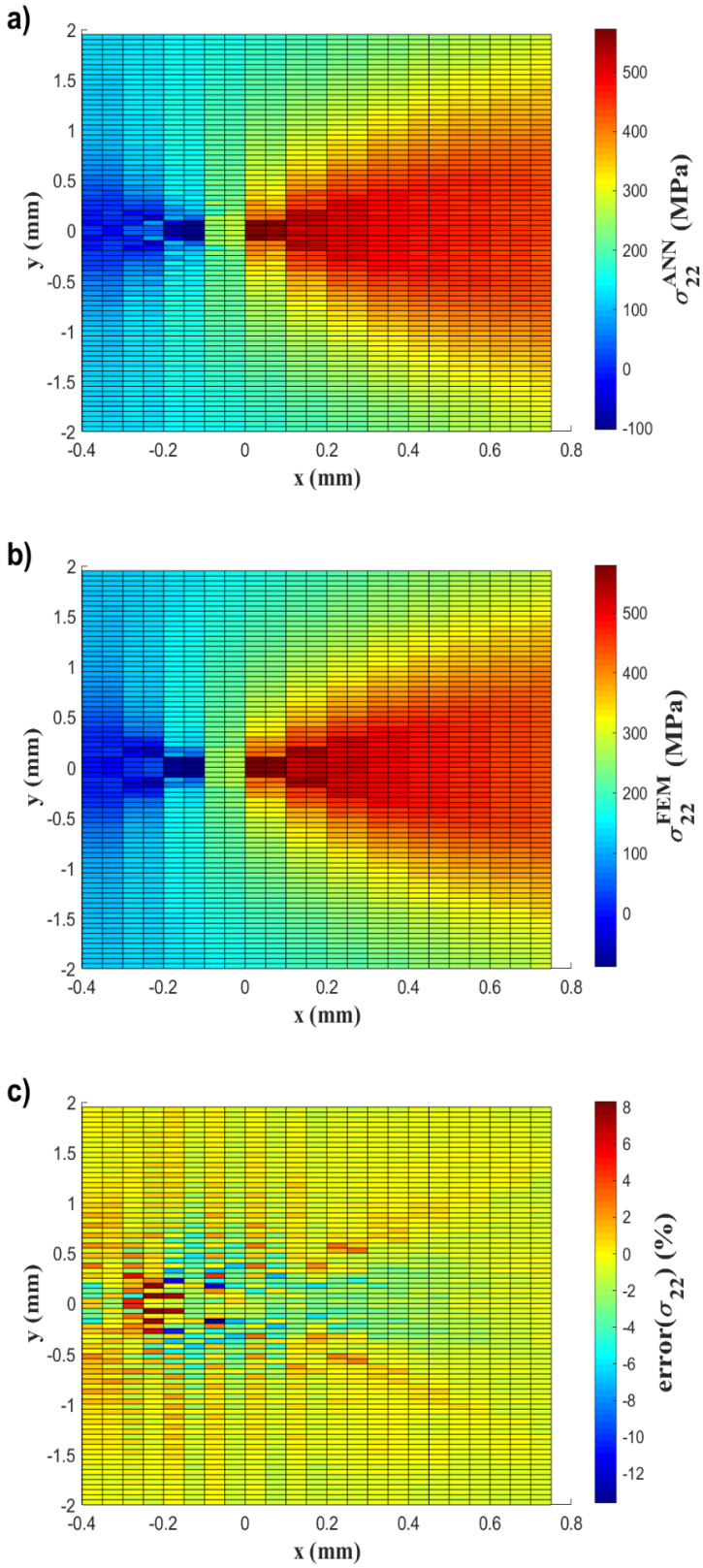

Figure 4.19 σ_{22} field for a=8.5 mm, F=20 KN, and increment 15. a) ANN prediction, b) FE results, c) prediction error.

Figure 4.22 shows the calculated shear strain (ε_{12}) fields around the crack tip for ANN and FE models in Figure 4.22a) and Figure 4.22b), respectively. The accuracy of the ANN model is almost in the POE range of -4 to +6%. Similar to the shear stress results in Figure 4.18, high POE values correspond to local narrow bands along direction of ± 45 degrees with respect to the crack axis. The learning rate in the case of strain distribution is 1e-5 which is one order lower than that of stress distribution. The reason is the fact that the values of strain is closer to each other and make a narrower range in comparison with the stress values. Although all of the data are normalized and are in the range of 0 to 1, the distribution of data between the 0 and 1 range may be different. It means the normal distribution of strain values has a narrower range than the one for the stress values. As expressed in Eq. (4.5), the first and second components of the displacement vector (u_1 and u_2) is required to determine the derivative of displacement ($\frac{du_1}{dx}$ and $\frac{du_2}{dx}$) in order to calculate J-integral. However, $\frac{du_1}{dx}$ is equal to the first strain component ε_{11} presented in Figure 4.20. Therefore only u_2 and $\frac{du_2}{dx}$ fields are discussed in the following parts. Figure 4.23 presents the second component of displacement field around the crack tip. The distribution of u_2 is accurately predicted by the ANN model. However, the POE values for the u_2 field are approximately in the range of -25 to +5%. The accuracy of the predicted displacement field by the ANN is lower than POE values obtained for stress and strain results. This can be attributed to the fact that training datasets in the case of displacement corresponds to the number of nodes, which is significantly less than the number of GPs used for stress and strain training datasets. The learning rate in the case of displacement distribution is 1e-8 which is noticeably smaller than that of stress and strain distribution. As discussed before, the reason is the closer data and narrower range of data in this case in comparison with the stress and strain distribution. The accuracy can be improved by increasing the number of load increments to provide larger training datasets. The same accuracy has been observed in the case of u_1. However, although the POE values in the range $\pm 15\%$ are considered to be acceptable in the case of stress and strain fields, that is not acceptable in the case of the displacement field. The reason is that taking derivatives with a numerical approach imposes greater error(s) that can be accumulatively added to the error of ANN models. With this in mind, an ANN model is developed to directly determine the derivative of the second displacement component vector, as shown in Figure 4.10. The predicted $\frac{du_2}{dx}$ is presented in Figure 4.24.

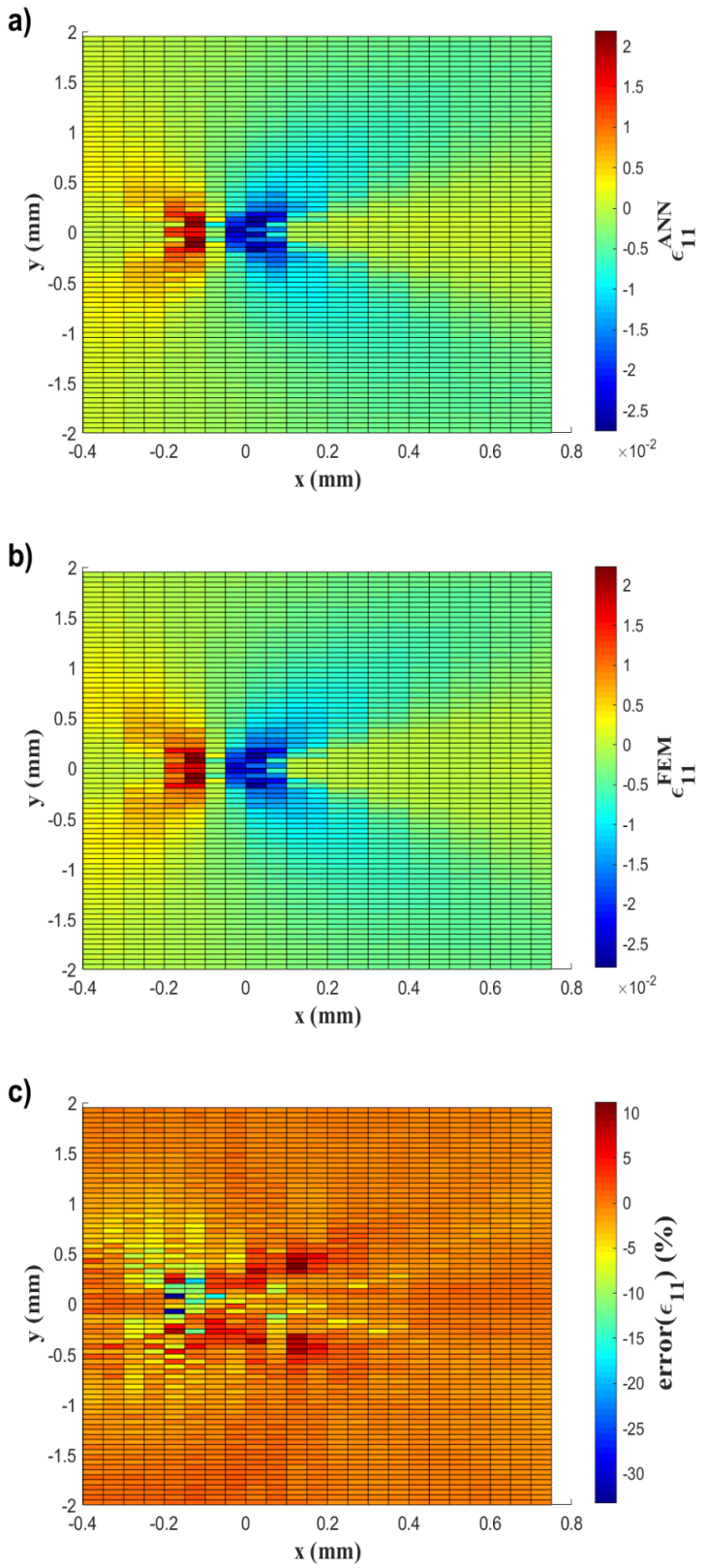

Figure 4.20 ε_{11} field for a=5.5 mm, F=20 KN, and increment 25. a) ANN prediction, b) FE results, c) prediction error.

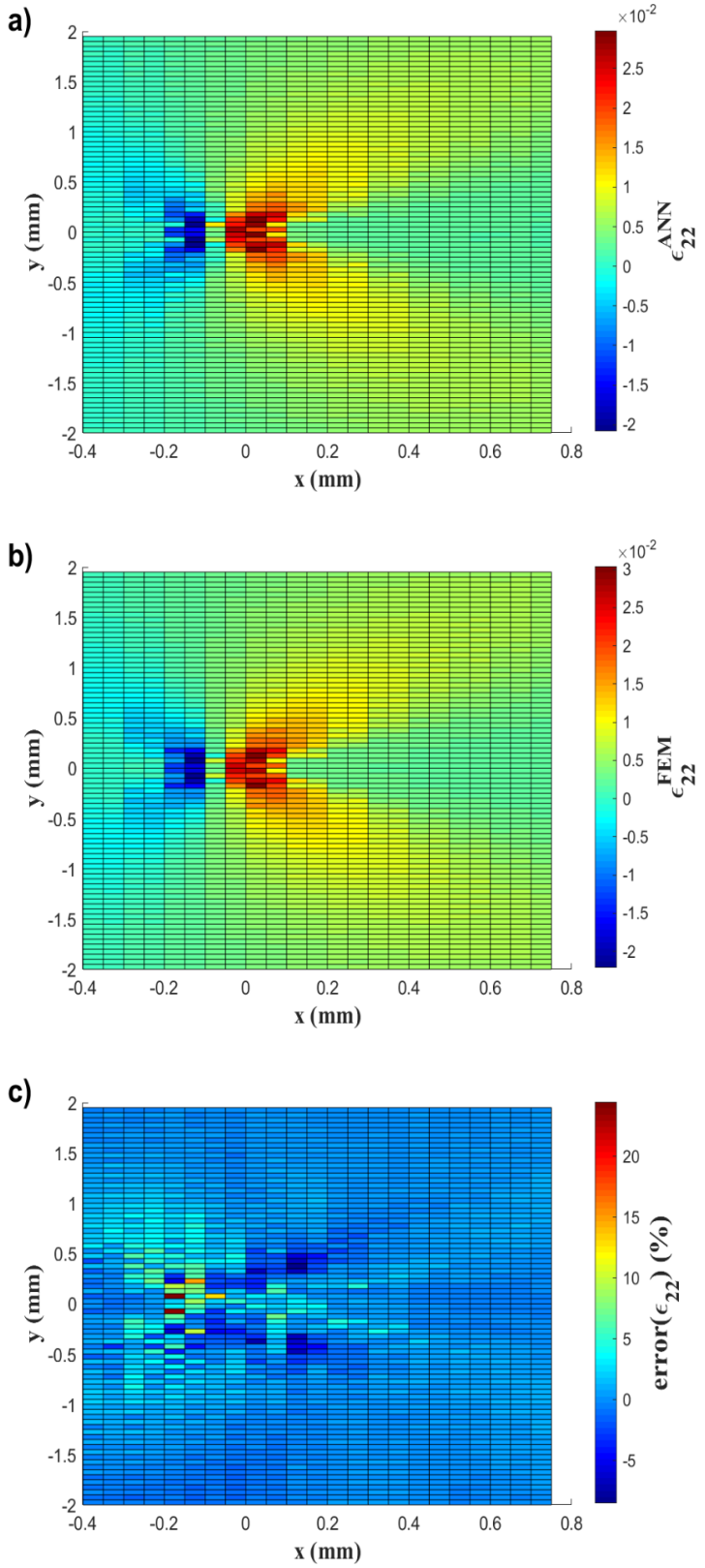

Figure 4.21 ε_{22} field for a=5.5 mm, F=20 KN, and increment 25. a) ANN prediction, b) FE results, c) prediction error.

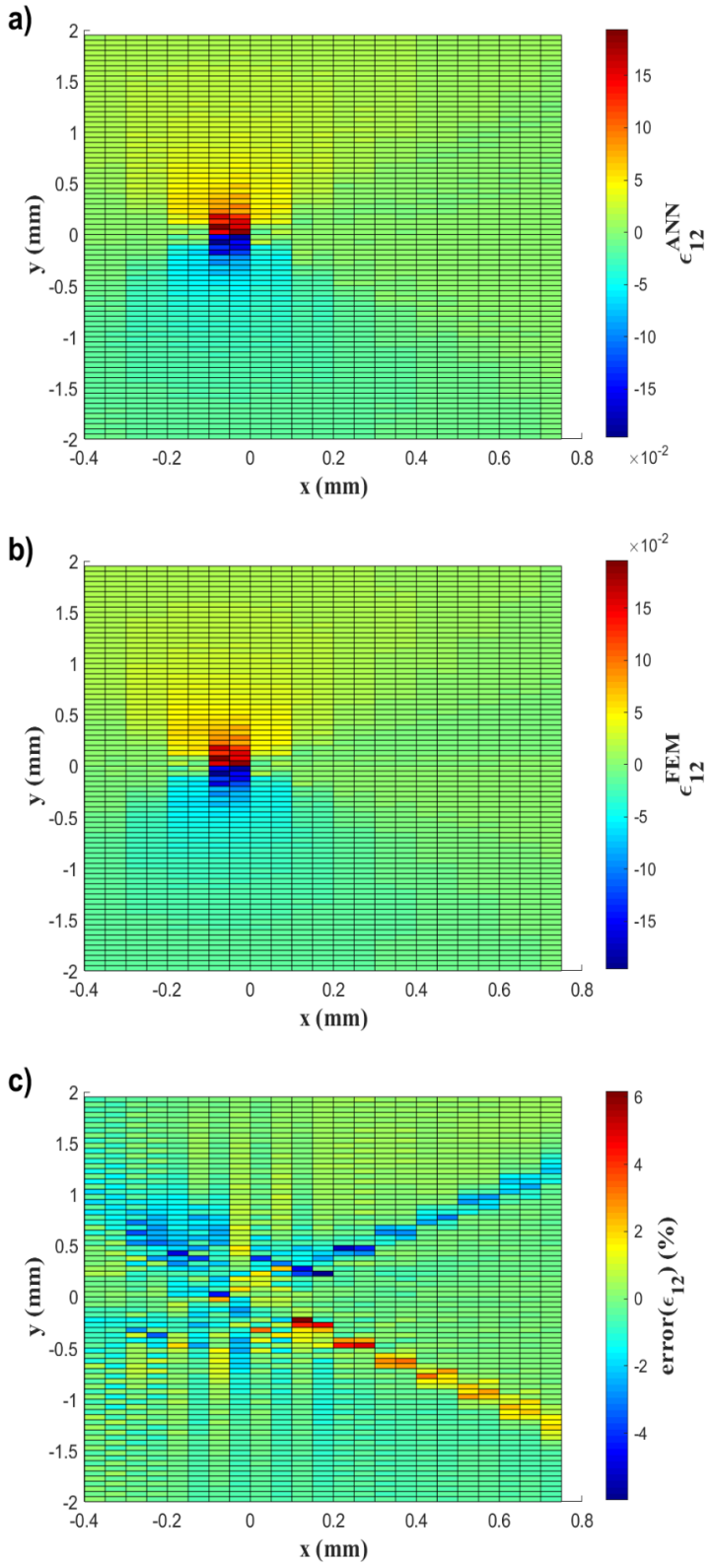

Figure 4.22 ε_{12} field for a=5.5 mm, F=20 KN, and increment 25. a) ANN prediction, b) FE results, c) prediction error.

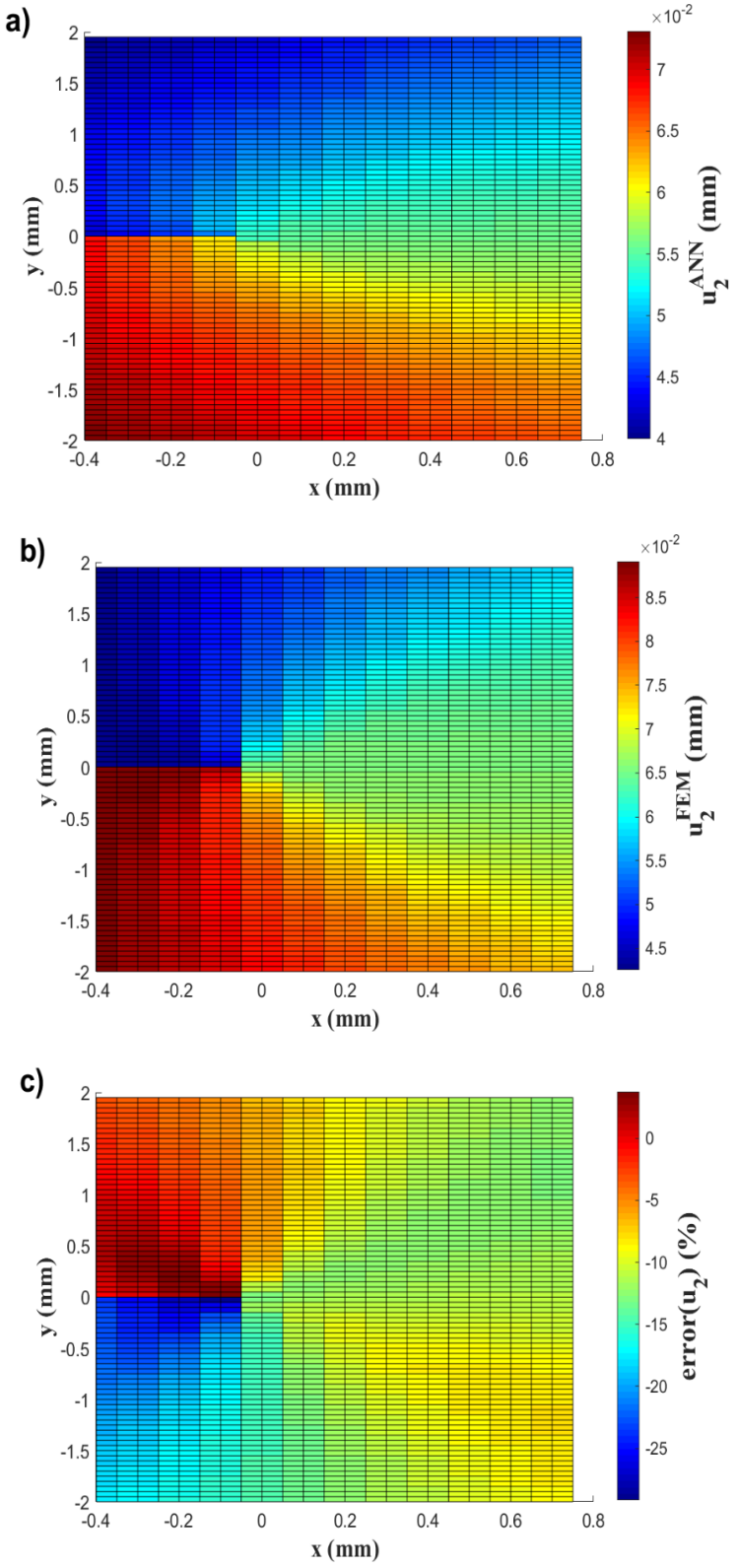

Figure 4.23 u_2 field for a=2.5 mm, F=20 KN, and increment 25. a) ANN prediction, b) FE results, c) prediction error.

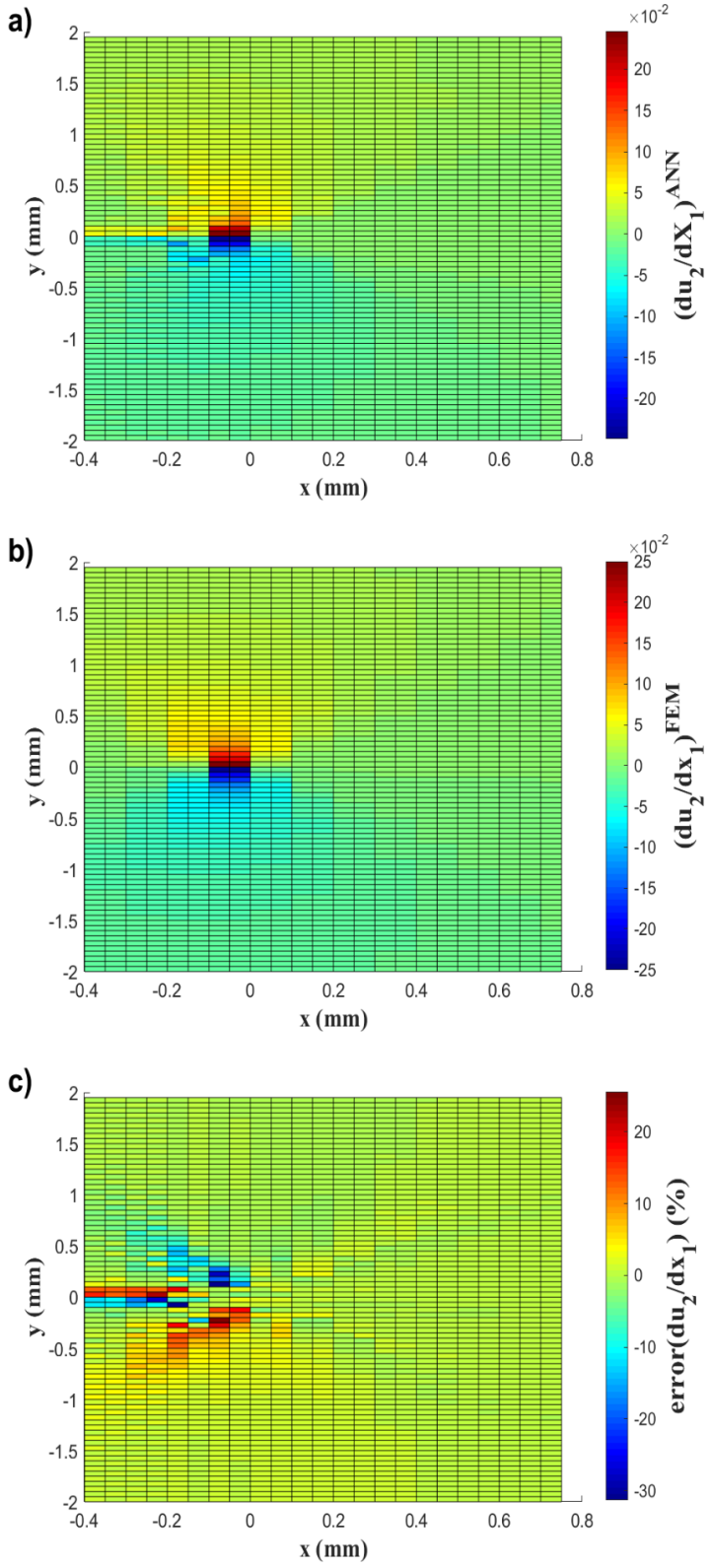

Figure 4.24 $\frac{du_2}{dx_1}$ field for a=8.5 mm, F=20 KN, and increment 25. a) ANN prediction, b) FE results, c) prediction error.

The POE in that case is between -30 to +20. It should be noticed that only a few locations show a relatively high error, such as -30 or 20%. In most areas, the POE is between -15 to +10. The learning rate in this case is 1e-4.

4.4.3. Predicted J-integral

In this section, the J-integral results determined by using stress, strain, displacement and derivative of displacement predicted by the ANN models are compared with those results obtained from elasto-plastic FEMs. In Figure 4.25, the solid black curve shows the J-integral values determined by the in-house model based on the EDI method. The dotted green curve shows the J-integral values calculated by the built-in functionality of ABAQUS based on the conventional method (see Figure 4.5a)). The blue densely dashed line corresponds to the developed in-house model based on post-processing script implemented in ABAQUS. The red loosely dashed line shows the J-integral calculation based on the ANN stress, strain, and displacement predictions. Finally, the yellow dash dotted line shows the results of J-integal based on the ANN stress, strain, and derivative of displacement. Figure 4.25 indicates J-integral values for the crack size of 18 mm under various load levels. The J-integral values calculated by using ANN predicted stress, strain, and displacement results shows unacceptable accuracy for relatively higher load levels. That can be attributed to the fact that displacement is not directly used for the J-integral calculation in Eq. (4.5). Taking the derivative of predicted displacement values by the numerical methods based on shape functions induced high prediction errors in J-integral calculations. It is shown that the error increases with the increase of the load level. The J-integral values determined by using the stress, strain, and derivative of displacement predicted by ANN models present good accuracy. Figure 4.26 shows the determined J-integral under 20 KN of loading for different crack lengths.

According to Table 4.2, new crack lengths (1.2, 2.2, 3.2, …, and 9.2 mm) are considered as new testing data that have not been utilized during training and verification stages. The J-integral curves correspond to the built-in functionality of ABAQUS and the in-house model as the references are almost collapsed onto each other. The accuracy of J-intregral calculation based on ANN predicted stress, strain, and displacement responses is considered to be poor. This poor prediction can be attributed to high error(s) induced by to the numerical derivative of displacement. Since the load level in Figure 4.26 is 20 KN which is significantly higher than load levels (0 to 10 KN) in Figure 4.25, the error of displacement and subsequently J-integral values are noticeably higher. It means J-integral calculations based on stress, strain, and displacement fields predicted by ANNs are reliable only under relatively low load levels. However, only ANN models computing on stress, strain, and derivative of displacement should be employed in order to calculate J-integral value(s) in the case of relatively high load levels. Figure 4.26 show that the accuracy of determined J-integral based on stress, strain, and derivative of displacement predicted by ANN is considered to be acceptable.

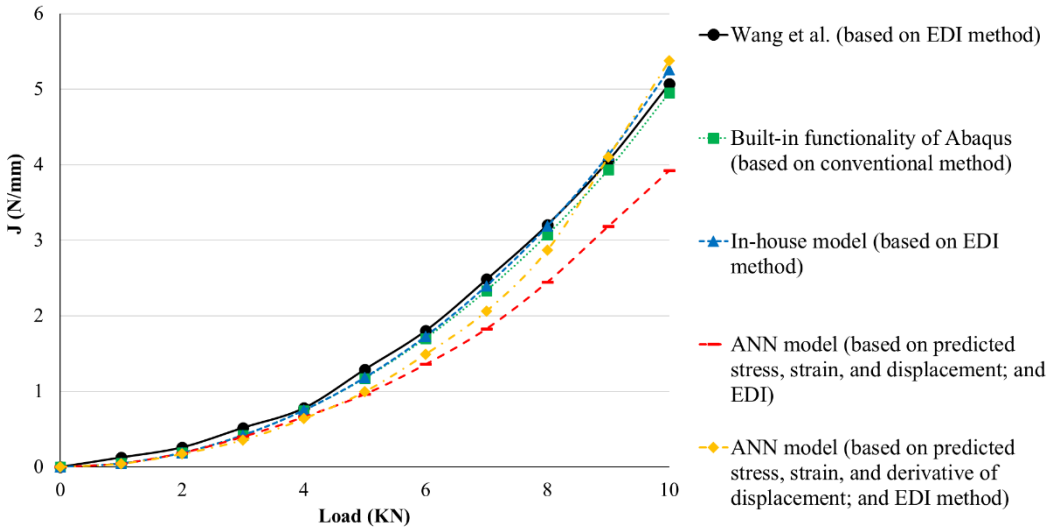

Figure 4.25 J-integral values with respect to the load level for the crack size of 18 mm.

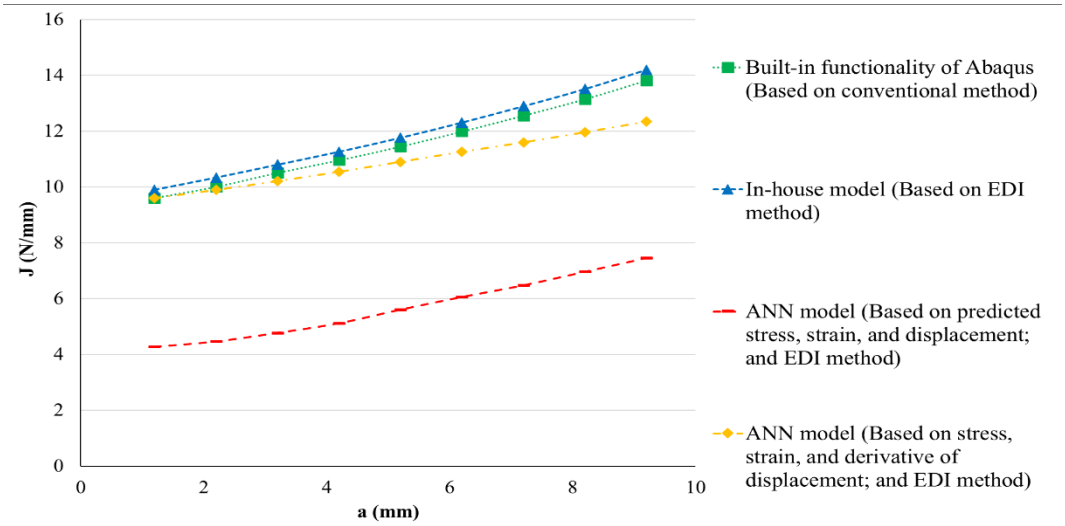

Figure 4.26 J-integral values with respect to the crack length under 20 KN of loading.

4.5. Conclusion

In the present chapter, ANN model(s) have been developed to predict elasto-plastic stress, strain, and displacement fields for a cracked body made of stainless steel (SS304) by only using hypothetical elastic stress, strain, and displacement results. The proposed ANN models have been verified by comparing results obtained from elasto-plastic FE analysis for various crack sizes. The stress, strain, and displacement fields in the vicinity of the crack tip determined by FE models are used to provide well-structured input and output datasets to train the developed ANN models. The stress, strain, and displacement fields obtained from FE models under elastic and elasto-plastic states are utilized as the inputs and outputs of the ANNs, respectively. The results showed that well-trained ANNs are able to predict the nonlinear relationships between the elastic and elasto-

plastic states of the material in the presence of cracks with reasonable accuracy. Furthermore, the ANNs predicted elasto-plastic stress/strain and derivative of displacement fields are used in house model to efficiently determine the J-integral as an EPFM parameter. The present modeling approach shows that ANN model(s) are powerful and efficient methods to compute elasto-plastic stress, strain and displacement fields around of a crack tip and determine elasto-plastic J-integral by utilizing results of elastic FE analysis rather than complex elasto-plastic FE analysis.

4.6. Declaration of Competing Interest

The authors declare that they have no known competing financial interests or personal relationships that could have appeared to influence the work reported in this paper.

4.7. Data availability

Data will be made available on request.

4.8. Acknowledgment

The authors would like to acknowledge the financial support of Natural Science and Engineering Research Council of Canada (NSERC) (DGECR-2018-00232).

Chapter 5

Artificial neural networks-based modeling approach for elastic-plastic cyclic J-integral prediction for cracked bodies

5.1. Abstract

This study aims to develop a new modeling framework to compute cyclic J-integral around a crack tip under elastic-plastic deformation state. The proposed modeling approach is based on the extension of authors' recent time-efficient J-integral computation method, which involves the integration of artificial neural networks (ANNs) with finite element (FE) analyses under monotonic loadings. The ANN-FE integration allows efficient and accurate prediction of elastic-plastic stresses, strains and displacement fields from the linear elastic FE solution for a crack body under cyclic loadings. Cyclic stress, strain, and displacement fields around the crack tip of stainless steel (SS304) are determined by FE analyses under both elastic and elasto-plastic states. ANNs models are developed to establish the nonlinear relationship between the two states. As a result, the suggested approach can predict the elasto-plastic ΔJ based on a time- efficient and linear FE analyses instead of a complicated elasto-plastic solution under cyclic loading. The results show that such an approach can accurately predict elasto-plastic cyclic ΔJ while avoiding the complex computation of elastic-plastic deformation fields around the crack tip under cyclic loading.

5.2. Introduction

The fatigue life of components is mainly assessed by three different methods. First is the "crack initiation method," considering the fatigue life as the number of cycles the component can tolerate before the nucleation of any crack. Such an approach can be either based on stress-life [3-5, 268] or strain-life [6-12]. Since almost all components have defects and cracks due to the fabrication processes, the crack initiation method is not theoretically defendable. However, it should be mentioned that the crack initiation method is used in many engineering industries where relatively high accuracy is not required. Second is the fracture mechanics approach, assuming the component already has the crack. Therefore, fatigue life is considered as the number of cycles that take the initial crack size to its final or critical size that causes the instantaneous fracture. Fracture mechanics characterizes the fatigue crack growth (FCG) rate based on a so-called driving force that accounts for controlling parameters affecting the crack propagation rate. That approach is either based on linear elastic fracture mechanics (LEFM) or elasto-plastic fracture mechanics (EPFM). LEFM mainly uses the stress intensity factor range (ΔK) to characterise FCG rate. The first and the most well-known ΔK-based model is the Paris' law [18] shows in Eq. (5.1):

$$\frac{da}{dN} = C(\Delta K)^m \tag{5.1}$$

where $\frac{da}{dN}$ is the FCG rate, and C and m are materials constants. Although Paris' law explains the fundamentals of fracture mechanics, it has significant shortcomings. One of the most important ones is that Paris' law cannot account for the mean stress or R-ratio, which is an important controlling parameter for the FCG rate. As a result, many researchers have tried to overcome that shortcoming. Such efforts are mainly based on the "crack-closure" concept and "unified approach". Crack-closure concept, introduced by Elber [20] and further developed by Newman [21], briefly states that the plastic deformation zone behind the crack tip tends to close the crack. Newman suggested that such a closing parameter is the missing part in the Paris' law and required to be quantified. The crack closure concept has received much interest and has been applied to characterize FCG rates in both the long crack (LC) and short crack (SC) regimes [24, 25, 27, 30-32, 34, 36, 38]. Unfortunately, the crack closure-based models have many constants required to be

determined by complicated calibrations. In addition, noticeable limitations have been observed in the case of the SC regime [13]. On the other hand, the unified approach or two-parameter driving force models, firstly introduced by Walker [41] and further improved by Vasudevan and Sadananda [44], briefly states that the maximum stress intensity factor (K_{max}) is required to be employed as the driving force in addition to the (ΔK). Unified approach has been received many modifications. However, one of the most recent and prominent ones is suggested by Noroozi et al. [46-48] as the UniGrow model. The UniGrow model shown in Eq. (5.2) can successfully determine the FCG rate for the LC regime and account for the missing effect of the R-ratio [48].

$$\frac{da}{dN} = C\left[\left(K_{max,tot}\right)^{p}(\Delta K_{tot})^{1-p}\right]^{\gamma} \tag{5.2}$$

Since the UniGrow model has shown a significant improvement in LEFM, it has been applied in many cases [55, 56]. Unfortunately, the UniGrow model cannot account for the SC regime [56]. The main reason for the limitations of both crack closure-based models and two-parameter driving force models is that ΔK is a LEFM parameter and cannot account for the plastic deformation zone around the crack tip. Plastic deformation zone around the crack tip under low stress levels, brittle materials, and in the presence of long cracks can be ignored. However, in the presence of relatively large-scale plasticity (e.g., in the case of the SC regime), an EPFM is needed. One of the most well-known EPFM parameters is J-integral introduced by Rice [79]. Dowling and Begeley [82] and Lamba [83] suggested that the J-integral can be used under cyclic loading and introduced ΔJ. Dowling and Begeley suggested that the ΔK in Eq. (5.1) can be replaced by ΔJ as an EPFM parameter. J-integral is the potential energy density release rate with respect to the crack extension under elastic state [79]. Tanaka [80] suggested that the ΔJ can be defined as a measure of energy dissipation to the heat around the crack tip during one cycle under elasto-plastic state. ΔJ- based models have received many interests to characterise FCG rate in both the LC and SC regimes [86-88]. The application of ΔJ-based models in the SC regime has been shown that such EPFM parameter has the potential to successfully account for SC regime as well [13, 86-88]. J and ΔJ can be determined based on either conventional method or more recent suggested method as equivalent domain integral method (EDI). Since it is possible to avoid dealing with the vicinity of the crack tip in EDI method, that approach has been received many interests by researchers [96-100]. ΔJ can be determined by analytical solution, experimental procedures, and finite element (FE) analyses [81]. Analytical and experimental techniques are limited to specific geometries [81]. On the other hand, FE analyses can be generalized for almost all of the geometries and cases [81, 91-93]. Unfortunately, the application of ΔJ in the characterization of FCG rate has been reported challenging and time-consuming [81, 89, 90]. Although EDI has facile the application of ΔJ, it is still considered a complex and significantly time-consuming approach to characterize FCG rate by means of ΔJ-based models in comparison with ΔK-based models. The reason is that a basic and straight-forward linear analyses is required to utilize ΔK for FCG characterization. However, a nonlinear and complicated elasto-plastic analysis is needed to determine elasto-plastic stress, strain and displacement fields around the crack tip and subsequently determine ΔJ based on those components [81].

The application of machine learning (ML) algorithms has spread in almost every fields in the recent years due to their promising potential to overcome many unsolved problems. Subsequently, those algorithms have received great interests among researchers to assess fatigue life of components and elasto-plastic mechanics. Any algorithm that is capable of detecting pattern(s) between the inputs and output(s) of a given dataset and subsequently establishing the

relationship(s) between them can be called an ML algorithm. One of the most well-known and extensively used ML algorithms is the neural network (NN). NN algorithms can be divided into artificial neural networks (ANNs), recurrent neural networks (RNNs), and convolutional neural networks (CNNs). ANNs have shown a noticeable potential to extract any pattern, nonlinear relationships included, through a given dataset. ANNs have been employed in different areas, such as material sciences [306-308], and solid mechanics [258, 259]. Since the FCG rate is a complicated function of many controlling parameters (e.g., mean stress, crack length, microstructure, mechanical properties of the material, geometry of specimen), ANN algorithms have been extensively used to reveal such complex functions. The majority of such researchers considered the FCG rate as the output and one or a few main controlling parameters as the inputs to characterize the FCG rate. For instance, Mohanty et al. [197] collected 195 experimental FCG rate data to investigate the effect of R-ratio on the FCG rate for aluminum alloys. The R-ratio, SIF range, and the maximum of SIF were chosen as the inputs. Subsequently, the FCG rate was selected as the output. The predictions of the suggested ANN algorithm showed an error of less than 5%. Mohanty et al. [200] used experimental FCG data to study the influence of mixed mode (I and II) overload on FCG rate for 7020 T7 and 2024 T3 aluminum alloys. The predicted residual fatigue life by the developed ANN model was reported to be in good agreement with the experimental data. Haque and Sudhakar [205] developed an ANN model to characterize corrosion-fatigue crack growth rate of dual phase (DP) steels. The input and output of the ANN model were SIF range and FCG rate, respectively. The results of predictions were in a good agreement with the experimental data. Similar researches can be found in the literature [212]. Mortazavi and Ince [298, 299] developed different ANNs to characterize FCG rates for both the SC and LC regimes for the first time. The experimental FCG rate data of Ti-6Al-4V titanium and 2024-T3 and 7075-T6 aluminum alloys were used to train the ANN models. The prediction results were in good agreement with the experimental data. Himmiche et al. [300] compared two types of ANNs (ELM and RBF-ANN) to characterize FCG rate in the SC regime. The prediction results showed a high potential of ANNs in the characterization of FCG rate even in the SC regime.

The application of ANNs has been proliferating in elasto-plastic mechanics [258, 259, 263, 264, 309]. The following reviewed literatures in the field of elasto-plastic mechanics should be distinguished as two different categories. First is the usage of NNs to establish the stress-strain behavior of material under elasto-plastic state. In other words, the input and output of NNs are the strain data and stress data, respectively. As a result, the aim of NNs application is detecting a function like f in Eq. (5.3). The superscript a refers to the actual elasto-plastic state. One may realize that in that application f is similar to the constitutive equations. Second is the application of NNs to establish the relationship between hypothetical elastic and actual elasto-plastic response of materials under loading. That being said, the hypothetical elastic stress and/or strain data are assigned as the input and the actual elasto-plastic stress and strain data are assigned as the output of the model. In this case, the aim is revealing a function like "g" in Eq. (5.4). The letter "e" refers to hypothetical elastic state.

$$\sigma^a = f(\varepsilon^a) \tag{5.3}$$

$$(\sigma^a, \varepsilon^a) = g(\sigma^e, \varepsilon^e) \tag{5.4}$$

Burghardt et al. [260] developed an ANN model to establish the relationship between elastic and elasto-plastic stress and strain in notch roots under uniaxial and multiaxial proportional loading. The results showed a noticeable potential for the suggested purpose. Kazeruni and Ince [261]

proposed the similar approach to predict the elasto-plastic stress-strain behavior of various materials based on their elastic response through an ANN algorithm. The suggested method showed a significant capability to predict the local elasto-plastic stress and strain in different positions of notch roots. Zhang and Mohr [262] suggested application of ANNs to detect the correlation of stress and strain under elasto-plastic state and isotropic hardening instead of constitutive equations. The results have been compared with the Von-Mises equation and promising agreement was observed. Huang et al. [310] performed a study to compare the potential of NNs with piecewise linear functions, radial basis functions, and radial basis function networks in order to detect the stress-strain behavior of materials. The observations showed that the application of NNs exceeds the other methods.

In addition to the ANNs, RNNs and CNNs have been applied for fatigue cracks and elasto-plastic mechanics. Gong et al. [311] used an RNN algorithm to study the effect of stop-hole diameters and loading angles on fatigue life and crack path under mixed-mode cyclic loading (mode I and II). The results were reported as encouraging to apply RNN algorithms for similar purposes. Zhang et al. [119] developed CNN models to estimate the fatigue life of components made of 316 austenitic stainless steel under fatigue, creep, and fatigue-creep conditions. The results were reported to be successful. Kamiyama et al. [304] suggested CNN algorithms to predict the development of fatigue cracks in thin metal films after 2000 cycles. The results showed a noticeable accuracy. Mozaffar et al. [265] compared the application of ANNs and RNNs to establish the path-dependent stress-strain relationship. The results showed that RNNs are superior from ANNs in that case. However, the number of data to train an RNN is dramatically larger than the one required for ANN training. In a similar study, Tancogne-Dejean et al. [266] and Wu et al. [267] developed RNNs to model path-dependent plasticity for the case of heterogenous materials.

RNNs and CNNs can be specified as higher levels of NN algorithms than ANN. However, ANNs are the most extensively used NN algorithms for fatigue life estimation [113]. One of the most important reasons for that is attributed to the fact that ANNs are more efficient and more straightforward to be applied. Since the primary goal of the present approach is to propose a time-efficient and facile method to determine ΔJ, ANN has been selected over RNN and CNN. A comprehensive review of NN applications for fatigue modeling can be found in the literature [113].

Considering the literature review discussed in the present section, employing a proper driving force like ΔJ is vital to account for relatively large plastic deformation near the crack tip for FCG characterization. However, the application of ΔJ has been reported to be difficult and dramatically time-consuming regarding the required elasto-plastic analysis. On the other hand, the application of ANNs for fatigue modeling has been reported very promising. The authors [309] recently suggested a time-efficient approach to determine the J-integral. The authors verified that robust ANNs can establish the relationship between the elastic and elasto-plastic response of the material around the crack tip under monotonic loading. As a result, J-integral can be calculated through an elastic FE analysis rather than complicated elasto-plastic analyses. In this chapter, the authors apply the same approach under cyclic loading in order to determine ΔJ through an elastic FE analysis. The good agreement between predicted ΔJ by ANN models and the ones calculated based on elasto-plastic FE analyses shows that the suggested approach facile the application of ΔJ for FCG characterization.

5.3. Modeling approach

In the present work, a time-efficient method is suggested to calculate ΔJ for a 2D cracked body specimen. In the first step, two separate elastic and elasto-plastic FE analyses have been developed to determine elastic and elasto-plastic stress, strain, and displacement fields around the crack tip under cyclic loading. The developed models have been operated for different crack sizes to provide a sufficiently large and comprehensive dataset. The dataset in the present study refers to the combination of elastic stress, strain, and displacement fields ($\sigma_{ij}^{e}, \varepsilon_{ij}^{e}, u_i^{e}$) as the input and their corresponding actual elasto-plastic stress, strain, and displacement fields ($\sigma_{ij}^{a}, \varepsilon_{ij}^{a}, u_i^{a}$) as the output. Then the dataset was divided into training, validation, and testing data. In the second step, three separate ANN models are developed to establish the relationship between the hypothetical elastic and actual elasto-plastic stress, strain, and displacement fields in the vicinity of the crack tip. The training and validation data in the first step were employed to train the ANN models. In the third step, an in-house model was developed to calculate ΔJ based on the EDI method as a function of stress, strain, and displacement fields around the crack tip. In the last step, the developed EDI method has been used to calculate ΔJ based on the elasto-plastic stress, strain, and displacement fields predicted by ANN models and calculated by elasto-plastic FE analyses for the testing data. Subsequently, the values of ΔJ based on the two approaches have been compared. The first two steps are schematically shown in Figure 5.1, and the two different approaches are schematically shown in Figure 5.2. Figure 5.2 illustrates how the present approach avoids dealing with complex non-linear elasto-plastic analyses and monotonic and cyclic plastic deformation zones around the crack tip for the calculation of elasto-plastic ΔJ. It should be mentioned that the elasto-plastic FE analyses should be operated for particular crack sizes in order to train the ANN models. However, after the training, only elastic analyses are required to determine ΔJ for any crack length. All of the developed models are discussed in detail in the following sections.

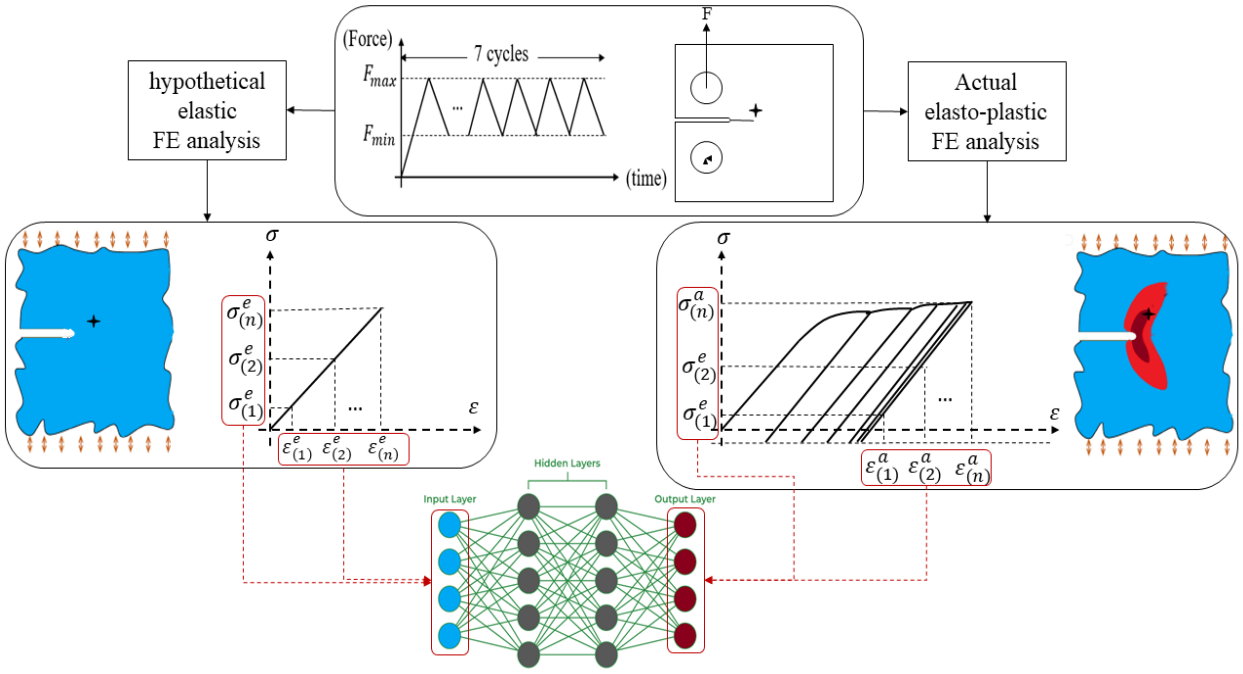

Figure 5.1 Schematic of the first two steps of present approach.

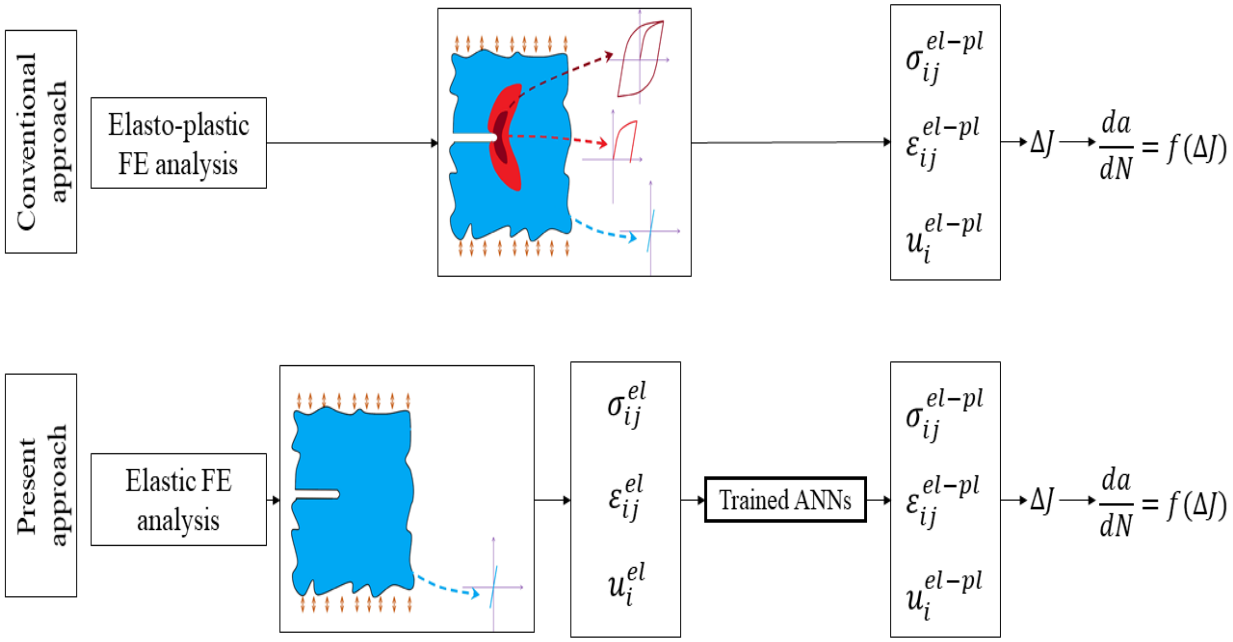

Figure 5.2 Schematics of conventional and present approach for ΔJ.

5.3.1. Finite element modeling

The elastic and elasto-plastic FE analyses, which aimed to calculate the stress, strain, and displacement fields in the vicinity of the crack tip, were conducted using the Abaqus commercial FE software package. FE models were developed using the Abaqus script file in Python to efficiently extract and process numerical data and easily operate the models for different crack sizes. The script file includes various parts such as designing the compact tension (CT) notched specimen, specification of material properties, assigning loads and boundary conditions, and mesh generation. In addition, the script file contains the extraction of FE models' results from the output databases (ODB) file generated by Abaqus. That being said, the script file also contains post-processing code to extract stress, strain, and displacement components of specific elements and nodes around the crack tip in the desired configuration for further use in ANN models. The structure of extracted data in order to feed to the ANNs is discussed in detail in section 5.2.3. The specimen dimensions, reference points (P_1 and P_2), boundary conditions are schematically shown in Figure 5.3.

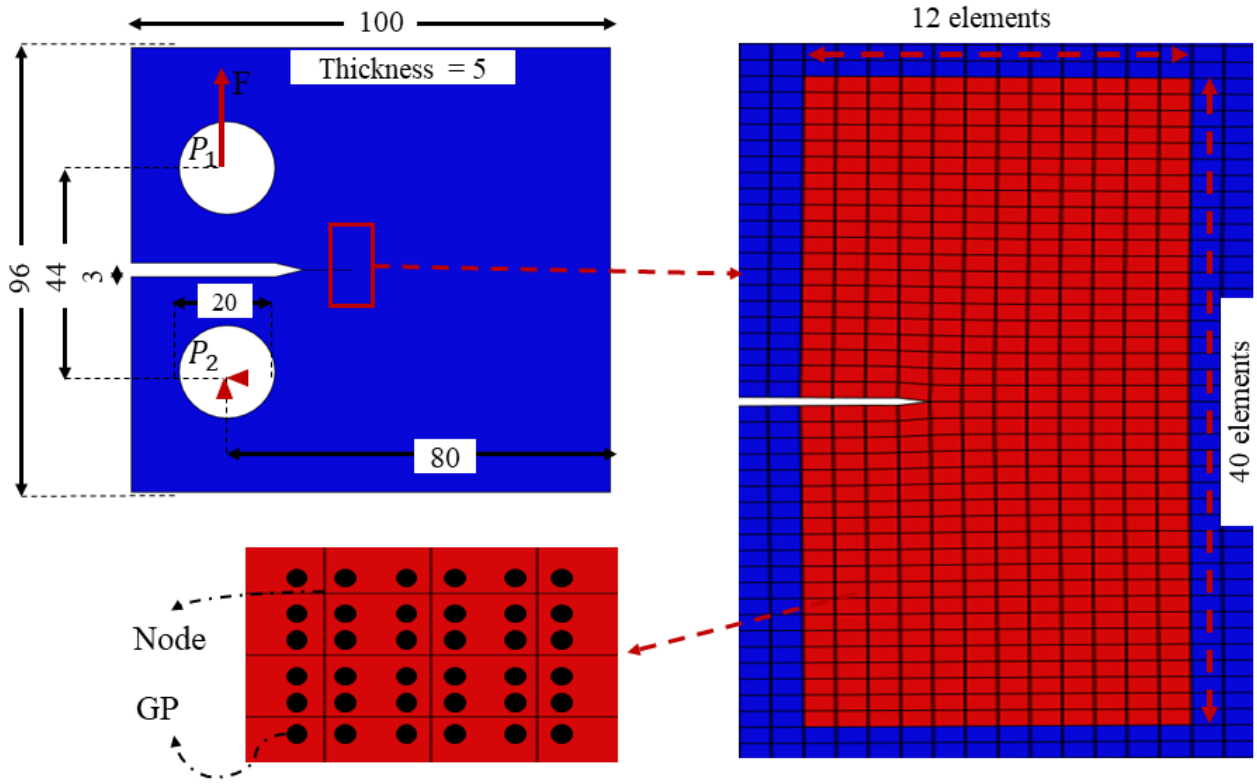

Figure 5.3 CT specimen dimensions, chosen area around the crack tip for data extraction, and nodes and GPs of elements.

As shown in Figure 5.3, 480 (12×40) elements around the crack tip have been chosen to extract the data to train the ANN models. In addition, the nodes of elements and the (Gauss points) GPs are schematically shown in Figure 5.3. It is crucial to distinguish the nodes and the GPs due to the fact that displacement fields are extracted from the nodes and the stress and strain fields are extracted from GPs in a FE analysis. The material used in this study is the 304 stainless-steel with the module of elasticity, Poisson's ratio, and yield stress of 195100 MPa, 0.267, and 206 MPa, respectively. The elastic-plastic model has been chosen as bilinear isotropic hardening. The specimen dimensions, material properties, mesh characteristics, reference points, and boundary conditions are kept the same as the FE model discussed in detail in section 4.2.1. The only difference between the present model in this chapter and the one discussed in the previous chapter is the loading conditions. As mentioned before, the authors investigate the proposed approach under monotonic loading in the literature [309], whereas this paper applies that under cyclic loading. The different cyclic loading conditions are specified in Table 5.1 and schematically shown in Figure 5.4. As shown in Figure 5.4, each loading half cycles has been divided to 50 increments. Since seven cycles of loading has been investigated in the present study, 350 (7×50) increments can be used to extract data to train the ANN model. As Wang et al. [81] and the current authors [309] investigated, 25 increments for each loading half cycle is adequate for accurate FE analyses. The number of increments is crucially essential to accurately calculate strain energy density (ΔW under cyclic loading and W under monotonic loading). The adequate number of increments is discussed in detail in the previous chapter. In this chapter 50 increments have been chosen to increase the number of data and subsequently the accuracy of ANN models.

Table 5.1 Loading conditions

Loading case	F_{min}(kN)	F_{max}(kN)	R-ratio	Number of cycles
1	0.8	8.0	0.1	3
2	1.47	7.33	0.2	3
3	2.03	6.77	0.3	3
4	2.51	6.29	0.4	3
5	2	20	0.1	7

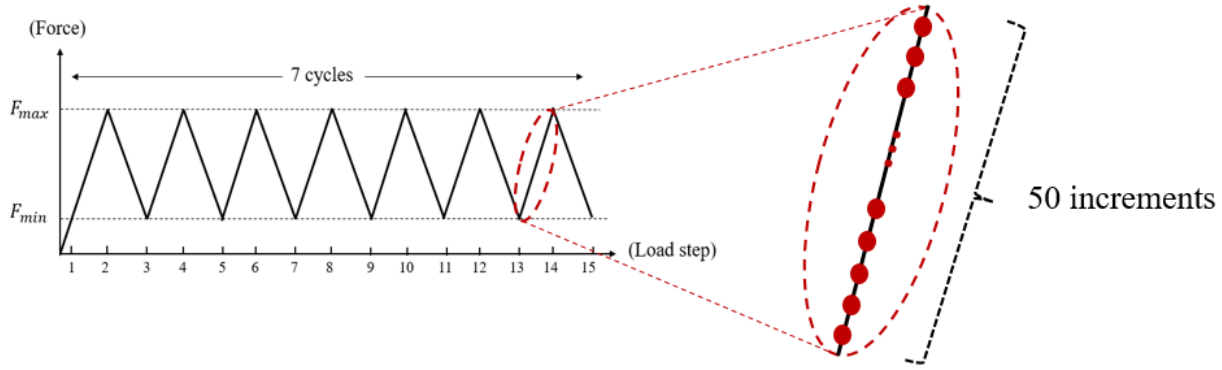

Figure 5.4 Number of cycles and increments in the FE analyses.

5.3.2. Determination of ΔJ based on equivalent domain integral method

ΔJ is a line integral in a 2D state that can be considered a surface integral according to Green's theorem, as shown in Eq. (5.5).

$$\Delta J = \int \left(\frac{\partial \Delta W}{\partial x} - \frac{\partial}{\partial x_j} \left(\Delta \sigma_{ij} \frac{\partial \Delta u_i}{\partial x} \right) \right) dA \tag{5.5}$$

where dA is an infinitesimal area element, Δu is the displacement vector corresponding to the maximum and minimum load under cyclic loading, ΔW is the difference between strain energy density corresponding to the maximum and minimum load under cyclic loading, and x (x_1) and y (x_2) are the cartesian axes. The crack is parallel to the x-axis. Equation (5.5) refers to the calculation of ΔJ based on the conventional method. However, it is possible to rewrite that equation based on the EDI method, as shown in Eq. (5.6).

$$\Delta J = \int_A \left(\Delta \sigma_{ij} \frac{\partial \Delta u_j}{\partial x} - \Delta W \delta_{1i} \right) \frac{\partial q}{\partial x_i} dA \tag{5.6}$$

where δ is Kronecker delta, and q is the weight function of coordinate axes. It should be pointed out that A in Eq. (5.5) corresponds to the area schematically shown in Figure 5.5a), whereas A in Eq. (5.6) is corresponded to the area schematically shown in Figure 5.5b). One may realize that

the privilege of the EDI method over the conventional method is avoiding dealing with the area relatively closer to the crack tip. One of the usages of such a method is that no extremely fine mesh is required around the crack tip to perform FE analyses. For a 2D problem, q has a value of one at the inner boundary and linearly decreases to 0 at the outer boundary.

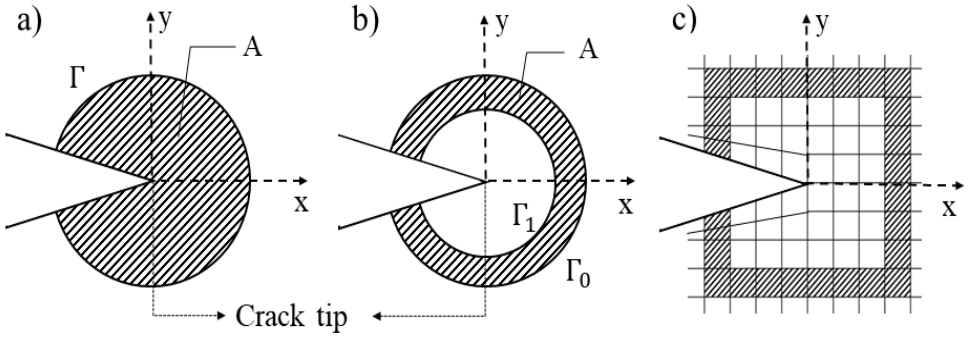

Figure 5.5 Different methods of ΔJ calculation. A) Conventional method, b) EDI method, c) EDI method in a FEM-based model [309].

The expansion of Eq. (5.6) can be written as follows:

$$\Delta J = \int_A \left[\left(\Delta\sigma_{11} \frac{\partial \Delta u_1}{\partial x} + \Delta\sigma_{12} \frac{\partial \Delta u_2}{\partial x} - \Delta W \right) \frac{\partial q}{\partial x} + \left(\Delta\sigma_{12} \frac{\partial \Delta u_1}{\partial x} + \Delta\sigma_{22} \frac{\partial \Delta u_2}{\partial x} \right) \frac{\partial q}{\partial y} \right] dA \qquad (5.7)$$

As mentioned earlier, Abaqus has been employed to perform the FE analyses. Since ΔJ is defined based on the deformation theory of plasticity, the calculation of ΔJ is not embedded as a built-in functionality in Abaqus. As a result, an in-house model has been developed to extract the results of FE analyses from ODB files and determine ΔJ based on Eq. (5.7). The in-house model directly extracts $\Delta\sigma_{ij}$, $\frac{\partial \Delta u_1}{\partial x} = \Delta\varepsilon_{11}$. However, other parameters of Eq. (5.7): $\frac{\partial \Delta u_2}{\partial x}$, ΔW, and $\frac{\partial q}{\partial x_i}$ should be determined in the in-house model as another part of the post-processing in the Abaqus script file discussed earlier. It should be pointed out that the developed in-house model is developed by Python, so it can directly be employed to calculate ΔJ based on the ANN predictions discussed in the following sections. Equation (5.7) shows that the ΔJ is a function of stress, strain, and displacement field around the crack tip.

5.3.3. Artificial neural networks models

Artificial neural networks (ANNs) are a type of machine learning algorithms inspired by the structure and function of biological neurons in the human brain. They are used for various applications, including function approximation. As schematically shown in Figure 5.6, the basic structure of an ANN consists of an input layer, one or more hidden layers, and an output layer. Each layer contains one or more nodes, also called neurons. The input layer receives the input data, and the output layer produces the output. The hidden layers perform calculations on the input data, transforming it into a form that can be used by the output layer. Each neuron in an ANN receives input from other neurons or the input data, performs a mathematical operation on the input, and produces an output. The output of each neuron is typically passed through an activation function, which determines whether the neuron should fire or not. The activation function introduces nonlinearity into the model, allowing it to approximate complex functions. The value of each

neuron may be multiplied by a weight (w) which is between 0 to 1. The higher value of the weight shows the greater influence of that neurons on the final output. Then the result may be added to a bias (b) and transferred to the activation function of the next neuron in the next hidden layer. The weights and biases of the connections between neurons are adjusted during training to minimize the difference between the actual output of the ANN and the desired output. ANNs can be used for function approximation by training the network on a set of input-output pairs. The network learns to approximate the underlying function that maps the input to the output. During training, the biases and weights in an ANN are updated using a process called backpropagation. Backpropagation is an optimization algorithm that adjusts the biases and weights to minimize the difference between the predicted output of the network and the actual output. The process begins with the forward pass, where the input data is passed through the network, and an output is produced.

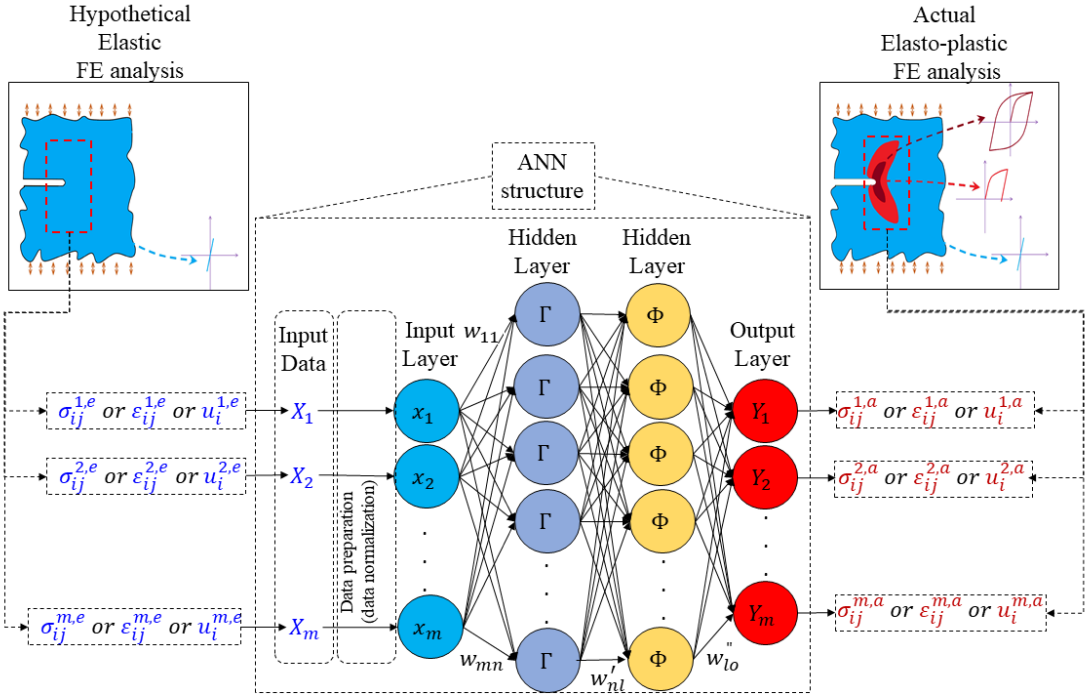

Figure 5.6 Schematic of developed ANN structure and the feeding dataset.

This output is then compared to the desired output, and the difference between the two is calculated using a loss function. The backpropagation algorithm then works backwards through the network, calculating the contribution of each neuron and connection to the overall error. This contribution is then used to update the biases and weights in each neuron, using a technique called gradient descent. The gradient descent algorithm works by taking the partial derivative of the loss function with respect to each weight and bias in the network. The gradient gives the direction of the steepest ascent, so to minimize the loss function, the weights, and biases are updated in the opposite direction of the gradient. The size of the update is controlled by a learning rate, which determines how much to change the weights and biases at each iteration. If the learning rate is too high, the network may converge too quickly and fail to find the optimal solution. If the learning rate is too low, the network may converge too slowly and take too long to find the optimal solution. The backpropagation algorithm is repeated over multiple iterations or epochs until the error between

the predicted output and the desired output is minimized. At this point, the network has learned to approximate the underlying function that maps the input to the output and can be used to predict new data. Three different types of data are employed to develop a well-trained ANN model. Training data is the initial dataset used to train the neural network. It is used to teach the network how to map inputs to outputs, forming the basis of the network's knowledge. The training data is used repeatedly to adjust the weights and biases of the network until it achieves a desired level of accuracy. Verification data is used once the network has been trained on the training data. It is crucial to evaluate its performance on a separate set of data to ensure that it has not overfit to the training data. The validation data is used to fine-tune the hyperparameters of the network, such as the learning rate. This helps to prevent the network from overfitting to the training data and to improve its generalization performance. After the network has been trained and validated, it is evaluated on a separate data set called testing data. The testing data is used to evaluate the network's performance on new, unseen data and to estimate its generalization performance. This is an essential step in assessing the quality of the network's performance and determining whether it is ready for deployment.

As discussed in the previous section, elasto-plastic stress, strain, and displacement fields are required to determine ΔJ. As a result, three separate ANN models are developed to predict those fields based on hypothetical elastic stress, strain, and displacement fields. Another possible approach would be training one ANN model to predict all three desirable fields. However, the determination of ΔJ based on ANN predictions is only one application of machine learning algorithms in this field. Developing three distinguished ANN can be employed for other problems, such as when only stress, strain, or displacement is needed. In addition, relationships between stress and strain (constitutive equation) and strain and displacement (Kinematic rules) may assist a single ANN model for the present purpose. Developing three separate ANN models avoid making use of such relationships and merely results in the relationships between elastic and elasto-plastic states.

As shown in Figure 5.3, 480 elements around the crack tip have been chosen to extract the data in order to feed to ANN models. According to the element type used in the FE analysis, each element has four GPs. As shown in Figure 5.4, the FE analyses have 350 (7×50) increments. However, only the data corresponding to the 50 increments of the last loading half-cycle has been employed to feed to the ANN models. The reason is to evaluate the proposed approach to predict ΔJ through the ANN models trained based on only the last cycle for the other cycles as well. The FE analyses under elastic and elasto-plastic states have been operated for 10, 6, and 12 different crack sizes to generate the training, validation, and testing data, respectively, as shown in Table 4.2. As a result, the dataset in the present study includes 960,000 ($4^{GP} \times 480^{element} \times 50^{increment} \times 10^{crack\ size}$) data for stress and strain. Since the FE analyses have been operated based on plain strain condition, each GP has four components for stress and three components for the strain. It should be pointed out that the displacement data has been extracted from the nodes (not GPs). As a result, the number of training data for the case of displacement filed is 268,500. Three separate ANN models have been developed to predict elasto-plastic stress, strain, and displacement fields around the crack tip based on elastic ones. That being said, the elastic components of stress ($\sigma_{11}^{i,e}, \sigma_{22}^{i,e}, \sigma_{33}^{i,e}, \sigma_{12}^{i,e}$), strain ($\varepsilon_{11}^{i,e}, \varepsilon_{22}^{i,e}, \varepsilon_{12}^{i,e}$), and displacement ($u_1^{i,e}, u_2^{i,e}$) have been adopted as the input, and their corresponding elasto-plastic stress ($\sigma_{11}^{i,a}, \sigma_{22}^{i,a}, \sigma_{33}^{i,a}, \sigma_{12}^{i,a}$), strain ($\varepsilon_{11}^{i,a}, \varepsilon_{22}^{i,a}, \varepsilon_{12}^{i,a}$), and displacement ($u_1^{i,a}, u_2^{i,a}$) have been assigned as the out put of the ANN models. For instance, the ANN model

trained in the case of stress field has the input of (X_i) and output (Y_i) as shown in Figure 5.6 and expressed in Eq. (5.8)-(5.9) as follows:

$$X_i = (\sigma_{11}^{i,e}, \sigma_{22}^{i,e}, \sigma_{33}^{i,e}, \sigma_{12}^{i,e}) \tag{5.8}$$

$$Y_i = (\sigma_{11}^{i,a}, \sigma_{22}^{i,a}, \sigma_{33}^{i,a}, \sigma_{12}^{i,a}) \tag{5.9}$$

As mentioned earlier, the superscript i in the case of stress varies between 1 to 960,00. However, that varies between 1 to 268,500 in the case of displacement. The superscript "e" and "a" refer to the elastic and actual elasto-plastic states, respectively. The format and the number of data for stress, strain, and displacement fields have been shown in Figure 4.7- Figure 4.9. As shown in Eq. (5.7), the derivative of displacement with respect to the coordinate axis is required to determine the ΔJ. As a result, the authors employed two different approaches to predict elasto-plastic displacement fields under monotonic loading in the literature [309] (Chapter 4). The first one, which has also been used in the present paper, is using the displacement fields under elastic and elasto-plastic as the input and output data for training the ANN model. The second one uses the displacement derivative under each state as the input and output data. The authors claimed that the accuracy of displacement prediction is lower than the ones in the case of stress and strain fields due to the smaller number of training data. If the first approach is applied, the error of displacement prediction will result in a higher error for the derivative of displacement. In other words, the error accumulatively increases through the sequence of steps as displacement predictions, taking derivative, and calculation of ΔJ. That is why the authors suggested the second approach in the previous study [309] (Chapter 4). However, in the present study (chapter), 50 increments (instead of 25 in the literature [309] (Chapter 4)) have been chosen to provide more data. As discussed in the result and discussion section, this number is large enough to provide adequate data even in the case of displacement fields. With this in mind, only the first approach has been employed in the present paper, and ΔJ calculation can be conducted based on the displacement fields directly predicted by the developed ANN model. The number of hidden layers, the number of neurons in each hidden layer, activation functions in each hidden layer, and learning rates , loss function, and data preparation method of the developed ANN models are kept the same as the ones used in the proposed approach in the case of monotonic loading shown in Table 4.3. Keras with TensorFlow is adopted in order to train the suggested ANN model in the present study.

5.4. Results and discussion

The results of the present chapter can be discussed in three distinguished parts. The first part is verifying the in-house model in order to determine the ΔJ around the crack tip based on the EDI method. The second part compares the stress, strain, and displacement fields predicted by developed ANN models with the ones determined by elasto-plastic FE analyses around the crack tip. The last part compared the ΔJ values predicted by the suggested approach against those determined by the FE analyses under different loading conditions.

5.4.1. Determination of elasto-plastic ΔJ based on the in-house equivalent domain integral model

In the present section, ΔJ values determined by the developed in-house model are compared with the ones calculated by Wang et al. [81]. All of the FE analysis parameters used in the present study are the same as the ones utilized by Wang et al., except for the element size and pattern around the

crack tip. A detailed discussion has been presented in the literature [309] (Chapter 4) on the element size when it comes to the EDI method in the current approach. The main point of that discussion shows that implementing the element size of 0.1 mm and 0.004 mm around the crack tip results in the same ΔJ values in the EDI method. The reason is the fact that the EDI method can be regarded as a mesh-independent approach [102]. As discussed earlier, the in-house model has been developed through Python and can be compiled as a post-processing calculation by Abaqus. The present in-house model has already been verified under monotonic loading in the literature [309] (Chapter 4). In the literature [309] (Chapter 4), the results of the in-house model have been compared with the results of Wang et al. [81] study and the built-in functionality of Abaqus, which can determine J-integral based on the conventional method under monotonic loading. Since the J-integral is defined based on the deformation theory of plasticity, it cannot be determined during unloading. As a result, the built-in functionality of Abaqus is not able to determine the ΔJ under cyclic loading. With all these in mind, the results of the in-house model is only compared with the ones of Wang et al. [81] under cyclic loading. The ΔJ values as the results of present in-house model have been compared with the ones in the literature under four different R-ratio as shown in Figure 5.7. Figure 5.7a) to Figure 5.7d) are corresponded to the R-ratio of 0.1, 0.2, 0.3, and 0.4 and the loading case 1 to 4 in Table 5.1, respectively. The difference between the results of the in-house model and the results of Wang et al. is not higher than -6.2%, -4.6%, -2.5%, and 4.3% in Figure 5.7a) to Figure 5.7d), respectively. It should be pointed out that the loading conditions 1 to 4 presented in Table 5.1 has been used in the study of Wang et al. [81].

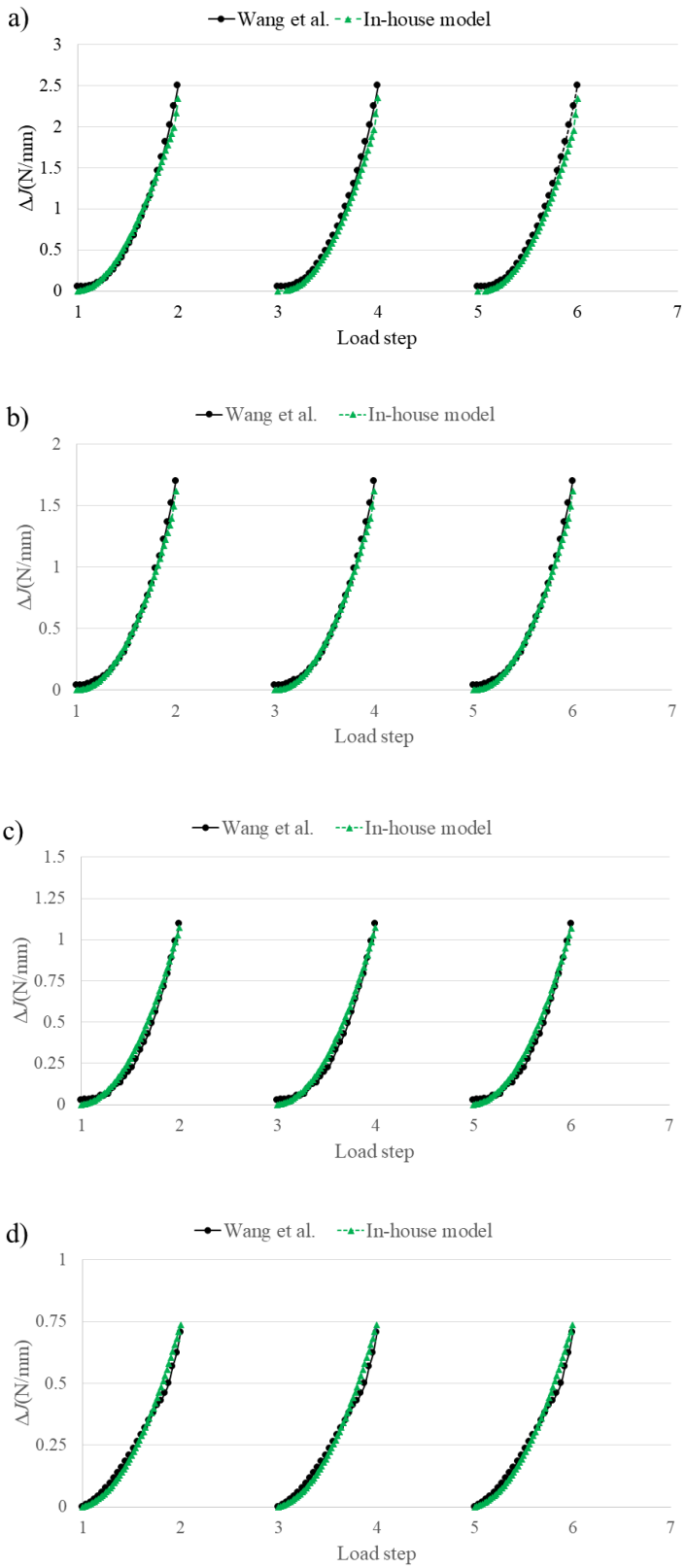

Figure 5.7 Comparison of ΔJ values under cyclic loading for a) R=0.1, b) R=0.2, c) R=0.3, and d) R=0.4.

5.4.2. ANN predicted stress, strain, and displacement fields under cyclic loading

In the present section, the ANNs predicted stress, strain, and displacement fields around the crack tip are compared with the ones determined through elasto-plastic FE analyses. As discussed earlier, three different types of data are used during the development of a well-trained ANN model: training, validation, and testing data. Since the primary purpose of developing an ANN model is to be applied for the unseen cases, only the results of testing data (for the crack size of 2.5, 5.5, and 8.5 mm) are discussed in this section. The percentage of error (POE) is used to quantify the accuracy of the developed models.

As mentioned earlier, overfitting and underfitting are the most common problems in ANN development. Overfitting occurs when the model is too complex and is trained too well on the training data to the point where it memorizes the training data instead of learning the underlying patterns. As a result, the model performs well on the training data but poorly on new, unseen data. This can happen when the model has too many parameters or when the training data is too small. On the other hand, underfitting occurs when the model is too simple and is unable to capture the underlying patterns in the data. As a result, the model performs poorly on both the training data and new, unseen data. This can happen when the model is too constrained or when the training data is insufficient. A few ways exist to determine whether a trained model has overfitting or underfitting issues. High training accuracy but low validation accuracy, a significant difference between training and validation accuracy, and/or poor performance on new data are the signs of overfitting problems. On the other hand, low training accuracy, low validation accuracy, and/or poor performance on training and testing data are the witnesses of the underfitting issue for a trained model. The performance of all three trained ANN models for testing data is investigated in detail in this section. In addition, the behavior of increasing accuracy (decreasing the MSE) for both the training and validation data has been monitored during the training process to ensure the absence of those issues in the present study. Such monitoring has been shown in Figure 5.8 for the ANN model developed to predict the elasto-plastic stress field.

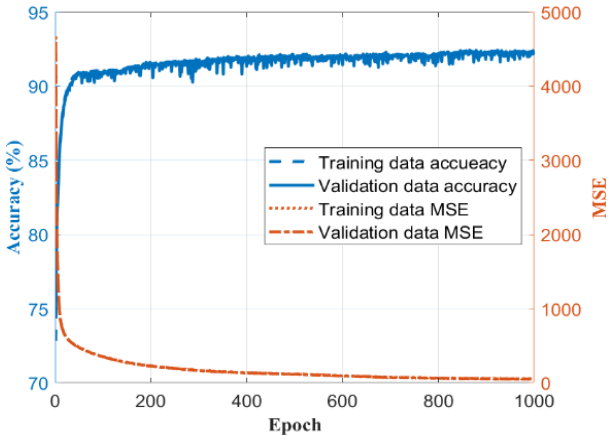

Figure 5.8 Accuracy and MSE values during training for validation and testing data for training the ANN model to predict stress distribution.

As shown in Figure 5.8, the accuracy (or MSE) graph for training and validation data are collapsed onto each other and reach a relatively high value (or low value) in the last epochs that guarantee the absence of overfitting and underfitting for the trained model. The same behavior has been

observed in the case of strain and displacement fields. There are two differences between Figure 5.8 (under cyclic loading) and Figure 4.14a) (under monotonic loading). First is the number of required epochs to reach the minimum of MSE, which is 1000 epochs for cyclic loading (see Figure 5.8) and 200 epochs for monotonic loading (see Figure 4.14a)). Second is the maximum accuracy which is 92 to 93% for cyclic loading and 98% for monotonic loading. The reason for the both differences is attributed to the fact that the number of data used in the case of cyclic loading is almost twice larger than the one used under monotonic loading. Also, predicting stress, strain, and displacement fields around the crack tip under cyclic loading is significantly more challenging for the ANN than predicting those under monotonic loading. The residual stress as the result of each cycle dramatically affects the stress, strain, and displacement fields of the next cycle, especially for the initial increments of each half-loading cycle. There is no such residual stress under monotonic loading. Figure 5.9 shows the stress field around the crack tip predicted by the developed ANN model and determined by elasto-plastic FE analysis for the crack size of 8.5 mm (as testing data) under loading case 5 described in Table 5.1 for the last increment. In all of the contours in the present paper, the crack tip is at the origin of the coordinate system, and the crack is parallel to the x direction. As shown in Figure 5.9a) and b), the developed ANN model can appropriately predict the distribution of σ_{11} around the crack tip. Figure 5.9c) shows that the POE of the developed ANN model for this case is not beyond -20%. However, the POE of such relatively high error are corresponded to only a few GPs (e.g., two GPs approximately located at x=0.2 & y=0). However, the majority of POEs are less than -15%. Figure 5.10- Figure 5.11 show the σ_{22} and σ_{33} around the crack tip under loading condition 5 in Table 5.1 for the crack length of 8.5 mm and the last increment. Figure 5.10a) and b) and Figure 5.11a) and b) show that the developed ANN model can properly predict the distribution of second and third components of the stress tensor. Figure 5.10c) and Figure 5.11c) show that the POE for the σ_{22} and σ_{33} is in the range of -10 to +6% and -14 to + 2%. As shown in Figure 5.10c) and Figure 5.11c), the relatively higher POE occurs at a small number of GPs. Figure 5.12 shows the capability of the developed model to predict the shear stress (σ_{12}). Regarding Figure 5.12a) and b), the developed ANN model can predict the shear stress distribution around the crack tip. Figure 5.12c) shows that the POE, in this case, is between -25 to + 20%, which is relatively higher in the case of normal stresses in Figure 5.9- Figure 5.11. Similar to the normal stresses, only the minority of GPs show relatively high POE close to -25 % or 20%. In addition, the positions having relatively higher POE show a particular pattern in the case of shear stress. As shown in Figure 5.12c), most GPs with relatively higher POE are located at the bisector of the first and fourth quadrant of the coordinate system. The reason is that those locations correspond to the maximum stress gradient in the case of shear stress. As a result, the number of data in that range of stress is smaller than the other ones. The other important point is that stress fields in the case of normal stresses are symmetric (the x-axis is the axis of symmetry). However, the sign of values is different in the case of shear stress. That being said, the number of data in the case of shear stress is half that of normal stresses. As a result, the accuracy is relatively lower for the shear stress. The other point is the difference between the accuracy of shear stress under cyclic loading (investigated in the present paper) and the one under monotonic loading (studied in the literature [309] (Chapter 4)). The highest POEs at the bisector of the first and fourth quadrant of the coordinate system are around $\pm$60% under monotonic loading (see Figure 4.18c)). However, those values are around $\pm$20% under cyclic loading. The reason is attributed to the fact that each loading half-cycle has been divided into 50 increments for cyclic loading, while the number of increments under monotonic loading was 25. As a result, the number of data available for training the ANN model is larger for the cyclic loading.

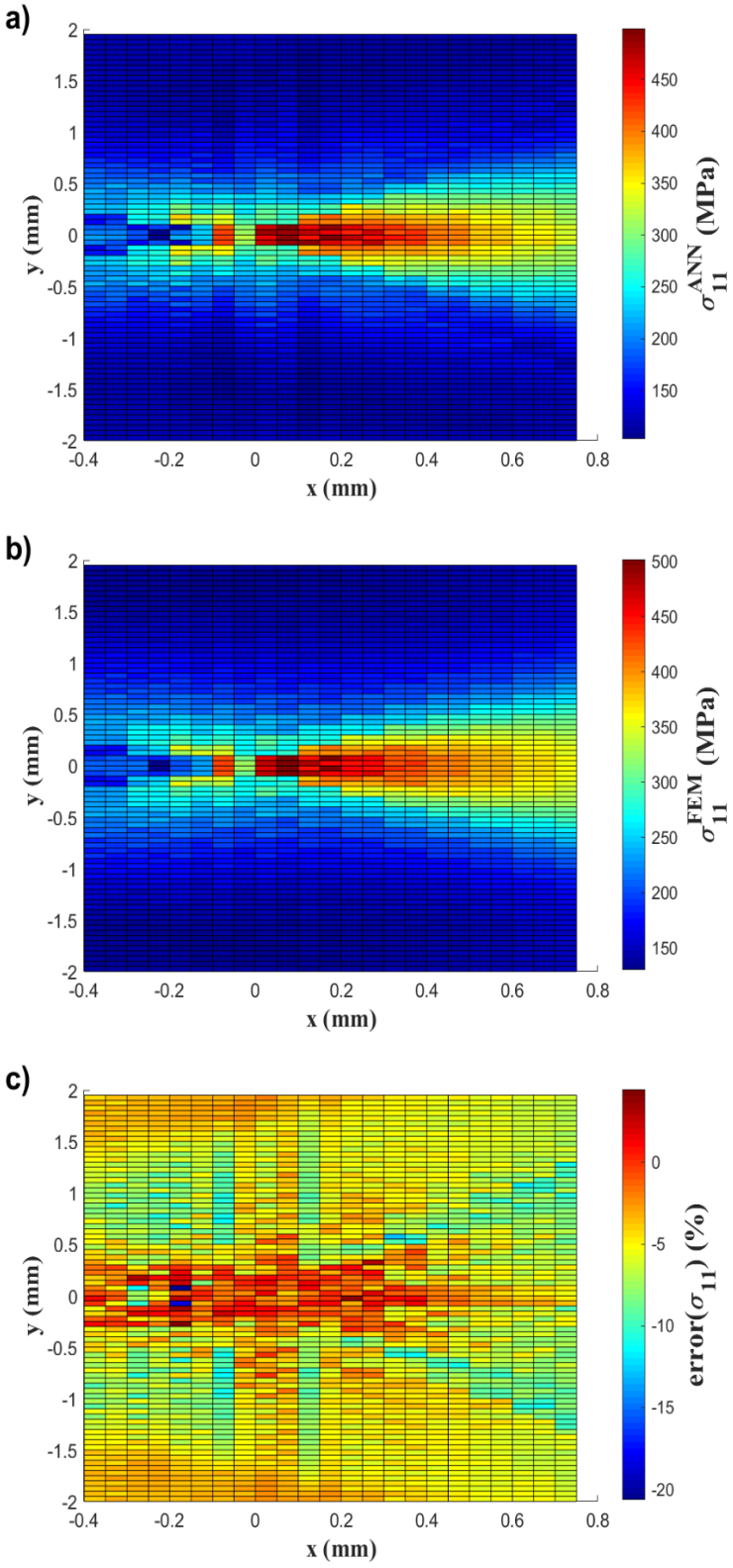

Figure 5.9 σ_{11} stress field for a = 8.5 mm and increment 50 and cycle 7th, loading case 5, a) ANN prediction, b) FE results, c) prediction error.

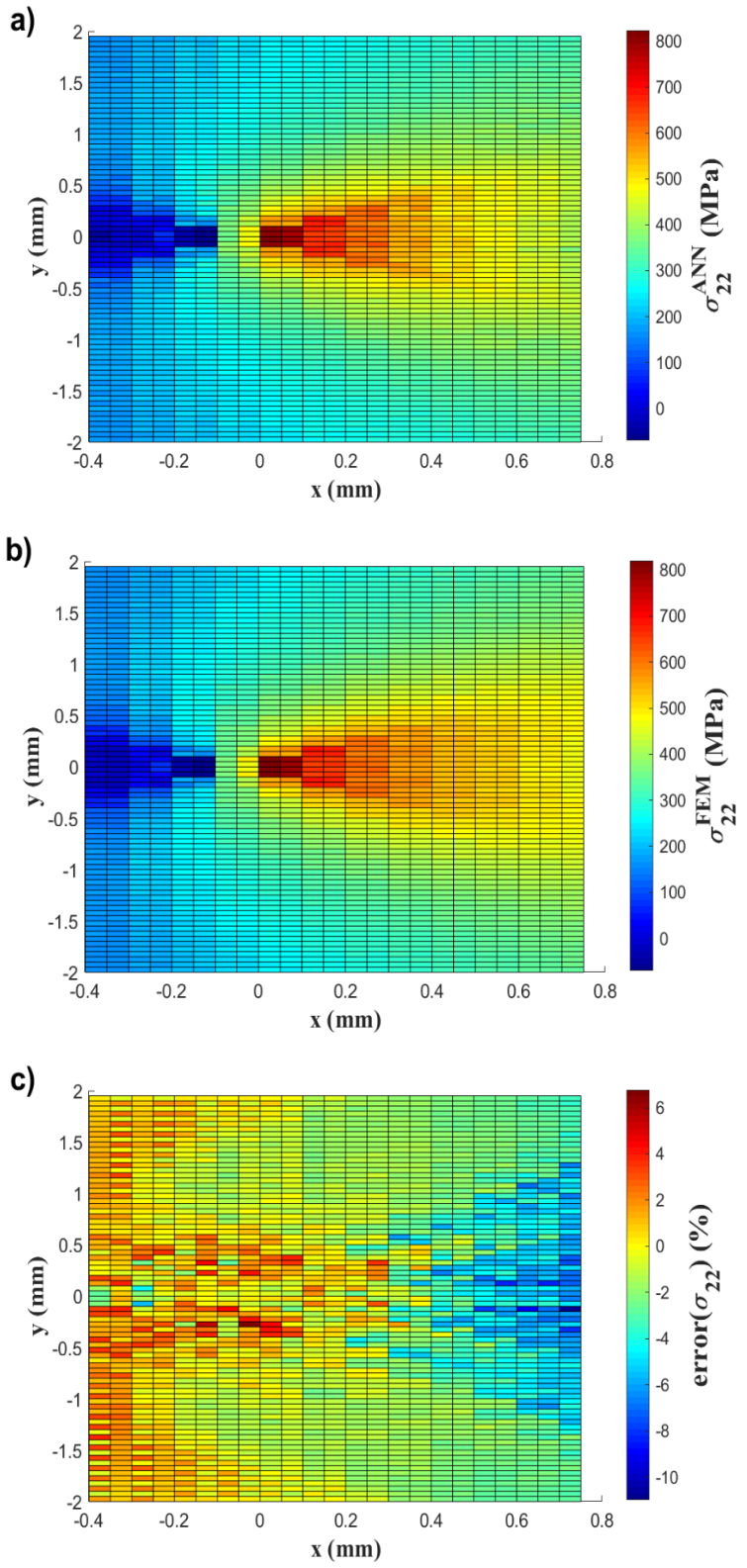

Figure 5.10 σ_{22} stress field for a = 8.5 mm and increment 50 and cycle 7th, loading case 5, a) ANN prediction, b) FE results, c) prediction error.

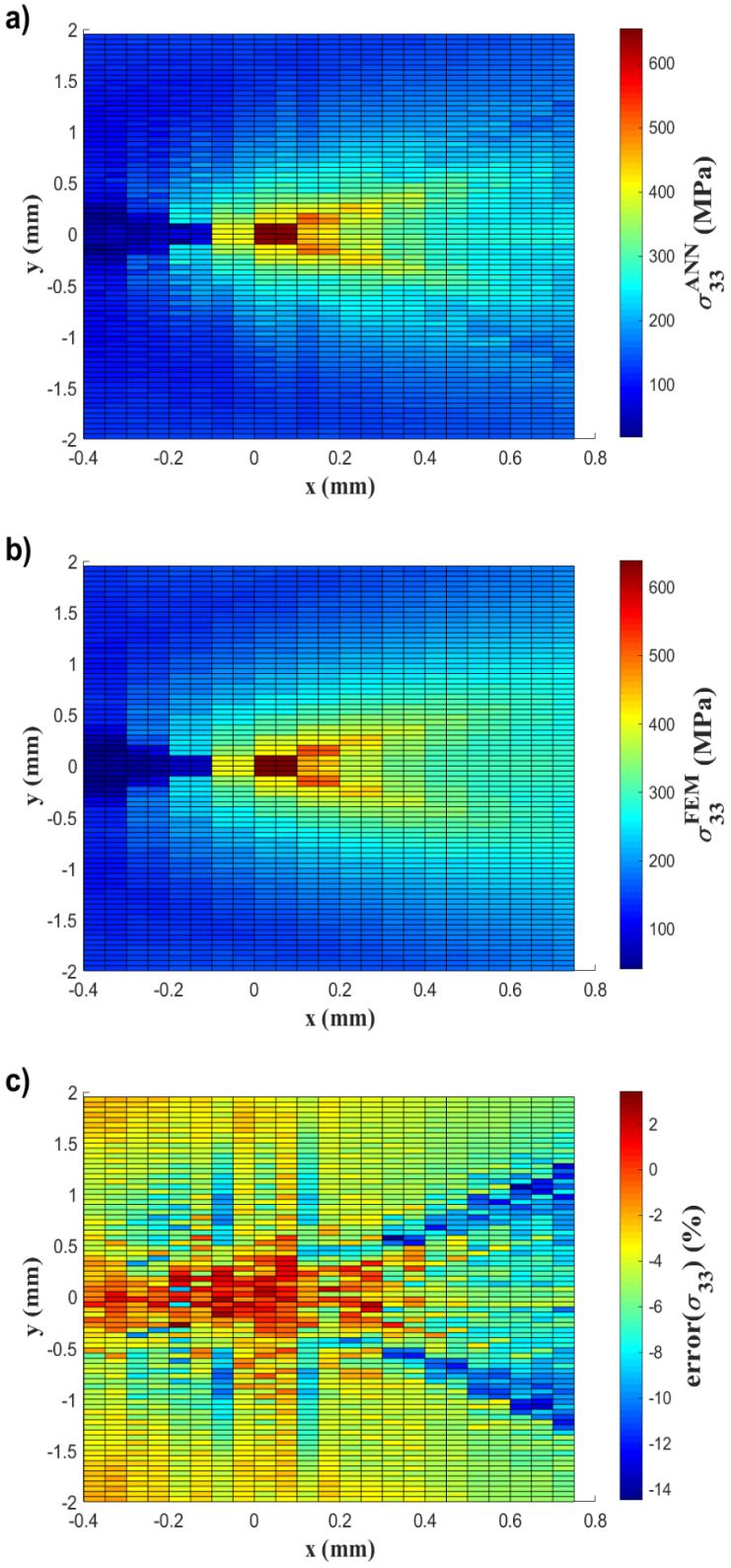

Figure 5.11 σ_{33} stress field for a = 8.5 mm and increment 50 and cycle 7th, loading case 5, a) ANN prediction, b) FE results, c) prediction error.

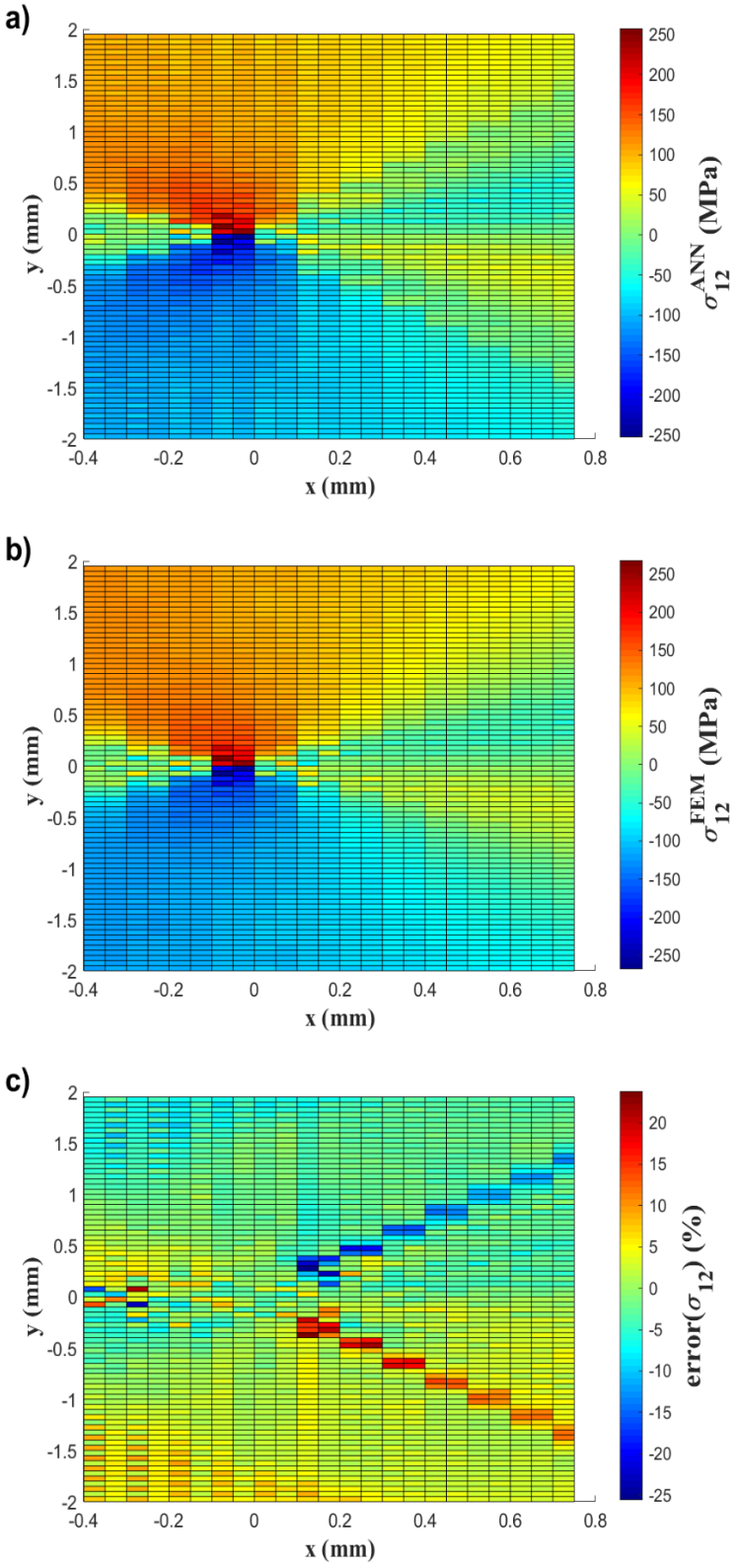

Figure 5.12 σ_{12} stress field for a = 8.5 mm and increment 50 and cycle 7th, loading case 5, a) ANN prediction, b) FE results, c) prediction error.

Although stress prediction under cyclic loading is more challenging for the developed ANN model, the accuracy of the developed ANN model under cyclic loading is higher than the one under monotonic loading for the σ_{12}. It should be reminded that the accuracy of stress prediction under cyclic loading is lower than the one under monotonic loading if all of the components of the stress tensor and all of the GPs are taken to account (compare Figure 5.8 with Figure 4.14a)). As mentioned earlier, Figure 5.9- Figure 5.12 correspond to the last increment (increment 50) of the last cycle (cycle 7th). The same accuracy has been observed in the case of other increments. Figure 5.13 shows the ε_{11} field around the crack tip of 5.5 mm as a testing data and loading case of 5 in Table 5.1 for the last increment. According to the Figure 5.13a) and b), the distribution of ε_{11} field has been accurately predicted by the developed ANN model. The POE in this case is between -20 to +10 percent, as shown in Figure 5.13c). Only ignorable locations reach the relatively high POE such as -20% in Figure 5.13c). Figure 5.14 compares the ε_{22} field predicted by the developed ANN model and determined by the FE analysis for the crack size of 5.5 mm under loading conditions depicted as case 5 in Table 5.1. Comparing Figure 5.14a) and b), the distribution of ε_{22} field as the ANN prediction is in good agreement with the one determined by the elasto-plastic FE analysis. The range of POE for this case is between -10 and +15%, as shown in Figure 5.14c). Only three to four GPs show the POF higher than 10%. Figure 5.15 compares the prediction of the developed ANN model and the results of elasto-plastic FE results for the shear strain (ε_{12}) under the same conditions as normal strains. The distribution of the shear stress field as the results of the ANN model and FE analysis are similar. The POE of the developed ANN model is between -12 to 8 %, which is acceptable for the present purpose. The relatively higher POEs are located in a particular pattern similar to the shear stress discussed earlier. Figure 5.13 to Figure 5.15 show that the developed ANN model can establish the relationship between elastic and elasto-plastic strain fields around the crack tip. Figure 5.13 to Figure 5.15 correspond to the last increment of loading in the last cycle as examples. Figure 5.16 shows the second component of the displacement vector around the crack tip for the crack length of 2.5 mm under the loading condition of case 5 in Table 5.1 for the last increment. The distribution of u_2 field has been accurately predicted by the developed ANN model considering Figure 5.16a) and b). The POE of the ANN prediction is between -14 to 6%, while only a few GPs show relatively higher errors. The important point is that the range of POE in Figure 5.16c) is almost half of the one in the case of monotonic loading in Figure 4.23c).

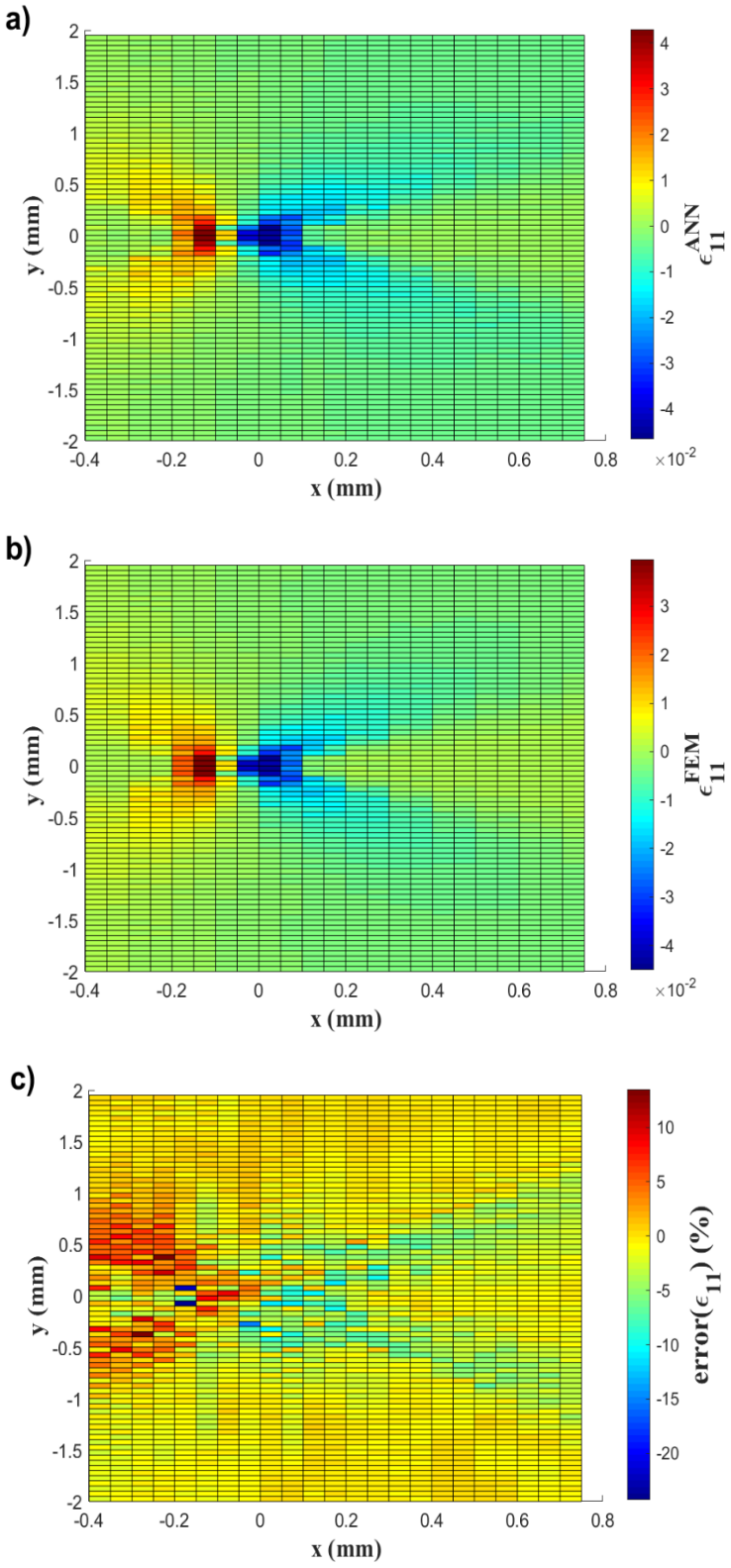

Figure 5.13 ε_{11} stress field for a = 5.5 mm and increment 50 and cycle 7th, loading case 5, a) ANN prediction, b) FE results, c) prediction error.

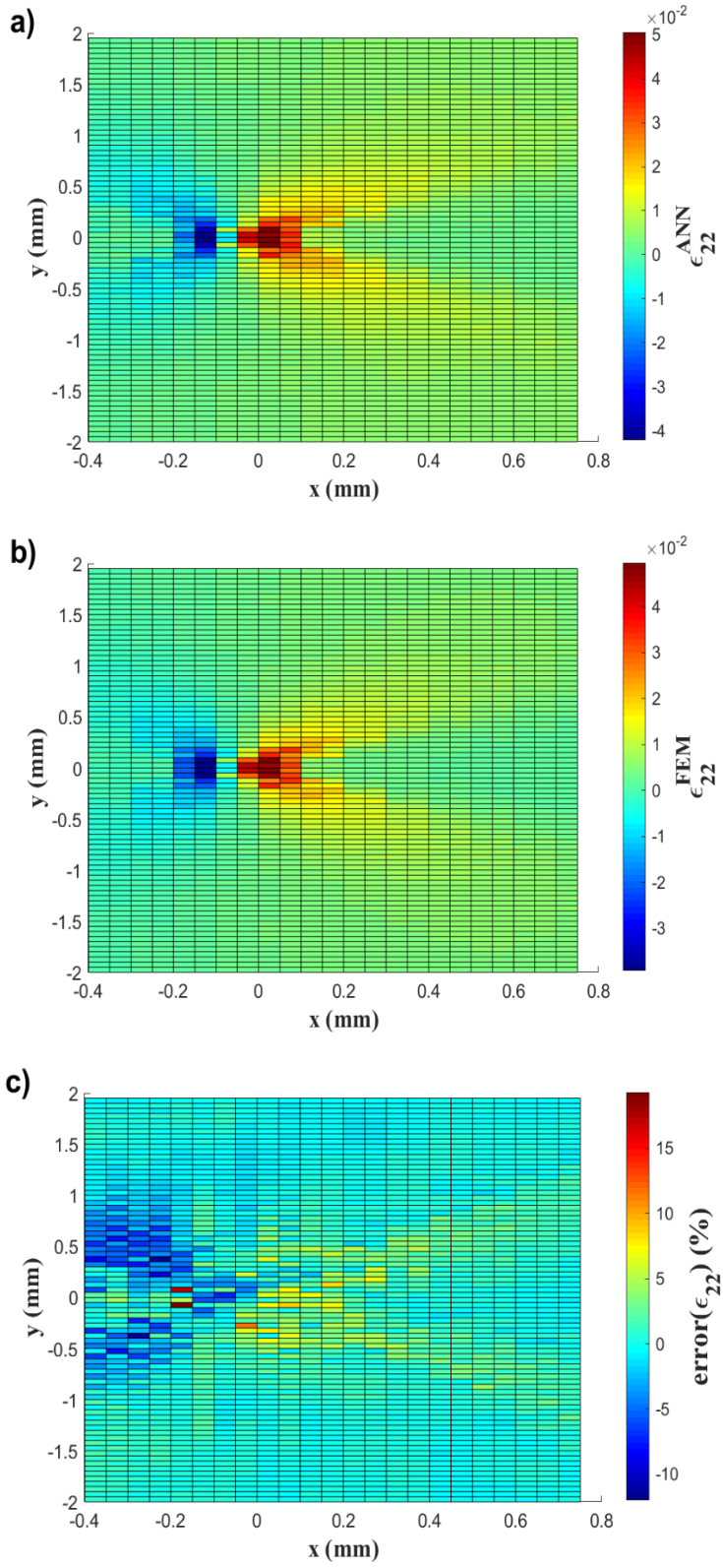

Figure 5.14 ε_{22} stress field for a = 5.5 mm and increment 50 and cycle 7th, loading case 5, a) ANN prediction, b) FE results, c) prediction error.

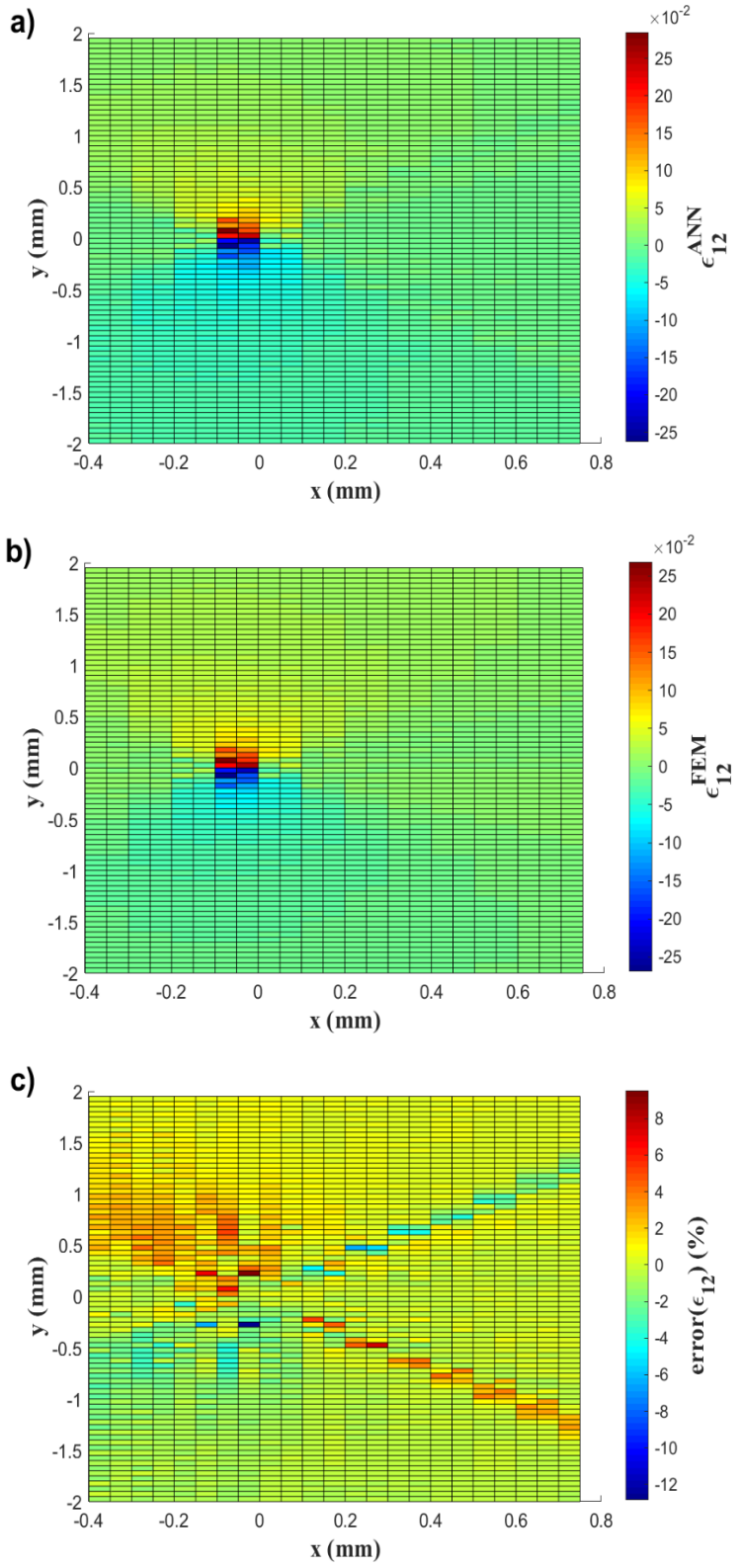

Figure 5.15 ε_{12} stress field for a = 5.5 mm and increment 50 and cycle 7th, loading case 5, a) ANN prediction, b) FE results, c) prediction error.

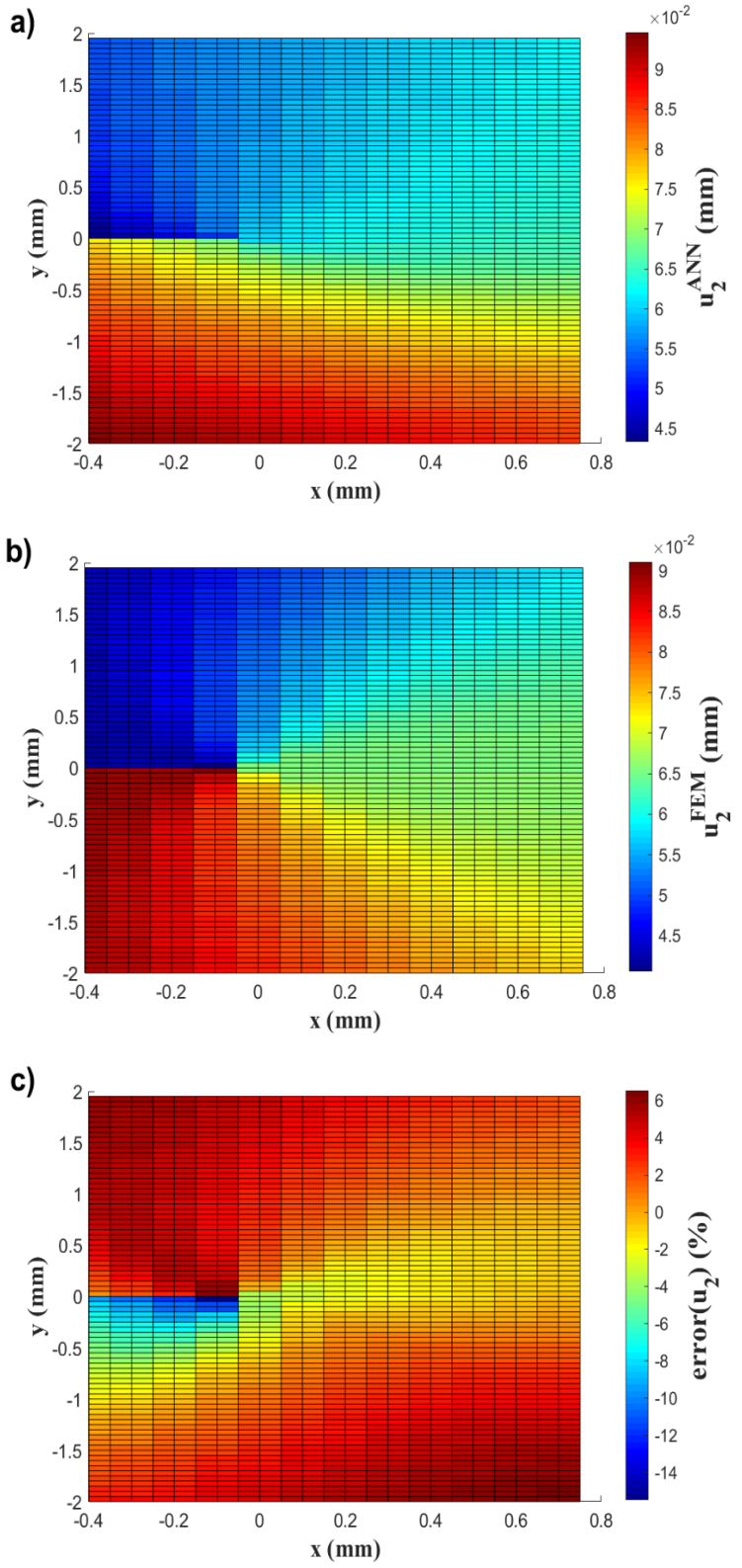

Figure 5.16 u_2 stress field for a = 5.5 mm and increment 50 and cycle 7th, loading case 5, a) ANN prediction, b) FE results, c) prediction error.

As mentioned earlier, the reason is the higher number of training data used in the case of cyclic loading. As a result, such prediction is adequately accurate to be used to calculate ΔJ, and there is no need to develop another ANN model to predict the derivative of displacement similar to the approach employed under monotonic loading. As shown in Eq. (5.7), the first component of the displacement vector (u_1) is included in ΔJ calculation as a strain component ($\varepsilon_{11} = \frac{\partial u_1}{\partial x}$), which can be predicted by the ANN model developed to predict strain tensor. However, an ANN model is required to indicate the displacement vector to predict the second component of the displacement vector (u_2) in order to calculate $\frac{\partial u_2}{\partial x}$ and subsequently ΔJ. As a result, only u_2 filed is discussed in the present paper while knowing that the same accuracy and performance of the ANN model has been observed in the case of u_1 field as well.

As mentioned earlier, there are two crucial differences between the suggested approach for the calculation of J and ΔJ under monotonic loading (discussed in the literature [309] (Chapter 4)) and cyclic loading (discussed in this chapter), respectively. First is that the number of data used to train the ANN models in the case of cyclic loading is larger than the one employed under monotonic loading. Second, predicting elasto-plastic stress, strain, and displacement fields under cyclic loading is inherently more complex than monotonic loading. The first factor potentially results in better predictions in the case of cyclic loading. Meanwhile, the second factor decreases the accuracy of ANN models. That is why in some cases of Figure 5.9 to Figure 5.16 the POE is smaller, and in some cases, it is larger than in the case of monotonic loading. However, it seems significantly increasing the number of data has had a stronger influence on the final result. The witness of such a claim is that the accuracy in the case of the displacement field has been improved significantly. Therefore, as discussed in part 5.3.3, it is not required to develop another ANN model to predict the derivative of the displacement field, such as the one developed under monotonic loading to determine ΔJ based on ANN predictions.

5.4.3. Predicted ΔJ

In this section, ΔJ values determined through the ANN predicted stress, strain, and displacement fields around the crack tip are compared with the ones calculated by elasto-plastic FE analyses. Figure 5.17 shows the ΔJ values under four different R-ratios, introduced as the loading conditions 1 to 4 in Table 5.1 for the crack size of 18 mm. The solid black curves present the ΔJ values calculated through an EDI method developed by Wang et al. in the literature [81]. The green dashed curves show those values determined by the in-house model based on the EDI method developed by the present authors. Finally, the red dash-dotted curves present the ΔJ values determined by the ANN-predicted stress, strain, and displacement fields around the crack tip. All three types of results collapse onto each other. The maximum POE of ANN predicted ΔJ with respect to the in-house model is 3.6, 1.8, 12.7, and 8.7 % for R-ratio of 0.1, 0.2, 0.3, and 0.4, respectively. It should be emphasized that the developed ANN models have been trained based on loading case of 5 in Table 5.1, with the maximum load of 20 kN and R-ratio of 0.1, and for crack sizes between 1 to 10 mm (introduced in Table 4.2). However, Figure 5.17 evaluates the trained ANN models for the crack size of 18 mm for different R-ratios and loading cases. In addition, the developed ANN models have been trained based on the datasets extracted from the last cycle (see Figure 5.4).

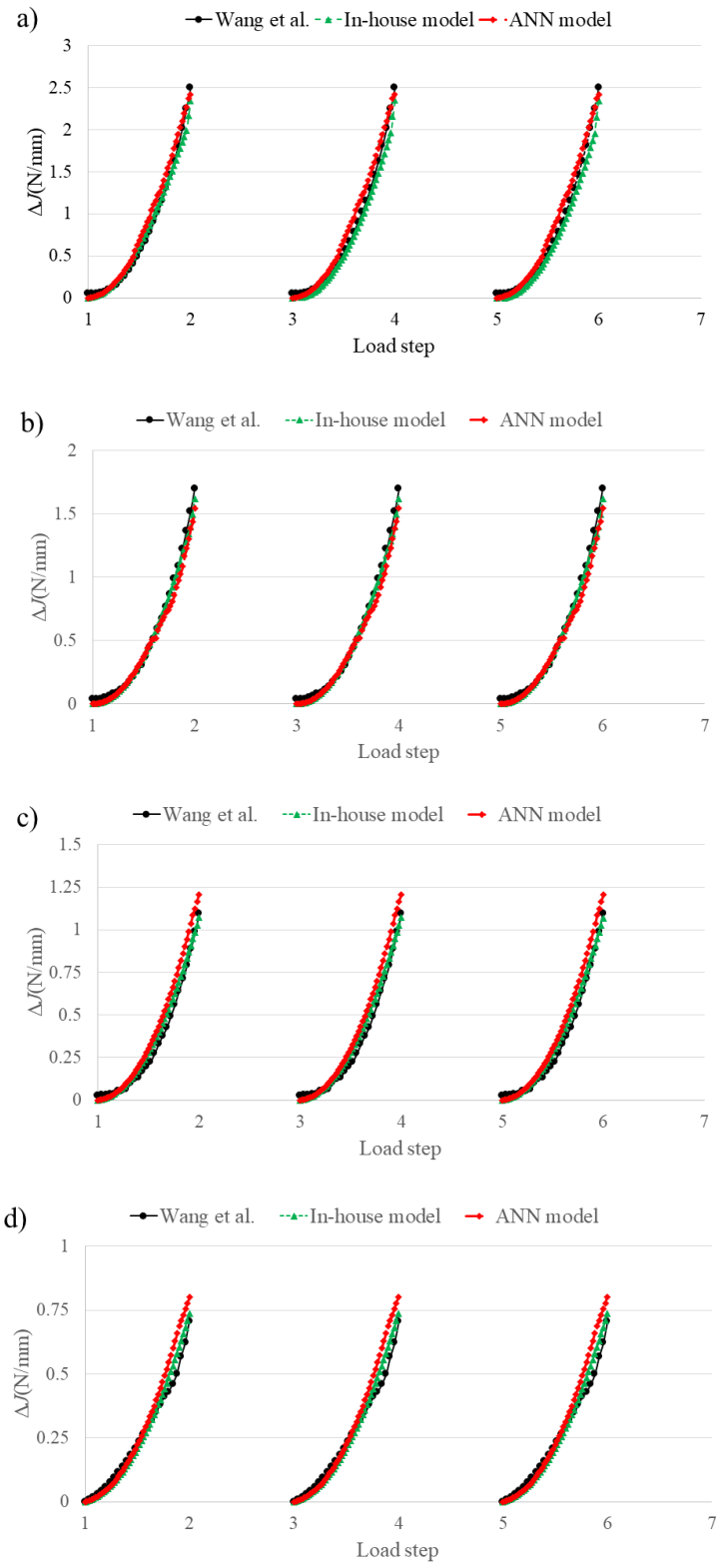

Figure 5.17 ΔJ values under cyclic loading for the crack length of 18 mm for the R-ratio of a) 0.1, b) 0.2, c) 0.3, and d) 0.4.

However, they can be used to calculate ΔJ values for other cycles as well, if the cyclically strain hardening/softening is ignorable. As discussed in Table 5.1, 5 different loading cases have been used in the present study. The number of cycles is 3 and 7 for loading cases 1 to 4 and 5, respectively. The reason is that the ΔJ value used for the FCG characterization for each crack size corresponds to the cycle(s) in which the stress-strain is completely cyclically stabilized. As shown in Figure 5.17, the ΔJ values for all of the loading half cycle is almost the same. Therefore, three cycles are enough to reach such a condition. However, seven cycles have been chosen for the last loading case, which has a significantly higher maximum load to ensure the stress-strain is cyclically stabilized. That is one of the interesting points about the proposed approach to calculate ΔJ. The reason is that the stress-strain behavior under the elastic state is completely reversible. As a result, the developed ANN models need to establish the relationship between the elastic response of the material under only the first cycle of loading and the elasto-plastic response of that for the last cycle (for the cycle that the stress-strain is stabilized). That being said, the proposed approach can avoid dealing with two time-consuming and complicated steps of ΔJ determination during fatigue crack propagation. First, elastic FE analyses are needed rather than complicated elasto-plastic ones. Second, only one cycle of loading is required to be modeled under the elastic state to predict the elasto-plastic ΔJ value corresponding to the last cycle of loading for each crack size. It should be reminded that elasto-plastic FE analyses are required to generate output data for training the ANN models for specific crack sizes. With all these in mind, the developed ANN models and, subsequently, the proposed approach has a high potential to determine ΔJ values through a time-efficient and not complicated manner with acceptable accuracy.

5.5. Conclusion

ANN models have been developed and trained to detect the relationship between the hypothetical elastic and elasto-plastic response of stainless steel (SS304) around the crack tip in terms of stress, strain, and displacement field under cyclic loading. Elastic and elasto-plastic FE analyses have been developed to provide well-structured data for different crack sizes to train ANN models. The ANNs predicted elasto-plastic stress, strain, and displacement fields have been compared with the ones determined by elasto-plastic FE analyses. The result showed that well-trained ANN models can accurately predict the elasto-plastic stress, strain, and displacement fields. Cyclic J-integral (ΔJ) has been calculated by the means of actual stress, strain, and displacement fields predicted by ANN models and compared with the ones determined based on conventional FE methods for different crack sizes and loading conditions. The results showed that the suggested method is able to accurately calculate (ΔJ) values without operating complex and non-linear elasto-plastic analyses for all of the crack sizes.

5.6. Declaration of Competing Interest

The authors declare that they have no known competing financial interests or personal relationships that could have appeared to influence the work reported in this paper.

5.7. Data availability

Data will be made available on request.

5.8. Acknowledgment

The authors would like to acknowledge the financial support of Natural Science and Engineering Research Council of Canada (NSERC) (DGECR-2018-00232).

Chapter 6:

Conclusions and Recommendations

In this chapter, the most valuable and significant outcomes of the study are highlighted. Additionally, several areas that offer potential for future research are listed.

6.1. Conclusion

In the present study, a novel approach that integrates artificial neural networks (ANNs) with fracture mechanics principals is proposed to overcome the limitations of the two most extensively used driving forces fatigue crack growth (FCG) characterization, namely ΔK and ΔJ. One of the most significant limitations of ΔK-based models is their inability to account for the SC regime. On the other hand, employing ΔJ for FCG characterization faces a significant difficulty due to the complicated, nonlinear, and time-consuming process required for ΔJ determination.

In the first phase of the project, robust ANNs are employed to unveil the nonlinear and intricate relationships between FCG rate and its controlling parameters in terms of the stress intensity factor range (ΔK) as defined within the framework of linear elastic fracture mechanics (LEFM). Through the process to subsequent project phases, ANNs are utilized to address the challenges of J and ΔJ determination. Furthermore, FE analyses are conducted to determine stress, strain, and displacement fields around the crack tip of a standard notched specimen made of SS304 under the both elastic and elasto-plastic states. The data obtained from the FE analyses were fed to the ANNs, enabling them to learn the relationships between hypothetical elastic and actual elasto-plastic materials responses under both monotonic and cyclic loadings. By using hypothetical elastic stress, strain, and displacement fields as input and the corresponding actual elasto-plastic fields as output for the ANNs, it is demonstrated that well-trained ANN models can accurately predict actual elasto-plastic stress, strain, and displacement fields near the crack tip based on the hypothetical elastic field data. This prediction method allows the efficient determination of J and ΔJ based on a simple linear elastic solution, thus avoiding the need for complex nonlinear calculations.

The most important outcomes can specifically list as follows:

- In the context of LEFM, FCG rate is characterized based on ΔK and R in the LC regime and ΔK, R, and stress level in the SC regime.
- Radial Basis Function Artificial Neural Network (RBF-ANN) is capable of establishing complex nonlinear relationships in FCG rates. This modeling approach is achieved by considering ΔK and R in the LC regime, and ΔK, R, and stress level in the SC regime.
- The accuracy of RBF-ANN strongly relies on several important factors such as data quantity, data distribution, and data density available for training.
- Although RBF-ANN is very promising in the case of interpolation purposes, they show relatively poor prediction performance in the case of extrapolation.
- Equivalent domain integral (EDI) method used computing J-integral and ΔJ offers a mesh-independent approach. To employ this method, fine mesh is required to have accurate stress, strain, and displacement fields around the crack tip rather than for the adjacent elements to the crack tip.
- Integration of FE analyses with ANNs can significantly improve the application of ANNs in many problems where experimental data is limited. Numerical methods such as FE analyses can provide well-structured datasets to comprehensively represent various aspects of problems for ANNs.
- ANNs can establish the relationships between hypothetical elastic and actual elasto-plastic stress, strain, and displacement fields around the crack tip. That being said, ANNs can

predict the elasto-plastic stress, strain, and displacement fields around the crack tip based the elastic state.

- J-integral and ΔJ values can be accurately determined based on the elasto-plastic stress, strain, and displacement fields predicted by ANNs.
- The quantity of available data strongly affects the accuracy of the ANNs. However, training times can be significantly extended by increasing the data size.
- ANNs can be trained based on a relatively lower R-ratio (e.g., R=0) under cyclic loading and subsequently be applied to predict behavior for relatively higher R-ratios (R>0).

6.2. Future works:

The results of this research suggest several areas that can be further explored:

- Physics-based ANNs can be developed by incorporating underlying physical principals in the ANN architecture/loss function. Physical-based ANN theoretically improve extrapolation capability of ANNs for given dataset. For instance, ANNs can be utilized to reveal the relationships between hypothetical elastic and actual elasto-plastic stress, strain, and/or displacement fields in the vicinity of the crack tip. However, a physical principal can be employed instead of purely mathematical criteria for optimizing the hyperparameters of ANNs during the training. In the present thesis, MSE is used to optimize the hyperparameters during the training procedures. However, J and/or ΔJ can be used as optimizing criteria. That being said, J and/or ΔJ can be calculated based on predicted stress, strain, and displacement fields as the output of the ANN model after each epoch during the training. The determined J and/or ΔJ can be compared with the real values of J and or ΔJ based on the known analytical or numerical solutions. The difference between these two values can be considered as the error, which need to be minimized based on gradient decent algorithm, instead of MSE (or any other purely mathematical errors).
- ANNs can be applied to directly determine K and J based on the elastic stress, strain, and displacement fields. In this scenario, the hypothetical elastic stress, strain, and displacement fields around the crack tip are provided as input. Subsequently, K and J can be assigned as the output(s) of the ANN(s).
- SIF has a closed-form relationship with J under elastic state. However, no relationships have been established between these driving forces under the elasto-plastic state. According to the promising results of the present thesis, ANNs may have the capability to establish the relationship(s) between K and J even under the elasto-plastic state.
- CNNs rather than ANNs can be applied for the same purpose of the present study. In this case, the contours of elastic and elasto-plastic stress, strain, and displacement fields (as the images) can be directly used as the input and output of CNN(s), respectively.
- RNNs rather than ANNs can be applied for the similar purpose. In this case, the path-dependency of loading conditions can be theoretically captured with the NNs.

References

[1] K. Sadananda, M.N. Babu, A. Vasudevan, A review of fatigue crack growth resistance in the short crack growth regime, Materials Science and Engineering: A, 754 (2019) 674-701.
[2] R.I. Stephens, A. Fatemi, R.R. Stephens, H.O. Fuchs, Metal fatigue in engineering, 2 ed., John Wiley & Sons, 2000.
[3] H. Gerber, Bestimmung der zulässigen spannungen in eisen-constructionen, Wolf, 1874.
[4] J. Goodman, Mechanics applied to engineering, 9 ed., Longmans Green, London, 1930.
[5] O. Basquin, The exponential law of endurance tests, in: Proc Am Soc Test Mater, 1910, pp. 625-630.
[6] R.N. Smith, P.P. Watson, T.H. Topper, Stress-strain function for the fatigue of metals, J mater, 5 (1970) 767-778.
[7] D. Socie, J. Morrow, Review of contemporary approaches to fatigue damage analysis, in: Risk and failure analysis for improved performance and reliability, Springer, 1980, pp. 141-194.
[8] A. Ince, G. Glinka, A modification of Morrow and Smith–Watson–Topper mean stress correction models, Fatigue & Fracture of Engineering Materials & Structures, 34 (2011) 854-867.
[9] D. Kujawski, A deviatoric version of the SWT parameter, International journal of fatigue, 67 (2014) 95-102.
[10] A. Ince, A mean stress correction model for tensile and compressive mean stress fatigue loadings, Fatigue & Fracture of Engineering Materials & Structures, 40 (2017) 939-948.
[11] A. Ince, G. Glinka, A generalized fatigue damage parameter for multiaxial fatigue life prediction under proportional and non-proportional loadings, International Journal of Fatigue, 62 (2014) 34-41.
[12] A. Ince, A generalized mean stress correction model based on distortional strain energy, International Journal of Fatigue, 104 (2017) 273-282.
[13] J. Hou, K. Tang, H. Wu, Short review on multiscale short fatigue crack growth model, Material Design & Processing Communications, 2 (2020) e93.
[14] Q. Wang, Y.W. Chung, Stress Intensity Factors, in: Encyclopedia of Tribology, Springer US, Boston, MA, 2013, pp. 3335-3340.
[15] J.B. Jordon, H. Rao, R. Amaro, P. Allison, Chapter 4 - Fatigue Crack Growth in Friction Stir Welds, in: Fatigue in Friction Stir Welding, Butterworth-Heinemann, 2019, pp. 61-86.
[16] G. Sih, On the Westergaard method of crack analysis, International Journal of Fracture Mechanics, 2 (1966) 628-631.
[17] M. Creager, P.C. Paris, Elastic field equations for blunt cracks with reference to stress corrosion cracking, International journal of fracture mechanics, 3 (1967) 247-252.
[18] P. Paris, F. Erdogan, A critical analysis of crack propagation laws, J. Basic Eng. , 85 (1963) 528-533.
[19] A. Russo, A. Sellitto, P. Curatolo, V. Acanfora, S. Saputo, A. Riccio, A Robust Numerical Methodology for Fatigue Damage Evolution Simulation in Composites, Materials, 14 (2021) 3348.
[20] W. Elber, The significance of fatigue crack closure, Damage tolerance in aircraft structures, 1971.
[21] J. Newman, Prediction of fatigue crack growth under variable-amplitude and spectrum loading using a closure model, ASTM International, 1982.
[22] R. Pippan, A. Hohenwarter, Fatigue crack closure: a review of the physical phenomena, Fatigue & fracture of engineering materials & structures, 40 (2017) 471-495.
[23] E. Astm, 647: Standard test method for measurement of fatigue crack growth rates, Annual book of ASTM standards, 3 (2011) 591-630.

[24] J. Newman, Behavior of short cracks in airframe components, in: AGARD Conference Proceedings, 1983, pp. 6.1-6.26.
[25] S. Suresh, R. Ritchie, Propagation of short fatigue cracks, International metals reviews, 29 (1984) 445-475.
[26] R. Ritchie, J. Lankford, Small fatigue cracks: a statement of the problem and potential solutions, Materials Science and Engineering, 84 (1986) 11-16.
[27] K. Miller, R. Akid, The application of microstructural fracture mechanics to various metal surface states, Materials Science, 33 (1997) 1-20.
[28] S. Hudak Jr, Small crack behavior and the prediction of fatigue life, J of Engineering Materials and Technology, 103 (1981) 26-35.
[29] J. Lankford, Initiation and early growth of fatigue cracks in high strength steel, Engineering Fracture Mechanics, 9 (1977) 617-624.
[30] D. Taylor, J. Knott, Fatigue crack propagation behaviour of short cracks; the effect of microstructure, Fatigue & Fracture of Engineering Materials & Structures, 4 (1981) 147-155.
[31] J. Lankford, T. Cook, G. Sheldon, Fatigue microcrack growth in a nickel-base superalloy, International Journal of Fracture, 17 (1981) 143-155.
[32] W. Morris, M. James, O. Buck, Growth rate models for short surface cracks in AI 2219-T851, Metallurgical Transactions A, 12 (1981) 57-64.
[33] J. Lankford, The growth of small fatigue cracks in 7075–T6 aluminum, Fatigue & Fracture of Engineering Materials & Structures, 5 (1982) 233-248.
[34] D. Taylor, Euromech colloquium on short fatigue cracks, Fatigue & Fracture of Engineering Materials & Structures, 5 (1982) 305-309.
[35] A. Zurek, M. James, W. Morris, The effect of grain size on fatigue growth of short cracks, Metallurgical Transactions A, 14 (1983) 1697-1705.
[36] Y. Hu, W. Floer, U. Krupp, H.-J. Christ, Microstructurally short fatigue crack initiation and growth in Ti-6.8 Mo-4.5 Fe-1.5 Al, Materials Science and Engineering: A, 278 (2000) 170-180.
[37] R.G. Forman, S.R. Mettu, Behavior of surface and corner cracks subjected to tensile and bending loads in Ti-6Al-4V alloy, in: Fracture Mechanics 22nd Symposium, 1992.
[38] M.R. Ayatollahi, S.M.J. Razavi, M.Y. Yahya, Mixed mode fatigue crack initiation and growth in a CT specimen repaired by stop hole technique, Engineering Fracture Mechanics, 145 (2015) 115-127.
[39] J. Toribio, V. Kharin, Simulations of fatigue crack growth by blunting–re-sharpening: Plasticity induced crack closure vs. alternative controlling variables, International journal of fatigue, 50 (2013) 72-82.
[40] M. Mohin, Y. Xu, A. Lewis, A. Chrysanthou, Effect of plastic deformation on compliance curve based crack closure measurement, in: Key Engineering Materials, Trans Tech Publ, 2016, pp. 240-243.
[41] K. Walker, The effect of stress ratio during crack propagation and fatigue for 2024-T3 and 7075-T6 aluminum, in: ASTM STP, 1970, pp. 1-14.
[42] K. Donald, P.C. Paris, An evaluation of ΔKeff estimation procedures on 6061-T6 and 2024-T3 aluminum alloys, International Journal of fatigue, 21 (1999) S47-S57.
[43] S. Dinda, D. Kujawski, Correlation and prediction of fatigue crack growth for different R-ratios using Kmax and ΔK+ parameters, Engineering Fracture Mechanics, 71 (2004) 1779-1790.
[44] A. Vasudeven, K. Sadananda, N. Louat, A review of crack closure, fatigue crack threshold and related phenomena, Materials Science and Engineering: A, 188 (1994) 1-22.

[45] A. Vasudevan, K. Sadananda, N. Louat, A review of crack closure, fatigue crack threshold and related phenomena, International Journal of Fatigue, 1 (1996) 62.
[46] A. Noroozi, G. Glinka, S. Lambert, A two parameter driving force for fatigue crack growth analysis, International Journal of Fatigue, 27 (2005) 1277-1296.
[47] A. Noroozi, G. Glinka, S. Lambert, A study of the stress ratio effects on fatigue crack growth using the unified two-parameter fatigue crack growth driving force, International journal of fatigue, 29 (2007) 1616-1633.
[48] A. Moftakhar, G. Glinka, Calculation of stress intensity factors by efficient integration of weight functions, Engineering Fracture Mechanics, 43 (1992) 749-756.
[49] S. Mikheevskiy, S. Bogdanov, G. Glinka, Statistical analysis of fatigue crack growth based on the unigrow model, in: Icaf 2011 structural integrity: Influence of efficiency and green imperatives, Springer, 2011, pp. 415-425.
[50] N.N. Abdullah, J.F. Correia, A.M. de Jesus, M.H. Hafezi, S. Abdullah, Assessment of fatigue crack growth data available for materials from Portuguese bridges based on UniGrow model, Procedia Engineering, 10 (2011) 971-976.
[51] S. Mikheevskiy, G. Glinka, D. Algera, Analysis of fatigue crack growth in an attachment lug based on the weight function technique and the UniGrow fatigue crack growth model, International journal of fatigue, 42 (2012) 88-94.
[52] S. Mikheevskiy, S. Bogdanov, G. Glinka, Analysis of fatigue crack growth under spectrum loading–The UniGrow fatigue crack growth model, Theoretical and Applied Fracture Mechanics, 79 (2015) 25-33.
[53] M.A. Lepore, A.R. Maligno, F. Berto, A unified approach to simulate the creep-fatigue crack growth in P91 steel at elevated temperature under SSY and SSC conditions, Engineering Failure Analysis, 127 (2021) 105569.
[54] B. Pedrosa, J. Correia, G. Lesiuk, C. Rebelo, M. Veljkovic, Fatigue crack growth modelling for S355 structural steel considering plasticity-induced crack-closure by means of UniGrow model, International Journal of Fatigue, 164 (2022) 107120.
[55] D. Bang, A. Ince, L. Tang, A modification of UniGrow 2-parameter driving force model for short fatigue crack growth, Fatigue & Fracture of Engineering Materials & Structures, 42 (2019) 45-60.
[56] D. Bang, A. Ince, M. Noban, Modeling approach for a unified crack growth model in short and long fatigue crack regimes, International Journal of Fatigue, 128 (2019) 105182.
[57] D. Bang, A. Ince, A short and long crack growth model based on 2-parameter driving force and crack growth thresholds, International Journal of Fatigue, 141 (2020) 105870.
[58] H. Neuber, Theory of stress concentration for shear-strained prismatical bodies with arbitrary nonlinear stress-strain law, J of Applied Mechanics, 28 (1961) 544-550.
[59] A. Ince, Numerical validation of computational stress and strain analysis model for notched components subject to non-proportional loadings, Theoretical and Applied Fracture Mechanics, 84 (2016) 26-37.
[60] T. Topper, R. Wetzel, J. Morrow, Neuber's rule applied to fatigue of notched specimens, J. mater, 4 (1969) 357-373.
[61] K. Molski, G. Glinka, A method of elastic-plastic stress and strain calculation at a notch root, Materials Science and Engineering, 50 (1981) 93-100.
[62] M. Hoffmann, T. Seeger, A generalized method for estimating multiaxial elastic-plastic notch stresses and strains, Part 1: Theory, J. Eng. Mater. Technol., 107 (1985) 250-254.

[63] A.A. Moftakhar, Calculation of time-independent and time-dependent strains and stresses in notches, in, University of Waterloo, Waterloo, 1994.
[64] A. Moftakhar, A. Buczynski, G. Glinka, Calculation of elasto-plastic strains and stresses in notches under multiaxial loading, International journal of fracture, 70 (1994) 357-373.
[65] D. Kujawski, P.C. Sree, On deviatoric interpretation of Neuber's rule and the SWT parameter, Theoretical and Applied Fracture Mechanics, 71 (2014) 44-50.
[66] A. Ince, D. Bang, Deviatoric Neuber method for stress and strain analysis at notches under multiaxial loadings, International Journal of Fatigue, 102 (2017) 229-240.
[67] K. Kolasangiani, K. Farhangdoost, M. Shariati, A. Varvani-Farahani, Ratcheting assessment of notched steel samples subjected to asymmetric loading cycles through coupled kinematic hardening-Neuber rules, International Journal of Mechanical Sciences, 144 (2018) 24-32.
[68] A. Ince, G. Glinka, Approximation modeling framework for elastic-plastic stress-strain fields near cracks with a small finite crack tip radius, Theoretical and Applied Fracture Mechanics, 121 (2022) 103452.
[69] J. Robinson, A. Tetelman, The relationship between crack tip opening displacement, local strain and specimen geometry, International Journal of Fracture, 11 (1975) 453-468.
[70] R.M. McMeeking, Finite deformation analysis of crack-tip opening in elastic-plastic materials and implications for fracture, Journal of the Mechanics and Physics of Solids, 25 (1977) 357-381.
[71] O. Kolednik, H. Stüwe, The stereophotogrammetric determination of the critical crack tip opening displacement, Engineering Fracture Mechanics, 21 (1985) 145-155.
[72] Y. Liu, Z. Lu, J. Xu, A simple analytical crack tip opening displacement approximation under random variable loadings, International journal of fracture, 173 (2012) 189-201.
[73] J. Xu, G. Wang, F. Xuan, S. Tu, Unified constraint parameter based on crack-tip opening displacement, Engineering Fracture Mechanics, 200 (2018) 175-188.
[74] A. Shyam, W. Milligan, A model for slip irreversibility, and its effect on the fatigue crack propagation threshold in a nickel-base superalloy, Acta materialia, 53 (2005) 835-844.
[75] A. Shyam, J. Allison, J. Jones, A small fatigue crack growth relationship and its application to cast aluminum, Acta materialia, 53 (2005) 1499-1509.
[76] A. Shyam, J.E. Allison, C.J. Szczepanski, T.M. Pollock, J.W. Jones, Small fatigue crack growth in metallic materials: A model and its application to engineering alloys, Acta Materialia, 55 (2007) 6606-6616.
[77] G.-J. Deng, S.-T. Tu, X.-C. Zhang, Q.-Q. Wang, C.-H. Qin, Grain size effect on the small fatigue crack initiation and growth mechanisms of nickel-based superalloy GH4169, Engineering Fracture Mechanics, 134 (2015) 433-450.
[78] G.-J. Deng, S.-T. Tu, X.-C. Zhang, J. Wang, C.-C. Zhang, X.-Y. Qian, Y.-N. Wang, Small fatigue crack initiation and growth mechanisms of nickel-based superalloy GH4169 at 650 C in air, Engineering Fracture Mechanics, 153 (2016) 35-49.
[79] J.R. Rice, A path independent integral and the approximate analysis of strain concentration by notches and cracks, J. of Applied Mechanics, 35 (1968) 379-386.
[80] K. Tanaka, The cyclicJ-integral as a criterion for fatigue crack growth, International Journal of Fracture, 22 (1983) 91-104.
[81] J. Wang, W. Jiang, Y. Li, Q. Wang, Q. Xu, Numerical assessment of cyclic J-integral△ J for predicting fatigue crack growth rate, Engineering Fracture Mechanics, 205 (2019) 455-469.
[82] N. Dowling, J. Begley, Fatigue crack growth during gross plasticity and the J-integral, in: Mechanics of crack growth. ASTM STP 590, 1976, pp. 82-103.

[83] H. Lamba, The J-integral applied to cyclic loading, Engineering Fracture Mechanics, 7 (1975) 693-703.
[84] N. Dowling, Geometry effects and the J-integral approach to elastic-plastic fatigue crack growth, ASTM International, 1976.
[85] M. El Haddad, N. Dowling, T. Topper, K. Smith, J integral applications for short fatigue cracks at notches, International Journal of Fracture, 16 (1980) 15-30.
[86] C. Chow, T. Lu, On the cyclic J-integral applied to fatigue cracking, International journal of fracture, 40 (1989) R53-R59.
[87] Y.L. Lu, H. Kobayashi, AN EXPERIMENTAL PARAMETER Jmax IN ELASTIC-PLASTIC FATIGUE CRACK GROWTH, Fatigue & Fracture of Engineering Materials & Structures, 19 (1996) 1081-1091.
[88] M.P. Wnuk, Effects of Energy Dissipation and Energy Screening on Fatigue Crack Extension in Viscoelastic-plastic Solids, in: Low Cycle Fatigue and Elasto-Plastic Behaviour of Materials—3, Springer, 1992, pp. 508-513.
[89] D.T. Ngoula, M. Madia, H.T. Beier, M. Vormwald, U. Zerbst, Cyclic J-integral: Numerical and analytical investigations for surface cracks in weldments, Engineering fracture mechanics, 198 (2018) 24-44.
[90] M. Metzger, T. Seifert, C. Schweizer, Does the cyclic J-integral ΔJ describe the crack-tip opening displacement in the presence of crack closure?, Engineering Fracture Mechanics, 134 (2015) 459-473.
[91] C. Wüthrich, The extension of the J-integral concept to fatigue cracks, International Journal of fracture, 20 (1982) R35-R37.
[92] K.B. Yoon, A. Saxena, An interpretation of ΔJ for cyclically unsaturated materials, International journal of fracture, 49 (1991) R3-R9.
[93] A. Ktari, N. Haddar, F. Rezai-Aria, H.F. Ayedi, On the assessment of train crankshafts fatigue life based on LCF tests and 2D-FE evaluation of J-integral, Engineering Failure Analysis, 66 (2016) 354-364.
[94] G. Gasiak, D. Rozumek, ΔJ-integral range estimation for fatigue crack growth rate description, International journal of fatigue, 26 (2004) 135-140.
[95] S. Courtin, C. Gardin, G. Bezine, H.B.H. Hamouda, Advantages of the J-integral approach for calculating stress intensity factors when using the commercial finite element software ABAQUS, Engineering Fracture Mechanics, 72 (2005) 2174-2185.
[96] N. Miyazaki, T. Watanabe, G. Yagawa, The virtual crack extension method for evaluation of J-and J-integrals, Engineering fracture mechanics, 22 (1985) 975-987.
[97] G. Nikishkov, S. Atluri, An equivalent domain integral method for computing crack-tip integral parameters in non-elastic, thermo-mechanical fracture, Engineering Fracture Mechanics, 26 (1987) 851-867.
[98] G. Nikishkov, S. Atluri, Calculation of fracture mechanics parameters for an arbitrary three-dimensional crack, by the 'equivalent domain integral'method, International journal for numerical methods in engineering, 24 (1987) 1801-1821.
[99] M. di Lorenzi, On the energy-release rate and the J-integral for 3-D crack configuration, International Journal of Fracture, 19 (1982) 183-193.
[100] K. Shivakumar, I. Raju, An equivalent domain integral method for three-dimensional mixed-mode fracture problems, Engineering fracture mechanics, 42 (1992) 935-959.
[101] R.S. Barsoum, On the use of isoparametric finite elements in linear fracture mechanics, International journal for numerical methods in engineering, 10 (1976) 25-37.

[102] G. Nikishkov, A. Vershinin, Y. Nikishkov, Mesh-independent equivalent domain integral method for J-integral evaluation, Advances in Engineering Software, 100 (2016) 308-318.
[103] I. Raju, K. Shivakumar, An equivalent domain integral method in the two-dimensional analysis of mixed mode crack problems, Engineering fracture mechanics, 37 (1990) 707-725.
[104] H. Okada, S. Ohata, Three-dimensional J-integral evaluation for cracks with arbitrary curvatures and kinks based on domain integral method for quadratic tetrahedral finite element, Engineering Fracture Mechanics, 109 (2013) 58-77.
[105] P.N. Huu, Q.T. Minh, An ANN-based gesture recognition algorithm for smart-home applications, KSII Transactions on Internet and Information Systems (TIIS), 14 (2020) 1967-1983.
[106] Z. Marinković, G. Crupi, A. Caddemi, V. Marković, D.M.P. Schreurs, A review on the artificial neural network applications for small-signal modeling of microwave FETs, International Journal of Numerical Modelling: Electronic Networks, Devices and Fields, 33 (2020) e2668.
[107] G. Sun, S. Wang, A review of the artificial neural network surrogate modeling in aerodynamic design, Proceedings of the Institution of Mechanical Engineers, Part G: Journal of Aerospace Engineering, 233 (2019) 5863-5872.
[108] W. Zhang, R. Zhang, C. Wu, A.T.C. Goh, S. Lacasse, Z. Liu, H. Liu, State-of-the-art review of soft computing applications in underground excavations, Geoscience Frontiers, 11 (2020) 1095-1106.
[109] O.I. Abiodun, A. Jantan, A.E. Omolara, K.V. Dada, A.M. Umar, O.U. Linus, H. Arshad, A.A. Kazaure, U. Gana, M.U. Kiru, Comprehensive review of artificial neural network applications to pattern recognition, IEEE Access, 7 (2019) 158820-158846.
[110] O.I. Abiodun, A. Jantan, A.E. Omolara, K.V. Dada, N.A. Mohamed, H. Arshad, State-of-the-art in artificial neural network applications: A survey, Heliyon, 4 (2018) e00938.
[111] F. Rosenblatt, Principles of neurodynamics. perceptrons and the theory of brain mechanisms, in, Cornell Aeronautical Lab Inc Buffalo NY, 1961.
[112] T. Gulikers, An integrated machine learning and finite element analysis framework, applied to composite substructures including damage, in: Department of Mechanical Engineering, Delf University of Technology, Delf, 2018.
[113] J. Chen, Y. Liu, Fatigue modeling using neural networks: A comprehensive review, Fatigue & Fracture of Engineering Materials & Structures, 45 (2022) 945-979.
[114] J.C.F. Pujol, J.M.A. Pinto, A neural network approach to fatigue life prediction, International Journal of Fatigue, 33 (2011) 313-322.
[115] E. Maleki, O. Unal, K.R. Kashyzadeh, Fatigue behavior prediction and analysis of shot peened mild carbon steels, International Journal of Fatigue, 116 (2018) 48-67.
[116] A.P. Vassilopoulos, E.F. Georgopoulos, V. Dionysopoulos, Artificial neural networks in spectrum fatigue life prediction of composite materials, International Journal of Fatigue, 29 (2007) 20-29.
[117] C. Yan, R. Gao, W. Huang, Asphalt mixture fatigue life prediction model based on neural network, in: CICTP 2017: Transportation Reform and Change—Equity, Inclusiveness, Sharing, and Innovation, American Society of Civil Engineers Reston, VA, 2018, pp. 1292-1299.
[118] K. Dresia, G. Waxenegger-Wilfing, J. Riccius, J.C. Deeken, M. Oschwald, Numerically efficient fatigue life prediction of rocket combustion chambers using artificial neural networks, in: Proceedings of the 8th European Conference for Aeronautics and Space Sciences, 2019.
[119] X.-C. Zhang, J.-G. Gong, F.-Z. Xuan, A deep learning based life prediction method for components under creep, fatigue and creep-fatigue conditions, International Journal of Fatigue, 148 (2021) 106236.

[120] D. Nowell, P. Nowell, A machine learning approach to the prediction of fretting fatigue life, Tribology International, 141 (2020) 105913.
[121] P. Artymiak, L. Bukowski, J. Feliks, S. Narberhaus, H. Zenner, Determination of S–N curves with the application of artificial neural networks, Fatigue & Fracture of Engineering Materials & Structures, 22 (1999) 723-728.
[122] V. Srinivasan, M. Valsan, K.B.S. Rao, S. Mannan, B. Raj, Low cycle fatigue and creep–fatigue interaction behavior of 316L (N) stainless steel and life prediction by artificial neural network approach, International Journal of Fatigue, 25 (2003) 1327-1338.
[123] M. Mathew, D.W. Kim, W.-S. Ryu, A neural network model to predict low cycle fatigue life of nitrogen-alloyed 316L stainless steel, Materials Science and Engineering: A, 474 (2008) 247-253.
[124] M. Susmikanti, The fatigue life prediction of aluminium alloy using genetic algorithm and neural network, in: AIP Conference Proceedings, American Institute of Physics, 2013, pp. 174-177.
[125] J. Lin, J. Zhang, G. Zhang, G. Ni, F. Bi, Aero-engine blade fatigue analysis based on nonlinear continuum damage model using neural networks, Chinese Journal of Mechanical Engineering, 25 (2012) 338-345.
[126] K. Zhou, X. Sun, S. Shi, K. Song, X. Chen, Machine learning-based genetic feature identification and fatigue life prediction, Fatigue & Fracture of Engineering Materials & Structures, 44 (2021) 2524-2537.
[127] P. Sangeetha, M. Shanmugapriya, Modeling and prediction of fatigue life of brass and EN24 steel using soft computing tool, Materials Today: Proceedings, 38 (2021) 2912-2918.
[128] J.A. Abdalla, R.A. Hawileh, Artificial neural network predictions of fatigue life of steel bars based on hysteretic energy, Journal of computing in civil engineering, 27 (2013) 489-496.
[129] H. Jin, S. Wu, Y. Peng, Prediction of contact fatigue life of alloy cast steel rolls using back-propagation neural network, Journal of materials engineering and performance, 22 (2013) 3631-3638.
[130] T. Sekercioglu, V. Kovan, Prediction of static shear force and fatigue life of adhesive joints by artificial neural network, METALLIC MATERIALS, 46 (2008) 51.
[131] Y.-L. Han, Artificial neural network technology as a method to evaluate the fatigue life of weldments with welding defects, International journal of pressure vessels and piping, 63 (1995) 205-209.
[132] Y.-L. Han, X. Liu, S.-H. Dai, Fatigue life calculation of flawed structures—based on artificial neural network with special learning set, International journal of pressure vessels and piping, 75 (1998) 263-269.
[133] J.M. Park, H.T. Kang, Prediction of fatigue life for spot welds using back-propagation neural networks, Materials & design, 28 (2007) 2577-2584.
[134] D. Ma, Z.Q. Chen, X.L. Shan, Forecasting of the fatigue life of metal weld joints based on combined genetic neural network, in: Key Engineering Materials, Trans Tech Publ, 2010, pp. 195-201.
[135] I.S. Sohn, D.H. Bae, Fatigue life prediction of spot-welded joint by strain energy density factor using artificial neural network, in: Key Engineering Materials, Trans Tech Publ, 2000, pp. 957-962.
[136] Ö. Karakas, Estimation of fatigue life for aluminium welded joints with the application of artificial neural networks, Material Science & Engineering Technology, 42 (2011) 888-893.

[137] Ö. Karakas, A. Tomasella, Fatigue life estimation of non-penetrated butt weldments in ligth metals by artificial neural network approach, Materials Science & Engineering Technology, 44 (2013) 847-855.
[138] N. Zhou, J. Zhang, F. Ju, S. Liu, Genetic Algorithm Coupled with the Neural Network for Fatigue Properties of Welding Joints Predicting, J. Comput., 7 (2012) 1887-1894.
[139] G. Majzoobi, M. Kazemi, A new investigation on the effect of re-shot peening on fretting fatigue behavior of A17075-T6, Tribology transactions, 56 (2013) 943-952.
[140] E. Maleki, K.R. Kashyzadeh, Effects of the hardened nickel coating on the fatigue behavior of CK45 steel: experimental, finite element method, and artificial neural network modeling, Iran J Mater Sci Eng, 14 (2017) 81-99.
[141] K. Reza Kashyzadeh, E. Maleki, Experimental investigation and artificial neural network modeling of warm galvanization and hardened chromium coatings thickness effects on fatigue life of AISI 1045 carbon steel, Journal of Failure Analysis and Prevention, 17 (2017) 1276-1287.
[142] T.T. Pleune, O.K. Chopra, Using artificial neural networks to predict the fatigue life of carbon and low-alloy steels, Nuclear Engineering and Design, 197 (2000) 1-12.
[143] V. Venkatesh, H. Rack, A neural network approach to elevated temperature creep–fatigue life prediction, International Journal of Fatigue, 21 (1999) 225-234.
[144] C.L. Xu, S.L. Lv, Z.G. Wang, W. Zhang, Predicting fatigue life of pre-corroded LC4 aluminum alloy by artificial neural network, in: Advanced Materials Research, Trans Tech Publ, 2010, pp. 221-225.
[145] X. Yang, L. Zou, W. Deng, Fatigue life prediction for welding components based on hybrid intelligent technique, Materials Science and Engineering: A, 642 (2015) 253-261.
[146] X. Yang, W. Deng, L. Zou, H. Zhao, J. Liu, Fatigue behaviors prediction method of welded joints based on soft computing methods, Materials Science and Engineering: A, 559 (2013) 574-582.
[147] Z. Zhan, H. Li, Machine learning based fatigue life prediction with effects of additive manufacturing process parameters for printed SS 316L, International Journal of Fatigue, 142 (2021) 105941.
[148] Z. Zhan, H. Li, A novel approach based on the elastoplastic fatigue damage and machine learning models for life prediction of aerospace alloy parts fabricated by additive manufacturing, International Journal of Fatigue, 145 (2021) 106089.
[149] I. Uygur, A. Cicek, E. Toklu, R. Kara, S. Saridemir, Fatigue life predictions of metal matrix composites using artificial neural networks, Archives of Metallurgy and Materials, 59 (2014) 97-103.
[150] Y. Al-Assaf, H. El Kadi, Fatigue life prediction of unidirectional glass fiber/epoxy composite laminae using neural networks, Composite Structures, 53 (2001) 65-71.
[151] A.P. Vassilopoulos, E.F. Georgopoulos, V. Dionysopoulos, Modelling fatigue life of multidirectional GFRP laminates under constant amplitude loading with artificial neural networks, Advanced Composites Letters, 15 (2006) 096369350601500201.
[152] K.-L. Xiang, P.-Y. Xiang, Y.-P. Wu, Prediction of the fatigue life of natural rubber composites by artificial neural network approaches, Materials & Design, 57 (2014) 180-185.
[153] J. Lee, S. Kim, Optimal design of engine mount rubber considering stiffness and fatigue strength, Proceedings of the Institution of Mechanical Engineers, Part D: Journal of Automobile Engineering, 221 (2007) 823-835.

[154] M.N. Rohman, M.I.P. Hidayat, A. Purniawan, Prediction of composite fatigue life under variable amplitude loading using artificial neural network trained by genetic algorithm, in: AIP Conference Proceedings, AIP Publishing LLC, 2018, pp. 020019.
[155] K. Salmalian, N. Nariman-Zadeh, H. Gharababei, H. Haftchenari, A. Varvani-Farahani, Multi-objective evolutionary optimization of polynomial neural networks for fatigue life modelling and prediction of unidirectional carbon-fibre-reinforced plastics composites, Proceedings of the Institution of Mechanical Engineers, Part L: Journal of Materials: Design and Applications, 224 (2010) 79-91.
[156] X.L. Liao, W.F. Xu, Z.Q. Gao, Application of artificial neural network to forecast the tensile fatigue life of carbon material, in: Key Engineering Materials, Trans Tech Publ, 2008, pp. 533-536.
[157] F. Xiao, S. Amirkhanian, C.H. Juang, Prediction of fatigue life of rubberized asphalt concrete mixtures containing reclaimed asphalt pavement using artificial neural networks, Journal of Materials in Civil Engineering, 21 (2009) 253-261.
[158] J. Yuan, S. Lv, X. Peng, L. You, M. Borges Cabrera, Investigation of strength and fatigue life of rubber asphalt mixture, Materials, 13 (2020) 3325.
[159] T.M. Ahmed, P.L. Green, H.A. Khalid, Predicting fatigue performance of hot mix asphalt using artificial neural networks, Road Materials and Pavement Design, 18 (2017) 141-154.
[160] M. Vadood, M.S. Johari, A.R. Rahai, Relationship between fatigue life of asphalt concrete and polypropylene/polyester fibers using artificial neural network and genetic algorithm, Journal of central south university, 22 (2015) 1937-1946.
[161] R.C.S.F. Júnior, A.D.D. Neto, E.M.F. de Aquino, Building of constant life diagrams of fatigue using artificialneural networks, International Journal of Fatigue, 27 (2005) 746-751.
[162] B.B.V. de Sena, R.C.S.F. Júnior, Criteria for the use of modular networks: fatigue in composite materials, Journal of composite materials, 46 (2012) 2973-2985.
[163] M.S. Pestana, R.B. Kalombo, R.C.S. Freire Júnior, J.L.A. Ferreira, C.R.M. da Silva, J.A. Araújo, Use of artificial neural network to assess the effect of mean stress on fatigue of overhead conductors, Fatigue & Fracture of Engineering Materials & Structures, 41 (2018) 2577-2586.
[164] R. Kalombo, M. Pestana, R.F. Júnior, J. Ferreira, C. Silva, L. Veloso, E. Câmara, J. Araújo, Fatigue life estimation of an all aluminium alloy 1055 MCM conductor for different mean stresses using an artificial neural network, International Journal of Fatigue, 140 (2020) 105814.
[165] E.C.B. Camara, R.B. Kalombo, J.L. Ferreira, J.A. Araujo, R.C.S. Freire Junior, Estimating fatigue behavior of a family of aluminum overhead conductors using ANNs, Fatigue & Fracture of Engineering Materials & Structures, 44 (2021) 983-996.
[166] M. Jimenez-Martinez, M. Alfaro-Ponce, Fatigue damage effect approach by artificial neural network, International Journal of Fatigue, 124 (2019) 42-47.
[167] K. Genel, Application of artificial neural network for predicting strain-life fatigue properties of steels on the basis of tensile tests, International Journal of Fatigue, 26 (2004) 1027-1035.
[168] M. Cai, D.-g. Yang, Q.-y. Li, L.-j. Zhong, Optimization of the fatigue life of epoxy molding compounds based on BP neural network prediction model, in: 2008 International Conference on Electronic Packaging Technology & High Density Packaging, IEEE, 2008, pp. 1-7.
[169] X. Huang, D. Zhang, Z. Wang, Back propagation neural network in predicting the thermal fatigue life of microelectronic chips, Inf. MIDEM Journal of Microelectronics, Electronic Components and Materials, 50 (2020) 15-24.
[170] Z. Han, X. Huang, GA-BP in thermal fatigue failure prediction of microelectronic chips, Electronics, 8 (2019) 542.

[171] I.A. Azid, L.K. Oon, O.K. Eu, K. Seetharamu, G.A. Quadir, Application of artificial neural network for fatigue life prediction, in: Key Engineering Materials, Trans Tech Publ, 2005, pp. 96-101.
[172] N. Li, W.P. Yan, F. Ye, L.Y. Ma, Creep-fatigue interaction life prediction for P91 steel based on improved Elman neural network model, in: Advanced Materials Research, Trans Tech Publ, 2012, pp. 674-677.
[173] J. Yang, G. Kang, Y. Liu, Q. Kan, A novel method of multiaxial fatigue life prediction based on deep learning, International Journal of Fatigue, 151 (2021) 106356.
[174] S. Guo, C. Li, J. Shi, F. Luan, X. Song, Effect of quenching media and tempering temperature on fatigue property and fatigue life estimation based on RBF neural network of 0.44% carbon steel, Mechanical Sciences, 10 (2019) 273-286.
[175] J.A. Abdalla, R. Hawileh, Modeling and simulation of low-cycle fatigue life of steel reinforcing bars using artificial neural network, Journal of the Franklin Institute, 348 (2011) 1393-1403.
[176] P. Zhi, Y. Li, B. Chen, X. Bai, Z. Sheng, Fuzzy design optimization-based fatigue reliability analysis of welding robots, IEEE Access, 8 (2020) 64906-64917.
[177] H.A. El Kadi, Y. Al-Assaf, The use of neural networks in the prediction of the fatigue life of different composite materials, in: Proceedings of 'A giant step towards environmental awareness: from green composites to aerospace', 16th international conference on composite materials (ICCM-16), 2007, pp. 7-13.
[178] H. El Kadi, Y. Al-Assaf, Energy-based fatigue life prediction of fiberglass/epoxy composites using modular neural networks, Composite Structures, 57 (2002) 85-89.
[179] R.C.S. Freire Jr, A.D.D. Neto, E.M.F. de Aquino, Use of modular networks in the building of constant life diagrams, International Journal of Fatigue, 29 (2007) 389-396.
[180] R.C.S.F. Júnior, A.D.D. Neto, E.M.F. De Aquino, Comparative study between ANN models and conventional equations in the analysis of fatigue failure of GFRP, International journal of fatigue, 31 (2009) 831-839.
[181] R. Zhou, Z. Xing, H. Wang, Z. Piao, Y. Huang, W. Guo, R. Ma, Prediction of contact fatigue life of AT40 ceramic coating based on neural network, Anti-Corrosion Methods and Materials, 67 (2020) 83-100.
[182] H.W. Ahmad, J.H. Hwang, K. Javed, U.M. Chaudry, D.H. Bae, Probabilistic fatigue life prediction of dissimilar material weld using accelerated life method and neural network approach, Computation, 7 (2019) 10.
[183] W. Solano-Alvarez, M. Peet, E. Pickering, J. Jaiswal, A. Bevan, H. Bhadeshia, Synchrotron and neural network analysis of the influence of composition and heat treatment on the rolling contact fatigue of hypereutectoid pearlitic steels, Materials Science and Engineering: A, 707 (2017) 259-269.
[184] M. Jarrah, Y. Al-Assaf, H.E. Kadi, Neuro-fuzzy modeling of fatigue life prediction of unidirectional glass fiber/epoxy composite laminates, Journal of composite materials, 36 (2002) 685-700.
[185] A.P. Vassilopoulos, R. Bedi, Adaptive neuro-fuzzy inference system in modelling fatigue life of multidirectional composite laminates, Computational Materials Science, 43 (2008) 1086-1093.
[186] Y. Al-Assaf, H. El Kadi, Fatigue life prediction of composite materials using polynomial classifiers and recurrent neural networks, Composite Structures, 77 (2007) 561-569.

[187] H. El Kadi, Y. Al-Assaf, Prediction of the fatigue life of unidirectional glass fiber/epoxy composite laminae using different neural network paradigms, Composite Structures, 55 (2002) 239-246.
[188] W.A. Altabey, M. Noori, Fatigue life prediction for carbon fibre/epoxy laminate composites under spectrum loading using two different neural network architectures, International Journal of Sustainable Materials and Structural Systems, 3 (2017) 53-78.
[189] M.S. Abdullatef, N. AlRazzaq, M.M. Hasan, Prediction fatigue life of aluminum alloy 7075 T73 using neural networks and neuro-Fuzzy models, Engineering and Technology Journal, 34 (2016) 272-283.
[190] M. Al-Assadi, H. El Kadi, I. Deiab, Predicting the fatigue life of different composite materials using artificial neural networks, Applied Composite Materials, 17 (2010) 1-14.
[191] M. Al-Assadi, H.A. El Kadi, I.M. Deiab, Using artificial neural networks to predict the fatigue life of different composite materials including the stress ratio effect, Applied Composite Materials, 18 (2011) 297-309.
[192] M.K. Mini, M. Sowmya, Neural network paradigms for fatigue strength prediction of fiber-reinforced composite materials, International Journal of Advanced Structural Engineering, 4 (2012) 1-14.
[193] H. Kumar, R. Swamy, Fatigue life prediction of glass fiber reinforced epoxy composites using artificial neural networks, Composites Communications, 26 (2021) 100812.
[194] K. Ziane, A. Ilinca, S.S. Karganroudi, M. Dimitrova, Neural network optimization algorithms to predict wind turbine blade fatigue life under variable hygrothermal conditions, Eng, 2 (2021) 278-295.
[195] A. Sedaghat, M. Alitavoli, A. Darvizeh, R. Ansari Khalkhali, Post-fatigue life prediction of glare subjected to low-velocity impact, Scientia Iranica, 28 (2021) 305-315.
[196] M. Jakubek, Z. Waszczyszyn, Neural analysis of concrete fatigue durability by the neuro-fuzzy FWNN, in: Artificial Intelligence and Soft Computing-ICAISC 2004: 7th International Conference, Zakopane, Poland, June 7-11, 2004. Proceedings 7, Springer, 2004, pp. 1075-1080.
[197] J. Mohanty, B. Verma, D. Parhi, P. Ray, Application of artificial neural network for predicting fatigue crack propagation life of aluminum alloys, Arch Comput Mater Sci Surf Eng., 1 (2009) 133-138.
[198] A. Raja, S.T. Chukka, R. Jayaganthan, Prediction of fatigue crack growth behaviour in ultrafine grained al 2014 alloy using machine learning, Metals, 10 (2020) 1349.
[199] H. Wang, W. Zhang, F. Sun, W. Zhang, A comparison study of machine learning based algorithms for fatigue crack growth calculation, Materials, 10 (2017) 543.
[200] J. Mohanty, D. Parhi, P. Ray, B. Verma, Prediction of residual fatigue life under interspersed mixed-mode (I and II) overloads by Artificial Neural Network, Fatigue & Fracture of Engineering Materials & Structures, 32 (2009) 1020-1031.
[201] G. Seed, G. Murphy, The applicability of neural networks in modelling the growth of short fatigue cracks, Fatigue & Fracture of Engineering Materials & Structures, 21 (1998) 183-190.
[202] J. Jia, J.F. Davalos, An artificial neural network for the fatigue study of bonded FRP–wood interfaces, Composite structures, 74 (2006) 106-114.
[203] A.A. Shittu, A. Mehmanparast, M. Shafiee, A. Kolios, P. Hart, K. Pilario, Structural reliability assessment of offshore wind turbine support structures subjected to pitting corrosion-fatigue: A damage tolerance modelling approach, Wind Energy, 23 (2020) 2004-2026.
[204] M. Haque, K. Sudhakar, ANN based prediction model for fatigue crack growth in DP steel, Fatigue & Fracture of Engineering Materials & Structures, 24 (2001) 63-68.

[205] M.E. Haque, K. Sudhakar, Prediction of corrosion–fatigue behavior of DP steel through artificial neural network, International Journal of Fatigue, 23 (2001) 1-4.
[206] H.B. Younis, K. Kamal, M.F. Sheikh, A. Hamza, T. Zafar, Prediction of fatigue crack growth rate in aircraft aluminum alloys using radial basis function neural network, in: 2018 Tenth International Conference on Advanced Computational Intelligence (ICACI), IEEE, 2018, pp. 825-830.
[207] A. Fotovati, T. Goswami, Prediction of elevated temperature fatigue crack growth rates in TI-6AL-4V alloy–neural network approach, Materials & design, 25 (2004) 547-554.
[208] M.A. Razzaq, K.A. Ariffin, A. El Shafie, S. Abdullah, Z. Sajuri, N. Akeel, Adaptive neural network modelling in fatigue life prediction under load history effects, in: Advanced Materials Research, Trans Tech Publ, 2011, pp. 1266-1270.
[209] D.-W. Lee, S.-H. Hong, S.-S. Cho, W.-S. Joo, A study on fatigue damage modeling using neural networks, Journal of mechanical science and technology, 19 (2005) 1393-1404.
[210] O. Yasnii, O. Pastukh, Y.I. Pyndus, N. Lutsyk, I. Didych, Prediction of the diagrams of fatigue fracture of D16T aluminum alloy by the methods of machine learning, Materials Science, 54 (2018) 333-338.
[211] J. Mohanty, B. Verma, P. Ray, D. Parhi, Application of artificial neural network for fatigue life prediction under interspersed mode-I spike overload, 38 (2010) 177-187.
[212] F. Iacoviello, D. Iacoviello, M. Cavallini, Analysis of stress ratio effects on fatigue propagation in a sintered duplex steel by experimentation and artificial neural network approaches, International Journal of Fatigue, 26 (2004) 819-828.
[213] G. Allegri, Modelling fatigue delamination growth in fibre-reinforced composites: Power-law equations or artificial neural networks?, Materials & Design, 155 (2018) 59-70.
[214] W. Zhang, Z. Bao, S. Jiang, J. He, An artificial neural network-based algorithm for evaluation of fatigue crack propagation considering nonlinear damage accumulation, Materials, 9 (2016) 483.
[215] A. Fathi, A. Aghakouchak, Prediction of fatigue crack growth rate in welded tubular joints using neural network, International journal of fatigue, 29 (2007) 261-275.
[216] J.-Y. Kang, J.-H. Song, Neural network applications in determining the fatigue crack opening load, International journal of fatigue, 20 (1998) 57-69.
[217] L. Xie, Y. Yang, Z. Zhou, J. Zheng, M. Tao, Z. Man, Dynamic neural modeling of fatigue crack growth process in ductile alloys, Information Sciences, 364 (2016) 167-183.
[218] M.E. Haque, K. Sudhakar, ANN back-propagation prediction model for fracture toughness in microalloy steel, International Journal of Fatigue, 24 (2002) 1003-1010.
[219] M. Abambres, E.O. Lantsoght, ANN-based fatigue strength of concrete under compression, Materials, 12 (2019) 3787.
[220] J. Durodola, N. Li, S. Ramachandra, A. Thite, A pattern recognition artificial neural network method for random fatigue loading life prediction, International Journal of Fatigue, 99 (2017) 55-67.
[221] S. Ramachandra, J. Durodola, N. Fellows, S. Gerguri, A. Thite, Experimental validation of an ANN model for random loading fatigue analysis, International Journal of Fatigue, 126 (2019) 112-121.
[222] J.F. Durodola, S. Ramachandra, S. Gerguri, N. Fellows, Artificial neural network for random fatigue loading analysis including the effect of mean stress, International Journal of fatigue, 111 (2018) 321-332.

[223] J. Durodola, Artificial neural network for Gaussian and non-Gaussian random fatigue loading analysis, Proceedings of the Institution of Mechanical Engineers, Part C: Journal of Mechanical Engineering Science, 233 (2019) 7525-7544.
[224] C. Tao, C. Zhang, H. Ji, J. Qiu, Application of neural network to model stiffness degradation for composite laminates under cyclic loadings, Composites Science and Technology, 203 (2021) 108573.
[225] E. Yang, Y. Tang, L. Li, W. Yan, B. Huang, Y. Qiu, Research on the recurrent neural network-based fatigue damage model of asphalt binder and the finite element analysis development, Construction and Building Materials, 267 (2021) 121761.
[226] H. Lee, H.J. Lim, T. Skinner, A. Chattopadhyay, A. Hall, Automated fatigue damage detection and classification technique for composite structures using Lamb waves and deep autoencoder, Mechanical Systems and Signal Processing, 163 (2022) 108148.
[227] C. Tao, C. Zhang, H. Ji, J. Qiu, Fatigue damage characterization for composite laminates using deep learning and laser ultrasonic, Composites Part B: Engineering, 216 (2021) 108816.
[228] C. Mylonas, I. Abdallah, E. Chatzi, Conditional variational autoencoders for probabilistic wind turbine blade fatigue estimation using Supervisory, Control, and Data Acquisition data, Wind Energy, 24 (2021) 1122-1139.
[229] S. Feng, X. Han, Z. Ma, G. Królczyk, Z. Li, Data-driven algorithm for real-time fatigue life prediction of structures with stochastic parameters, Computer Methods in Applied Mechanics and Engineering, 372 (2020) 113373.
[230] N. Gebraeel, M. Lawley, R. Liu, V. Parmeshwaran, Residual life predictions from vibration-based degradation signals: a neural network approach, IEEE Transactions on industrial electronics, 51 (2004) 694-700.
[231] N. Amiri, G. Farrahi, K.R. Kashyzadeh, M. Chizari, Applications of ultrasonic testing and machine learning methods to predict the static & fatigue behavior of spot-welded joints, Journal of Manufacturing Processes, 52 (2020) 26-34.
[232] S. Chatterjee, A. Keprate, Predicting remaining fatigue life of topside piping using deep learning, in: 2021 International Conference on Applied Artificial Intelligence (ICAPAI), IEEE, 2021, pp. 1-6.
[233] S. Saon, T. Hiyama, Predicting remaining useful life of rotating machinery based artificial neural network, Computers & Mathematics with Applications, 60 (2010) 1078-1087.
[234] R. Huang, L. Xi, X. Li, C.R. Liu, H. Qiu, J. Lee, Residual life predictions for ball bearings based on self-organizing map and back propagation neural network methods, Mechanical systems and signal processing, 21 (2007) 193-207.
[235] F.F. Barsoum, E.V. Hill, J. Suleman, A. Korcak, Y. Zhang, Neural network fatigue life prediction in notched bridge steel I-beams from acoustic emission amplitude data, Journal of acoustic emission, 29 (2011) 251-259.
[236] H.J. Lim, H. Sohn, Y. Kim, Data-driven fatigue crack quantification and prognosis using nonlinear ultrasonic modulation, Mechanical Systems and Signal Processing, 109 (2018) 185-195.
[237] Y.A. Yucesan, F.A. Viana, Wind Turbine Main Bearing Fatigue Life Estimation with Physicsinformed Neural Networks, in: Annual conference of the PHM society, 2019, pp. 1-14.
[238] Y.A. Yucesan, F.A. Viana, A physics-informed neural network for wind turbine main bearing fatigue, International Journal of Prognostics and Health Management, 11 (2020) 1-17.
[239] F.A. Viana, R.G. Nascimento, A. Dourado, Y.A. Yucesan, Estimating model inadequacy in ordinary differential equations with physics-informed neural networks, Computers & Structures, 245 (2021) 106458.

[240] A. Dourado, F.A. Viana, Physics-informed neural networks for missing physics estimation in cumulative damage models: a case study in corrosion fatigue, Journal of Computing and Information Science in Engineering, 20 (2020) 061007.
[241] E. Fathalla, Y. Tanaka, K. Maekawa, Remaining fatigue life assessment of in-service road bridge decks based upon artificial neural networks, Engineering Structures, 171 (2018) 602-616.
[242] B. Lotfi, P. Beiss, Application of neural networking for fatigue limit prediction of powder metallurgy steel parts, Materials & Design, 50 (2013) 440-445.
[243] Y.M. Zhao, H.C. Kou, W. Wu, Y. Deng, B. Tang, J.S. Li, Prediction of high cycle fatigue property of Ti-6Al-4V alloy using artificial neural network, in: Materials Science Forum, Trans Tech Publ, 2016, pp. 360-367.
[244] A. Agrawal, A. Choudhary, An online tool for predicting fatigue strength of steel alloys based on ensemble data mining, International Journal of Fatigue, 113 (2018) 389-400.
[245] A. Agrawal, P.D. Deshpande, A. Cecen, G.P. Basavarsu, A.N. Choudhary, S.R. Kalidindi, Exploration of data science techniques to predict fatigue strength of steel from composition and processing parameters, Integrating Materials and Manufacturing Innovation, 3 (2014) 90-108.
[246] C. Gebhardt, T. Trimborn, F. Weber, A. Bezold, C. Broeckmann, M. Herty, Simplified ResNet approach for data driven prediction of microstructure-fatigue relationship, Mechanics of Materials, 151 (2020) 103625.
[247] T. Shiraiwa, Y. Miyazawa, M. Enoki, Prediction of fatigue strength in steels by linear regression and neural network, Materials Transactions, 60 (2018) 189-198.
[248] F. Aymerich, M. Serra, Prediction of fatigue strength of composite laminates by means of neural networks, Key Engineering Materials, 144 (1997) 231-242.
[249] E. Maleki, O. Unal, Fatigue limit prediction and analysis of nano-structured AISI 304 steel by severe shot peening via ANN, Engineering with Computers, 37 (2021) 2663-2678.
[250] S. Malinov, W. Sha, J. McKeown, Modelling the correlation between processing parameters and properties in titanium alloys using artificial neural network, Computational materials science, 21 (2001) 375-394.
[251] R. Cabell, C. Fuller, W. O'Brien, Neural network modelling of oscillatory loads and fatigue damage estimation of helicopter components, Journal of Sound and Vibration, 209 (1998) 329-342.
[252] L. Vera-Tudela, M. Kühn, Analysing wind turbine fatigue load prediction: The impact of wind farm flow conditions, Renewable Energy, 107 (2017) 352-360.
[253] Y. Tjiptowidjojo, C. Przybyla, M. Shenoy, D.L. McDowell, Microstructure-sensitive notch root analysis for dwell fatigue in Ni-base superalloys, International Journal of Fatigue, 31 (2009) 515-525.
[254] A. Samir, A. Simon, A. Scholz, C. Berger, Service-type creep-fatigue experiments with cruciform specimens and modelling of deformation, International Journal of Fatigue, 28 (2006) 643-651.
[255] X. Xu, K. Shi, X. Li, Z. Li, R. Wang, Y. Chen, Optimization analysis method of new orthotropic steel deck based on backpropagation neural network-simulated annealing algorithm, Advances in Civil Engineering, 2021 (2021) 1-16.
[256] R. Chen, Y.M. Low, Reducing uncertainty in time domain fatigue analysis of offshore structures using control variates, Mechanical Systems and Signal Processing, 149 (2021) 107192.
[257] J. Chen, S. Liu, W. Zhang, Y. Liu, Uncertainty quantification of fatigue SN curves with sparse data using hierarchical Bayesian data augmentation, International Journal of Fatigue, 134 (2020) 105511.

[258] F. Hajializadeh, A. Ince, Finite element–based numerical modeling framework for additive manufacturing process, Material Design & Processing Communications, 1 (2019) e28.
[259] F. Hajializadeh, A. Ince, Integration of artificial neural network with finite element analysis for residual stress prediction of direct metal deposition process, Materials Today Communications, 27 (2021) 102197.
[260] R. Burghardt, M. Wächter, L. Masendorf, A. Esderts, Estimation of elastic–plastic notch strains and stresses using artificial neural networks, Fatigue & Fracture of Engineering Materials & Structures, 44 (2021) 2718-2735.
[261] M. Kazeruni, A. Ince, Data-driven artificial neural network for elastic plastic stress and strain computation for notched bodies, Theoretical and Applied Fracture Mechanics, 125 (2023) 103917.
[262] A. Zhang, D. Mohr, Using neural networks to represent von Mises plasticity with isotropic hardening, International Journal of Plasticity, 132 (2020) 102732.
[263] F. Masi, I. Stefanou, P. Vannucci, V. Maffi-Berthier, Material modeling via thermodynamics-based artificial neural networks, in: Workshop on Joint Structures and Common Foundations of Statistical Physics, Information Geometry and Inference for Learning, Springer, 2020, pp. 308-329.
[264] F. Masi, I. Stefanou, P. Vannucci, V. Maffi-Berthier, Thermodynamics-based artificial neural networks for constitutive modeling, Journal of the Mechanics and Physics of Solids, 147 (2021) 104277.
[265] M. Mozaffar, R. Bostanabad, W. Chen, K. Ehmann, J. Cao, M. Bessa, Deep learning predicts path-dependent plasticity, Proceedings of the National Academy of Sciences, 116 (2019) 26414-26420.
[266] T. Tancogne-Dejean, M.B. Gorji, J. Zhu, D. Mohr, Recurrent neural network modeling of the large deformation of lithium-ion battery cells, International Journal of Plasticity, 146 (2021) 103072.
[267] L. Wu, N.G. Kilingar, L. Noels, A recurrent neural network-accelerated multi-scale model for elasto-plastic heterogeneous materials subjected to random cyclic and non-proportional loading paths, Computer Methods in Applied Mechanics and Engineering, 369 (2020) 113234.
[268] S. Manson, G. Halford, Practical implementation of the double linear damage rule and damage curve approach for treating cumulative fatigue damage, International journal of fracture, 17 (1981) 169-192.
[269] Z. Xiulin, M.A. Hirt, Fatigue crack propagation in steels, Engineering Fracture Mechanics, 18 (1983) 965-973.
[270] M.D. Chapetti, Fatigue propagation threshold of short cracks under constant amplitude loading, International Journal of Fatigue, 25 (2003) 1319-1326.
[271] J. Peters, B. Boyce, X. Chen, J. McNaney, J. Hutchinson, R. Ritchie, On the application of the Kitagawa–Takahashi diagram to foreign-object damage and high-cycle fatigue, Engineering fracture mechanics, 69 (2002) 1425-1446.
[272] S. Ye, X.C. Zhang, J.G. Gong, S.T. Tu, C.C. Zhang, Multi-scale fatigue crack propagation in 304 stainless steel: experiments and modelling, Fatigue & Fracture of Engineering Materials & Structures, 40 (2017) 1928-1941.
[273] K. Tanaka, Y. Akiniwa, Resistance-curve method for predicting propagation threshold of short fatigue cracks at notches, Engineering Fracture Mechanics, 30 (1988) 863-876.
[274] J. POLÁK, P. ZEZULKA, Short crack growth and fatigue life in austenitic-ferritic duplex stainless steel, Fatigue & Fracture of Engineering Materials & Structures, 28 (2005) 923-935.

[275] R. Döring, J. Hoffmeyer, T. Seeger, M. Vormwald, Short fatigue crack growth under nonproportional multiaxial elastic–plastic strains, International Journal of Fatigue, 28 (2006) 972-982.
[276] S. Rabbolini, S. Beretta, S. Foletti, A. Riva, Short crack propagation in LCF regime at room and high temperature in Q & T rotor steels, International Journal of Fatigue, 75 (2015) 10-18.
[277] V.H.C. de Albuquerque, A.R. de Alexandria, P.C. Cortez, J.M.R. Tavares, Evaluation of multilayer perceptron and self-organizing map neural network topologies applied on microstructure segmentation from metallographic images, NDT & E International, 42 (2009) 644-651.
[278] V.H.C. De Albuquerque, J.M.R. Tavares, P.C. Cortez, Quantification of the microstructures of hypoeutectic white cast iron using mathematical morphology and an artificial neural network, International Journal of Microstructure and Materials Properties, 5 (2010) 52-64.
[279] V.H.C. de Albuquerque, P.C. Cortez, A.R. de Alexandria, J.M.R. Tavares, A new solution for automatic microstructures analysis from images based on a backpropagation artificial neural network, Nondestructive Testing and Evaluation, 23 (2008) 273-283.
[280] J.F. Barbosa, J.A. Correia, R.F. Júnior, A.M. De Jesus, Fatigue life prediction of metallic materials considering mean stress effects by means of an artificial neural network, International Journal of fatigue, 135 (2020) 105527.
[281] A. Muc, Fuzzy approach in modeling static and fatigue strength of composite materials and structures, Neurocomputing, 393 (2020) 156-164.
[282] S. Ghandehari, M.M. Montazer-Rahmati, M. Asghari, Modeling the flux decline during protein microfiltration: a comparison between feed-forward back propagation and radial basis function neural networks, Separation Science and Technology, 48 (2013) 1324-1330.
[283] X. Huang, T. Moan, Improved modeling of the effect of R-ratio on crack growth rate, International Journal of fatigue, 29 (2007) 591-602.
[284] Swain, Zhao, Ding, Small-crack growth and fatigue life predictions for high-strength aluminium alloys. Part II: crack closure and fatigue analyses, Fatigue & fracture of engineering materials & structures, 23 (2000) 59-72.
[285] P. Edwards, J.C. Newman Jr, Short-crack growth behaviour in various aircraft materials. AGARD-R-767, Neuilly-sur-Seine, France, 1990.
[286] J. Newman Jr, Analyses of fatigue and fatigue-crack growth under constant-and variable-amplitude loading, Mechanics of Materials Branch NASA Langley Research Center Hampton, Virginia USA, 1999.
[287] K. Wang, F. Wang, W. Cui, T. Hayat, B. Ahmad, Prediction of short fatigue crack growth of Ti-6Al-4V, Fatigue & Fracture of Engineering Materials & Structures, 37 (2014) 1075-1086.
[288] R. Cook, The Growth of Short Fatigue Cracks in an Aluminium Alloy, Technical Report, Farnborough, Hampshire, 1992.
[289] J. Newman Jr, X. Wu, S. Venneri, C. Li, Small-crack effects in high-strength aluminum alloys, NASA Langley Research Center, Hampton, VA, United States, 1994.
[290] P. Chong-Myong, S. Ji-Ho, Crack growth and closure behavior of short fatigue cracks, Engineering fracture mechanics, 47 (1994) 327-343.
[291] J.C. Newman, P. Edwards, Short-crack growth behaviour in an aluminum alloy: an AGARD cooperative test programme, in, AGARD, 1988.
[292] R. Ritchie, B. Boyce, J. Campbell, O. Roder, A. Thompson, W. Milligan, Thresholds for high-cycle fatigue in a turbine engine Ti–6Al–4V alloy, International Journal of Fatigue, 21 (1999) 653-662.

[293] J. Newman, A crack-closure model for predicting fatigue crack growth under aircraft spectrum loading, in, STP 748 Methods and models for predicting fatigue crack growth under random loading, ASTM International, 1981.
[294] K. Sadananda, A. Vasudevan, R. Holtz, Extension of the unified approach to fatigue crack growth to environmental interactions, International Journal of Fatigue, 23 (2001) 277-286.
[295] K. Sadananda, S. Sarkar, D. Kujawski, A. Vasudevan, A two-parameter analysis of S–N fatigue life using Δσ and σmax, International Journal of Fatigue, 31 (2009) 1648-1659.
[296] W. Chen, H. Chen, Cyclic J-integral using the linear matching method, International Journal of Pressure Vessels and Piping, 108 (2013) 72-80.
[297] L. Gan, H. Wu, Z. Zhong, Fatigue life prediction considering mean stress effect based on random forests and kernel extreme learning machine, International Journal of Fatigue, 158 (2022) 106761.
[298] S.N.S. Mortazavi, A. Ince, An artificial neural network modeling approach for short and long fatigue crack propagation, Computational Materials Science, 185 (2020) 109962.
[299] S.N.S. Mortazavi, A. Ince, A radial basis function artificial neural network methodology for short and long fatigue crack propagation, Proc. Can. Soc. Mech. Eng. Int. Congr, 2021 (2021).
[300] S. Himmiche, S.N.S. Mortazavi, A. Ince, Comparative Study of Neural Network–Based Models for Fatigue Crack Growth Predictions of Short Cracks, Journal of Peridynamics and Nonlocal Modeling, 4 (2022) 501-5226.
[301] B. Wang, L. Xie, J. Song, B. Zhao, C. Li, Z. Zhao, Curved fatigue crack growth prediction under variable amplitude loading by artificial neural network, International Journal of Fatigue, 142 (2021) 105886.
[302] H.T. Thai, Machine learning for structural engineering: A state-of-the-art review, in: Structures, Elsevier, 2022, pp. 448-491.
[303] S. Sony, K. Dunphy, A. Sadhu, M. Capretz, A systematic review of convolutional neural network-based structural condition assessment techniques, Engineering Structures, 226 (2021) 111347.
[304] M. Kamiyama, K. Shimizu, Y. Akiniwa, Prediction of low-cycle fatigue crack development of sputtered Cu thin film using deep convolutional neural network, International Journal of Fatigue, 162 (2022) 106998.
[305] Z. Nie, H. Jiang, L.B. Kara, Stress field prediction in cantilevered structures using convolutional neural networks, Journal of Computing and Information Science in Engineering, 20 (2020) 011002.
[306] A. Powar, P. Date, Modeling of microstructure and mechanical properties of heat treated components by using Artificial Neural Network, Materials Science and Engineering: A, 628 (2015) 89-97.
[307] S. Guessasma, C. Coddet, Microstructure of APS alumina–titania coatings analysed using artificial neural network, Acta Materialia, 52 (2004) 5157-5164.
[308] J. Kusiak, R. Kuziak, Modelling of microstructure and mechanical properties of steel using the artificial neural network, Journal of materials processing technology, 127 (2002) 115-121.
[309] S.N.S. Mortazavi, A. Ince, Artificial neural networks-based J-integral prediction for cracked bodies under elasto-plastic deformation state–monotonic loading, International Journal of Fatigue, 167 (2023) 107311.
[310] D.Z. Huang, K. Xu, C. Farhat, E. Darve, Learning constitutive relations from indirect observations using deep neural networks, Journal of Computational Physics, 416 (2020) 109491.

[311] H. Gong, Z.G. Jin, F.P. Yang, W.T. Mao, Analysis of stop-hole effects on mode I-II fatigue crack behavior for Q420 steel using experiments, FEM and variable length RNN approaches, Theoretical and Applied Fracture Mechanics, 124 (2023) 103823.

Appendix A

General formulation of the equivalent domain integral (EDI) method under mode I and II loading in cracked bodies.

In the present appendix, mode I and mode II of loading are discussed. Similar formulation can be developed for mode III as well.

Figure 1 schematically shows a tube with radius of ε that embeds a segment of crack front with the length of Δ. The limit of Δ and ε/Δ tends to zero. The J-integral with respect to volume surrounded by the surface A_ε is defined as Eq. 1:

$$\int_\Delta J_{x_k}\, dx_3 = \lim_{\substack{\varepsilon/\Delta\to 0 \\ \Delta\to 0}} \int \left[W n_k - \sigma_{ij} \frac{\partial u_i}{\partial x_k} n_j \right] dA \tag{1}$$

where W is the strain energy density, σ_{ij} is the stress tensor, u_i is the displacement vector, and n_k is the normal vector on the closed surface A_ε. In the present notation, i and j take the values 1, 2, and 3, and k takes the values 1 and 2 corresponding to the mode I and II, respectively. As a result, J_{x_k} is the total energy flux leaving the closed surface A_ε per unit crack front length in the direction of k. As shown in Fig. 1, x_1 and x_3 are in the crack plane and are normal and tangential to crack front, respectively. x_2 is normal to crack plane. The complete surface integral with respect to the surfaces shown in Fig.1 can be written as Eq. 2 as follows:

$$\int_\Delta J_{x_k}\, dx_3 = \int_{A_\varepsilon} Q\, dA + \int_{A_{\varepsilon_1}+A_{\varepsilon_2}} Q\, dA + \int_{A_{\varepsilon_{ct}}+A_{\varepsilon_{cb}}} Q\, dA \tag{2}$$

where A_{ε_1} and A_{ε_2} are cross-sectional areas of the tube at the points O_1 and O_2, respectively. The subscripts ct and cb represent the crack surfaces at the top and bottom of the crack, respectively, and Q and W are defined as follows:

$$Q = \left[W n_k - \sigma_{ij} \frac{\partial u_i}{\partial x_k} n_j \right] \tag{3}$$

$$W = \int_0^{\varepsilon_{ij}} \sigma_{ij} d\varepsilon_{ij} \tag{4}$$

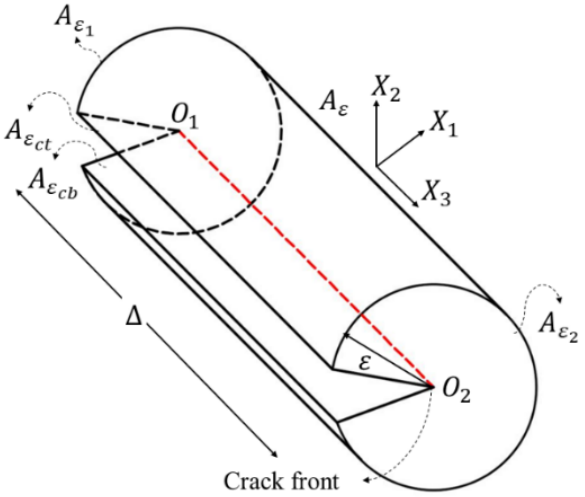

Fig. 1 Crack front and enclosed surface A_ε in the conventional approach.

Figure 2 shows two tubular surfaces A_ε and A spanning along cross-sectional areas at O_1 and O_2 on the crack front. The tube A is arbitrary and encloses the tube A_ε on which the J-integral is determined. The right hind side of Eq. 2 can be multiplied by unity as follows:

$$\int_\Delta J_{x_k}\, dx_3 = 1.\int_{A_\varepsilon} Q\, dA + 1.\int_{A_{\varepsilon_1}+A_{\varepsilon_2}} Q\, dA + 1.\int_{A_{\varepsilon_{ct}}+A_{\varepsilon_{cb}}} Q\, dA - 0.\int_A Q\, dA \tag{5}$$

It should be noted that Eq. 5 assumes a unit extension of the crack front segment along x_1. If an arbitrary virtual extension of crack front is considered, Eq. 5 is required to be modified as:

$$\int_\Delta J_{x_k} S\ dx_3 = 1.\int_{A_\varepsilon} QS\, dA + 1.\int_{A_{\varepsilon_1}+A_{\varepsilon_2}} QS\, dA + 1.\int_{A_{\varepsilon_{ct}}+A_{\varepsilon_{cb}}} QS\, dA - 0.\int_A QS\, dA \tag{6}$$

where $S(x_1, x_2, x_3)$ is an arbitrary and continuous function with the following properties:

$$S(x_1, x_2, x_3) = 0 \quad \text{at surface } A \tag{7}$$

$$S(x_1, x_2, x_3) = 0 \quad \text{at end surfaces } (O_1 \text{ and } O_2) \text{ of the tubes} \tag{8}$$

$$S(x_1, x_2, x_3) = S(x_3) \text{ on the surface } A_\varepsilon \tag{9}$$

The function S is shown as q as a typical notation in a 2D cracked specimen. Since $\lim \Delta \to 0$, J_{x_k} can be considered as a constant along the crack front segment length Δ. Thus, Eq. 6 can be written as:

$$J_{x_k}.f = \int_{A_\varepsilon} QS\, dA + \int_{A_{\varepsilon_1}+A_{\varepsilon_2}} QS\, dA + \int_{A_{\varepsilon_{ct}}+A_{\varepsilon_{cb}}} QS\, dA - \int_A QS\, dA \tag{10}$$

where

$$f = \int_{O_1}^{O_2} S(x_3) dx_3 \tag{11}$$

According to the Eq. 7-9, Eq. 10 can be rewritten as:

$$J_{x_k}.f = -\int_{A+(A-A_\varepsilon)_{ct}+A_\varepsilon+(A_\varepsilon-A)_{cb}} QS\, dA + \int_{(A-A_\varepsilon)_{ct}} QS\, dA + \int_{(A_\varepsilon-A)_{cb}} QS\, dA + \int_{A_{\varepsilon_{ct}}+A_{\varepsilon_{cb}}} Q\, dA \tag{12}$$

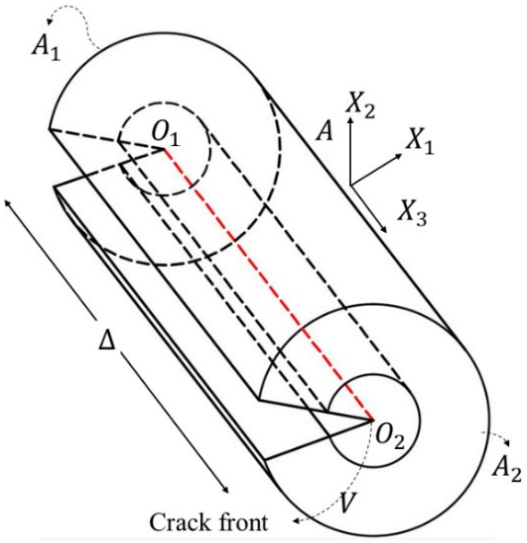

Fig. 2 Domain around the crack front in equivalent domain integral method.

The left-hand side of Eq. 12 can be expressed as:

$$J_{x_k}.f = \left(J_{x_k}.f\right)_{domain} + \left(J_{x_k}.f\right)_{crack\ faces} \tag{13}$$

For traction free crack faces $\left(J_{x_k}.f\right)_{crack\ faces}$ vanishes. Thus, with using Green's divergence theorem, the closed surface integrals of Eq. 12 can be written as:

$$J_{x_k}.f = -\int QS\,dA = -\int \left[W n_k - \sigma_{ij}\frac{\partial u_i}{\partial x_k} n_j\right] SdA \tag{14}$$

$$J_{x_k}.f = -\int_{(V-V_\varepsilon)} \left[\frac{\partial (WS)}{\partial x_k} - \frac{\partial}{\partial x_j}\left(\sigma_{ij}\frac{\partial u_i}{\partial x_k} S\right)\right] dV \tag{15}$$

Hence:

$$J_{x_k}.f = -\int_{(V-V_\varepsilon)} \left[W\frac{\partial S}{\partial x_k} - \sigma_{ij}\frac{\partial u_i}{\partial x_k}\frac{\partial S}{\partial x_j}\right] dV - \int_{(V-V_\varepsilon)} \left[\frac{\partial W}{\partial x_k} - \sigma_{ij}\frac{\partial \varepsilon_{ij}}{\partial x_k}\right] S\,dV \tag{16}$$

In the case of mashing behavior:

$$W = \int \sigma_{ij} d\varepsilon_{ij} \ \rightarrow \frac{\partial W}{\partial \varepsilon_{ij}} = \sigma_{ij} \tag{17}$$

$$\frac{\partial W}{\partial x_k} = \frac{\partial W}{\partial \varepsilon_{ij}}\frac{\partial \varepsilon_{ij}}{\partial x_k} \tag{18}$$

As a result:

$$\int_{(V-V_\varepsilon)} \left[\frac{\partial W}{\partial x_k} - \sigma_{ij}\frac{\partial \varepsilon_{ij}}{\partial x_k}\right] S\,dV = 0 \tag{19}$$

Thus:

$$J_{x_k}.f = \int_{(V-V_\varepsilon)} \left[\sigma_{ij}\frac{\partial u_i}{\partial x_k}\frac{\partial S}{\partial x_j} - W\frac{\partial S}{\partial x_k}\right] dV \tag{20}$$

$$J_{x_k}.f = \int_{(V-V_\varepsilon)} \left[\sigma_{ij}\frac{\partial u_i}{\partial x_k} - W\right]\frac{\partial S}{\partial x_j} dV \tag{21}$$